Experimental characterization, modelling and simulation at the microscale of the mechanical behavior of fibre bundles

Xinling Song

UNIVERSITÉ D'ORLÉANS

École doctorale énergie, matériaux, sciences de la terre et de l'univers

Laboratoire de Mécanique Gabriel Lamé

THÈSE présentée par :

Xinling SONG

soutenue le : **17 juillet 2024**

pour obtenir le grade de : **Docteur de l'Université d'Orléans**

Discipline/ Spécialité : Génie Mécanique

Experimental characterization, modelling and simulation at the microscale of the mechanical behaviour of fibre bundles

THÈSE dirigée par :

M. HIVET Gilles	Professeur, Université Orléans, Directeur.

RAPPORTEURS :

M. LEGRAND Xavier	Professeur, GEMTEX, Université de Lille, Rapporteur.
M. WANG Peng	Professeur, LPMT, Université de Haute-Alsace, Rapporteur.

JURY :

M. ALLAOUI Samir	Professeur, Université de Reims, Président du jury.
M. DO Duc Phi	Maître de conférences, Université Orléans, Examinateur.
M. GUXHO Genti	Professeur, Doyen d'université, Examinateur.
Mme HIVET Audrey	Maître de conférences, Université Orléans, Co-encadrant.
M. LEGRAND Xavier	Professeur, GEMTEX, Université de Lille, Rapporteur.
M. SHANWAN Anwar	Maître de conférences, Université Orléans, Co-encadrant.
M. WANG Peng	Professeur, LPMT, Université de Haute-Alsace, Rapporteur.

Résumé de la thèse

Introduction

Les matériaux composites sont utilisés dans de nombreuses applications, et tout particulièrement dans les transports. L'attrait pour ces matériaux est lié à leur ratio performance mécanique/masse très intéressant. Parmi les plus répandus, on trouve les matériaux composites à renfort fibreux, mais la fabrication des pièces en matériaux composites à renfort fibreux présente de nombreuses problématiques, ce qui freine leur développement. En effet, la maitrise et la mise au point des procédés résulte aujourd'hui d'un savoir-faire et d'une expérience issue d'une démarche empirique, bien plus que d'une maitrise complète des phénomènes physiques mis en jeu. Lors de la mise en œuvre de ces matériaux, la première étape consiste très souvent à mettre en forme un renfort fibreux sec ou avec la résine en phase liquide. Le comportement mécanique du renfort est donc un point clé lors de cette première étape d'autant plus que celle-ci aura également un impact fort sur les étapes suivantes de la fabrication. Or, un renfort fibreux est une structure complexe puisqu'elle résulte du tissage de milliers de fils, eux-mêmes constitués de l'assemblage de dizaines de milliers de fibres de quelques microns de diamètre. Ainsi, le comportement mécanique des renforts est obtenu par une somme de réponses obtenues expérimentalement à des sollicitations spécifiques (compression, traction, flexion, cisaillement, etc.). Ces réponses mécaniques sont par la suite modélisées par des équations dont la forme est obtenue par des hypothèses et un lissage sur les paramètres influents, sans approche véritablement rigoureuse de la physique mise en jeu qui est complexe (nombre important de fibres, variabilité, enchevêtrement, ensimage, etc.). C'est notamment le cas du comportement en compression pour lequel il est admis une relation directe entre la rigidité de compression et la fraction volumique de fibres par une loi empirique, qui, si elle fonctionne correctement, nécessite une identification à chaque nouveau type de fil et ne permet pas de faire ressortir les paramètres de structure qui pourraient permettre d'améliorer ou de concevoir des structures plus performantes mais aussi d'anticiper le comportement mécanique d'un renfort sans avoir à le réaliser et à le tester. L'objectif de cette thèse est donc de pouvoir s'attaquer à ce manque en étudiant le comportement mécanique d'un assemblage de fibres quasi parallèles qui sont les structures fibreuses les plus utilisées pour les applications techniques. Plusieurs stratégies sont possibles pour lever ce verrou ; une approche purement expérimentale induirait un très grand nombre d'essais puisque beaucoup de chemins de déformation et un grand nombre d'enchevêtrements possibles existent. Il est donc nécessaire de pouvoir passer par des

approches numériques efficaces permettant une étude paramétrique, c'est à dire réaliser un grand nombre de tests dans des temps réduits. La stratégie choisie est donc de pouvoir construire un estimateur virtuel du comportement d'un assemblage fibreux, validé par des essais. L'une des complexités pour l'étude du comportement de mèches de fibres est sans aucun doute la taille des fibres (quelques micromètres) qui les rendent très difficiles à manipuler, à observer individuellement. L'objectif étant de comprendre la phénoménologie de déformations des assemblages fibreux, des fibres modèles d'une échelle supérieure (500 Microns) sont utilisées dans un premier temps dans le cadre de ce travail avant de conclure sur des simulations avec des fibres à l'échelle ''réelle''. Pour atteindre cet objectif, plusieurs étapes doivent être franchies. La première est de mettre au point une stratégie numérique permettant de simuler de façon efficace, à l'échelle de la fibre, la déformation de l'architecture sous diverses sollicitations. La seconde est de mettre en place des protocoles de validation expérimentale afin d'assurer la cohérence entre l'estimateur virtuel et l'expérimentation. La troisième est de disposer d'indicateurs de la microstructure permettant d'analyser les résultats. Enfin, il est nécessaire de pouvoir créer différentes architectures avec des paramètres cibles et d'appliquer différents trajets de chargement pour analyser la réponse mécanique de la structure. Une première approche a été réalisée dans la cadre de la thèse d'Oussama HAJI (Haji Oussama, 2018). Celle-ci a permis de mettre en évidence la faisabilité des deux premières étapes mais il est maintenant nécessaire de pouvoir les améliorer et surtout de réaliser les deux dernières étapes ainsi que d'exploiter l'ensemble de la stratégie pour mener à bien des études paramétriques et conclure sur leur influence sur le comportement mécanique. Dans ce cadre, ce manuscrit de thèse est donc structuré selon trois chapitres principaux et neuf sections. Au début de chaque chapitre un bref résumé en français de son contenu est présenté.

Le premier chapitre est composé des sections 1, 2 et 3 et présente une étude bibliographique sur le comportement mécanique des matériaux fibreux lors de la compaction/compression et les méthodes de modélisation et simulation aux différentes échelles (macroscopique, mésoscopique et microscopique). Cette étude bibliographique permet, outre le choix de l'échelle d'étude, de montrer la pertinence de l'essai de compression pour une analyse phénoménologique riche. Ce chapitre présente également les méthodes de caractérisation des milieux fibreux ainsi que les développements de modèles virtuels nécessaires aux études numériques.

Le deuxième chapitre est composé des sections 4, 5 et 6 et présente la technique d'observation de la compaction des fibres via la tomographie et le procédé de reconstruction numérique en

3D d'un paquet de fibre. Ce chapitre présente également l'optimisation des paramètres de simulation du modèle numérique et le développement des indicateurs d'analyse de la microstructure d'un paquet de fibres. Aussi, des simulations numériques des essais de compaction/compression de fibres sont réalisées et comparées aux essais expérimentaux.
Le troisième chapitre est composé des sections 7, 8 et 9 et présente la stratégie de mise en place d'un générateur numérique de paquets de fibres virtuelles et aléatoires. Ce générateur virtuel est validé par comparaison avec des résultats expérimentaux puis des modèles d'assemblages fibreux sont créés avec d'étudier l'impact des paramètres microstructuraux sur le comportement en compaction/compression de l'assemblage fibreux.

Chapitre I : Mécanique des renforts fibreux : Comportement en compactage

Le premier chapitre de ce manuscrit porte sur une étude bibliographique focalisée sur des points différents en lien avec le sujet de la thèse. Une présentation des composantes principales d'un matériau composite est présentée en début du chapitre. Celle-ci focalise sur les matrices polymères, métalliques et céramiques les plus utilisées avec un accent plus particulier sur les matrices polymères thermoplastiques et thermodurcissables. Ensuite, les différents types des matériaux fibreux sont présentés étant donné que ceux-ci, avec leurs dispositions géométriques à différentes échelles, influent sur les propriétés mécaniques des matériaux composites. Ainsi, les matériaux fibreux peuvent se présenter à l'échelle macroscopique sous forme des renforts tissés 2D, des renforts 2.5D, des renforts 3D, des NCF (Non Crimp Fabric), renforts tricotés, etc. Quant à l'échelle mésoscopique, les fibres sont associées entre elles avec un certain niveau de cohésion et assemblées sous forme des câbles, des mèches, des torons torsadés, etc. La fibre elle-même constitue l'échelle microscopique qui peut être de matériaux différents, avec ou sans traitement de surface, mais aussi avec des sections de formes différentes. Il s'avère que les lois de modélisation utilisées pour la simulation de la compaction d'un paquet de fibres sont différentes en fonction de la forme de la section des fibres qui régit le contact entre les fibres.
Etant donné que les différentes échelles d'une structure fibreuse aient des dispositions matérielles et géométriques différentes, le comportement mécanique d'un renfort fibreux est tributaire du comportement à chacun échelle : macroscopique, mésoscopique et microscopique. Ainsi, dans un procédé de mise en forme d'un renfort fibreux, en vue de fabriquer un matériau composite, la caractérisation du comportement mécanique des structures fibreuses pourrait nécessiter un nombre très important des essais expérimentales afin d'étudier la phénoménologie de la mise en forme et comprendre éventuellement les mécanismes d'apparition des défauts de

mise en forme. La dépendance des essais expérimentales implique beaucoup de temps et d'investissement pour atteindre cet objectif. Afin de pallier cette contrainte, la mise en place des modèles dédiés à la simulation numérique s'avère donc très utile. La communauté scientifique s'intéresse par trois niveaux de simulation qui existent dans la littérature. Cette thèse s'intéresse plus particulièrement par l'échelle d'un paquet d'environ 40 fibres en polyester, où les fibres peuvent être considérées comme un matériau homogène et continu. De plus, la littérature montre que le comportement en compression qu'un paquet de fibres, comme les fibres synthétiques, a un aspect élastique linéaire et que ce comportement est fonction de la section des fibres qui, elle-même, peut être différente d'un matériau à l'autre. Pour ce qui est des fibres en polyester utilisées dans cette thèse, la section pourrait être circulaire selon la littérature, ce qui a été confirmé par des observations microscopiques également. En revanche, la surface des fibres n'est pas forcément lisse et le frottement doit ainsi être pris en compte dans la simulation numérique.

Ce chapitre présente aussi une synthèse des simulations de compaction des fibres qui existent dans la littérature sur les trois échelles d'une structure fibreuse et pour différents matériaux et structures. Il en ressort qu'une meilleure compréhension du comportement en compaction est obtenue lorsque l'on modélise le comportement à l'échelle microscopique afin de mieux comprendre l'interaction entre les fibres. Les études bibliographiques montrent que le comportement en compaction d'un paquet de fibre est non linéaire et irréversibles avec une hystérésis plus ou moins importante en fonction du matériau et de la réorganisation géométrique initiale des fibres dans la structure fibreuse. Les études montrent aussi que le comportement en compaction est influencé par plusieurs paramètres comme la rigidité des fibres en flexion, le nombre de contact et la fraction volumique des fibres. La compaction pourra aussi provoquer une relaxation pendant la compression qui, elle-même, est fonction de la vitesse de compaction.

La littérature cite également plusieurs études qui utilisent la technique de la tomographie pour investiguer la structure interne d'un milieu fibreux. Il en ressort que les tomographes peuvent utiliser différents types de rayonnements comme X-ray, Gamma-ray et les signales électriques et acoustiques. Cependant, la tomographie par des rayons X est souvent utilisée pour des applications industrielles (applications textiles) pour leur qualité d'avoir des images de très haute précision. La technologie de la tomographie consiste en deux phases : la projection de la partie scannée en 2D via des rayons X qui traversent la matière et la reconstruction en 3D de la structure scannée par des algorithmes de traitement d'images. La reconstruction d'un milieux fibreux par la tomographie est déjà utilisée par (Zheng et al., 2024) qui l'ont employée pour la

compaction des renforts trissés. En revanche, la technique de reconstruction 3D utilisée ma thèse est inspirée des travaux de (Latil et al., 2011), portés sur la compaction d'un paquet de fibres à l'échelle mésoscopique.

Ce chapitre résume également des études qui existent sur la mise en place des modèles géométriques dépendant de la tomographie pour reconstruire la structure 3D d'un milieu fibreux. En revanche, cette dépendance est chère et longue. Ainsi, nous nous sommes intéressés par des études qui portent sur des générateurs virtuels des structures fibreuses, de différentes géométries, à l'échelle mésoscopique. Un état d'art est fait sur les générateurs à l'échelle macroscopique mais aussi sur la génération d'un paquet de fibres à l'échelle mésoscopique. La simulation de la compression est détaillée via des modèles par des éléments discrets et d'autres par des éléments finis. Dans ces simulations, une bonne partie des études prend en compte l'effet du coefficient du frottement fibre/fibre et fibre/paroi sur le comportement en compaction des fibres.

Aussi, ce chapitre synthétise sur les différents types des éléments utilisés dans les simulations où le choix du type d'éléments est crucial pour une simulation correcte. Par exemple, des éléments de type ''treillis'' ne peuvent pas être adaptés pour les simulations d'un milieux fibreux en cisaillement, en torsion ou en flexion. Ainsi, comme les éléments discrets se basent sur la théorie des solides indéformables, ces éléments ne peuvent pas convenir pour nos simulations qui doivent prendre en compte la déformation des fibres en flexion. Ainsi, pour des simulations de compaction, où la flexion est la mode de sollicitation principale, le choix s'oriente vers des éléments finis où les fibres sont modélisées par des éléments de poutre. D'autres types de simulations se base aussi sur des simulations hybrides par des éléments discrets et des éléments finis en même temps, ce qui permet de définir les propriétés des fibres en traction et en flexion dans des structures classiques comme les renforts tissés. Ce type des simulations hybrides a été utilisé par exemple par (Daelemans et al., 2021). Dans ces dernières simulations, le comportement en compression semble être influencé par plusieurs paramètres comme le volume de la fibre et de son ratio Length/Diameter, le coefficient de frottement entre les fibres et la rigidité des fibres en flexion.

Pour finir ce chapitre, ma thèse actuelle prend le relais de la thèse de Haji qui porte sur la simulation de la compaction d'un paquet de plusieurs fibres en polyester. Son travail se base sur la reconstruction 3D d'un paquet de fibre par une reconstruction 3D grâce à une microtopographie à rayon X. La stratégie proposée dans la thèse d'Haji permet de définir, pour chaque slice (section), le centre de la section de chaque image 2D des slices issus du

tomographe. Ensuite, à partir de l'ensemble des slices, il a pu reconstruire l'axe de la fibre. Ensuite, une simulation a été faite par des éléments finis de type poutre (B31) via un modèle explicite. Haji a fait l'extraction des 39 fibres numériques à partir des fibres réelles et a simulé la compaction de ces fibres. En revanche, son travail présente une erreur de position entre les fibres simulées et les fibres réelles. De plus son modèle ne prend pas en compte le contact entre les fibres, la courbure et l'orientation des fibres. Par conséquent, ma thèse vient pour prendre en compte ses lacunes et porte sur la compaction des 40 fibres en PE de diamètre de 500 μm et de longueur de 15 mm. Les fibres sont disposées parallèles et légèrement enchevêtrées et la mode de déformation choisie est celle de la compaction.

Chapitre II : Développement des outils d'analyse numérique de la compaction des fibres

Le chapitre 2 porte focalise sur le développement des outils d'analyses numériques de la microstructure d'un paquet de fibres lors de la compaction. Dans ce cadre, le chapitre aborde trois sections majeures.

La première section porte sur la reconstruction d'une géométrie 3D pour un paquet de fibres en polyester lors de leur compaction via une machine de compaction située dans un tomographe. La géométrie initiale des fibres est scannée avant de commencer la compaction. Une fois scannée, un logiciel du tomographe est utilisé pour reconstruire le volume 3D du paquet. Ensuite, des essais de compaction avec asservissement en déplacement sont effectué à plusieurs pas de compaction. Après chaque étape de compaction, un scan de la géométrie est effectué par le tomographe. Les essais de compactions sont des effectuées en quasi statique avec une vitesse de compaction de 1mm/min. les essais montrent que l'évolution de la force de compaction suit une courbe exponentielle et la force de compaction se caractérise par une relaxation après chaque compaction, ce qui s'expliquer par une réorganisation des fibres afin de retrouver une nouvelle position d'équilibre. Après avoir reconstruit la géométrie 3D des fibres par le tomographe, la géométrie reconstruite servira, grâce à un code Matlab, à définir les points du centre des sections successives de chaque fibre. Ces points sont ensuite assemblés pour retrouver les trajets des fibres. La structure reconstruite est ensuite exportée vers Abaques comme une géométrie modèle pour paquet de fibres afin qu'elle soit utilisée pour des simulations de compaction. La résolution spatiale du scanner (taille des voxels) influent sur la précision de la reconstruction 3D parce qu'il pourrait impacter la précision de la définition des centres des sections et les diamètres de fibres.

La deuxième partie du chapitre 2 explique la méthodologie de génération d'un modèle géométrique d'un paquet de fibres en 3D par un estimateur numérique virtuel. Celui-ci consiste en deux phase : la génération d'un paquet de fibres à partir des fibres scannées par un tomographe et la simulation de la compaction des fibres générées. La stratégie de génération dépend avant tout d'un prétraitement par software FIJI des images de chaque section des fibres, récupérée par le tomographe. Ce prétraitement effectue une analyse de la distribution de l'intensité lumineuse des pixels appartenant aux sections de fibres individuelles, ce qui permet de séparer les fibres et les isoler de leur environnement. Une fois les images traitées par FIJI®, un code Matlab permet de détecter le centre de chaque section et le diamètre de chaque de fibre dans chaque slice via une fonction spécifique de Matlab ''Circle Hoff Transform (CHT)''. Le code Matlab est utilisé pour connecter les centres des sections et retrouver les axes des fibres à partir des centres des sections identifiés. Ensuite, une simulation de la compaction des fibres est effectuée par Abaqus ABAQUS®/EXPLICIT sur la base d'une stratégie mise en place dans la thèse de Haji. Dans le cadre de la thèse actuelle, la stratégie de Haji est développée par la prise en compte de la gravité et complétée par des nouvelles simulations. Dans celles-ci, les mors de compression sont modélisés par des éléments discrets du fait que les plateaux de compression soient extraits par CATIA V5® où il n'y avait pas la possibilité de choisir d'autre type d'éléments. Il était donc possible d'utiliser des éléments discrets uniquement. En revanche, pour la simulation de la compaction des fibres créées, des éléments analytiques ont été utilisés. Il parait que la précision des deux types d'éléments est la même mais les éléments analytiques sont plus efficaces pour leur temps de calculs et simulation. Les éléments utilisés pour les fibres sont ainsi des éléments B31 de type poutre. Afin de mener à bien les simulations, une définition d'un ensemble de paramètres intrinsèques était nécessaire. Ainsi, la valeur du coefficient de frottement, nécessaire pour modéliser le contact entre fibres, a été définie par μ=0.2 selon la thèse de (Gassara, 2016) ; Le coefficient de poisson est de ν=0.25 selon la thèse de Haji. Quant à la valeur du module de l'élasticité, des essais de tractions monotones et cycliques ont été effectués pour trouver cette valeur et décrire le comportement des fibres. Il en ressort par conséquent un comportement elastoplastique des fibres, ce qui a été introduit dans les simulations, et un module de Young de 6 Gpa alors que la déformation maximale de Hencky de 22.5 à 30%.

Cependant, la détections des centres des sections de chaque fibre présente des erreurs de l'ordre de ± 1 pixel dans la stratégie actuelle, ce qui signifie que la géométrie des fibres exportées dans les codes des éléments finis pourra provoquer des pénétrations des fibres dans Abaqus alors

qu'elles ne le sont pas réellement. En revanche, les résultats montrent malgré tout que la stratégie reste cohérente puisque l'erreur de pénétration ne présente que 2% du diamètre des fibres. De plus, une stratégie de correction de la pénétration a été proposée dans la thèse actuelle et prend en compte l'effet de la gravité sur la disposition spatiale des fibres.

La dernière partie du chapitre porte sur la mise en place des outils numériques pour analyser la microstructure d'un paquet de fibre et observer l'évolution de la compaction en définissant des indicateurs intrinsèques comme la position des fibres, le nombre entre les fibres, l'ondulation et les orientations spatiales des fibres, l'angle décrivant la disposition des sections des fibres, les unes par rapports aux autres, dans le plan d'une slice donnée, l'angle entre deux fibres mesurées dans un plan perpendiculaire au plan des slices, le rayon de courbure et l'ondulation des fibres dans un plan et la torsion des fibres, l'orientation des fibres. Ensuite, ces indicateurs ont été codés pour analyser la compaction numérique et expérimentale automatiquement. Toutefois, la mise en place des indicateurs fiables constitue un défi pour ces simulations parce qu'il pourrait y a voir deux sources d'erreur : la première pourrait être due à la reconstruction des fibres et la deuxième pourrait venir des erreurs de calculs des indicateurs. Enfin, les indicateurs développés dans cette thèse ont été utilisés pour analyser des structures numériques et d'autres structures scannées par le tomographe afin décrire l'évolution de la compaction et définir les orientations des fibres, les contacts entre les fibres elles-mêmes, les contacts entre les fibres et les plateaux de compression et plein d'autres paramètres. Les analysent montre que cette démarche numérique, de modélisation et de simulation, reste très satisfaisante puisque les erreurs de l'estimateur numérique restent très raisonnables. A titre d'exemple, l'erreur de la position des fibres est l'ordre de 2% du diamètre des fibres.

Étant donné que l'estimateur numérique est prouvé d'être fiable, il sera possible de générer plusieurs modèles géométriques des paquets de fibres et d'y apporter une étude paramétrique de la compaction, ce qui fera l'objet du chapitre suivant.

Chapter III : Générateur d'un paquet de fibres aléatoires et analyse de l'influence des paramètres de génération

Le chapitre III a pour objectif la création d'un générateur de paquets de fibres virtuel, sa validation et son utilisation afin de tester différents paramètres microstructuraux sur la réponse sous différentes sollicitations. Il est composé des sections suivantes :

- Section 7, qui présente la stratégie de création du générateur virtuel et sa validation

- Section 8, qui présente l'effet des paramètres microstructuraux des paquets de fibres sur le comportement en compression
- Section 9, qui étudie l'effet de différents trajets de chargement, de la vitesse de sollicitation et de la densité de fibres sur le comportement en compression

Section 7 : stratégie création d'un générateur virtuel d'assemblages de fibres et vérification de sa faisabilité

Cette section expose la stratégie de création d'un générateur de paquets de fibres virtuel, permettant de contrôler les paramètres microstructuraux établi au Chapitre II à partir des observations tomographiques ; il s'agit par exemple du nombre de fibres, de l'élancement des fibres, de l'ondulation, etc.

La méthode choisie repose sur une stratégie simple et efficace en 3 étapes et nécessitant 2 logiciels déjà utilisés dans le reste de l'étude : Matlab pour les 2 premières étapes et Abaqus® pour la dernière. La première étape consiste en la création de fibres droites aléatoirement orientées, la longueur étant contrôlée par la longueur totale du modèle ; si on considère une boite représentant l'assemblage fibreux final, la longueur de la boite est égale à l'écart entre la section de début et la section de fin de chaque fibre. A ce stade, le modèle est composé de plusieurs strates contenant chacune une fibre droite de section circulaire constante. Une fois toutes les fibres créées, la seconde étape consiste à leur imposer une ondulation par l'insertion d'un ou plusieurs points d'ondulation. A cette étape, chaque fibre est encore isolée dans sa strate, de sorte à éviter toute pénétration. La troisième étape consiste alors à mettre les fibres en contact; cela se fait par simulation numérique Abaqus®, en imposant un step de gravité au modèle.

L'ensemble de la méthode est schématisé en Figure i.

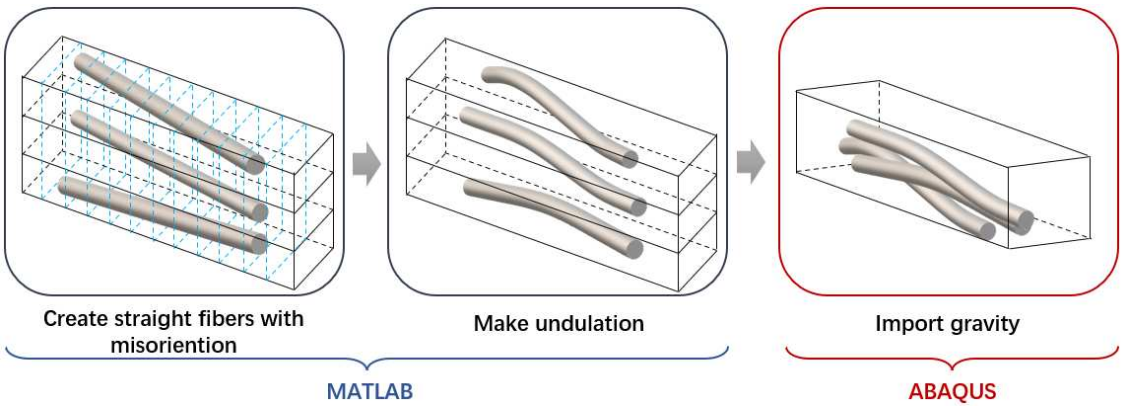

Figure i Main step of virtual numerical random fiber bundle generator.

Afin de valider le générateur, trois modèles ont été créés avec les mêmes paramètres microstructuraux que l'assemblage modèle utilisé au Chapitre II pour les essais expérimentaux et des simulations ont été réalisées en reproduisant le même trajet de chargement. Les résultats obtenus montrent des courbes pression de compression en fonction de la fraction volumique de fibres cohérentes avec celles des essais expérimentaux pour les trois modèles virtuels ; bien que certaines différences existent concernant la répartition des fibres en cours de calcul, elles restent faibles et tendent à s'atténuer lorsque la pression augmente.
Cela permet de vérifier la fiabilité du générateur d'assemblages fibreux virtuel et d'utiliser cet outil pour générer des assemblages de paramètres microstructuraux différents afin d'investiguer leur impact sur le comportement de l'assemblage fibreux sous diverses sollicitations, notamment ici, la compression.

Section 8 : Effet des paramètres microstructuraux des paquets de fibres sur le comportement en compression

Cette section a pour objectif d'analyser l'effet des caractéristiques microstructurales sur le comportement en compression d'un assemblage fibreux. Ces caractéristiques sont l'ondulation des fibres, leur élancement et le coefficient de frottement.
Afin d'étudier l'effet de l'orientation et l'ondulation, 8 assemblages virtuels sont créés dont quatre avec des fibres droites, organisées sous forme d'un assemblage compact, sous forme d'un assemblage rectangle et 2 de manière aléatoire par deux méthodes différentes. Pour les quatre autres géométries, une ondulation est créée avec un, deux, trois puis quatre points d'ondulation. Chaque résultat est analysé, avant et après compression, à travers différents indicateurs :

- Courbe de pression de compression en fonction de la fraction volumique de fibres.
- Orientation et désorientation, par l'analyse du tenseur d'orientation A_{33}.
- Nombre de contact et angles entre les fibres en contact.
- Undulation.

Les courbes de pression de compression en fonction de la fraction volumique de fibres montrent des comportements similaires pour les deux assemblages de fibres droites aléatoirement orientées, avec une pression de compression qui reste nulle aux premiers instants du calcul et jusqu'à ce que la fraction volumique de fibres augmente aux environs de 72%. Cela confirme une première étape de réarrangement des fibres à faible pression, liée à la faible rigidité de

flexion des fibres, qui leur permet de combler les espaces libres et ainsi de diminuer le volume. Dans un second temps, la pression augmente jusqu'à atteindre un maximum avant de rediminuer, ce qui correspond à une augmentation des contacts entre fibres et donc une pression de contact à vaincre pour mettre les fibres en mouvement. Durant cette étape, le mouvement des fibres domine. Enfin, et au-delà de 75% environ de fraction volumique de fibres, les courbes rejoignent celles des assemblages rectangle et compact. Pour ces deux derniers assemblages, les fibres sont déjà dans une configuration ''verrouillée'' et les réarrangements ne sont plus possibles. Il y a donc peu de mouvements de fibres, comme le confirme la composante A_{33} du tenseur d'orientation. Cette capacité à se réorganiser est confirmée par les deux autres indicateurs : le nombre de contacts augmente pour les assemblages de fibres aléatoirement orientées, de même que la répartition des angles de contact.

Quatre modèles de fibres ondulées sont ensuite comparés ; la fraction volumique de fibres initiales varie entre 27.8% et 46.7% mais une première étape de pré-compression est réalisée jusqu'à ce que tous les assemblages atteignent 46.7% de fraction volumique de fibres, état qui est alors pris comme référence pour la comparaison des résultats, afin d'exclure les effets liés à la variation de fraction volumique. Les courbes de pression en fonction de la fraction volumique de fibres montrent des comportements similaires à ceux des fibres droites aléatoirement orientées. De plus, pour tous les échantillons une limite structurelle semble exister, pour laquelle toutes les fibres sont en contact et peu d'espaces libres subsistent ; la fraction volumique de fibres atteint alors sont maximum. De même que précédemment, le réarrangement des fibres se confirme par l'ensemble des indicateurs et l'influence de l'ondulation sur le comportement en compression est montrée.

En second point, l'effet de l'élancement des fibres est étudié. Pour ce faire, trois assemblages sont créés et comparés ; le premier est celui de référence correspondant à l'échantillon du Chapitre II. Le diamètre des fibres est de 0.5mm, correspondant à un élancement S_0 de 3.64%. Les élancements sont ensuite divisés par 10 et par 50 pour créer les deux autres échantillons. Les résultats obtenus montrent que plus les fibres sont élancées, plus la pression de compression est faible pour une même fraction volumique de fibres. Cela s'explique par la capacité des fibres à se réarranger d'autant plus que leur rigidité de flexion est faible et donc d'autant plus que leur diamètre diminue. Cela se confirme par des contacts qui augmentent largement plus le rayon diminue.

Enfin, l'effet du frottement entre fibres est analysé, en faisant varier les coefficients de frottement de 0.2 à 0.8 et les résultats montrent que, pour les faibles fractions volumiques de

fibres, la pression de compression augmente avec le coefficient de frottement mais, pour les assemblages plus denses, les effets de l'augmentation du coefficient de frottement disparaissent. En effet, pour les faibles fractions volumiques de fibres, les espaces entre fibres étant plus nombreux, les fibres sont plus libres de se mouvoir et donc le coefficient de frottement a un impact direct sur la pression de compression nécessaire pour mettre les fibres en mouvement. Lorsque la densité augmente, les espaces entre fibres diminuent et le réarrangement devient chaotique et met en jeu la déformation transverse des fibres quel que soit le coefficient de frottement.

L'ensemble de ces résultats montre que les paramètres structuraux des assemblages fibreux impactent le comportement en compression. La question qui se pose alors est celle de l'impact des paramètres d'essais sur le comportement en compression et c'est ce qui est investigué dans la section 9.

Section 9 : Effet des paramètres d'essais sur le comportement en compression

Cette section analyse l'effet du trajet de chargement, de la vitesse de compaction et de la densité de fibres initiale sur le comportement en compression de l'assemblage fibreux.

Afin d'investiguer l'effet du trajet de chargement sur la réponse en compaction, différents trajets de compaction biaxiale sont créés avec des déformations finales de 6% et 12%. Les résultats montrent que les différents trajets de chargement testés conduisent à une différence significative dans le comportement en compression mais ne conduisent pas à des différences significatives des contacts. Cependant, lorsque les assemblages atteignent la même fraction volumique de fibres avec différents trajets de chargement, les angles au niveau du contact sont différents. Ce résultat semble indiquer que l'état de déformation ne peut être directement mis en relation avec l'état de contraintes dans les assemblages fibreux mais également que le nombre de contacts ne permet pas à lui seul de décrire la rigidité d'une microstructure.

En outre, et afin de comprendre l'effet de la vitesse de sollicitation, les simulations sont réalisées avec 9 vitesses de sollicitations différentes : V_0, $0.5V_0$, $2V_0$, $3V_0$, $4V_0$, $5V_0$, $10V_0$, $20V_0$, $100V_0$ et un damping $\alpha = 10^5$. Le principal constat qui en découle sont que, lorsque la vitesse de sollicitation augmente, la pression nécessaire pour atteindre la même fraction volumique de fibres augmente également. En effet, une vitesse faible laisse plus de temps aux fibres pour s'adapter à la nouvelle configuration, ce qui permet à la structure interne et aux propriétés mécaniques d'évoluer. La vitesse de compaction a donc un effet important sur le comportement en compaction et les effets de relaxation des assemblages fibreux, ce qui a également été

constaté lors des essais expérimentaux.

Enfin, la fraction volumique de fibre est un paramètre clé dans les résultats en compaction puisqu'elle affecte la densité, les propriétés mécaniques et la microstructure de l'assemblage fibreux. La densité finale semble impacter la relaxation qui est plus importante lorsque V_f augmente. De plus, lorsque V_f atteint un certain niveau le blocage de la microstructure tend à réduire ses effets.

Ces deux derniers points permettent d'illustrer la viscosité du comportement de ces microstructures qui doit être considérée et approfondie.

Conclusion et perspectives

Les travaux présentés dans ce manuscrit ont pour enjeu de valider un estimateur virtuel du comportement mécanique de faisceaux de fibres de type rovings afin de pouvoir réaliser des études paramétriques et de sensibilité des différents paramètres de l'architecture. Pour cela, le comportement en compaction/compression a été choisi car il est le plus complexe mettant le plus en jeu la réorganisation du réseau. Pour réaliser l'étude, un modèle contenant 40 fibres de polyester légèrement enchevêtrées, quasi parallèles et de diamètre 0.5 mm a été choisi comme échantillon modèle. Le choix de l'échantillon est fait dans la recherche d'un compromis entre la possibilité d'apparition des phénomènes physiques et la minimisation des temps de calcul. Enfin, l'essai de compression a été choisi comme essai de validation.

La stratégie mise en place, afin de développer des modèles précis d'assemblages fibreux, repose sur des simulations numériques de compaction/compression couplées à de la tomographie à rayons X. L'objectif est d'obtenir la véritable microstructure initiale de l'échantillon ainsi que son évolution au cours de la compaction/compression et finalement, d'obtenir les courbes de comportement de l'échantillon sous compaction/compression. Pour ce faire, une stratégie de post-traitement d'images de tomographie du paquet de fibres a été établie et repose sur l'extraction des lignes moyennes des fibres dans le but de les modéliser, par la suite, par des éléments poutres dans ABAQUS®/EXPLICIT. L'approche proposée permet une extraction automatique, rapide et précise des lignes moyennes des fibres de l'assemblage fibreux ; cette extraction/reconstruction a été validée par la superposition des images de tomographie avec les profils reconstruits. De plus, la cassette contenant les fibres lors de la tomographie a été extraite et modélisée via CATIA V5® pour la géométrie puis modélisée dans Abaqus® par un modèle rigide discret.

Afin d'alimenter les paramètres de simulation, des essais expérimentaux de traction monotone

et cyclique ont été réalisés sur les fibres pour déterminer leur module de Young ; un travail a également été réalisé sur la taille optimale des éléments afin de diminuer les temps de calcul. Enfin, un contrôle de la pénétration a été réalisé. En effet, la résolution spatiale du tomographe et la précision du programme de détection des contours automatique de Matlab peuvent conduire à de légers décalages de la position initiale des fibres, ce qui peut conduire à des différences entre les positions des fibres issus de la simulation et celles issus de l'expérimentation après essai. Une stratégie de correction de la pénétration a donc été mise en œuvre.

Afin de pouvoir étudier la microstructure à l'état déformée, des indicateurs ont été définis et les outils d'analyse associés ont été construits. Les indicateurs de comparaison sont le nombre de contacts au sein de l'assemblage fibreux, la répartition des angles de contact, l'ondulation des fibres (courbure et rayon de courbure) et l'orientation des fibres (tenseur d'orientation et désorientation autour de l'axe Z de la direction des fibres), ainsi que les courbes de pression de compression en fonction de la fraction volumique de fibres.

Une fois les outils créés et les paramètres de simulation mis au point, trois échantillons ont été utilisés pour valider la stratégie par comparaison entre la simulation numérique et les essais expérimentaux sous tomographe de compaction confinée. Les résultats montrent des écarts entre expérimental et numérique de quelques pourcents sur l'ensemble des indicateurs. Bien que ces résultats pourraient encore être améliorés, ils permettent de valider la stratégie de simulation et les outils d'analyse de la microstructure développés. L'ensemble de la démarche peut alors être utilisée pour travailler sur les réponses mécaniques de nouveaux assemblages fibreux à différentes sollicitations, en s'affranchissant d'essais expérimentaux.

Il est alors nécessaire de créer des modèles stochastiques virtuels réalistes de ces assemblages. Une stratégie de création de géométries de paquets de fibres aléatoires numériques virtuels avec des paramètres de structure contrôlés a ainsi été développée. Dans cette stratégie, afin d'éviter les pénétrations, les N fibres sont générées dans N strates et la génération du paquet final est réalisée en 3 étapes : à l'aide d'un programme Matlab chaque fibre droite est créée avec une position aléatoire, une désorientation autour de l'axe des fibres est insérée ; un point ou plusieurs points d'ondulation sont insérés sur les fibres. Puis, afin de rendre l'assemblage réaliste, un step de gravité est imposé dans ABAQUS®. Cette stratégie de création d'un paquet de fibres a été validée par des simulations de compaction/compression de 3 géométries dont les paramètres microstructuraux correspondent à ceux de l'échantillon 2 utilisé pour les essais expérimentaux. Même si le comportement macro en compression montre quelques faibles

différences entre le paquet de fibres généré et l'expérience, les résultats restent très cohérents et le générateur virtuel créé a donc pu être utilisé pour réaliser de nombreux essais virtuels dans le but de comprendre l'influence des différents paramètres structuraux et de chargement.

Les paramètres structuraux étudiés sont l'ondulation des fibres, l'élancement et le coefficient de frottement entre fibres. Les résultats obtenus et l'analyse des indicateurs de microstructure implémentés ont permis de dresser quelques premières conclusions, permettant ainsi de montrer le potentiel de la stratégie développée.

Tout d'abord, l'alignement initial des fibres est un facteur important dans la capacité du réseau à se réarranger et à se déformer ; en effet, pour des fibres parfaitement parallèles et alignées, le peu d'espaces entre fibres ne leur permet pas de se mouvoir pendant l'essai ; à l'opposé, les fibres droites arbitrairement alignées permettent plus d'interactions en cours d'essai, faisant apparaitre, par exemple, du glissement et de la flexion. Ces interactions engendrent des déformations longitudinales et peuvent produire des réarrangements locaux. Enfin, pour les fibres ondulées, l'ondulation augmente la capacité des fibres à interagir entre elles. Plus les fibres sont ondulées, plus elles sont en mesure de former des structures complexes pendant la compaction, augmentant ainsi l'enchevêtrement par conséquent la rigidité de compression.

Deuxièmement, afin de tester l'effet de l'élancement des fibres, trois modèles ont été comparés avec des diamètres de fibres différents (0.5 mm, 0.05 mm et 0.01 mm). Comme l'élancement est un paramètre essentiel de la rigidité de flexion, les fibres de diamètres plus faibles ont plus la capacité de se déformer sous efforts extérieurs et donc plus en capacité de remplir les espaces vides, conduisant à des assemblages plus compactés sous pressions plus faibles. Ainsi, il a été montré l'influence de la rigidité de flexion des fibres sur la rigidité de compression.

Enfin, afin de tester l'impact du coefficient de frottement, 4 modèles ont été créés, avec des coefficients de 0.2, 0.4, 0.6 et 0.8 et montrent que pour les faibles fractions volumiques de fibres, en début d'essais, plus le coefficient de frottement est élevé, plus la rigidité de compression est élevée ; pour les fractions volumiques de fibres plus élevées, l'effet du coefficient de frottement sur la rigidité de compression disparait du fait du verrouillage de la microstructure. Le coefficient de frottement est donc un paramètre important en début de compression mais ses effets diminuent en cours d'essais jusqu'à ne plus être prédominants.

L'ensemble de ces analyses ont également permis également de montrer que le nombre de contacts dans les microstructures, s'il est un paramètre influent, ne permet pas à lui seul de rendre compte de la l'évolution de rigidité de compression, même dans la phase de compaction. Les ondulations, les angles des fibres et de contact sont également à prendre en compte.

Finalement, l'influence des paramètres de chargement a été abordée : le trajet de chargement ainsi que de la vitesse de sollicitation et la relaxation. Pour analyser l'impact de ces paramètres, plusieurs modèles ont été créés en faisant varier les fractions volumiques de fibres et les vitesses de sollicitation. Les résultats ont pu illustrer l'influence de ces paramètres sur la microstructure et sur le comportement en compression. Si le trajet de chargement n'a pas d'influence significatives sur le nombre de contacts et l'embuvage des fibres lorsque les déformations finales sont les mêmes, ils impactent le réarrangement des fibres, et notamment les angles de contact ce qui conduit à une modification de la transmission des efforts. Il en résulte une modification de la relation efforts/déformations. Ainsi, il semble qu'un même état de déformation ne conduise pas systématiquement à un même état d'efforts en fonction du trajet de chargement, ce qui est un point clé pour une modélisation aux échelles supérieures.
L'effet de la vitesse est également intéressant et a pu mettre en évidence que plus la vitesse augmente, plus la pression nécessaire pour atteindre la même fraction volumique de fibres augmente, mettant en lumière la capacité des fibres à se réorganiser lorsque les vitesses de sollicitation sont faibles et donc l'importance du phénomène de relaxation à faible vitesse. Le phénomène de relaxation, constaté lors des essais a été également abordé. Il est bien reproduit par le modèle et il semble que la fraction volumique joue un rôle dans l'intensité de la relaxation. Ces deux derniers points mettent en évidence un comportement visqueux, qu'il serait intéressant d'étudier plus en détail et qui, une fois, encore serait à prendre en compte dans les modélisations aux échelles supérieures.

Tout cela met en lumière le travail important réalisé pour mettre en place tous les outils nécessaires à l'analyse de la microstructure d'assemblages fibreux et les résultats présentés bien que préliminaires, illustrent le potentiel de la stratégie. Cependant, il reste encore beaucoup de pistes à confirmer et à explorer. Désormais, les indicateurs ont été définis et les outils nécessaires à leur extraction mis en place. Il faudrait maintenant pouvoir dépouiller de façon beaucoup plus fine la microstructure des assemblages fibreux via ces outils. De même, un travail conséquent subsiste quant à la réalisation de simulations pour prendre en compte l'ensemble des paramètres, parmi lesquels :

- Trajets de chargement:
    - Dans cette étude, les chargements simulés sont la compression uniaxiale ou biaxiale avec différents trajets. Cependant, la base de données constituée doit être enrichie par de nouvelles microstructures et de nouveaux points de comparaison pour

confirmer les conclusions qui sont d'une importance majeure pour la modélisation du comportement mécanique.

- D'autres trajets pourraient être intéressants, tels que la compaction non confinée ; pendant la compaction non confinée, à cause des libertés latérales, les interactions entre fibres et leurs déformations présentent une liberté plus grande, permettant aux fibres de se mouvoir et de se repositionner librement dans la direction non compactée.
- D'autres types de chargements sont également à tester pour observer la réponse de la microstructure mais également, des chargements plus complexes et des chargements composés dans des ordres différents avec validation expérimentales sous tomographe. Des essais de compression biaxiale sous tomographe seraient notamment intéressants pour confirmer les résultats.

- Phénomènes d'hystérésis : il pourrait être intéressant de simuler des cycles de chargement/déchargement afin de comprendre les réponses aux phénomènes d'hystérésis, de pouvoir estimer la déformation résiduelle de la microstructure et son évolution.
- Forme du réseau fibreux : une autre piste intéressante est de varier la forme du réseau fibreux. Par exemple, Pham et al.(Pham, Ha-Minh, Chu, Kanit, & Imad, 2020) ont réalisé des simulations de compaction de mèches lenticulaires, ce qui ouvre une nouvelle perspective à cette étude ; en effet, dans leur étude, l'assemblage fibreux a une forme lenticulaire idéalisée (avec différents rapports a/b, Figure ii) et est soumis à de la compaction uniaxiale ou biaxiale afin d'observer l'effet de différentes morphologies d'assemblages fibreux et leur changement de microstructure durant la compaction. Cette approche aide à comprendre la dynamique des réseaux fibreux sous compaction.

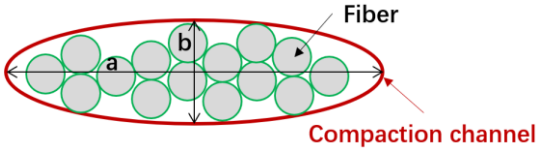

Figure ii The lens-shaped compaction cannel.

- Influence des paramètres microstructuraux : la stratégie de simulation développée ici a également permis d'étudier l'influence des paramètres microstructuraux sur le comportement mécanique. Le générateur créé a permis de prendre en compte différents paramètres de la microstructure, tels que l'élancement, la courbure, la déviation des fibres dans les différents plans. Bien que les courbures et élancements des fibres aient été largement étudiés ici, il reste beaucoup d'analyses à mener sur la déviation, notamment

d’un point de vue quantitatif. Il pourrait être intéressant, par exemple, d’explorer plus en profondeur comment le degré de déviation des fibres au sein du réseau affecte le comportement en compaction. En outre, il est important de noter que, pendant le procédé de stabilisation des contacts par gravité, le degré de déviation des fibres peut évoluer et impacter la précision des résultats. C’est pourquoi, des travaux futurs pourraient améliorer le générateur pour réduire cette erreur et s’assurer que le degré de déviation des fibres pendant la simulation correspond parfaitement à la géométrie initiale.

- Nombre de fibres : dans cette étude, un échantillon modèle de 40 fibres de 0.5mm de diamètre a été pris en compte. Cependant, les mèches de fibres techniques actuelles sont composées de centaines à plusieurs milliers de fibres de quelques dizaines de microns de diamètre. A l’avenir, il conviendra de réaliser des assemblages fibreux se rapprochant de plus en plus de la réalité et de tester leur comportement sous diverses sollicitations.

Effet de l’ensimage : la prise en compte de l’ensimage dans les simulations est une piste fondamentale également et un challenge dans les recherches actuelles. Le procédé d’ensimage, durant lequel les mèches sont trempées dans une solution, permet d’améliorer leurs propriétés, telles que le coefficient de frottement analysé dans cette étude. Cependant, l’ensimage permet également d’obtenir d’autres propriétés qui ne sont pas étudiées ici et représente un challenge du fait de leur diversité : composition chimique, viscosité, quantité, etc. La définition des paramètres de simulation pour la prise en compte de ces propriétés nécessitera également un nombre conséquent d’essais expérimentaux. Pour palier à cela, plusieurs stratégies peuvent être mises en œuvre comme l’utilisation de techniques d’imagerie de haute résolution pour visualiser la distribution de l’ensimage sur les mèches et alimenter les paramètres microscopiques nécessaire au développement de modèles de mèches plus complexes.

Acknowledgement

As my PHD journey of three and a half years comes to an end, I would like to express my gratitude to my friends and supervisors who have supported me along the way. Reflecting on my time in France, I would like to thank myself for my perseverance throughout this process. It has been a period to make me strong, independent, and thinking.

I am profoundly grateful to my supervisor, Gilles HIVET, and co-supervisors Audrey HIVET, and Anwar SHANWAN. Their patience and encouragement kept me confident to complete my thesis. We work as a team and they not only guide me in my work, but more importantly their attitude towards work and life influences me. Especially when it comes to problems, Gilles always provides new ideas and inspiration, so we always find a way to solve the problem. Especially in the final stages, even in the evenings or on vacation, we can always meet to discuss my thesis.

I would like to thank Amélie MARDUEL and Christelle MARLY-CHANTELOUP in my laboratory for their encouragement and help. I would also like to thank all my colleagues and professors in the laboratory, whose company and support are the important for my daily academic life.

Specially, thanks to Mathieu Venin of the CERMEL laboratory for his patient support of my tomography research. His professional knowledge helped me to overcome many difficulties in my thesis.

My friends, both in France and in China, and my master supervisor Jianbo LEI. They have always given me encouragement. Their support has been unwavering, we share each other's lives and happiness, it’s the important part of my life.

I am really want to thank to my family and my boyfriend, whose given me so much support. Even though I only saw my family once during my four years in France, and even though I was far away, I could still feel the love and understanding from my family. My boyfriend Heyu SONG was there during my hard period, he helped me with housework and preparing meals so that I could concentrate fully on my thesis, and he always support my work and my life.

I also appreciate the financial support from the China Scholarship Council (CSC), which was crucial in funding my academic journey.

In the last but the end, I want to express my gratitude to all the, friends, and family and my supervisors who have supported me through this journey again.

Thank myself once again.
To all of us, the future is promising!

Résumé

Le comportement mécanique d'un renfort fibreux est fondamental lors de sa mise en forme pour la fabrication des matériaux composites. Afin de prédire ce comportement, des essais mécaniques seuls ne sont pas suffisants. Il est donc nécessaire d'obtenir une véritable loi de comportement du renfort en fonction des paramètres de la structure fibreuse. L'objectif de cette thèse est d'étudier le comportement mécanique d'un assemblage de fibres quasi parallèles. Pour atteindre cet objectif, il est donc nécessaire de comprendre et quantifier l'influence des paramètres de l'architecture fibreuse sur son comportement mécanique. Une démarche mixte expérimentale/numérique est proposée. La stratégie numérique consiste à réaliser des simulations numériques par éléments finis, en dynamique explicite, en modélisant chaque fibre par une poutre B31, en contact les unes avec les autres. Au niveau expérimental, et en utilisant des assemblages de quelques dizaines de fibres modèles de 500 microns, des essais de compaction/compression sous tomographe sont réalisés. Ces essais permettent d'obtenir l'évolution de l'architecture fibreuse en fonction du chargement imposé et des conditions aux bords appliquées. Des indicateurs d'évolution de la microstructure sont alors définis afin d'analyser et post-traiter les résultats. Un algorithme de reconstruction permet de reconstruire un modèle numérique représentatif de l'assemblage testé, où chaque fibre est modélisée par une poutre B31. L'identification de la loi de comportement de la fibre permet alors de réaliser les simulations de la structure testée. La comparaison sur plusieurs types d'échantillons permet de valider la démarche numérique et ainsi de mettre au point un estimateur virtuel utilisable pour simuler le comportement d'assemblage non existant. Par la suite, une stratégie de création d'architectures fibreuses virtuelles est mise au point pour l'étude paramétrique. Celle-ci permet de créer rapidement des architectures de tout type avec des paramètres d'architectures maitrisés. Grâce à l'ensemble des étapes précédentes une étude paramétrique peut être menée et ainsi l'influence de certains paramètres peut être établie : paramètre de la microstructure initiale, diamètre des fibres, facteur de frottement fibre/fibre et trajet de chargement. Cette dernière étape permet de démontrer l'efficacité de la démarche propose et ouvre également de nombreuses perspectives.

Mots clés : Fibres, Composites, Mécanique, échelle microscopique, Modélisation

Abstract

The mechanical behavior of a fibrous reinforcement is fundamental during its shaping for the manufacturing of composite materials. To predict this behavior, mechanical tests alone are not sufficient. It is therefore necessary to obtain a true behavior law of the reinforcement based on the parameters of the fibrous structure. The objective of this thesis is to study the mechanical behavior of an assembly of quasi-parallel fibers. To achieve this objective, it is essential to understand and quantify the influence of the fibrous architecture's parameters on its mechanical behavior. A mixed experimental/numerical approach is proposed. The numerical strategy involves conducting finite element simulations using explicit dynamics, where each fiber is modeled as a B31 beam, in contact with the others. Experimentally, using assemblies of a few dozen model fibers of 500 microns, compaction/compression tests are conducted under tomography. These tests allow for the observation of the evolution of the fibrous architecture depending on the imposed load and the applied boundary conditions. Microstructure evolution indicators are then defined to analyze and process the results. A reconstruction algorithm enables the creation of a representative numerical model of the tested assembly, where each fiber is modeled by a B31 beam. The identification of the fiber's behavior law then allows for the simulation of the tested structure. Comparisons across several types of samples validate the numerical approach, thus enabling the development of a virtual estimator that can simulate the behavior of non-existent assemblies. Subsequently, a strategy for creating virtual fibrous architectures is developed for parametric studies. This strategy allows for the rapid creation of various architectures with controlled parameters. With all the preceding steps, a parametric study can be conducted, establishing the influence of certain parameters: initial microstructure parameters, fiber diameter, fiber/fiber friction factor, and loading path. This final step demonstrates the effectiveness of the proposed approach and also opens up numerous future perspectives.

Key words: Fibers, Composites, Mechanical behavior, Microscale, Modeling

Content

Content of figures

Content of Tables

Introduction

Composite materials are used for different industrial applications like transports. The popularity of these materials is due to their interesting mechanical performance to the mass ratio. Among the most widespread, one can find composite materials based on fibrous reinforcements, but the manufacturing of these materials presents several difficulties that prevents their development. Indeed, the mastery and development of processes today results from know-how and experience resulting from an empirical approach, much more than from a complete mastery of the physical phenomena involved. The manufacturing of composite parts starts usually by the preforming of dry or pre-impregnated fabrics according to a defined mold, sometimes complex, before the resin is injected. The mechanical behavior of the fabric is therefore crucial during the preforming process because it influences the next steps of the manufacturing process. However, a fibrous reinforcement is a complex structure since it results from the weaving of thousands of yarns, themselves made up of the assembly of tens of thousands of fibers of few microns diameter. Thus, the mechanical behavior of the reinforcements is obtained by a sum of responses obtained experimentally to specific loading path (compression, tension, bending, shear, etc.). These mechanical responses are subsequently modeled by equations whose form is obtained by hypotheses on the most influent parameters, without a truly rigorous approach of the complex physics involved (large number of fibers, variability, undulation of fibers, sizing, etc.). This is particularly the case for compression behavior in which a direct relationship is assumed between the compression stiffness and the fibers volume fraction according to an empirical law. If this law works correctly, it requires an identification for each new type of yarn and does not allow to highlight the structural parameters, which can improve the structure performances and to anticipate the mechanical behavior of fabrics without having to create and test it. The goal of this thesis is therefore to be able to tackle this lack by studying the mechanical behavior of an assembly of quasi-parallel fibers which represent the fibrous structures most used for technical applications. In order to achieve this goal, several solutions exist; an experimental approach couldn't be sufficient as it requires a very important number of experiences, because there are many loading paths, and an important number of undulations exist. It is therefore necessary to be able to use effective numerical approaches allowing a parametric study, i.e. carrying out many tests in a short time. The chosen strategy is therefore to be able to create a virtual estimator of the behavior of a fibrous assembly and to validate it by experiments. One of the most important difficulties to study the behavior of fiber assembly

is undoubtedly the size of the fibers (a few micrometers) which make them very difficult to handle and observe individually. As the goal of this study is to understand the strain phenomenology of fibrous assemblies, a model of fibers is done at larger scale (500 microns) as a first approach in this study; in a second stage, simulations with fibers at a “real” scale are performed. To achieve this goal, many steps should by carried-out successfully. The first is to develop a numerical strategy to efficiently simulate, at the fiber scale, the strain of the architecture under various solicitation. The second step is to define experimental solution of validation to ensure the reliability of this virtual estimator by comparing its results with experimental results. The third step aims to define indicators of the microstructure that allow to analyze the results. Finally, it is necessary to use this strategy to create any type of architecture with a defined parameters and apply different paths of loadings to analyze the mechanical response of the structure. A first numerical approach was established by the thesis of Oussama HAJI (Haji Oussama, 2018). This approach allowed to highlight the feasibility of the first and the second step of the strategy, but it is now necessary to be able to improve them and especially to carry out the last two steps as well as to exploit the entire strategy to carry out parametric studies and conclude on their influence on the mechanical behavior. In this context, this thesis manuscript is therefore structured in three chapters (nine sections). At the beginning of each chapter a brief summary in French of its content is presented.

The first chapter is made up of sections 1, 2 and 3 and presents a bibliographic study on the mechanical behavior of fibrous materials during compaction/compression, furthermore, modeling and simulation methods at different scales (macroscopic, mesoscopic and microscopic). This bibliographic study allows, in addition to the choice of the study scale, to show the relevance of the compression test for a rich phenomenological analysis. This chapter also presents the methods to characterize fibrous media as well as the development of virtual models necessary for numerical studies.

The second chapter is made up of sections 4, 5 and 6 and presents the observation method of the compaction of fibers combined tomography and 3D numerical reconstruction process of a fiber bundle. This chapter also presents the optimization of the simulation parameters of the numerical model, and the development of indicators for analyzing the microstructure of fiber bundle. Numerical simulations of fiber compaction/compression tests are carried out and compared to experimental tests.

The third chapter is made up of sections 7, 8 and 9 and presents the strategy for created a numerical generator of virtual and random fiber bundle. This virtual generator is validated by

comparison with experimental results; then models of fibrous assemblies are created to study the impact of microstructural parameters on the compaction/compression behavior of the fibrous assembly.

Chapter I Mechanics of fibrous reinforcements: Behavior in compaction

Chapter 1 presents a general overview of fiber-reinforced materials used in the manufacture of composites and their mechanical properties, with an emphasis on compaction properties. For this purpose, the chapter is divided into three parts:

Section 1 provides an overview of the structure and composition of fiber-reinforced materials. By analyzing its shape, the model medium for this study is initially identified.

Section 2 and section 3 present the mechanical properties of fiber-reinforced materials during compaction. Section 2 presents the compaction behavior of fiber-reinforced materials from an experimental point of view, and section 3 presents the compaction behavior of fiber-reinforced materials from a numerical point of view.

Section 1 General information on fibrous reinforcements

1.1 Definition of fiber composite material

Fiber-reinforced composites are heterogeneous materials consisting of at least two immiscible components: fiber reinforcement (discontinuous phase) and matrix (continuous phase). Compared to the constituent elements alone, composites exhibit improved physical and chemical properties. The primary role of the matrix is to transfer forces and the mechanical stresses between the fibers in different directions. The matrix may be polymer-based, metal-based or ceramic-based. Polymer-based matrices are the most common because they allow complex shaped parts to be manufactured at a reasonable cost. The role of the reinforcement is to ensure the mechanical properties of the composite in the direction of the fibers, and it usually consists of continuous or discontinuous fibers, particles, or skeletal structures. Here, the fiber reinforcing materials will be focused on in detail next as this is the subject of this study.

1.2 Fibrous reinforcements

As mentioned above, textile-reinforced composites enhance the overall mechanical properties of the material mainly through fiber reinforcement. This reinforcement is not only dependent on the type of fiber material chosen, but also on the architecture of the fiber structure as well as the interwoven configuration of the constituent yarns. Textile reinforcement is a multiscale heterogeneous structure (Figure 1.1). The fibers themselves serve as the base units, which are combined by specific processes such as winding, braiding, or needling to form yarns with specific performance characteristics. These yarns are further woven, knotted, sewn, etc. to form textiles with various structures (Figure 1.2). The multiscale structure concept of textile reinforced materials is crucial. This is because it controls of the mechanical behavior of the composite material by adjusting the arrangement of the fibers, the weaving density of the yarns, and the hierarchical structure of the textile.

Before going into details, it is wise to first present a brief discussion of the main structures of fiber-reinforced materials, and their components (yarns and fibers).

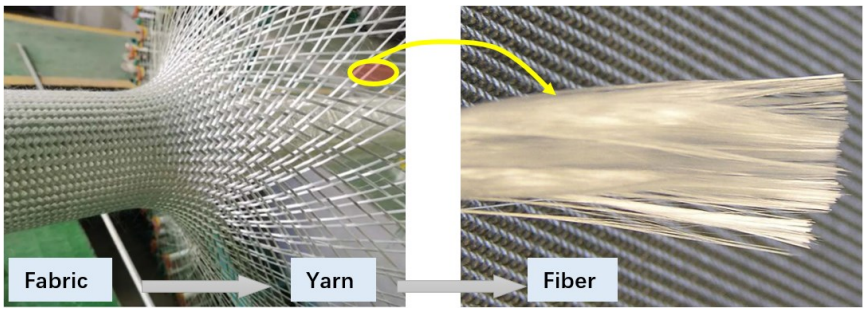

Figure 1.1 Multi-scale structure of fibrous reinforcements.

1.2.1 Structure of fabric reinforcement

In composites materials, several types of reinforcement structures are used in addition to the single filaments used in the deposition (building and shaping of the material layer by layer) or twisting (twisting the fibers around a core material) processes. These can be divided into the following main categories, shown in Figure 1.2 (Haji Oussama, 2018):

- Woven fabrics: They are made by interweaving weft and warp threads, as shown in Figure 1.2 (a, b).
- Braids: Braids are structures formed by crossing and weaving multiple wires over each other, as shown in Figure 1.2 (c).
- Non-Crimp Fabrics (NCFs), shown in Figure 1.2 (d): These materials are not made through the traditional process of weaving, but by keeping the fibers together by other means, usually in the form of a laminate. This type of structure is characterized by the fact that the fibers remain straight due to the absence of interlacement, so they are better able to carry tensile loads.
- Knits: Knits are formed by interlocking continuous loops of threads, as shown in Figure 1.2 (e). These structures are usually used to provide a significant elastic behavior of the reinforcement before the injection of the matrix.

In terms of the type of structure, reinforcing materials can be further distinguished as follows: Two-Dimensional Structures (2D): These are usually qualified as plane, with the fibers unfolding in only two directions. Three-dimensional structures (3D): their fibers unfold in three spatial directions, providing better mechanical properties in the thickness direction.

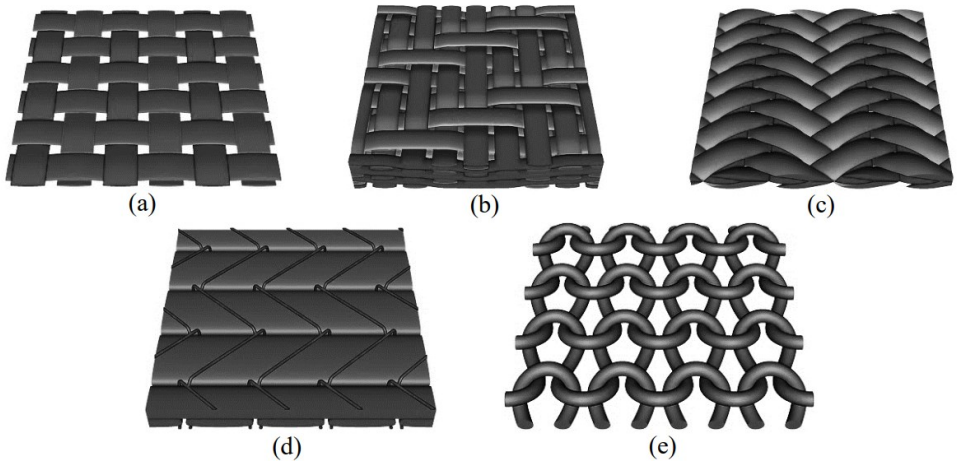

Figure 1.2 Main structures of textile reinforcements (Haji Oussama, 2018)**. (a) 2D fabric. (b) 3D fabric. (c) Braids. (d) NCF (Non-Crimp Fabric). (e) Knits.**

All these reinforcements are composed of many yarns, themselves are composed of thousands of fibers. The characteristics of these elements are developed in the next part.

1.2.2 Fiber reinforcement components

a) Yarns

In the textile industry, fibers are assembled and then either twisted into threads or placed side by side to form untwist or quasi untwist bundles, usually named as roving. The resulting yarn is then a network of quasi parallel fibers. Due to its constitution, the cohesion of the yarn is initially weak and is then ensured by sizing, which consists in impregnating it with a pre-prepared sizing chemical. The sizing increases the yarn cohesion but also increases yarn strength and abrasion resistance, and reduces yarn hairiness. The sizing step can also be used to add specific properties to the fibers.

An untwisted bundle can contain thousands of fibers which can be described by characteristics such as linear mass, the type of fiber combination, and the materials that make up the fibers (see in Figure 1.3 (a)). Such almost parallel bundles of fibers are able to reach important volume fractions during compaction. They are also more suitable for 2D constructions to obtain better flatness and uniform coverage of the used surface.

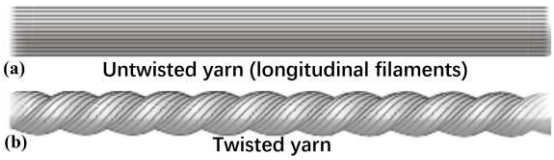

Figure 1.3 Staple and Filament ("TEXTILES AND TEXTILE TECHNOLOGY," n.d.)**.**

Twisted yarn is a made by adding a twist to a single yarn (or multiple strands of a single yarn) during the spinning process. Twist is used to describe the number of twists (twists per inch) in a yarn. Increasing twist improves the strength, elasticity, and abrasion resistance of the yarn. Twisted yarn is divided into: single yarn (Figure 1.3(b)), ply yarn (Figure 1.4), and cable.

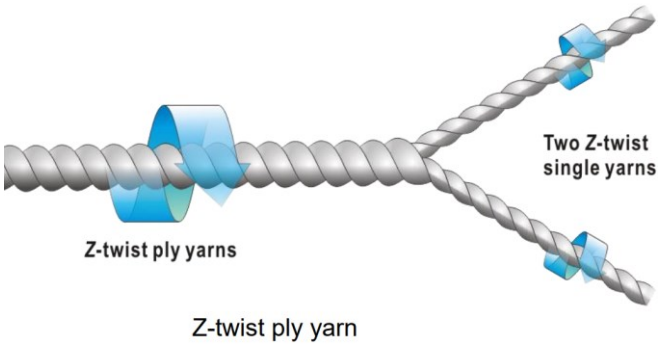

Figure 1.4 Single yarn and ply yarn (TEXTILES AND TEXTILE TECHNOLOGY, n.d.).

b) Fibers

Fibers are often characterized by their constituent materials and geometry. According to its composition, it can be divided into two categories: natural fibers and chemical fibers. Natural fibers can be divided into plant fibers (flax), animal fibers (wool); And chemical fibers can be divided into artificial fibers (polyester) and synthetic and inorganic fibers (glass fiber).

Fibers often undergo surface treatments, especially coatings. These treatments may be in the form of chemical coatings. The purpose is to provide specific physical and chemical properties relevant to their processing and end use. For example: lubricating fibers, enhancing cohesion of untwisted strands, and reinforcing fiber/matrix bonding.

From a geometric point of view, a fiber is usually described by its aspect ratio $\boldsymbol{L}$, which is defined as the ratio of the fiber length l_{fibre} to its diameter $\emptyset_{fibre}$, $\boldsymbol{L} = l_{fibre}/\emptyset_{fibre}$. Two types of fibers can then be distinguished: (i) Discontinuous fibers, whose aspect ratio is usually less than 1000. These fibers are often used in fabrics that are laid flat in random directions. (ii) Continuous fibers with higher aspect ratio. The fiber is also characterized by its cross-section shape. Some fibers may have a cross-section of complex shapes, especially natural fibers. As

shown in Figure 1.5, the cross-section of cotton fiber is irregular. Artificial fibers are usually still modeled as cylinders with circular cross sections. For example, for polymer fibers, the cross section can be considered circular (Dalfi, Yousaf, Selver, & Potluri, 2022; Gassara, 2016) (Figure 1.5 (c, d)). However, they may not be perfectly circular, which can lead to some difficulties in fiber scale modeling. In terms of the geometric properties of the fiber, the crimp of the fiber is also one of its geometric characteristics, defined as the ratio between the length between the fiber's end points and the total length of the fiber. In the case of polyester fibers, especially from the surface characteristics, it can be noted that the fiber surface has streaks along its axis, which are due to the spinning process (Figure 1.5 (e)) (Bier, Redel, & Schubert, 2023; Gassara, 2016; Merchiers et al., 2020). Therefore, whether it is an irregular fiber or a round fiber, its surface is not absolutely smooth. There are friction coefficients between fibers, and the coefficient of friction depends on the direction of relative motion between the fibers. A recent study says the friction between fibers doesn't depend on the fiber's material only but also on the relative direction between fibers (Shanwan, Gassara, Barbier, & Sinoimeri, 2017; Tourlonias, Bueno, Fassi, Aktas, & Wielhorski, 2019).

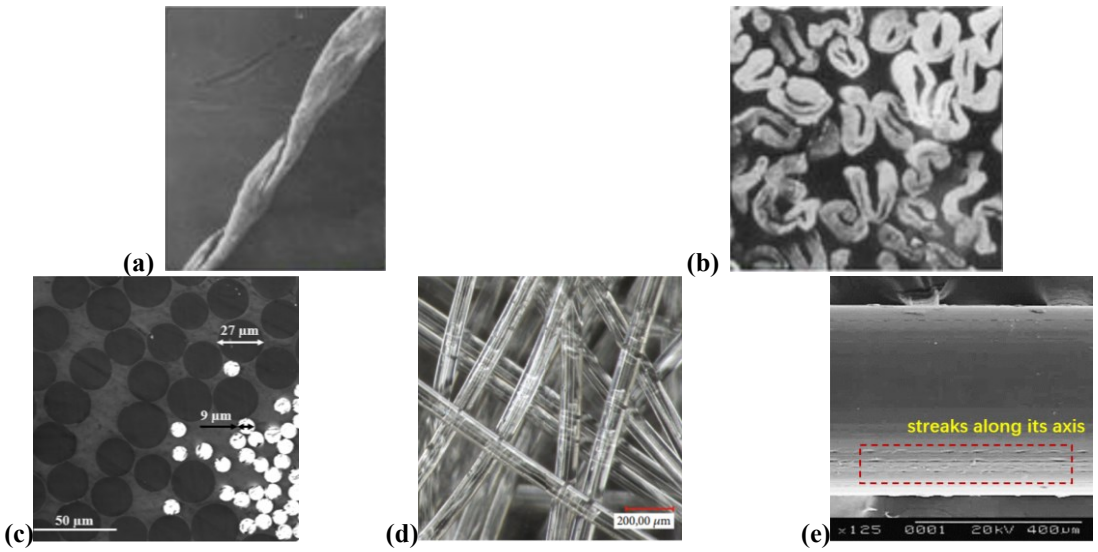

Figure 1.5 (a) Longitudinal form of cotton fiber. (b) Cross-section form of cotton fiber. (c) Cross-section of polymer fiber (black) and glass fiber (white) (Dalfi et al., 2022)**. (d, e) Longitudinal form of polymer fiber** (Bier et al., 2023; Gassara, 2016)**.**

1.2.3 Modeling scale for fiber reinforced materials

The resin transfer molding (RTM) process is one of the used technologies for the manufacturing of fiber composite materials of complex geometries. During the forming stage, there is a strong

interaction between the reinforcement and the mold at the scale from yarns to fibers, which can lead to defects, especially wrinkles, slippage and buckles, the latter of which decreasing the mechanical properties of the final composite part (P. Boisse, Hamila, & Madeo, 2016; Schmachtenberg, Schulte Zur Heide, & Töpker, 2005).

Therefore, it is important to predict and control the occurrence of these defects, which means it is necessary to understand the mechanical behavior of reinforcements during the forming process. Practically, it would be very long and complex to achieve the study of defects only considering experimental methods in order to understand the fiber behavior such as fiber orientation, as well as porosity, etc. So, numerical simulations are needed to complement the experiments. As mentioned earlier, fiber reinforcement is a multi-scale structure. Therefore, as will be described next part, it is necessary to choose the best scale in order to obtain, as faithfully as possible, the looked for information about the behavior of the fiber-reinforced material.

3 scales of modeling are classically considered for that purpose:

Macroscopic scale: At this scale, fiber reinforcement could be considered as a continuous uniform homogeneous material, as shown in Figure 1.6. For example, in the case of 2D reinforcements, the reinforcement can be modeled as a membrane or shell. The thickness is small compared to other dimensions. Fiber reinforcement models do not explicitly consider the behavior and interweaving of yarns in the reinforcement at this scale (Fiumarella, Boria, Belingardi, & Scattina, 2021).

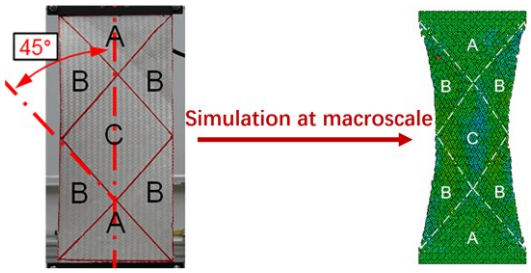

Figure 1.6 Macroscale reinforcement modeling: Reinforcement is treated as a homogeneous material (Fiumarella et al., 2021)**.**

Mesoscopic scale: Yarn is considered as a continuous homogeneous material (Figure 1.7). The cross-section of the yarn is usually assumed to be oval, lenticular but more complex shapes can also be considered (Wendling, Hivet, Vidal-Sallé, & Boisse, 2014). But this shape can actually vary depending on its geometric position within the reinforcement material. At this modeling scale, the geometry of the reinforcement takes explicitly the interlacing of yarns into account. This requires efficient modeling of the geometric position of the strands and the contact between

them (Hivet & Boisse, 2008; Rinaldi, Blacklock, Bale, Begley, & Cox, 2012), as well as the mechanical behavior of the yarn in a continuous approach (Badel, Gauthier, Vidal-Sallé, & Boisse, 2009; Philippe Boisse et al., 2010; Charmetant, Vidal-Sallé, & Boisse, 2011).

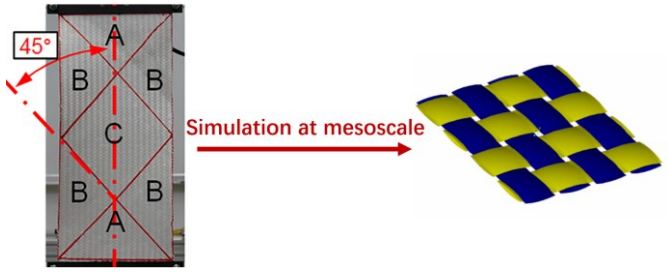

Figure 1.7 Modeling of reinforced materials at the mesoscopic scale: the untwisted fiber bundle is treated as a homogeneous material.

Microscopic scale: the scale (Figure 1.8) the individual fibers that are considered to be homogeneous materials (D. Durville, 2011; Damien Durville, 2008, 2010) . They usually have linear elastic behavior, especially in the case of synthetic fibers. However, this scale requires reliable modeling of the fiber geometry, their position within the yarn, and their interactions.

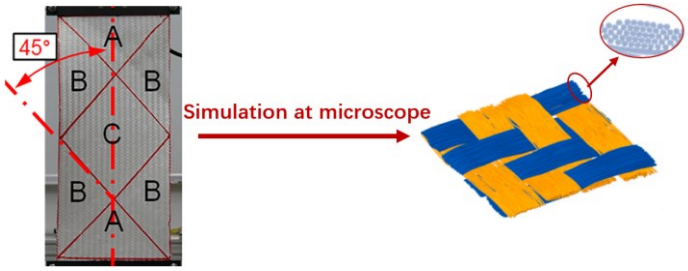

Figure 1.8 Modeling of reinforcements at the microscale: the fiber is treated as a homogeneous material.

Each scale has its own benefits and drawbacks; models from the macroscale are suitable for simulating the mechanical behavior of the entire part. However, it does not provide sufficiently fine data to accurately predict the mechanical behavior and, for example, defect formation processes at the fiber level. However, it is often the small defects (on yarns or fibers) that lead to reduce of the performance of the part. Further, mesoscopic scale models can provide more details about the intertwining and deformation of the yarn, thus providing a deeper understanding of the behavior of the reinforcing material. However, the current mesoscopic models are still inadequate in accurately predicting the mechanical response of yarns, thus it calls for in-depth research and refinement. In order to have a more comprehensive understanding of the physical mechanisms of fiber-fiber interactions, microscale studies are crucial. At the smallest scale of studies, the fibers are the basic units constituting the

reinforcements, and their behaviors and interactions directly affect the properties of the whole part.

Haji created the first micro virtual estimator (Haji Oussama, 2018). His work attempts to simulate the compaction behavior of a fiber bundle (0.5 mm diameter, 39 Polyester fiber) and validates it using X-ray tomography measurements. Haji's work demonstrates the feasibility and consistency of this approach. In his work, the fiber bundle (39 fibers) was reconstructed by XCT technique: the numerical fiber bundle centerline was obtained by processing the XCT slices of the fiber cross section. The compaction simulation of the fiber bundle with beam element (B31) was performed by ABAQUS®/EXPLICIT. And the compaction simulation speed ($V = 1000mm/min$) and damping ($\alpha = 10^5$) were used by the rearrangement simulation of 3 fibers (Figure 1.9). By determining the V and α parameters, the CPU time of the rearrangement simulation of the fibers was optimized, to ensure that the compaction and rearrangement of the fibers were quasi-static (Figure 1.9 (b)) under these parameters, avoiding inertial effects (Figure 1.9 (c)) . And the parameters of hertz contact were determined by compaction of two fibers.

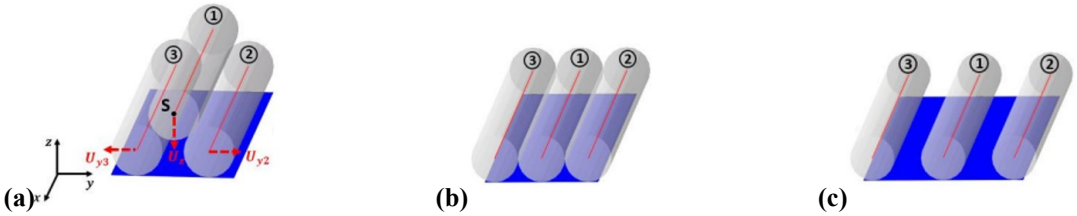

Figure 1.9 Rearrangement simulation with 3 beams. (a) Initial model before compaction. (b) Quasi-static. (c) Inertia effect (Haji Oussama, 2018)**.**

By simulating the compaction of 39 fibers, a comparison of the simulated and experimental compaction curves, fiber positions, and 3D rendering of fiber bundles was obtained as shown in Figure 1.10. Haji's work provides initial validation of the feasibility of extracting numerical fiber bundles from real fiber bundles, as well as verifying its accuracy through compaction simulations. However, there is still an error between the experiment and the simulation in terms of the centerline position of the fibers, and Haji does not define this error and analyze the reason of the error. His study of microstructure only involves the position of fibers, but the contact between fibers, curvature and orientation of fibers are not characterized. The work deserves further development and research: (i) improve the accuracy of Haji's model; (ii) characterize the micro-structure indicators of the fiber bundle, and analyze the relationship between these indicators and the compaction behavior of fiber bundle.

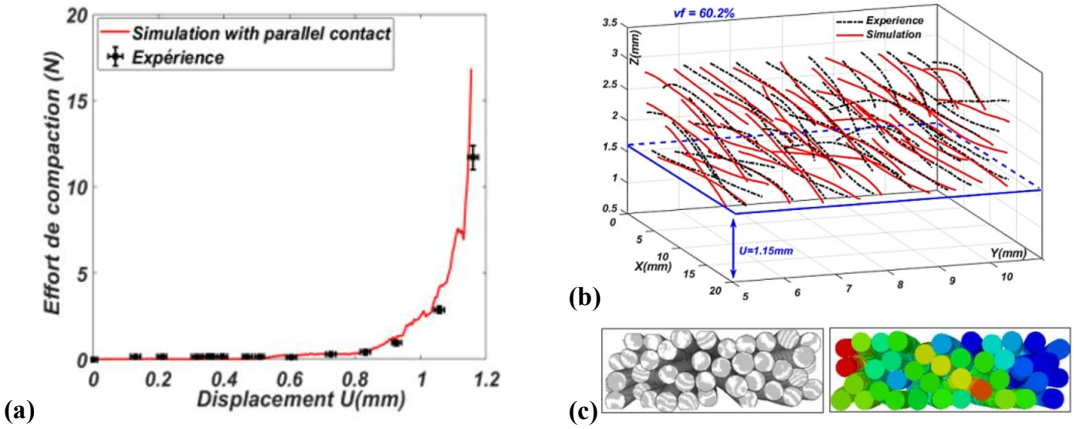

Figure 1.10 The compaction simulation of 39 fibers. (a) The relationship between displacement of compaction plate and compaction force. (b) Centerline of fiber bundle at the last compaction step. (c) 3D geometry of fiber bundle at the last compaction step (Haji Oussama, 2018).

Therefore, this thesis builds on the virtual numerical estimator developed by Haji and enhances it in terms of fiber reconstruction and simulation parameters (in ABAQUS®) (Haji et al., 2023; Haji Oussama, 2018). In addition, several tomography compaction experiments are conducted to verify the accuracy of the developed model. Furthermore, characterization tools of micro-indicators (contact between fibers, curvature of fibers, orientation, etc.) were developed to analyze the internal structure of fiber bundle. The errors between the compaction experiments and the simulated fiber positions were also characterized. The new developed tools help us to analyze in depth the relationship between the geometrical arrangement, orientation and mechanical behavior of the fibers, which mean that the interactions between fibers affect the mechanical properties of the fiber bundle.

In addition, this thesis presents a strategy to create a generator for virtual numerical random fiber bundles. The strategy allows to set: fiber size (slenderness ratio), number of fibers, curvature of fibers, etc. The influence of fiber curvature, compaction path, fiber aspect ratio, and friction coefficient on the behavior of fiber compaction is discussed.

1.3 Conclusion

In this section, the different structures of fiber reinforcements are presented. These reinforcements are multi-scale structures made of yarns, which themselves are composed of thousands of fibers. During the forming step of RTM, fiber reinforcements are subjected to different mechanical loads, resulting in relative movement and deformation at the yarn and fiber levels. Therefore, it is necessary to understand and model the phenomena occurring during this

critical stage. For this purpose, three numerical simulation scales were presented as a complement of the experimental methods. Corresponding to the multi-scale structure of fiber-reinforced materials, numerical simulations models that exist in the literature were mentioned for the three scales of a fibrous structure (macroscopic, mesoscopic and microscopic).

Thus, it is concluded that modeling at the microscale (fiber level) is interesting and will help us to understand and model phenomena at the fiber scale. Through this research, it is found that synthetic polyester fiber's section is a regular circle, so numerical modeling of the fiber is feasible, and modeling from the regular cross-section of the fiber can be considered. However, its surface is not smooth, and its surface friction should be considered.

This section also presents the fiber microscopic numerical estimator that has been developed in a previous work (Haji Oussama, 2018) which opens to the necessity of further improvements. Microscopic result analysis indicators must be developed to discuss the relationship between fiber bundle microstructural parameters and mechanical behavior, and a generator for virtual numerical random fiber bundles has also to be developed.

The next section analyzes the loading path imposed on the fiber reinforced material during the molding process, and the extraction of the geometric model of the fiber material through computed tomography technology.

Section 2 Behavior of fiber reinforcing materials during compaction and characterization methods

2.1 Loading path

During composite forming, especially in processes such as RTM, fiber-reinforced materials undergo complex mechanical loading. These materials, due to their inherent multiscale nature, exhibit specific deformation behavior at different scales of structure during loading. Therefore, when understanding and predicting the behavior of materials, it is necessary to take all levels into account from the macroscopic to the microscopic.

To accurately model and predict the microscopic deformation mechanisms, choosing the appropriate loading path is crucial. In practice, this means that we need to have a deep understanding and control of these loading paths, to reproduce in simulation of the deformation patterns observed in experiments. Long and Clifford descripted the mechanical loading path of fiber reinforced material (Long A C & Clifford M J, 2007). Cornelissen summarized the microscale deformation mechanisms, shown in Figure 2.1(Cornelissen, 2013).

Long A C and Cornelissen's work helped to define the different deformation mechanisms of the fiber that may be experienced during the forming process.

Cornelissen analyzed these four loading paths of the textile, the changes in the fibers at the microscopic level corresponding to each loading. This work is summarized here. The same phenomenon happens of four loading paths in micro level: relative sliding between fibers according the longitudinal and the transverse directions, and fiber rearrangement. But the different behaviors for following loading path:

- Tensile: And the fiber extension along the longitudinal axis.
- Bending: Fiber relatively obvious bending.
- Shear and compaction: Fiber relatively slight bending.

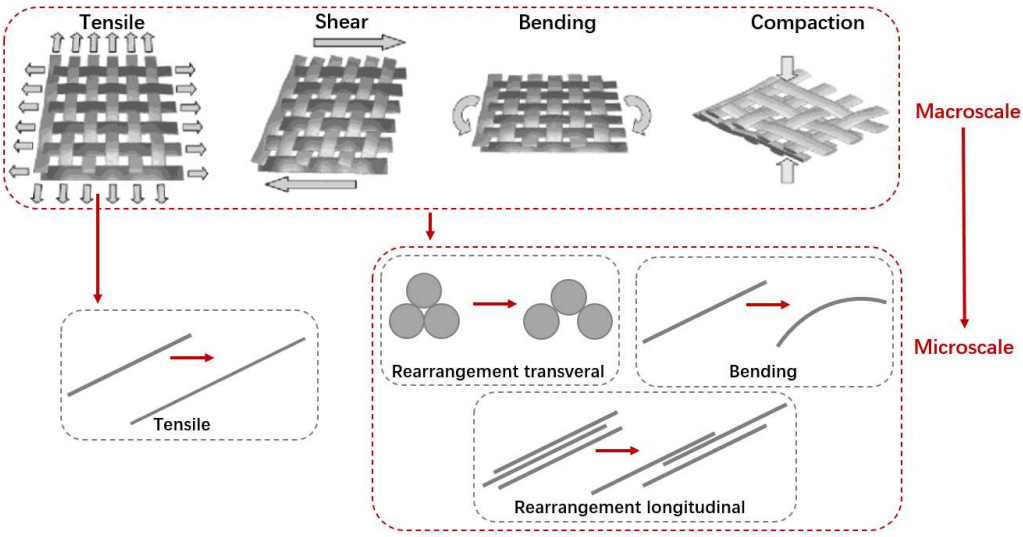

Figure 2.1 The principle of microstructural deformation, and the relationship between macrostructural deformation(Long A C & Clifford M J, 2007).

In most of these mechanisms, fiber-to-fiber friction plays a key role. The most interesting type of loading involving all these mechanisms to be studied at the micro scale is compaction. This is because, compaction loading path that is most likely to produce the phenomenon of fiber displacement within the fiber assemblage. This phenomenon reflects the rearrangement and the sliding between fibers. Therefore, the compaction path will be considered in the present work and used in the mechanical experiments of the fiber medium. This micro model is in the developmental and validation state, and when considering compaction, the fiber rearrangement and sliding are sufficient to challenge the accuracy of the model. In addition, the compaction loading will influence fiber's indicators such as curvature, orientation and the contact between the fibers. So that, it's possible to analyze the microstructure of the fibers with the compaction loading path. The other loading paths of fibers might be used in the further validation of the model. And, as previously discussed, other mechanical solicitations also produce compaction between fibers, and bending deformation. The microscopic effects of these mechanical paths are closely related.

A micro-compaction machine is consequently used to facilitate the combination with the tomography scanner. In addition, an accurate model of the fiber medium is also to be investigated in this thesis. The model obtained from real fiber media, and extracting the fiber media by tomography is a reasonable and accurate method, which will be discussed in Section 2.6

2.2 Phenomenology of reinforcement fibers compaction

Before starting to analyze the modeling and simulation of a fibrous medium in compression, it is necessary to analyze this type of loading and its experimental testing on different types of fibers. Figure 2.2 (a) shows the compression curves obtained after testing a fiber assemblage of different materials (glass, steel, cotton, hair, etc.) (Mezeix, Bouvet, Huez, & Poquillon, 2009; Poquillon, Viguier, & Andrieu, 2005). Unloading was also performed at the same loading rate (6 mm/min). The behavior obviously depends on the material of the fibers, and the shape of the compression curves is the same for all tested materials. In fact, the behavior of the fiber assemblies in compression is nonlinear and exhibits hysteresis. For all materials, a permanent deformation was observed. This is attributed to the irreversible rearrangement of the fibers during compressive loading, which depends on the intensity of the loading. Indeed, if the first compressive loading is strong enough, the fibers will rearrange by changing the morphology of the fiber assemblage. The assemblage will not regain its initial morphology due to plastic deformation of the fibers (steel wool) and friction between the fibers. For example, glass fibers exhibit the greatest residual deformation. This is because of the large smooth and regular surface of the fibers, which minimizes friction and promotes rearrangement. In addition, the compaction curves of entangled (surface deboned) and non-entangled carbon fibers are illustrated in Figure 2.2(b). Entanglement allows the fibers to move and rearrange more easily at lower stresses, which results in a larger slope at the beginning of the compaction curve.

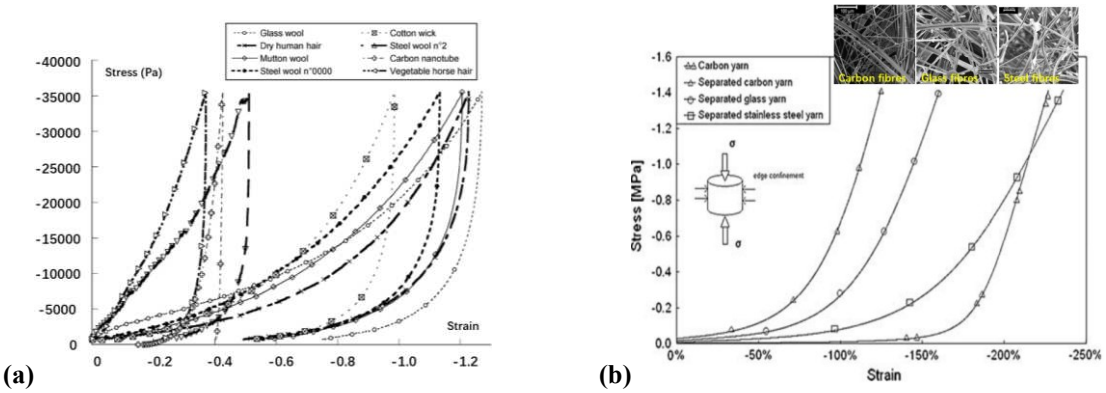

Figure 2.2 Compression effect of different types of fiber assembly. (a) with same initial density 150Kg/m^3 (Poquillon et al., 2005)**. (b) compresses deformation at 6 mm/min (Mezeix et al., 2009).**

The test presented in Figure 2.3 (a) considers the initial relative density of the assemblage (Mezeix et al., 2009). The initial structure of the fibers assemblies is also a key parameter in compression studies. At high initial density (200 Kg/m^3), the slope of the onset of the

compaction curve is large. This is attributed to the fact that the interactions between the fibers affect the compaction process earlier, making higher required stresses to achieve further compression. In contrast, fiber samples with low initial density (100 Kg/m^3) are more easily compressible during the initial compression stage. However, their subsequent compression becomes more difficult as the voids decrease. The initial relative density of the fiber structure influences the porosity between the fibers, and thus determines the ability of the fibers to displace between them.

Studies conducted on fiber assemblies in compression/unloading cycles have shown that the microstructure of the fiber medium changes as the number of cycles increases (Comas-Cardona, Le Grognec, Binetruy, & Krawczak, 2007; Long Li, Zhao, Yang, Zhang, & Duan, 2015; Robitaille & Gauvin, 1999; Stankovic, 2008). However, starting from a particular number of cycles, the compaction behavior shows a negligible evolution. To illustrate this point, a loading/unloading cyclic test was carried out on a carbon NCFs, and the results are shown in Figure 2.3 (b) (Long Li et al., 2015). It indicates that the compression behavior changes very little from 4th cycle. In fact, after the first few compression cycles, the morphology of the fiber assemblage, as well as the movement and contact between the fibers, allow barely evolution of the microstructure during the other cycles.

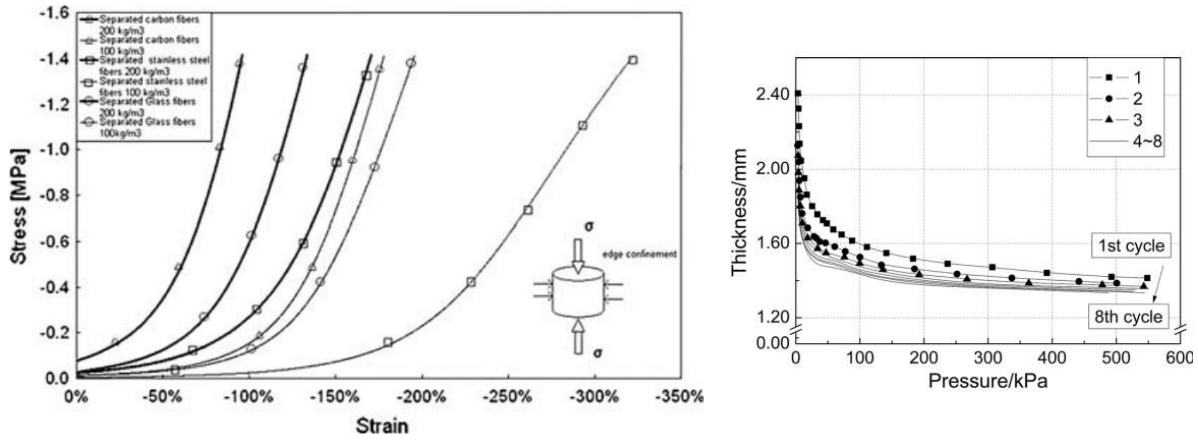

(a) **(b)**

Figure 2.3 (a) Comparison of compression stress/strain curves for different initial densities (Mezeix et al., 2009)**. (b)Effect of the number of loading cycles on compaction** (Long Li et al., 2015)**.**

2.3 Effect of loading speed on fiber components

Somashekar carried out compaction tests on continuous filament random mat with different compaction speeds and final V_f (Somashekar, 2009. Figure 2.4 (a)). As the compaction speed

increases, the compressive stress increases for a given strain. This means that at faster speeds, a greater force is required to compress the material to the same strain. Indeed, the rearrangement of the fibers dominates in the early stages of compression, as shown by the large variation of the fiber volume fraction. Thus, the behavior of the fiber assemblage is influenced from the beginning by the relative motion between the fibers. This relative motion is dependent on the compression speed: compression at lower speeds will allow the fibers to rearrange and fill the largest voids within the fiber medium, leading to higher compression rates. This also explains why the relaxation rate is higher as the speed increases (Figure 2.4(b)): in this case, the contact forces between the fibers increase rapidly while the voids between the fibers are still increasing. Once relaxed, the fibers begin to reorganize and align towards an overall equilibrium state and the contact forces decrease. It should be emphasized that the rate of stress relaxation depends not only on the loading rate, but also on the orientation of the fibers: the better the fibers are aligned, the less relaxation they experience (Kim, McCarthy, & Fanucci, 1991).

In addition, Figure 2.4(c) reflects the increase in stress relaxation with increasing final compaction volume fraction. The stress relaxation occurs after the cessation of compaction due to the fact that: some of the fibers experience plastic deformation during compaction, and after the cessation of loading, this part of the fibers rearranges itself to find a lower energy state to seek stability. A high compaction volume fraction means that the fibers are more tightly arranged, then the contact between the fibers increases and the friction increases. This is because tighter compaction results in more contact points between the fibers and more internal friction, resulting in higher pressures at the same strain. Therefore, after loading is stopped again, the rearrangement of the internal structure and fewer contact points have a greater effect on the pressure, and stress relaxation becomes more pronounced.

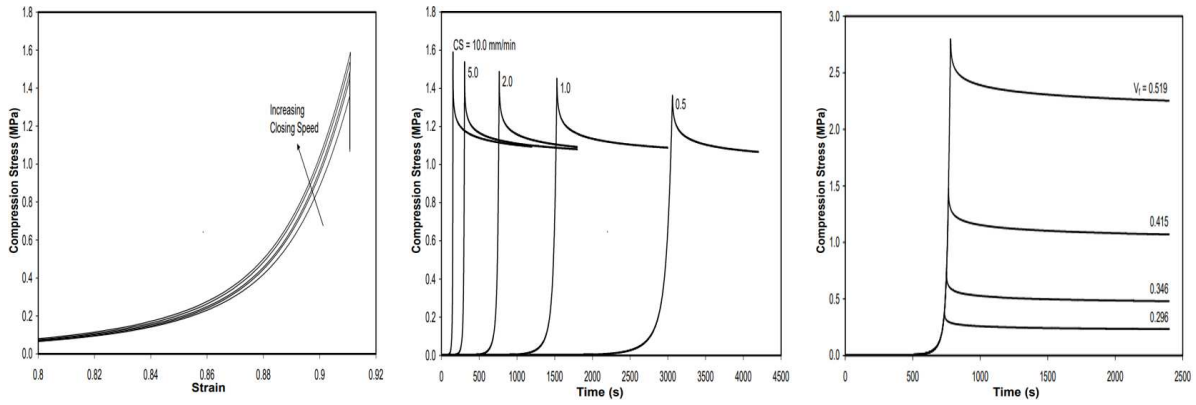

(a) **(b)** **(c)**

Figure 2.4 Continuous Filament Random Mat (CFRM) Compaction tests. (a) Compaction speed tests, V_f (volume fraction at end of compaction) = 0.415. (b) Compaction/relaxation speed tests, V_f = 0.415 (c) Compaction level (V_f) tests, CS=2.0mm/min (Arcot Arumugam Somashekar, 2009)**.**

2.4 Characterization of the compaction behavior of fiber assemblies

The previous section highlighted the nonlinear behavior of fiber assemblies during compaction. This behavior is often demonstrated by the variation of the ‘‘compressive stress’’ (defined as the ratio of the compressive force to the apparent contact area between the tool and the sample) with the ‘‘fiber volume fraction’’ V_f. This variation is described in fiber media compaction as a power law relationship, as described in the following equation (van Wyk, 1946):

$$P = \frac{KEm^3}{\rho^3}\left(\frac{1}{{V_f}^3} - \frac{1}{{V_{f_0}}^3}\right) \tag{2.1}$$

Where V_f and V_{f_0} are respectively the end and initial volume fraction of fiber assembly. V_{f_0} is ideally the value of V_f for the uncompressed state. The factors K is adjustable parameters to account for other parameters not described in Equation 2.1, such as fiber orientation and tortuosity. E is the Young's modulus of the fiber, m is the mass of the fiber assembly and ρ is the density of the wool (about 1.3 g/cm^3) (Beil & Roberts, 2002; van Wyk, 1946).

The compressive behavior of the fiber assemblage can be divided into three stages. These stages have been summarized by Toll in a qualitative manner for the main types of fiber assemblages: three-dimensional assemblages in which the fibers are initially randomly oriented, and two-dimensional assemblages in which the fibers are randomly oriented or approximately parallel (Toll, 1998). Figure 2.5 illustrates this qualitative differentiation of compressive stress P relative to volume fraction $\emptyset$ in a log/log coordinate system. In the first stage, when the relative density is below $\emptyset_0$, the mechanical response of the fiber assemblage is almost

negligible. In the second stage, the fibers begin to rearrange and start to contact each other. For example, in the case of curved, fibers may undergo elastic deformation such as bending. This stage is usually represented by a compression model in which the mechanical behavior of the fibers is considered elastic (Equation 2.1). When the compressive load is high enough, the behavior of the fiber assemblage enters a third stage, in which the fibers deform in inelastic regions (Figure 2.5). Depending on the nature of the fibers, two modes of behavior can be distinguished: (i) the behavior of brittle fibers, in which the fibers may break, resulting in a loss of stiffness of the fiber assemblage. When the fiber fragments are unable to break further, the stiffness increases again. (ii) the behavior of ductile fibers, in which the fibers undergo plastic deformation. However, this does not significantly change the evolution of the compression curve.

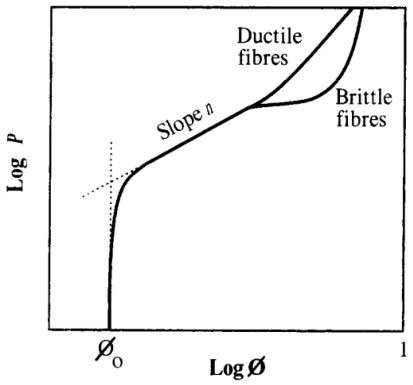

Figure 2.5 Three phase of the compressive response of a general fiber assembly (Toll, 1998)**.**

2.5 Effect of the morphology of the fiber components

Fiber assemblies can assume different morphologies, such as 3D (a ball of wool), 2D (a mat) or 1D (a bundle of roving). The initial geometric morphology of a fiber assemblage is characterized by several parameters, including the orientation of the fibers. This parameter (such as morphology) has a strong influence on the compression behavior (Masse, Salvo, Rodney, Bréchet, & Bouaziz, 2006; Toll, 1998). Indeed, the indices n and m that determine the compression curve, as well as the initial relative density V_{f_0}, are related to the morphology of the fiber assemblage:

Toll hypothesized that the number of contacts is proportional to the volume fraction, so, he deduced a more general compaction law than van Wyk (Toll, 1998):

$$P = KE({V_f}^n - {V_{f_0}}^n) \tag{2.2}$$

Where the n is the exponent. When n = 3, equation 2.2 is Van Wyks compaction equation of wool assemblies (Beil & Roberts, 2002; van Wyk, 1946)]. Masse validated the relationship between Young's modulus E and density ρ (Masse et al., 2006):

$$E = \beta\rho^m \tag{2.3}$$

Where the m is the exponent, β is the coefficient. Compaction of fiber assemblages of different morphology types, in particular wools (3D), mats (2D) and unidirectional roving have been studied. The variation of compressive stress with relative density is demonstrated in the log/log coordinate system of Figure 2.6 (Toll, 1998).

The 3D morphology leads to an exponent $n = 3$, whereas roving, whose fibers are almost parallel (1D morphology), take larger values of the exponent n. This can be explained by the presence of linear contacts between the almost parallel fibers in roving, whereas in other types of fiber assemblages the contacts are mainly punctiform.

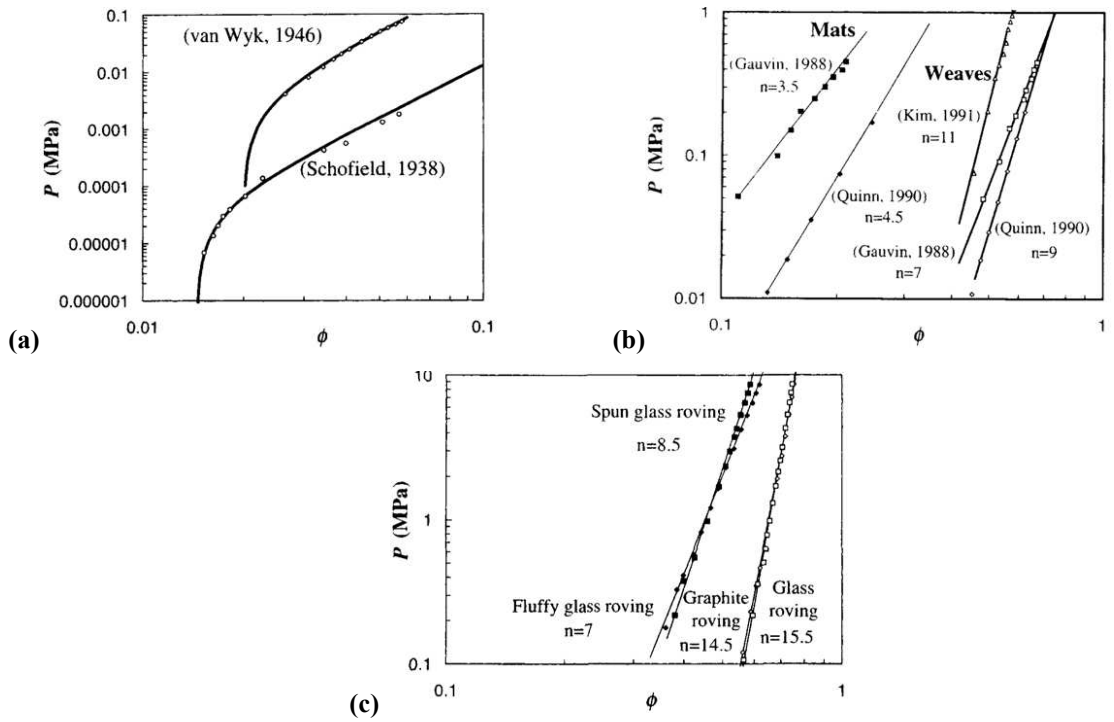

Figure 2.6 Effect of the morphology for the fiber assembly (a) 3D ($P = KE(V_f{}^3 - V_{f_0}{}^3)$), (b) 2D ($P = KEV_f{}^n$), (c) 1D ($P = KEV_f{}^n$) (Toll, 1998)**.**

Metallic wool with different initial unit area masses were tested, so the samples with different initial orientations. The larger the initial unit area mass, the more the fibers tend to align in a preferred direction (as the medium becomes denser). Thus, the initial unit area mass is an indicator of fiber orientation. This indicator is associated with two indices, n (Equation 2.2) and m (Equation 2.3). Indeed, Figure 2.7 shows the variation of indices n and m with initial

unit area mass. The indices vary between 3 and 5, which is consistent with the 3D morphology (n=3) and 2D morphology (n=5) found in the work of Wyk and Toll (Toll, 1998; van Wyk, 1946).

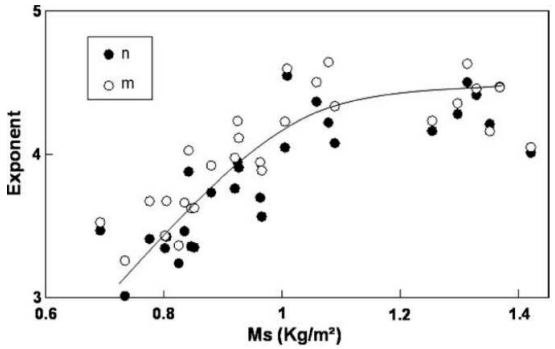

Figure 2.7 Variation of the two exponents n and m with the initial surface mass (Masse et al., 2006)

The fiber orientation is usually characterized by the orientation tensor A, where the component A_{ii} denotes the degree of alignment of the fibers along the direction of X_i. the calculation of A shows that A_{22} is the dominant term, which corresponds to the orientation of the fibers along the direction of X_2 as shown in Figure 2.8(a). Figure 2.8 (b) shows the variation of the initial unit area mass of the steel wool sheep versus A_{22}. The mass per unit area here is defined as the ratio of the total mass of the sample to the surface area perpendicular to the direction of compression. This surface area remains fixed during the constrained compression.

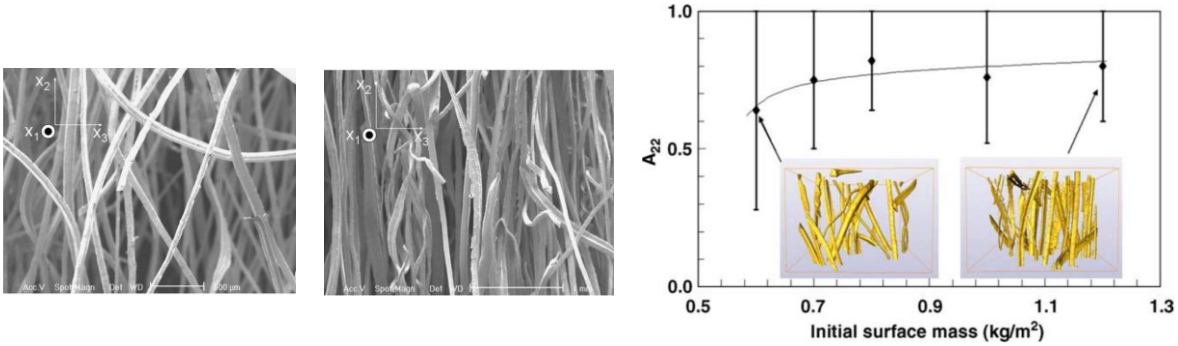

(a) **(b)** **(c)**

Figure 2.8 The relationship between initial state of fiber assembly and fiber orientation. SEM view of the metallic wools in the thickness in a band of surface mass: (a) 0.7 and (b) 1.3 kg/m^2. (c) Influence of surface mass on the component A_{22} of the orientation tensor of the fibers (Masse et al., 2006)**.**

In addition, the orientation of the fibers within the fiber assembly may be indicated by the deflection angle, shown in Figure 2.9 (Chatti, Bouvet, Michon, & Poquillon, 2020; Czabaj, Riccio, & Whitacre, 2014). These works provide inspiration for the subsequent creation of free but bounded by certain orientations fiber bundles.

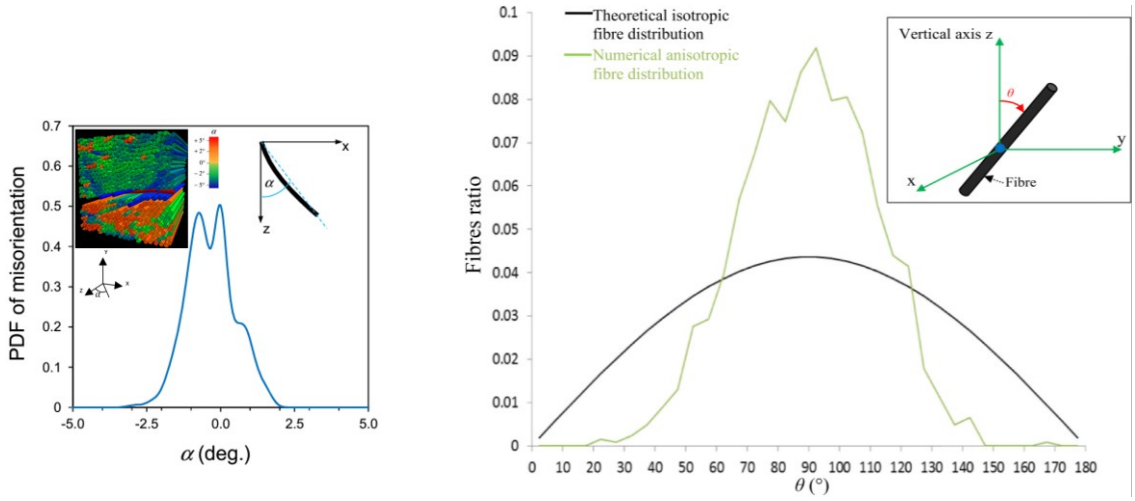

(a) (b)

Figure 2.9 Fiber orientation expressed by deflection angle. (a) PDF of fiber misalignment angle α relative to the z-axis and the 3D CAD rendition of the segmented fibers with color scheme representing the α (Czabaj et al., 2014)**. (b) Different fiber orientation distributions charactered by the angle between the fiber direction and the vertical Z-axis θ** (Chatti et al., 2020)**.**

2.6 Characterization of fiber media by X-ray tomography

Computed Tomography (CT) is a kind of three-dimensional imaging technique. According to the physical signals, CT technology mainly includes X-ray CT, gamma-ray CT, electrical CT, and acoustic CT. Both of these CT technologies utilize different types of physical signals to pass through the object under test, and reconstruct the internal structure of the object based on the changes in the received signals (Meng, 2022; Zhang et al., 2023). For example, (i) X-ray CT and gamma-ray CT are mainly used to obtain high-resolution images of internal structures and are often used for medical and industrial inspections (Villarraga-Gómez, Herazo, & Smith, 2019; Withers et al., 2021); (ii) Electrical CT techniques are mainly used for industrial process monitoring and are suitable for real-time imaging of dynamic processes (Meng, 2022). Of these, X-ray CT (XCT) is widely used in the study of textile composites. The XCT technique is able to reveal the complex internal structure of fibrous media at micro- and mesoscopic scales. It provides direct visual information and quantitative data for understanding its deformation mechanisms under different loading conditions. (i) Through 3D reconstruction of high-resolution XCT images, it is possible to obtain a detailed observation of the alignment, distribution, and curvature of fibers. In addition, (ii) the non-destructive inspection feature of XCT allows continuous observation of the same sample at different loading stages. Therefore, it is possible to track and analyze the deformation process of the internal structure of the material under the loading path, and reveal the microscopic mechanism of its deformation. This

information is essential for building more accurate mechanical models, predicting the mechanical behavior of materials, and optimizing the design and manufacturing process of composite materials.

2.6.1 The working principle of X-ray Computed Tomography (XCT)

This paragraph will briefly describe the working principle of XCT, the information is obtained with (Prabhu, Naveen, Bangera, & Subrahmanya Bhat, 2020).

From the perspective of wave-particle duality in quantum mechanics, X-rays can be described both as waves and as particles. This means that the X-rays can be viewed as waves of frequency v , or a set of particles with photon energy $E = hv$. X-rays were discovered in 1895 by the German physicist Wilhelm Roentgen, who realized that these rays could penetrate biological organization, and so on. As a result, they were initially used in medical science. After a long period of development and research, this technology has been expanded to industrial applications. And it is well suited for the study of heterogeneous materials, such as fiber-reinforced materials. The process of X-ray characterization of an object consists of two parts: (i) a 2D projection of the sample from different views, and (ii) a reconstruction algorithm is used to obtain the 3D structure of the scanned sample from the projection. The main steps of the process are shown in Figure 2.10. X-rays are generated by X-tube, synchrotron Radiation, field emission X-ray and so on.

Figure 2.10 The main steps of the XCT analysis process.

Figure 2.11 is a schematic diagram of the operation of an X-ray tube. The essential components of an X-ray tube include a tungsten filament for the anode target and the cathode. The cathode, connected via a power supply, is heated by the Joule effect, causing the cathode temperature to rise. This increase in temperature causes an increase in the kinetic energy of the free electrons, which cause the electrons vibration. When the kinetic energy of the electrons is strong enough to overcome the electrostatic bond with the atoms of the tungsten filament, these electrons break away from the metal surface and move towards the anode accelerated by the potential difference. In the process, the anode is strongly bombarded by high-speed electrons. In brief, when the high-speed electrons generated at the cathode hit the anode target, the energy of their motion is

partially converted into the radiant energy of the X-ray photons, which are emitted in the form of X-rays.

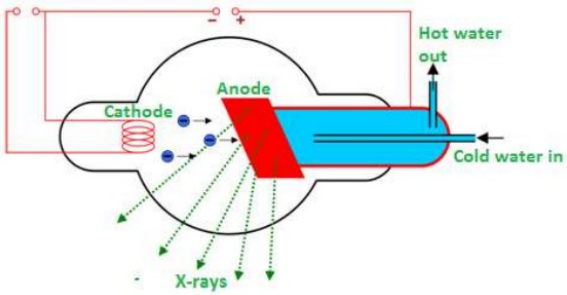

Figure 2.11 Production of X-RAYS using X-RAY Tube (Prabhu et al., 2020)**.**

X-ray of wavelength λ and intensity $I_0(\lambda)$ emitted from an X-ray tube passes through a sample of a thickness t. The interaction between the incident X-ray and the material exhibits various phenomena as shown in the Figure 2.12. A portion of the X-ray decay in intensity after passing through the material to the extent shown in:

$$I(\lambda) = I_0(\lambda)e^{-\left(\frac{\mu}{\rho}\right)\rho t} = I_0(\lambda)e^{-\mu_m \rho t}$$

Where the t is the thickness of sample, ρ is the density of the sample, μ_m is the mass absorption coefficient of the sample. This is related to the intensity of the incident X-ray, the properties of the substance, including the composition and density of the substance, and so on. The attenuation is of the number of photons in the X-ray, not the energy, and the transmitted X-ray essentially propagate in their original direction. When incident X-ray are absorbed by sample, they also produce the photoelectric effect, fluorescent radiation, scattered rays, and thermal energy. About 99% of the energy is converted into heat, while the remaining energy is converted into X-ray (Liang Yu, 2007).

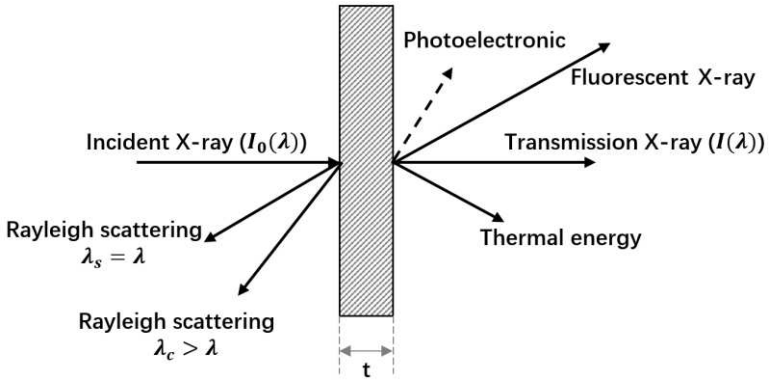

Figure 2.12 The interaction between the incident X-ray and the material exhibits various phenomena(Liang Yu, 2007)**.**

The general principle of reconstruction is illustrated in Figure 2.13 (THIERY, 2013). In order to reconstruct an image made up of m × n points, called pixels (image elements), the scanned object must be rotated to n positions. At same time, projecting each position $\boldsymbol{p}$ ($1 \leqslant \boldsymbol{p} \leqslant \boldsymbol{n}$) onto m detectors.

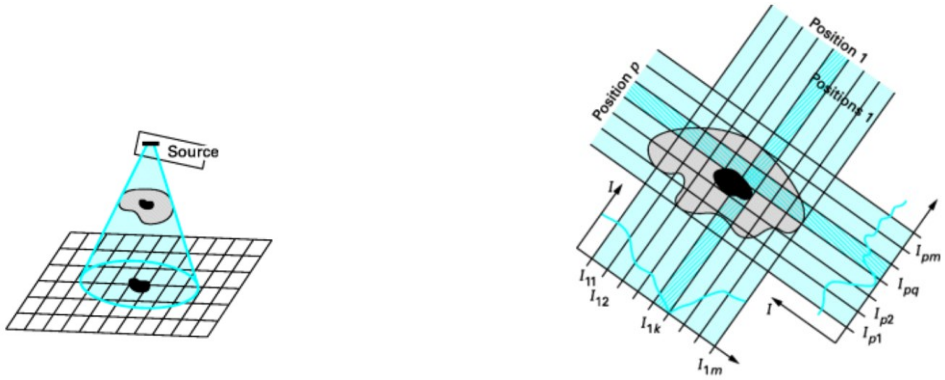

(a) **(b)**

Figure 2.13 XCT reconstruction principle (THIERY, 2013)**.**

And each assigned an absorption coefficient μ_{ij} that needs to be determined. The intensity measured by detector k when the detector array is in position 1(I_{1k}):

$$\ln\left(\frac{I_0}{I_{1k}}\right) \infty \sum_{ij} \mu_{ij}$$

2.6.2 X-ray tomograph characterization at the meso- and microscopic scale

The aim of this section is to illustrate the contribution of X-ray tomography in characterizing and understanding the behavior of fibers subjected to loading path. Studies will be carried out on microscopic and mesoscopic scales. The reason for studying from the micro-scale is that this paper investigates the mechanical response of fiber bundles under the compaction path. The mesoscopic scale is studied because the developed model will be used for mesoscopic scale modeling.

Mesoscopic scale

During the pre-molding stage of the RTM (Resin Transfer Molding) process, the roving in the fiber reinforcement undergoes significant displacements and deformations: consolidation, stretching, bending, twisting, shearing and compaction (Hwang, Um, & Kim, 2023; Jeon et al., 2023; Stepan V Lomov, 2011; Xiao, Wang, Soulat, & Gao, 2020; Xiao, Wang, Soulat, Legrand, & Gao, 2019).

A.A. Somashekar investigated the permanent and elastic deformation of a biaxial stitched glass (BSF) fiber reinforcement during compression by micro-CT technique (A. A. Somashekar,

Bickerton, & Bhattacharyya, 2011). A.A. Somashekar studied the cross shape of weft and warp yarn after compaction with different conditions (speed, initial structure of BSF), validated the hypothesis: the cross-sectional shape and size of the fiber bundle influence the permanent and elastic deformations. In addition, it explored the relationship between deformation over time and fiber bundle displacement in the direction of the compaction load.

Wang reconstructed the fiber fabric before and after compaction by XCT, and compare the 3D shapes of yarn with simulation and experiment after loading (D. Wang, Naouar, Vidal-Salle, & Boisse, 2018). In addition, the Poisson's ratio of the yarn in the model was determined by longitudinal compaction experiments (Figure 2.14 (a)). The simulation of the longitudinal compaction and transverse extension of the fabric on the mid-conceptual scale is shown in Figure 2.14(b, c), and the yarn is considered as a homogeneous medium in the simulation. The deformation state of the yarn obtained from the simulation is consistent with the deformation state obtained from the XCT reconstruction.

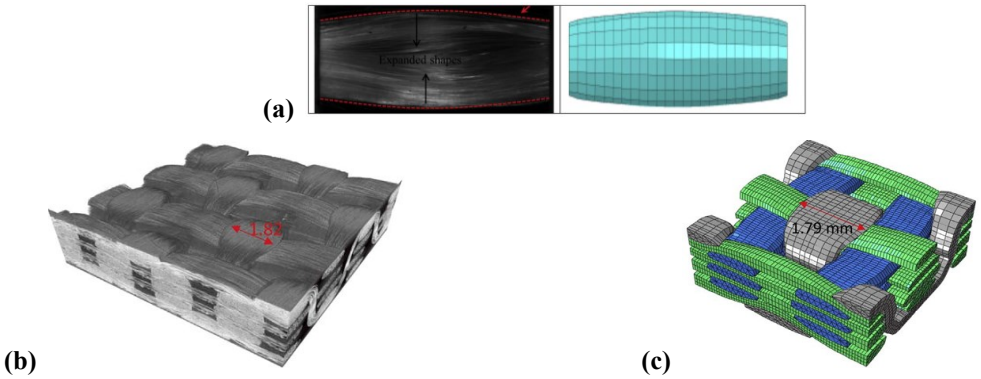

Figure 2.14 Comparison of the 3D shapes. (a) The yarn, experiment (left), simulation (right) (b) X-ray tomography. (c) with longitudinal compression and transverse extension model (D. Wang et al., 2018)**.**

Zheng created tools that automatically identify mesomorphic features of damaged woven composite fabrics with XCT (Zheng et al., 2024). The braided composite material was subjected to compaction experiments, which resulted in damage (cracks), deformation, and fracture within the sample. A tool to automatically reconstruct the 3D structure of the sample is created by 3D reconstruction of the sample using XCT technology and neural network training. Analyzed the data of mesomorphic parameters (including cracks, deformation rates, and fracture rates) of damaged samples, shown in Figure 2.15.

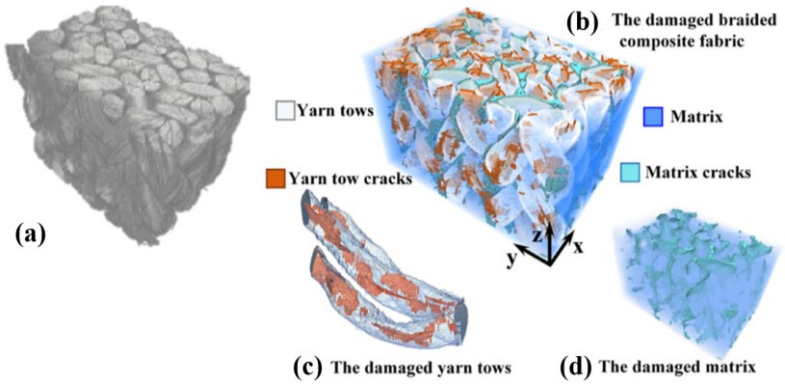

Figure 2.15 3D volume rendering images. (a) the 3D XCT reconstruction. (b) the 3D model of the damaged braided composite fabric (c) crack existed in the individual yarn. (c) the cracks existed in matrix (Zheng et al., 2024)**.**

Microscopic scale

Masse (Masse et al., 2013; Masse & Poquillon, 2013) also used X-ray tomography to characterize the wool assembly's structure. A wool sample with an initial relative density of 2.5% was used, whose constituent fibers were irregular in shape and length (mean length = 5.6 mm, mean diameter = 80 µm). The structural characterization was based on XCT images and the skeletonized structure of the samples was extracted (Masse et al., 2013). Toda also analyzes the structure of individual fiber strands (bundles) by means of XCT (Toda, Grabowska, & Ciesielska-Wróbel, 2017).

Latil (Latil, Orgéas, Geindreau, Dumont, & Rolland du Roscoat, 2011).provide a method to quantitatively analyze the mechanism of fiber bundle deformation The method is based on the scanning of fiber bundles by means of the XCT technique and the analysis of slices of fiber bundles. The studied samples were extracted from fluorocarbon (PVDF) fishing line containing 69 fibers with length L=11 mm, diameter D=150 μm and Young's modulus E=2 Gpa. The samples were wrapped in olive oil at 5 °C to approximate the rheological effect of the polymer collectives and to provide a certain consistency treatment to the fiber medium, prior to mechanical testing. Single compaction experiments were performed on the samples. Latil skeletonized the reconstructed microstructural model of fiber bundles, as shown in Figure 2.16. And the contact and curvature changes at different compaction stages are discussed. This study provides fiber reconstruction ideas for the present thesis.

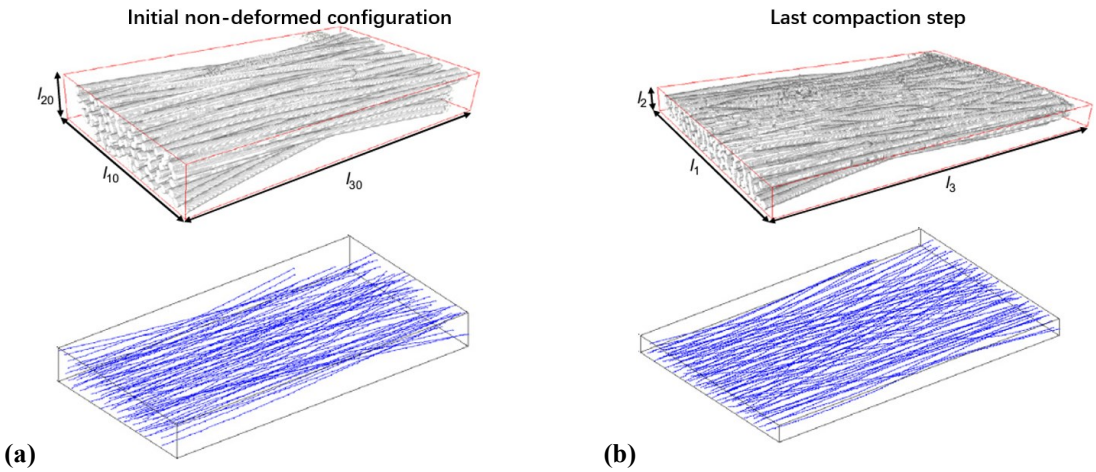

Figure 2.16 3D geometry and centerline of reconstruction of 69 fibers. (a) before compaction. (b) last compaction step(Latil et al., 2011)**.**

2.7 Conclusion

Concerning the mechanical loading path, a uniaxial compaction path is considered. Unlike alternative loading paths such as stretching and bending, the compaction pathway predominantly led to a reduction in the volume fraction, and a rearrangement between fibers in internal structure of the fiber bundle. In other words, the compaction process is intrinsically associated with changing in the density of the fiber bundle and the inter-fiber interactions. In addition, an analysis of the bibliography shows that even if some physical phenomenon and parameters have been pointed out, the compaction/compression behavior of a fiber bundle is far from being perfectly understood and mastered. Models proposed for this behavior are then based on empirical approaches requiring an inverse identification of coefficients on an experiment. This relationship between these coefficients and the yarn properties/parameters is in addition not established. Consequently, on the road to obtain a physically based behavior law of yarns, the compaction/compression behavior is undoubtedly the most important and interesting and will focus our attention is this document.

This section permits to conclude that the use and post-treatment of XCT during the compression might enable to rebuild the microstructure and then to characterize it as a function of the load. It then appears as the essential tool to build the initial microstructure of real sample, but also to validate the numerical modeling.

In addition, analyzing previous studies on this topic in the literature, we can still define some preliminary parameters based on what has been presented so far:

- Modeling scale: as discussed in the previous chapters and in the general introduction, the modeling will be performed on a microscopic scale.
- Structure of the model medium: In accordance with section 1.3.2, untwisted bundles (consisting of fibers placed side by side, slightly tangled and almost parallel) will be considered. Therefore, the model medium will be a collection of tangled and almost parallel fibers.
- Number of fibers: This parameter presents a challenge in microscale modeling, as an untwisted bundle contains thousands of fibers. Given that the goal is to define a research medium, multiple post-processing and test simulations will be required, whose processing time depends on the number of fibers. The initial goal is to define and validate an effective strategy, which for this study will be considered for about dozen fibers (40 fibers).
- Material and geometry of the fibers: in order to be able to experimentally characterize them using reasonable technical means, polyester fibers with a diameter of 0.5 mm and a length of 15 mm, supplied by LPMT in Mulhouse, will be used. Moreover, its mechanical behavior and friction coefficient have been studied in recent literature (Gassara, 2016; Gassara, Barbier, Wagner Kocher, Sinoimeri, & Pumo, 2018).
- The cross-section of the fibers is considered as a circle, primarily to simplify the analytical process. Preliminary construction of the model (construction of the numerical model of the fiber bundle): an X-ray tomography scanner combined with a micro-compactor was used to construct a numerical model of the fiber bundle before and after compaction. In the tomography slices, the fiber's section could be considered as regular circle, which consistent with the condition mentioned above that fibers are regarded as circles.

If the initial geometry of a real sample can be obtained efficiently through XCT scans, the parametric study, required to understand the influence of the geometrical and material parameters of a yarn, imposes to be able to build non existing fiber bundles with controlled parameters. The next section then proposes ideas for creating our own virtual fiber bundle model as well as a discussion of the simulation parameters in the model.

Section 3 Creation of virtual numerical models of fiber media

According to the above lines, there have been a large number of researchers who have created geometric models of the fibrous medium through XCT technology (Latil et al., 2011; Masse et al., 2013; D. Wang et al., 2018). However, these geometrical models are completely dependent on the XCT experiment, thus obviously on the existence of the bundle and are limited to the time costs. Therefore, it is crucial to create virtual an efficient generator that can generate a large number of virtual textile samples. There are currently scholars creating virtual fiber media from mesoscopic and microscopic perspectives.

3.1 Creation of virtual fabrics at the mesoscopic scale

Renaud G. Rinaldi (Rinaldi et al., 2012) describes an efficient method to generate virtual textile composite specimens via Monte Carlo algorithms and Markov chain operations. The virtual model created is based on geometric data of the actual textile composite collected using high-resolution X-ray micro-CT technology, as shown in Figure 3.1 (a). And followed by algorithms to generate virtual representations of three-dimensional fiber bundles (tow), shown in Figure 3.1 (b). The analysis process involves the definition of topological and geometrical rules to correctly model the interweaving and alignment between fiber bundles.

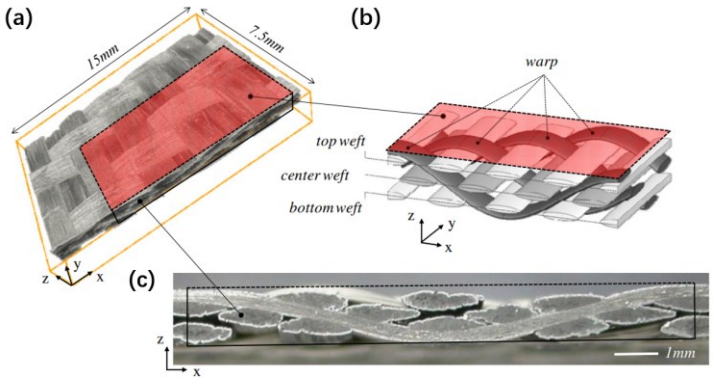

Figure 3.1 The angle interlock architecture of the subject material: (a) 3D micro-CT image, (b) optical image of a cross-section along the warp direction, (c) idealized schematic of the unit cell (Rinaldi et al., 2012)**.**

The tow geometry is described in terms of the tow cross-section perpendicular to its nominal axis, which is usually chosen to be the axis in the global Cartesian system. For each tow (m), the coordinates of centroid of its cross-section, $(\xi, z)^{(m)}$ ($\xi \equiv y$ for warp tows, $\xi \equiv x$ for weft tows, z for thickness direction) are specified as continuously varying functions of

position along the tow. $\{\xi^{(m)}, z^{(m)}, A^{(m)}, ar^{(m)}, \theta^{(m)}\}$ describe the geometry of tow m at each sequence of sections, where $A^{(m)}$ is its area, $ar^{(m)}$ is aspect ratio, $\theta^{(m)}$ is orientation (rotation about the tow axis).

The conclusions highlight the ability of this method to provide accurate microstructural models for the simulation of thermomechanical properties and damage evolution of fiber-reinforced composites, while preserving the statistical characteristics of the complex interactions between fiber bundles. Thus, the experimental data are presented in set $\{\xi^{(m)}, z^{(m)}, A^{(m)}, ar^{(m)}, \theta^{(m)}\}$.

The generation step of 3D virtual weave fabric shown in Figure 3.2 (a) through the modification and adjustment of warp and weft tows, avoid the initial interpenetration, shown in Figure 3.2 (b). In addition, the finial 3D virtual fabric geometry is shown in Figure 3.2 (c, d).

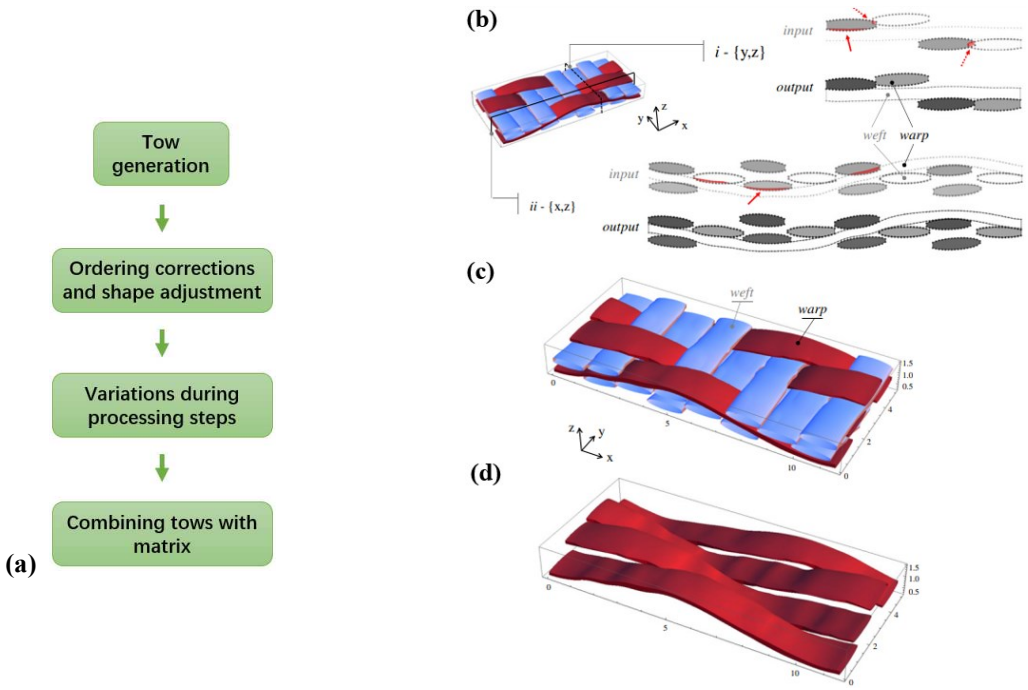

Figure 3.2 (a) Generation step of 3D virtual fabric. (b-d) Virtual specimen one unit cell in size, defined on a grid with Nx¼120 and Ny¼60: (b) Illustration of interpenetration removal on two different cross sections. (c) 3D rendering of the output corrected virtual specimen. (c) 3D rendering of the output warp tows only (Rinaldi et al., 2012)**.**

Finally, compare the cross-sectional area, aspect ratio, and y and z coordinates of the tow locus with experimental and simulation results. The resulting virtual model not only accurately reflects the arrangement and interweaving of yarns geometry, but it represents also and statistically the microstructural properties of actual materials.

Other authors have proposed to use XCT scans and image treatment to build a consistent and representative geometry and a finite element mesh for mechanical simulations (Fourrier et al.,

2023; Naouar, Vidal-Sallé, Schneider, Maire, & Boisse, 2014) for instance. However, since the mesoscale is considered, our micro modeling cannot be directly inspired by the latter.

3.2 Creation of virtual fiber bundle (tow) at the microscopic scale

The modeling of fiber bundles from the microscopic scale can provide information about fiber deformation, rearrangement, and the contact within fibers. In the references, fibers are mainly modeled in the following methods:

- Undeformable discrete element.
- Deformable finite element.

3.2.1 Creation model with discrete element method (DEM)

The Discrete Element Method (DEM) involves modeling collisions between discrete particles and with other surfaces in what is usually an explicit dynamics simulation. Each particle is modeled by a rigid sphere/polyhedron (in the case of particles) or cylinder (in the case of fibers) with degrees of freedom for movement and rotation. Their motion is governed by classical equilibrium equations and interactions are usually modeled by combinations between springs and dampers. Other contact energy potentials inspired by molecular dynamics can also be used.

Guo presents a uniaxial compression model of flexible fibers based on the discrete element method (DEM) (Guo et al., 2021). The flexible fiber model based on bonded sphero-cylinders is described in detail and the accuracy of the model is verified experimentally. The fiber consists of a connected plurality of identical spherical prisms, each of which consists of a cylinder and hemispheres at both ends. Based on the work of Kidokoro (Kidokoro, Arai, & Saeki, 2015), the contact forces were accurately calculated by means of different contact types between the spherical prisms (Figure 3.3), and a specific contact force model specified for each contact type. In particular, the simulation results are in good agreement with the experimental results when the Mindlin model and the geometry-dependent normal contact force model are used.

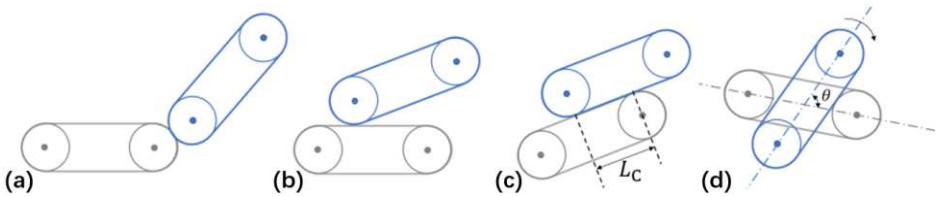

Figure 3.3 Contact model (a) Hemisphere-hemisphere contact, (b) hemisphere-cylinder contact, (c) parallel cylinder contact, and (d) skewed cylinder-cylinder contact (Guo et al., 2021)**.**

In addition, the simulation results showed that the fiber-fiber friction coefficient and the fiber-wall friction coefficient have a significant effect on the compression force (Figure 3.4). As the fiber-fiber friction coefficient μ_{ff} increases, the compression force initially increases and eventually saturates. The increase in fiber-wall friction coefficient μ_{fw} leads to a linear increase in compression force and wall shear force with respect to the normal force ratio.

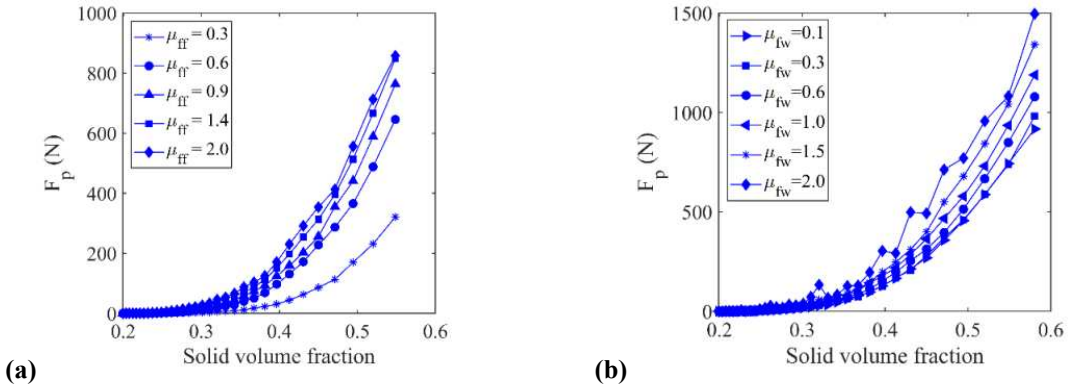

Figure 3.4 Effects of (a) fiber-fiber friction coefficient μ_{ff} and (b) fiber-wall friction coefficient μ_{fw}on the loading curves in the uniaxial compression tests(Guo et al., 2021)**.**

In uniaxial compression simulations of fibers, the effect of static friction is considered. In particular, static friction is more dominant than dynamic friction when the fiber-fiber friction coefficient increases, shown in Figure 3.5.

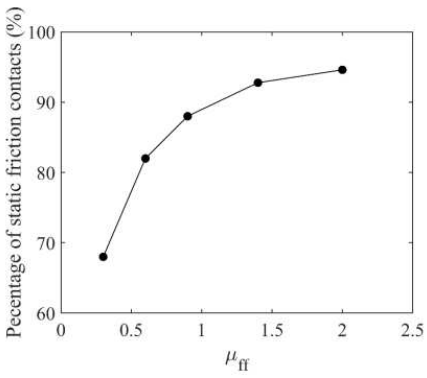

Figure 3.5 Percentages of static friction contacts with various fiber-fiber friction coefficients μ_{ff}. The fiber-wall friction coefficient μ_{fw} is set to 0.6(Guo et al., 2021)**.**

Guo's work not only considered the effect of the fiber-fiber friction coefficients and fiber-wall friction coefficient on the compressive behavior, but also the influence of static friction between fibers. However, in his model, he did not consider that both friction coefficients have a greater effect on the compressive behavior of the fibers. His work has provided new ideas for this study, and it may be necessary to consider the friction force between the medium fiber and the

compacted channel.

In order to analyze the slender shapes and flexibility of materials such as fabrics or fibers (strings), Park developed long and flexible geometric models of fiber models using discrete element (DE) computational methods. They can be further classified as rigid fiber (RF) models and fully flexible fiber (CFF) models (Park & Kang, 2009). RF models are suitable for simulating dynamic problems with rigid objects, while CFF models are useful in dealing with dynamics and vibration of flexible materials, especially when large deformations and nonlinear effects need to be considered. Shown in Figure 3.6 (a), the RF model shows a good agreement between the simulation results and the analytical solution. The error of the simulations increases with the initial rod angle, but the maximum error is about 2%. The simulation results of the CFF model are able to accurately predict the dynamic and vibrational properties of the vibrating string. Comparisons are made with numerical solutions of nonlinear string models (such as the Duffing equation based on the Kirchhoff equation). In Figure 3.6 (b), the calculated frequency error decreases gradually with the increase of the particles number in the model, and the error remains within 2% for different initial amplitude conditions.

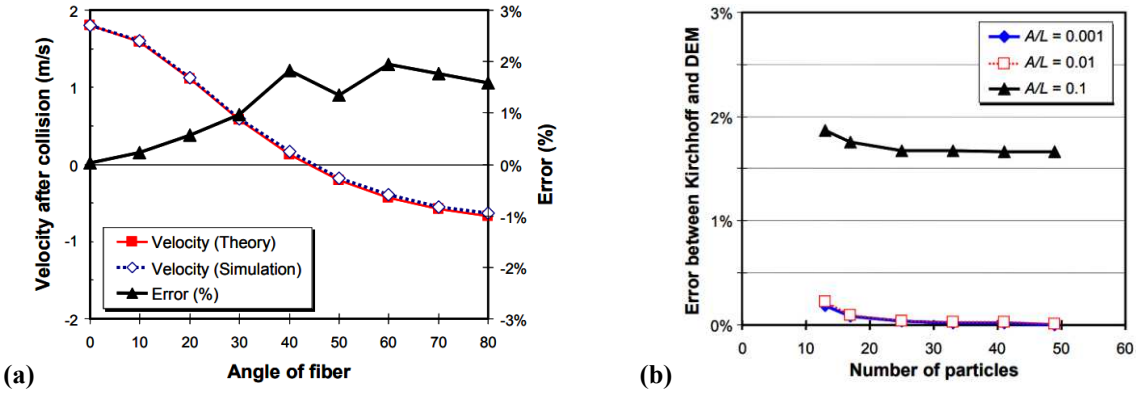

Figure 3.6 (a) Velocity and error of the rigid fiber after collision. (b) The errors of a vibrating string in frequency with respect to the number of particles when computed by the CFF model (A/L is a dimensionless proportional parameter used to express the ratio of vibration amplitude to string length.)(Park & Kang, 2009).

From Park's model, the number of particles in the model will influence the accuracy of simulation results. When the threshold of number of particles is reached, the error of the simulation result does not change. Therefore, the number of elements of the fiber will be discussed in this thesis to improve the accuracy of the model while maintaining the optimal calculation time.

Crassous presented an algorithm based on the DEM for modeling the behavior of elastic fibers in frictional contact (Crassous, 2023). The fibers are modeled as chains of cylindrical segments connected by springs, taking into account elongation, bending and torsion forces. The frictional contact between the fibers is simulated using the Cundall and Strack models commonly used in granular material simulations.

For the mechanical behavior of single fibers, Crassous performed contactless simulations with elastic rods and static bending-free simulations with Capstan. The mechanical response of single fibers is observed and analyzed by applying different forces and torques: the effect of bending and friction on the tension distribution. As shown in Figure 3.7 (a), the bending behavior of the elastic rod under different point forces as well as the torsion behavior are in good agreement with the theoretical predictions and the available experimental results. In Figure 3.7 (b), The validity of Capstan's equation in describing the tension distribution of a rope wrapped around a cylinder is demonstrated. Illustrating the role of friction in the fiber system, especially in the transmission and distribution of forces. Static elastic knot simulations with bending examine the behavior of elastic fibers forming knot structure in response to external forces (Figure 3.7 (c)), revealing the role of the friction in the formation of the structure and the maintenance of its stability. The behavior of a fiber bundles under torsion and tension is simulated. The results show a significant effect of the torsion angle and the friction coefficient on the strength of fiber interactions and overall structural stability.

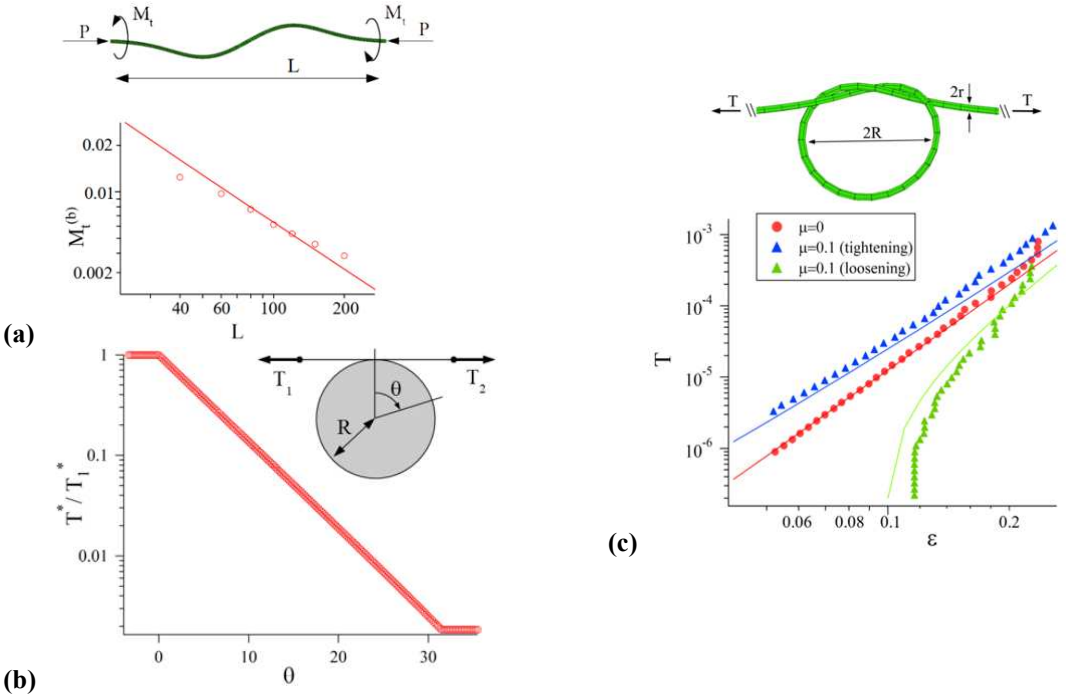

Figure 3.7 (a) Buckling of an elastic rod. Torque applied at ends at the torsional buckling threshold as a function of the rod length. (b) Tension in a rolled string around a cylinder: T^* is the tension in the string, and θ is the rolling angle. Circles are symbol, plain line is an exponential fit. (c) Tension as a function of $\varepsilon = \sqrt{r/R}$ for frictionless and frictional strings(Crassous, 2023)**.**

Furthermore, the effect of the friction coefficient of the fibers on the compressive force was not considered in Crassous' work. However, Crassous' simulation results show the importance of friction on the strength of fiber interactions and the stabilization of the fiber structure. Therefore, the friction inside the fiber bundle needs to be considered in the fiber bundle model.

Subramanian and Picu (Subramanian & Picu, 2011) used a numerical model to investigate the mechanical behavior of unbonded 3D random fiber networks under triaxial compression. The model shows the power law dependence of stress on volumetric strain and the hysteresis phenomenon during loading and unloading. After the first loading and unloading cycles, a stable hysteresis loop is formed.

Figure 3.8 (a) show the stress changes corresponding to bending, extension and fiber contact (obtained by partial derivatives of the bending, traction and contact energies with respect to the relative density, respectively) as a function of $\Delta = E_{ii}$ (Δ is the trace of the deformation tensor and therefore the volume change). The stress is inversely proportional to the relative density φ. In the early stages of compression, the strain energy is mainly associated to the bending of the fibers, while at higher densities it is mainly stored in the axial deformation mode.

However, for larger relative densities φ, when Δ is small, the fiber extension mode dominates the bending mode. The contact stress is an order of magnitude lower than the other two stresses. Figure 3.8 (b) shows an increase in slip distance (tangential relative motion $\delta_{||}$) and interpenetration between fibers (normal relative motion $\delta_{\perp}$) as the compaction process proceeds. $\delta_{||}$and $\delta_{\perp}$ seem to be limited by friction. Consideration of inter-fiber friction does not change the functional form or exponent of the stress-strain relationship. The mechanistic difference between this system and a bonded random network: the relative sliding of the fiber contact points and the consequent rearrangement of fibers in an unbonded system. By suppressing sliding, a stiffer response can result. These results indicate that the exponent of the stress-strain power law is determined by the fiber bending and the formation of new contacts. It is also affected by the relative sliding between fibers and axial deformation.

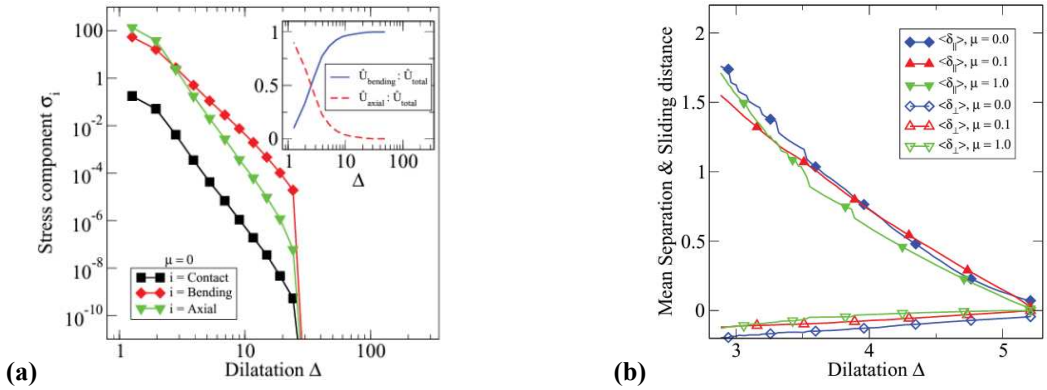

Figure 3.8 Compaction of a 3D fibrous assembly. (a) Evolution of fiber contact, bending and tensile stresses as a function of Δ. (b) Evolution of relative sliding and interpenetration distances between fibers for different friction coefficients μ(Subramanian & Picu, 2011).

Subramanian et al. shows that the strain energy is mainly related to the bending of fibers in the early stage of compression, while it is mainly stored in the axial deformation pattern at higher densities. This suggests that we need to consider multiple modes of fiber deformation and their dynamic transformation with density changes in the simulation process. In addition, the relative sliding between fibers and the rearrangement of contact points have significant effects on the mechanical response of the system. And it's efficient to understand the compaction behavior from energy perspective.

Truss element chains are structural systems consisting of multiple straight beams. Each truss element typically has two nodes and is assumed to have a cross-section that remains constant along its full length. Truss elements are subjected to axial tensile or compressive forces only. It

does not have the ability to simulate bending, shear, or torsion. In multiscale numerical models, chains of truss elements are used to construct virtual fibers that compose yarns and later form woven structures. Wang developed a microscale computational tool based on the explicit digital element method (Figure 3.9) for numerical simulation of ballistic impact and penetration of textile fabrics (Y. Wang et al., 2010). The authors have gone through experimental ballistic impact experiments for comparison and the simulations approximate the experimental results.

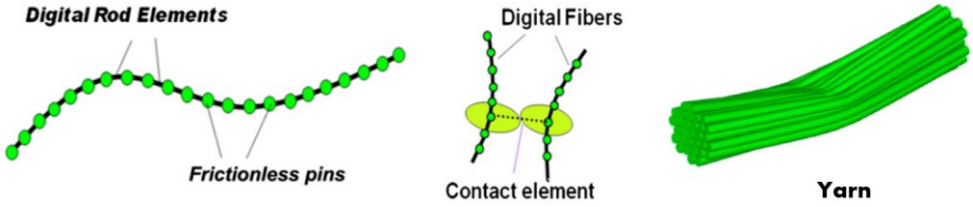

Figure 3.9 Concept of digital element (truss element) simulation(Y. Wang et al., 2010)**.**

Discrete element modeling emphasizes the effects of friction, contact, initial structure, and interactions between fibers on fiber network behavior. In addition, the behavior of fiber networks can be understood through energy studies, which can understand the interaction and deformation of fibers in the compaction simulation. Therefore, this study will also make use of this method. However, these models indicate that rigid elements require the use of linear and torsional springs to simulate the deformation of the fiber, and the interaction is modeled by a combination between the spring and the damper. The non-deformable discrete elements are mainly based on the dynamics of rigid bodies. In this thesis, the mechanical simulation of fiber bundle model should not only consider the dynamic behavior of fiber, but also mainly consider the deformation of fibers. As it has been discussed many techniques and improvements have been made on discrete elements to account and model the fiber deformation, however, this leads to a wide increase of the complexity and calculation time because it is not its initial purpose.
So, modeling through discrete elements seems not to be the most suitable method in order to achieve the purpose of this thesis. Therefore, exploring deformable finite element modeling becomes more necessary.

3.2.2 Creation model with finite element method (FEM)

In most finite element models of fibrous media, the fibers are slender. The fibers are modeled with beam element to optimize the computation time.

Xing developed a micromechanical model of aligned fiber bundles with high fiber volume fraction (Xing, Chen, & Li, 2010), to study the elastic deformation behavior under bulk compressive pressure and longitudinal stress. An improved representative fiber cell was present to get the deflection of a bending fiber under transverse and axial force. Numerical results show that the transverse compressive stress and its deformation are related to the wave amplitude and the available fiber volume fraction. The deformation behavior of well-aligned fiber bundles under compression and axial stresses was obtained using a similar approach to the Cai model. The greater transverse stiffness indicates that the model is able to align the fiber bundles well at high fiber content.

Abd El-Rahman and Tucker successfully created virtual fiber networks with actual fiber volume fractions for the RSA method (Ahmed I. Abd El-Rahman & Tucker, 2013). and performed compaction simulation with virtual fiber networks (A. I. Abd El-Rahman & Tucker, 2013). The model consists of 5000 fibers of length of 100 mm and the compression process of the fiber network is simulated using the finite element method. In Figure 3.10, the compaction volume fraction goes from 5% to 25% where each fiber is represented by a 3D beam element. Explicit time integration and general contact algorithm processing were performed through ABAQUS/Explicit. Mass scaling and contact amortization (contact damping) are used to control the computational time and model stabilizers, as well as oscillations in the results, respectively.

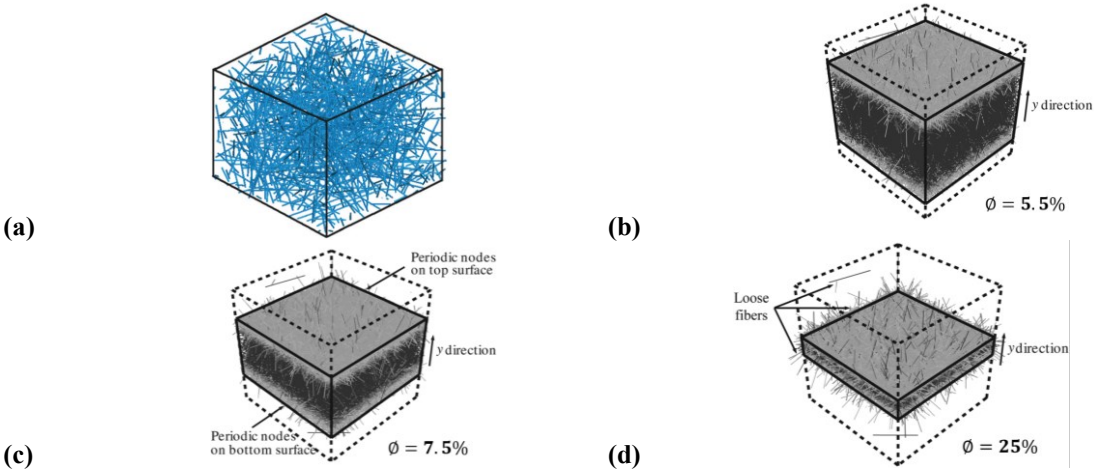

Figure 3.10 (a) A typical unit cell, containing 692 child fibers. (b-d) Three steps of compaction simulation with 5000 fibers(A. I. Abd El-Rahman & Tucker, 2013; Ahmed I. Abd El-Rahman & Tucker, 2013)**.**

The compaction curve is obtained for 3 friction coefficients: μ=0.3, 0.6 and 1.0, as shown in Figure 3.11. The one corresponding to μ=1 (to decrease slip) seems to be consistent with Van

Wyk's theory (since this theory neglects slip between fibers) for low volume fractions (φ < 15%). The evolution of the number of contacts is also investigated for μ=1, with results similar to Toll's theory. No validation against experimental tests was carried out.

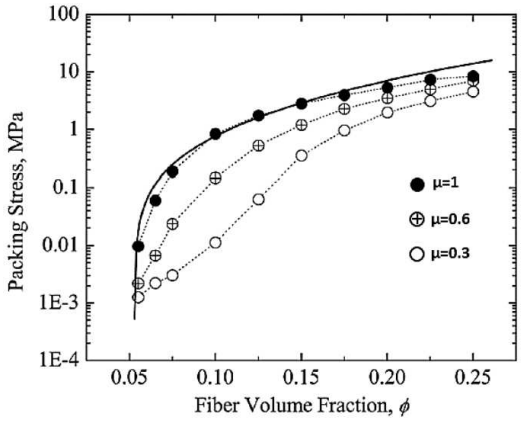

Figure 3.11 The influence of the friction coefficient on the comparative compaction behavior compared to Van Wyk model (A. I. Abd El-Rahman & Tucker, 2013)**.**

This model highlights the contribution of explicit kinetic calculations in the management of contact between fibers and control of computational time, as well as the usefulness of damping in stability simulations. But, this model considers the high entangled fiber network, and not consider the fibers with almost single direction.

Durville presented a simulation of compaction of entangled fiber bundles using the finite element method (Damien Durville, 2005). In his model, the fibers are modeled as beams. In fact, the cross-sectional kinematics of each fiber is described by three vectors: one for the translation of the cross-sectional center of mass, and two others to describe the planar and linear deformation of the cross-section. Normal contact between fibers is modeled by a penalty function law that relates normal forces to mutual penetration. Friction is modeled through Coulomb's law. The effect of fiber bending was investigated by compacting a fiber combination containing 50 fibers with a diameter of 0.015 mm, the geometries are shown in Figure 3.12. In Figure 3.13, the results show that for low compaction rates, the compaction curves are consistent with Van Wyk's theory. The correlation with this theory is better at increasing fiber tortuosity. For higher compression rates, the behavior is closer to that predicted by Baudequin (Baudequin, Ryschenkow, & Roux, 1999), who studied the compression of glass wool samples up to 95% compression.

Durville also studied the number of contacts and found that the variation follows a relationship proportional to the relative density $\varphi^{\frac{2}{3}}$: $Nc \propto \varphi^{\frac{2}{3}}$, shown in Figure 3.13(b).

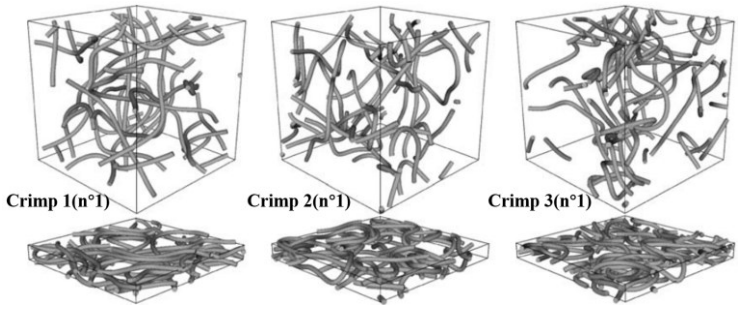

Figure 3.12 Initial and final configurations of the 3 samples for the three different crimps (Damien Durville, 2005)**.**

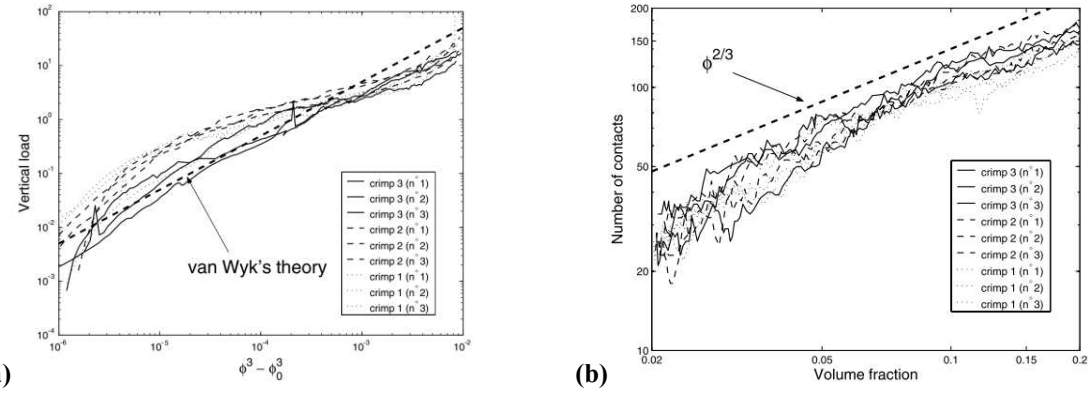

Figure 3.13 (a)Comparison of loading curves with van Wyk's theory. (b) Comparison between the evolutions of numbers of contacts versus volume fraction (Damien Durville, 2005)**.**

Durville proposed that the number of contacts is proportional to the volume fraction of the fiber network. With the increase of crimp, the number of contacts between fibers also increased, but its change was not obvious in the low volume fraction part. At the end of compaction, the number of contacts with different crimp is basically the same. This phenomenon is worthy of verification, and small diameter fibers are used in this model, so it is worth considering whether the same results can be obtained for the fibers used in this thesis.

Durville used a finite element method for simulating the mechanical behavior of woven textile materials at the fiber level (D. Durville, 2011; Damien Durville, 2008, 2010). The modeling process models the fibers as 3D beam elements and takes into account the contact-friction interactions between them, enabling the simulation of patches composed of hundreds of fibers.

The initial configuration of the woven structure is determined by simulating the weaving process, as shown in Figure 3.14.

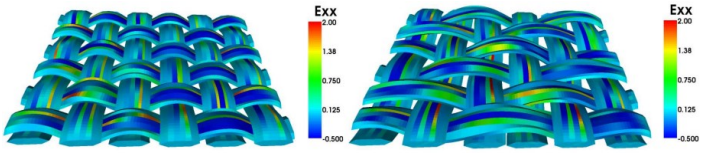

Figure 3.14 Horizontal strains in yarns generated by the simulation of the weaving process (Damien Durville, 2008).

The mechanical properties of two types of woven fabrics (plain and twill) were investigated by simulating different loading path (biaxial tension loading, shear loading). Thus, the complexity of the fabric behavior and stress distribution at the fiber level is revealed. The curve describing the axial force as a function of axial strain Figure 3.15 (a), exhibits non-linear behavior at the initial increments of the traction simulation. This is attributed to the rearrangement of the fibers and the reduction of their curvatures under the traction force. Regarding shear behavior, the curve of shear force as a function of shear angle in Figure 3.15 (b) is non-linear, similarly to the results of (Cao et al., 2008). The shear force increases until it reaches a value corresponding to the locking angle of the reinforcement.

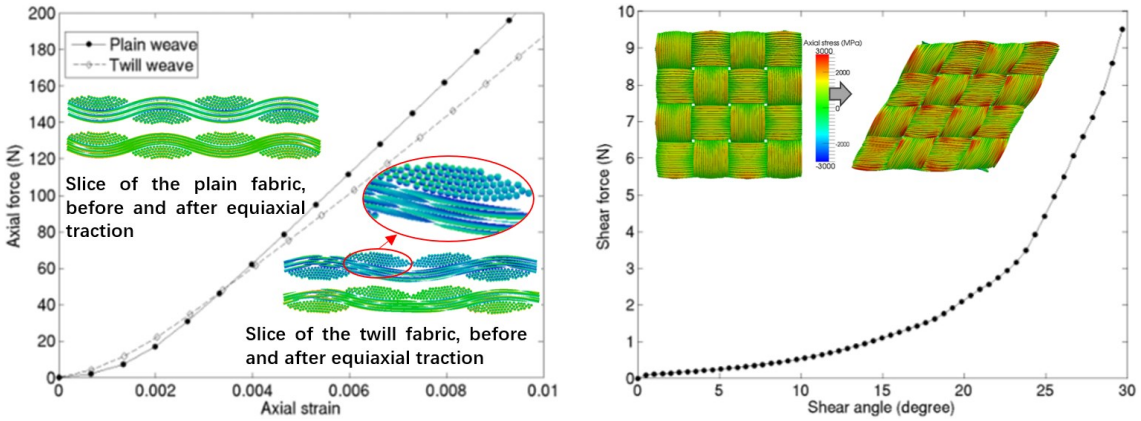

(a) **(b)**

Figure 3.15 (a) Simulation of the bi-axial traction of twill and plain weave fabric: axial force as a function of the axial deformation. (b) Simulation of shearing of plain weave: shear force as a function of shear angle(D. Durville, 2011)**.**

Subsequently, Moustaghfir describes a methodology used to generate a geometric model of a fiber bundle, then the mechanical simulations are performed (Moustaghfir, El-Ghezal Jeguirim,

Durville, Fontaine, & Wagner-Kocher, 2013). The geometrical model of the roving was created based on the Durville's model, the 3D geometry of different twist roving shown in Figure 3.16.

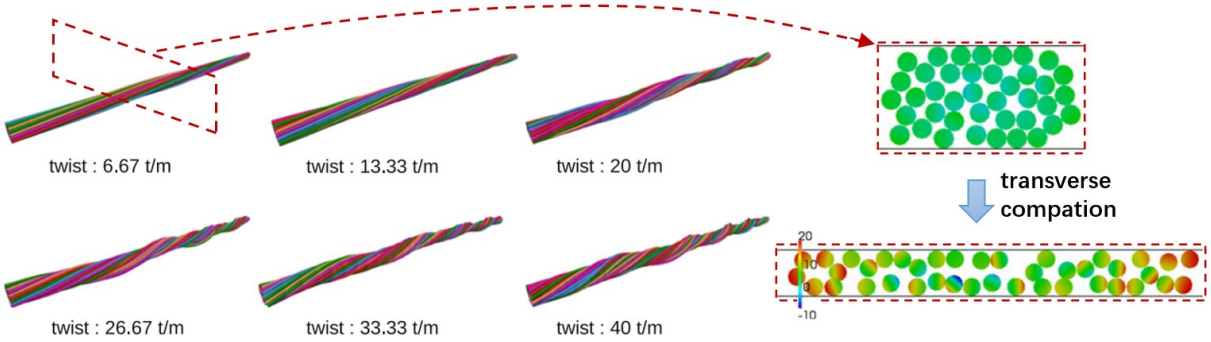

Figure 3.16 Roving geometries with different twist and transverse compression simulation(Moustaghfir et al., 2013)**.**

Then, the roving model was simulated with transverse compaction using FEA method. In this simulation, the compaction plates consider as rigid part. By comparing the experimental data with the simulation results, the study verified the accuracy and reliability of the model (Figure 3.17).

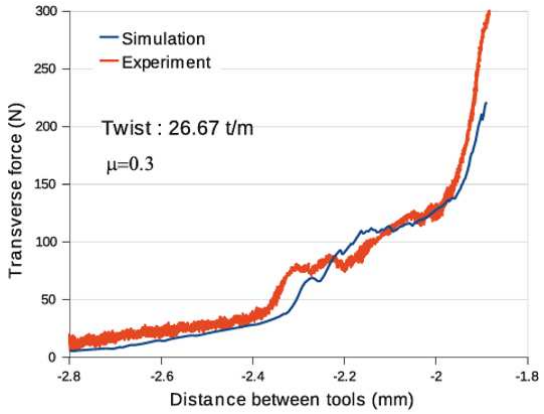

Figure 3.17 Validate the simulation with experiment (Moustaghfir et al., 2013)**.**

As shown in Figure 3.18 (a), the transverse compression stiffness of roving increases when its twist increase. This is since twisted roving makes it more difficult for the fibers to slide and rearrange each other. In addition, the change in the coefficient of friction has the same effect on the model as shown in Figure 3.18 (b), where the increase in the coefficient of friction also restricts the sliding between the fibers. The numerical results are compared with the tests carried out by Jeguirim (El-Ghezal Jeguirim, Fontaine, Wagner-Kocher, Moustaghfir, & Durville, 2012).

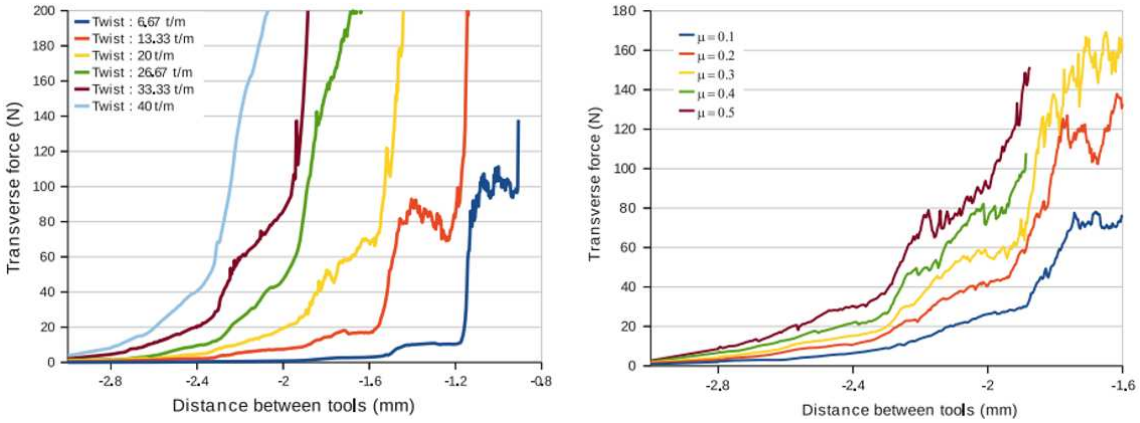

(a) **(b)**

Figure 3.18 The compression force in function of distance between two compaction plates. (a) with different roving geometry. (b) with different friction coefficient (Moustaghfir et al., 2013)**.**

Moustaghfir et al 's analyzed the compaction behavior of yarns with different twist, but they did not consider the volume fraction of fibers in relation to different yarns. In addition, the compaction experiment was unconstrained compaction.

Q. Hoan Phama focused on the transverse behavior of a Kevlar® KM2 yarn at a microscopic and homogenized scale (Pham et al., 2020). A yarn consisting of hundreds of fibers was modeled microscopically under the assumption of 2D plane strain. As shown in the Figure 3.19 (a), the fibers are closely aligned inside the fiber bundle.

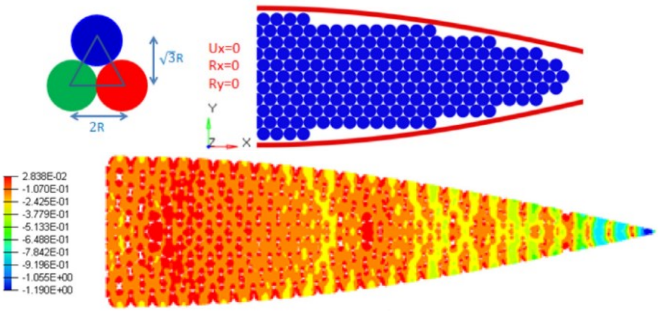

(a)

(b)

Figure 3.19 (a) Geometry of the numerical model. (b) True strain in YY direction at displacements 34.5 μm(Pham et al., 2020).

Then, based on the microscopic behavior, the numerical homogenization technique was used to obtain the effective homogenization behavior law of the yarn. The homogenization behavior laws were implemented in ABAQUS®/Standard through user subroutines. The transverse compressive behavior was performed with homogenized yarns and microscopic yarns. The true strain in YY direction with displacement 34.5 μm of microscopic yarn shown in Figure 3.19 (b). And the compaction behavior of these two models shown in Figure 3.20.

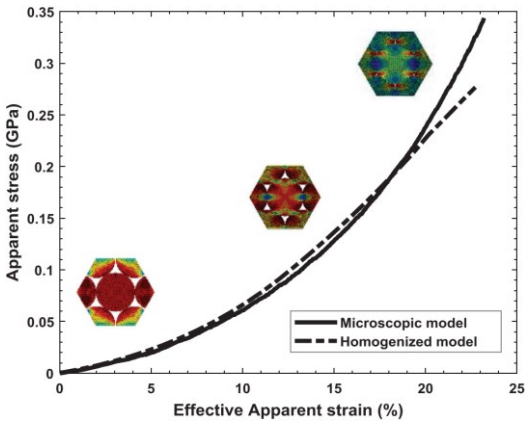

Figure 3.20 The comparison between microscopic and homogenized model (Pham et al., 2020)**.**

The study neatly and closely aligned fibers were subjected to compaction simulations. The reliability of creating fiber bundles and performing compaction was verified by comparing with homogenized model. However, this arrangement of fibers is idealized, for which a model of freely arranged fiber bundles was created in this thesis.

Li presented the process of creating a virtual 3D fiber bundle structure in ANSYS® (Li et al., 2011). This strategy (i) generates random fiber cross sections in 2D planes and ensure that the circle do not undergo initial penetration; (ii) Generate fiber cross sections in 2D planes spaced at z in the direction of fiber length, represented as fiber center coordinate (x, y). And so on to generate n 2D planes; (iii) The centerlines of each fiber are connected, and (iv) its rendered 3D structure. Thus, morphology of fiber bundle on micro scale is reproduced, and fiber bundle model is truly and visually obtained.

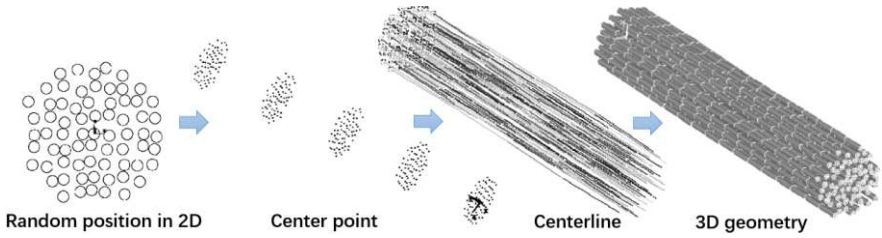

Figure 3.21 Creation step of 3D fiber bundle structure (L. Li et al., 2011)**.**

Li creates fibers in a manner consistent with the theory of tomographic reconstruction of fibers: creating a geometric model of the fiber's centerline. This provides an idea for the creation of a fiber bundle model with a free arrangement of fibers in this thesis.

3.2.3 Combine the DEM and FEM method

Daelemans combine the advantage of DEM and FEM method, created a hybrid virtual fabric model and simulated its compaction behavior (Daelemans et al., 2021). It combines truss elements to determine properties in the direction of the fibers, and beam elements for fiber bending, shown in Figure 3.22 (b). The base structure of the fiber fabric was created using Dynamic Fabric Mechanical Analyzer (DFMA, www.fabricmechanics.com). DFMA was created by WANG (Y. Wang et al., 2010; Y. Wang & Sun, 2001; Zhou, Sun, & Wang, 2004) of the Fabric Mechanics group at Kansas State University. The samples were also scanned by micro-CT to compare the created virtual fabric with the microstructure of the samples, shown in Figure 3.22 (a).

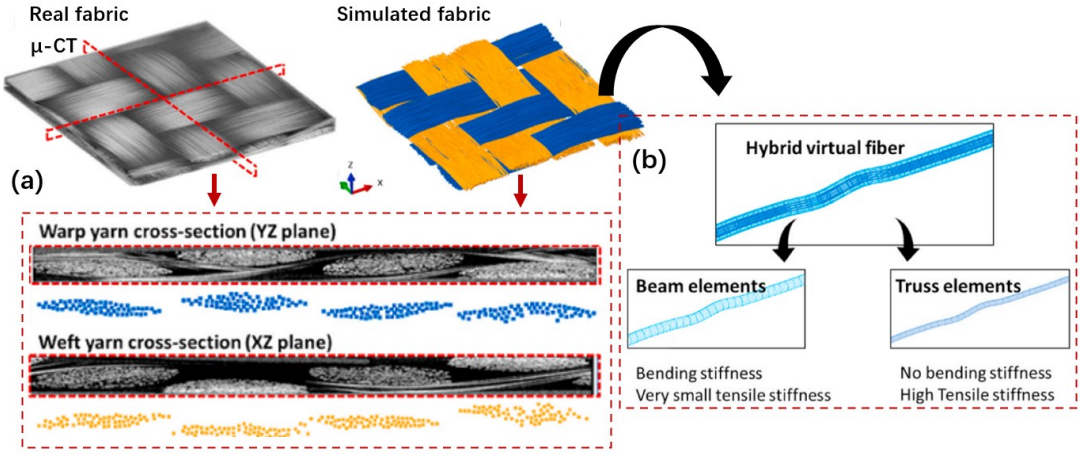

Figure 3.22 (a) Comparison of real fabric from Micro-CT experiments (left) and simulated fabric (micro-)geometry (right) shows good visual agreement between both. (b) The fabric is constructed of hybrid virtual fibers that consist of a chain of beam elements for bending stiffness and truss element for tensile stiffness (Daelemans et al., 2021)**.**

In the simulation analysis of vertical compaction of fibrous fabrics, several important parameters are discussed, including fiber size (L/D ratio), coefficient of friction (μ), and bending stiffness of fibers (EI). The relationship between the compaction displacement and the pressure is shown in Figure 3.23. Lower L/D ratios ($L/D = 1$ and 0.5) showed higher bending strain energy in the simulations, which resulted in more buckling of the virtual fibers during compaction. This explains why these simulations show a more rigid compaction response. A higher range of friction coefficients ($\mu = 0.3 - 0.4$) was considered more appropriate during compression through the longitudinal direction, considering that almost no in-plane tensile forces are involved. Increasing the bending stiffness had a significant effect on the compression

response of the simulated fabrics. For the baseline bending stiffness, the simulated fabric thickness was slightly underestimated for some pressures. However, the simulated compression curves were similar to the experimental ones. The agreement between simulation and experiments improves as the bending stiffness is increased until two to five times the baseline. Higher bending stiffnesses ($10(EI)$ to $100(EI)$) resulted in an overestimation of the compression response at low compression levels, suggesting that values in this range were too high.

The macroscopic compression response of the fabric was well predicted by correctly setting the simulation parameters. Moreover, the microscopic deformation mechanisms (performed by Micro-CT scans), as well as the hysteresis losses resulting from fiber rearrangement and friction were also well predicted and explained. The setting of bending stiffness can also accurately predict the mechanical response of the fiber fabric during longitudinal compaction.

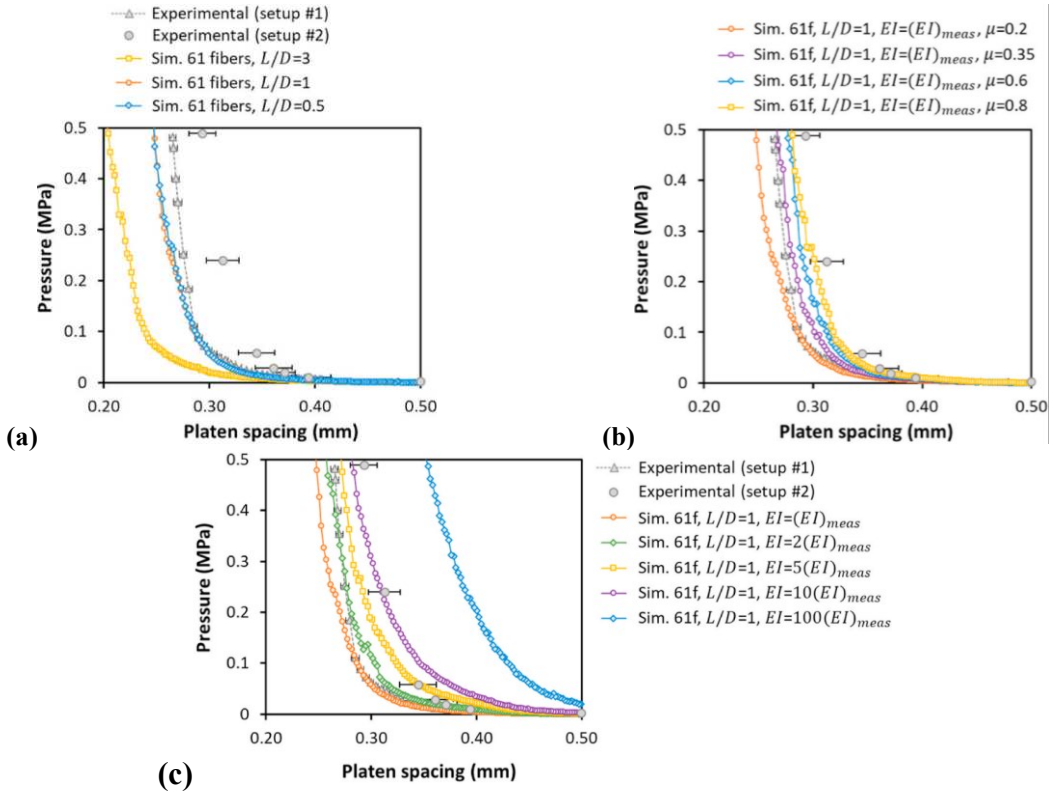

Figure 3.23 The effect of the (a) L/D, (b) frictional and (c) bending stiffness constant on the compressive response. (a) shows compressive response converges for $L/D \leq 1$. (b) shows that higher frictional constants result in better agreement with the experimentally determined response. (c) shows better agreement between the simulated and experimental responses is obtained for a bending stiffness in the range of 25 (EI)measured (from Peirce's cantilever method) (Daelemans et al., 2021)**.**

The general contact algorithm of ABAQUS/explicit was used in its simulation. The general

contact algorithm is a kinematic forcing algorithm that allows the contacting surfaces to "penetrate" into each other at each time step in proportion to k (where k is the penalized stiffness). While this design provides some flexibility in dealing with the contact problem, it also makes surface penetration more pronounced under high compression conditions, shown in Figure 3.24.

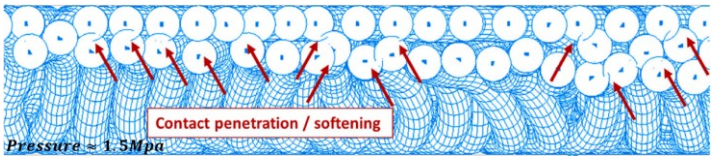

Figure 3.24 Contact overclosures/penetrations (softening) between neighboring fibers occur in large amounts at pressures 1.5 Mpa (Daelemans et al., 2021)**.**

Daelemans' study of the slenderness and friction coefficient of fiber bundles was intentional, but it did not correlate the volume fraction of fibers into the results. In their study, it was shown that penetration occurs between fibers in a high-pressure state, this phenomenon that was also confirmed in this thesis.

3.3 Conclusion

As discussed in section 1, fiber-reinforced materials are multi-scale media, and fiber is the smallest homogeneous constituent units. So, micro-scale (fiber level) is the most accurate level to study fiber materials within a continuum mechanics approach. In order to accurately study the mechanical properties of fiber bundles, in section 2, it was considered to use the compaction path as the loading path to study its mechanical properties. Furthermore, tomography technology combined with micro-compactor appears as an effective way to extract the three-dimensional morphology of fiber bundles at different compaction stages. Finally, the existing research on modeling of fiber media at mesoscopic and microscopic scales is discussed. These researches complement those previously cited in terms of experimental testing (section 1). It also provides a basis for the construction of the fiber bundle mechanics simulation model in this thesis. The microstructural parameters can be changed to study their effect on compaction, twist (Moustaghfir et al., 2013), friction coefficient (Guo et al., 2021), etc.

However, these studies did not consider the compaction simulation method by extracting real fiber bundles, which is an effective method to verify the accuracy of the model (simulation parameters). Latil (Latil et al., 2011) extracted the fiber bundle model through XCT technology and performed a compaction simulation on it, and the simulation was similar to the experiment.

But, the relationship between the internal structural parameters of the fiber bundle and the compaction behavior was not considered in his study.
Durville et al (Damien Durville, 2005; L. Li et al., 2011; Pham et al., 2020) performed mechanical simulations by creating fiber bundles. The simulations in these studies were consistent with experimental or theoretical results.
These works are inspiring for our own approach, however, none of them have been used as virtual estimators in order to investigate the mechanical behavior of the roving as a function of their constitution. This challenge imposes an accurate experimental validation to ensure a high consistency of the model, coupled to a numerical efficiency for the numerous calculations required to quantify the impact of all the parameters.

This section provides ideas for create fiber bundles and the simulation parameters.
From a fiber modeling perspective, rigid discrete elements and deformable finite elements are potentially available. In addition, it has been repeatedly demonstrated that fiber bending is a major factor in compaction modeling, especially in the case of initially bent fibers. Therefore, beam elements seem to be a suitable choice for the modeling of such deformations (bending), especially in the case of large numbers of contacts. In particular, researchers like Durville, Tucker and O. Haji, have been able to demonstrate their potential. For compaction plates (compaction channels), rigid body part simulations are used. From a numerical point of view, the ABAQUS/explicit is used. But for quasi-static simulations (see the effect of loading speed, section 2.2), the computational parameters contact damping and mass scaling (artificial variations of the finite element density) have to be added to optimize computational time and reduce oscillations. For fiber-fiber interactions, the contact forces consist of normal forces and friction-induced tangential forces, so general contact is used. Researchers have emphasized the importance of the friction coefficient in fiber-scale modeling. Gassara has recently carried out an experimental study of friction between the polyester fibers that will be used in this study (Gassara, 2016; Gassara et al., 2018), and the results obtained make it is possible to provide a sufficient coefficient of friction $\mu = 0.2$ to be used in this thesis.

As mentioned before, the purpose of this paper is to improve an existing virtual fiber bundle estimators and develop fiber bundle microstructure parameter analysis tools. All the above model parameters have been verified by Dr. Haji (Haji Oussama, 2018) and the numerical model of the fiber bundle constructed in this thesis is based on the model he has previously

developed. It is enhanced from the following perspectives:(i) Several experiments combining XCT and compaction are conducted to verify the accuracy of the model. (ii) Experiments were performed using higher XCT resolution and the post-processing details of the XCT images were enhanced. (iii) Creation of a fiber bundle microstructure analysis tool to discuss the relationship between compaction and microstructural parameters (discussed in Chapter II).

In Chapter III, the creation of a virtual numerical quasi parallel fibers bundle generator is discussed. It then permits to obtain the first targeted results about the influence of the structural parameters (undulation, angles, friction, etc.) but also of the loading (compaction path, speed,) on the compression behavior.

Chapter II Development of micro-structure analysis tool for numerical fiber bundle

Chapter II contains sections 4 to 6 presenting the results of the microtomography experiments, the reconstruction of the fiber bundles, and a proposed method for the microstructural analysis of the fiber bundles.

Section 4 shows the process of a fiber bundle micro-compaction experiments, and the results of the analysis.

Section 5 describes the virtual numerical estimator which consists of two parts: the reconstruction of a numerical fiber bundle geometry, and the simulation strategy.

Section 6 introduces the creation of the analysis tools for fiber microstructure: from fiber position to indicators such as contact between fibers, crimp and orientation.

Section 4 Micro-compaction experiment with tomography: process and results

This section describes the micro-compaction experiment on fiber bundles. The experiment is combined with tomography for in situ imaging of fiber bundles. The experiment provides data for the virtual numerical estimator in section 5 and the microstructure analysis tool in section 6.

4.1 Preparation of samples

Two fiber bundle samples consisting of 40 dry polyester fibers, without matrix or sizing, were manually prepared, where a single fiber length is approximately 14-14.5 mm. The sample contained only 40 fibers since considering that (i) the numerical virtual estimator is still in the validated stage, a large number of numerical simulations are required, with a reasonable number of fibers to control the simulation time; (ii) the fiber samples are prepared manually, so it is difficult to prepare a large number of fiber samples.

During the preparation of a fiber bundle, the cutting of fibers might affect the compaction behavior. The cross sections of a single fiber prepared by two different cutting methods illustrates this issue: the first one by using scissors whereas the second depend on a needle to cut the fibers. The sections obtained by these two methods are shown in Figure 4.1(a-b). Figure 4.1(c, d) shows the initial microstructures of the fiber bundle ends of two samples 1 and 2, obtained by the two cutting methods.

The presence of irregular “burrs” in the cross-section of the fibers ends in sample1 is due to a plastic deformation of the section when the fiber is cut by scissors.

Burrs may affect the relative motion of the fibers during the compaction and change their kinematics. Thereby altering the kinematics of the fiber bundle, even though this study focused on the overall motion of the fiber bundle under compaction. And the “burrs” affect is boundary effect. And these burrs are irregularly shaped, it’s difficult to import to model. So, this boundary effect will not be incorporated into the numerical simulations of this study.

Indeed, the purpose of this chapter is to investigate the kinematics of a multi-fibers assembly, rather than the effect of the boundary conditions on its motion. In addition, the complexity in the modeling induced if accounting of this phenomenon is huge since it doesn’t enable to assume the cross-section of the fiber to be circular and regular. Consequently, each fiber was

individually cut, and the cross-section was then checked under a microscope to ensure that the profile was flat and smooth.

Before the start of the compaction experiment, an initial scan of the prepared sample is required in order to reconstruct and import it into ABAQUS®/CAE as a geometric model of the fiber bundle. The initial scan of the fiber bundle is used to check whether the sample position is initially correct before starting the compaction experiments.

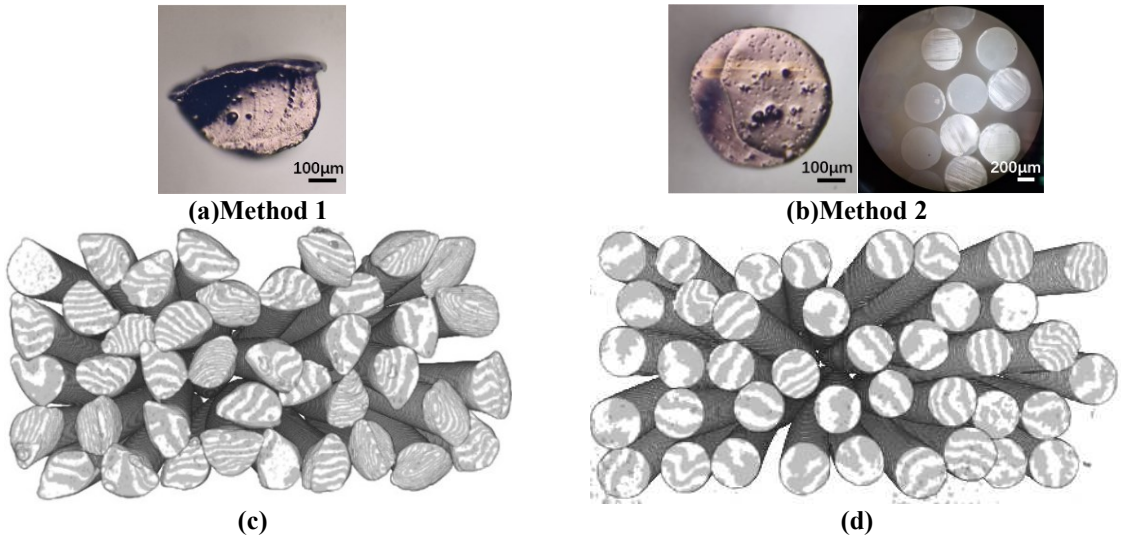

Figure 4.1 Cross-section microscope images of single fibers for different methods of cutting fibers: (a) cutting method 1, (b) cutting method 2, tomography images of cross-sections at the end of fiber bundles: (c) sample obtained with cutting method 1, (d) sample obtained with cutting method 2.

The sample is placed in a transparent support of PMMA (Poly methyl methacrylate) as shown in Figure 4.2 (a). This material has a low absorption of X-rays and is therefore used in the tomography experiments to obtain high-quality images (Figure 4.2 (b)), while samples put inside a PVC support and tomography scanned can present a lower image quality (Figure 4.2 (c)). Here, the confined compaction support was used, because there is no adhesive between the fibers (dry fibers) in an unconfined support, the fibers will appear to lay flat (Figure 4.2(a)-right). In this case, compaction of fiber bundles will not be characterized by strong rearrangement between fibers, but mainly by compaction of the fiber cross-section (deformation of the fiber cross-section). So, the free lateral conditions were not considered, which typically observed during the forming stage of textile reinforcement in RTM process.

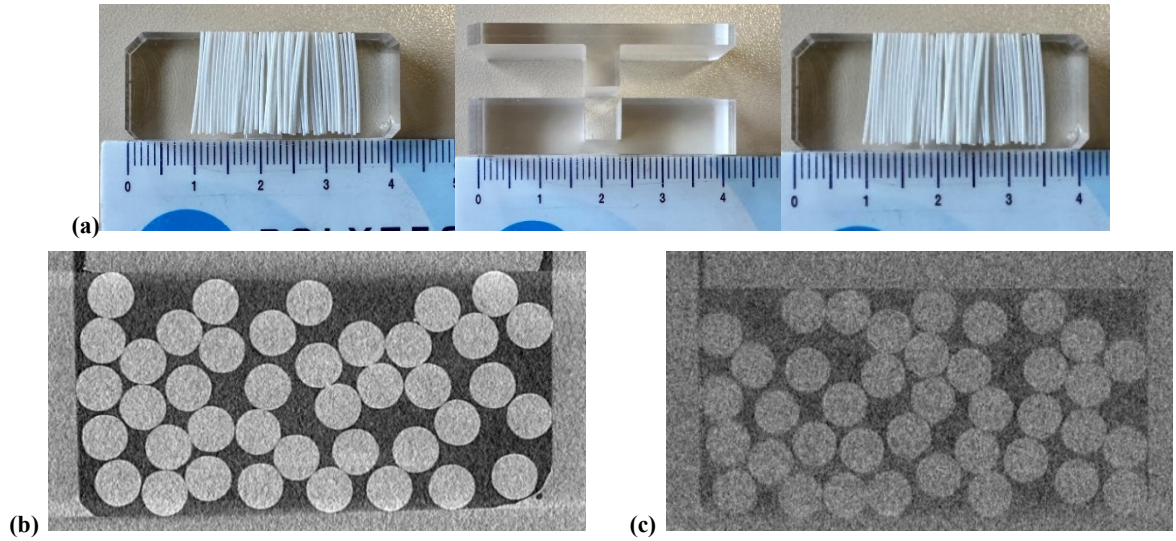

Figure 4.2 The sample cassette of compaction.

For sample 1, the fibers have a length of 14 mm, and the size of the initial compaction space was 5*4*14 mm. It's difficulty to place the fibers at the center of the compaction channel with same length, that's means the end of the bundle was not scanned completely, and about 0.2 mm was lost due to the fact that when the fibers were placed, these errors, and "burrs" effect will influence the accurate of generate numerical fiber bundle geometry. Therefore, for the sample 2, the method of cutting and chosen a good length of the fibers was changed to avoid these problems. In addition, the length of the compaction channel was increased to 15 mm to ensure that the fiber bundle stay completely inside the compaction tools. By this way, fibers are completely scanned, the reconstructed geometry of the fiber bundle is complete, and both end of fibers section was flat (Figure 4.8).

4.2 X-ray tomography and micro compaction machine

a) X-ray tomography

This study used an X-ray tomography system (model EasyTom Nano 160, Figure 4.3 (a)) to scan the samples. The tomography machine produces X-rays with a conical geometry, as shown in Figure 4.3 (b). The conical X-rays across the samples while they rotate from 0° to 360°. The slices (sections) of the fiber bundle cross-section were obtained by three-dimensional reconstruction of the tomography data processing by using the software "Xact''.

The position of the sample relative to the X-ray source plays an important role in the quality of the scan. The spatial resolution (voxel size) can be controlled by adjusting the distance between

the tested object and the X-ray source (SOD), the distance between the X-ray source and the screen is SDD. The voxel size range of the EasyTom Nano 160 tomograph is $\frac{P1}{P2} = \frac{SOD}{SDD}$, where P_1 is the voxel size at the SOD distance, and P_2 is the pixel size of the screen. For the post-treatment of tomography images, the fiber cross-section is treated as a circle, and the numerical model of the fiber bundle is obtained by extracting the center points of the fiber cross-section. Therefore, the spatial resolution (voxel size) of the tomography image is important for the accurate extraction of the center point of the ‘‘circle’’, but also for an accurate evaluation of the circle radius. The higher the spatial resolution, the more pixel points that make up a single fiber cross-section, and the more accurate the extraction of the center point of the "circle". However, the space occupied by the micro-compaction machine must be considered, and when scanning the sample, the total sample must be scanned. In our experiments, the length of this sample is 16 mm. This length does not allow the SOD to be too small. Therefore, the minimum voxel size that we obtained was 9 µm.

The parameters of the X-ray scanning system for experiments were: the tube power of 12 W for the X-ray generator, the tube voltage of 60 KV (max: 160 KV), and tube intensity of 200 µA.

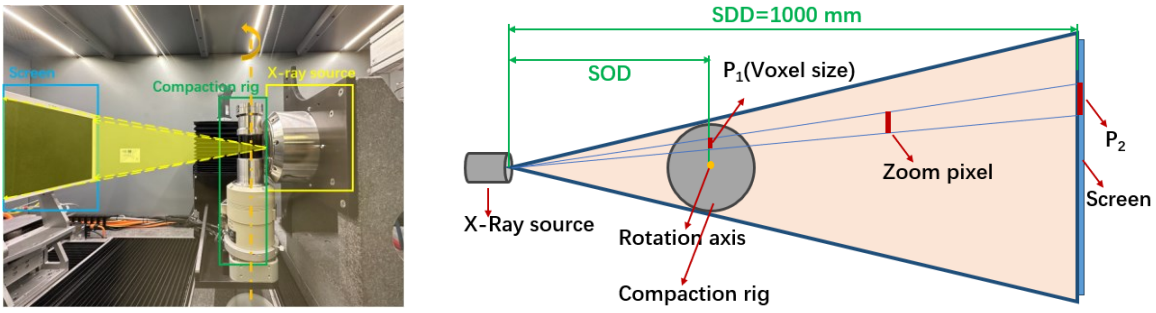

(a) **(b)**

Figure 4.3 (a)X-ray tomography system, (b) Schematic diagram of the effect of sample location on spatial resolution (voxel size).

b) Micro automatic compaction machine

The micro-compaction machine (Deben, Figure 4.4) is equipped with two compaction plates, upper and lower. The upper compaction plate is always fixe, while the lower one is movable and connected to a piezoelectric linear motor installed at the bottom of the compaction machine. The maximum distance between the two compaction plates is 15 mm. The sample is compressed vertically in the "scan channel". The sensor is located in the upper part of the machine Deben, and there are two force sensors: 500 N and 5000 N. During this experiment, the sensor of 500N was used and has the following characteristics:

- The precision class of the sensor is the class 1.
- When the measured force is less than 2 N, the precision is not ensured (not guaranteed).
- Between 2 N and 500 N, the accuracy is 1% of the measured value.
- To avoid the influence of inertial effects on the fiber rearrangement, it was crucial to maintain quasi-static compression. The speed of compaction was fixed to $V_{compaction}$ =1 mm/min.
- The sampling time of the compaction experiment data was 100 ms.

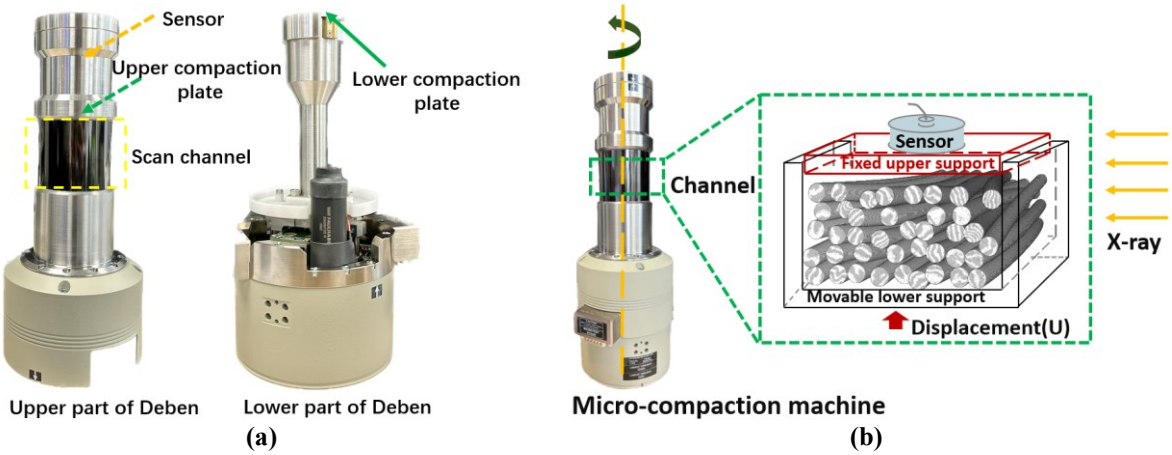

Figure 4.4 Compaction machine (Deben).

Due to the low accuracy of the sensor during the initial compaction part (compaction force < 2 N), the compaction experiments will be controlled by displacement. The upper and lower compaction jaws of the sample are fixed at the upper and lower compaction plates of the Deben, respectively. The lower jaw (lower part of the sample support) is fixed in the center of the lower compaction plate, and then the upper sample jaw is coated by an adhesive material to be connected to the upper plate of the machine. During the compaction of the fibers bundle, the compaction is obtained due to the displacement of the lower plate of the machine.

4.3 The compaction process and results

As mentioned above, before starting the compaction experiment, the initial state of the fiber bundle is scanned to obtain the initial geometry that should be compacted later. It should be noted that the first step is to make sure that the sample contact with the upper compression plate of the Deben, “the contact” has just occurred and there is almost no compression force.

In this compression test, the initial contact occurs when the Deben motor pushed the lower plate until the first fiber of the bundle get in contact with the upper plate. However, this phenomenon is not so easy to define in situ. Therefore, for a such compaction experiments, there are two

methods to define a repeatable initial “contact” state for all the samples:

1) Define the contact point by the compressive generated force. However, due to the low compaction stiffness of the fibers bundle and the non-guaranteed accuracy sensor for a measurement less than 2 N as well as the sensor resolution (0.01 N), it is almost impossible to distinguish between the compressive force at the initial contact and the measurement noise of the sensor. This method is almost suitable for media with high stiffness only.

2) Check contact by using the tomography live observations, as shown in Figure 4.5. When the lower plate moves upwards, and the highest point of the fiber bundle comes in contact with the upper plate, the lower plate displacement is fixed, and the compaction could be started. There is a time delay between observing the 3D morphology of the fiber bundles through the tomography window and the movement of the lower plate, which needs this plate to be stopped after each upward micro movement to observe the contact between the fibers and the upper channel of the compaction. Even if it is time consuming, this technique is useable to define accurately enough the initial state.

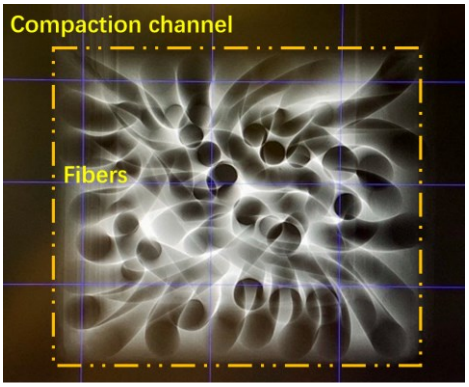

Figure 4.5 The 3D morphology of the fiber bundles through the tomography window.

After setting the fibers bundle with using the method 2, the initial contact force is almost 0N. This position is considered as the initial position that will be compared with the position of the maximum compaction force at the end of compaction experiments.

For the sample 2, after scanning of the fiber bundle initial geometry, the lower plate displacement is started to compact the fiber bundle. after each step of displacement, the new arrangement of the bundle geometry is scanned (Figure 4.6). As mentioned before, in order to verify the consistency of the microstructure of the fibers between the numerical model and the compaction experiments, it is necessary to reconstruct the fiber bundles under different compaction steps by X-ray scanning. In the experiment presented hereafter, there is 15 tomography scans steps, including the initial geometry (step 0).

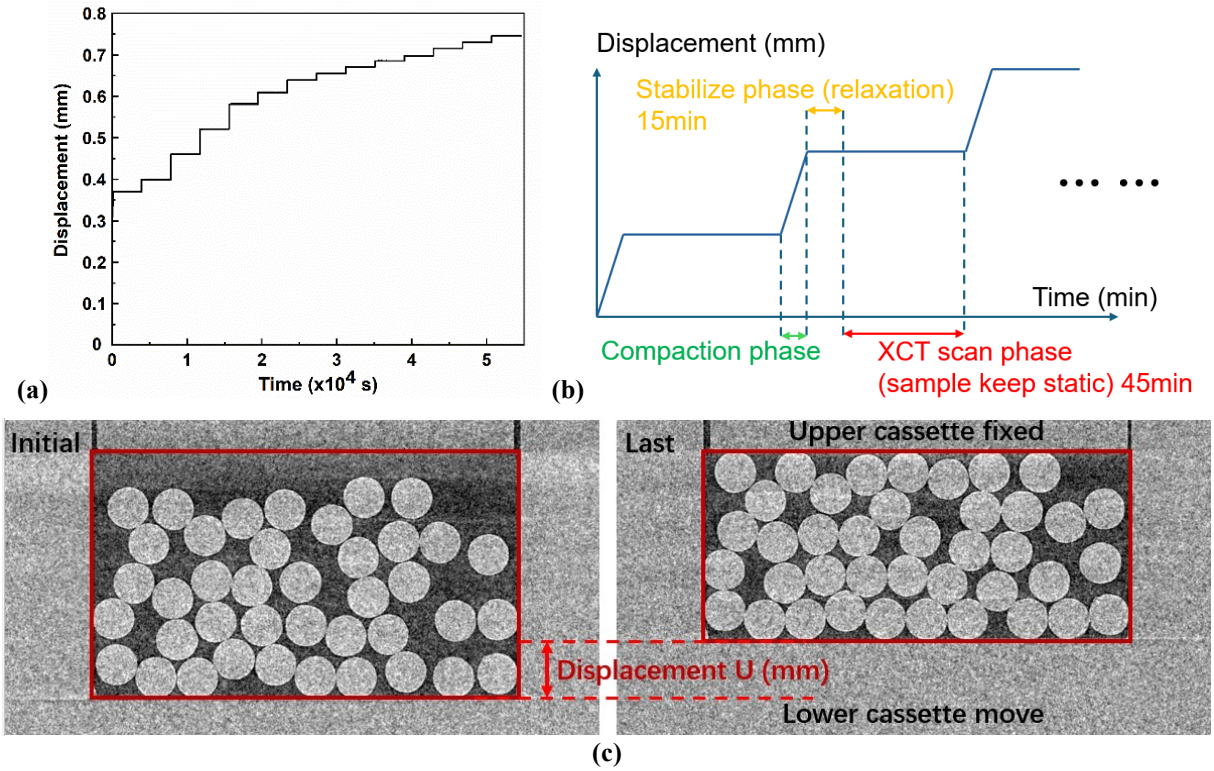

Figure 4.6 Compact path imposed by displacement.

The Figure 4.7 (a) illustrates the relationship between the compaction forces and the compaction time, where the relaxation effect is manifested, the compaction force decreases after each compaction, due to the fact that the fibers move slightly away from each other and re-achieve a static equilibrium after each compaction step stops, leading to fiber's rearrangement. Thus, changes in the fibers microstructure result in the relaxation of the compaction force (Figure 4.7 (a)).

The relaxation effect is proportional to the compaction force, and defined by:

$$R_{step_j} = \frac{F_{max_j} - F_{relax_j}}{F_{relax_j}} \times 100\% \quad (4.1)$$

Where F_{max_j} and F_{relax_j} is the maximum force and the force after relaxation of compaction step j, respectively.

But in this experiment (e.g., Figure 4.7 (b)), after the 13th compaction, the $R_{step_{13}}$ is 34.2%, which is significantly higher than $R_{step_{12}}$(12.43 %). This is due to the large slip between the fibers, where the fibers move to fill the voids during the relaxation step. From Figure 4.7 (c), the fibers move significantly after compaction step 12. Before step 5, the relaxation effect varied irregularly and insignificantly. Since the accuracy of the mechanical sensors of the previously mentioned micro-compaction machines cannot be estimated when the force is less than 2 N, so

its relaxation effect is ignored until the step 5.

After each compaction step, the tomography scan lasts 60min (Figure 4.6 (b)), including 15 minutes where the topography machine calibrates the color before the start of the scanning. During this presetting time, the sample keep immobile. However, this presetting time is useful for our experiments since it makes sure that the tomography images are not affected by the relaxation of the fiber bundle, that takes place after each compaction. So, consider the presetting time as relaxation time $t_{relax} = 15\,min$; the sample is X-ray scanned for 45 min, to obtain sample's tomography data.

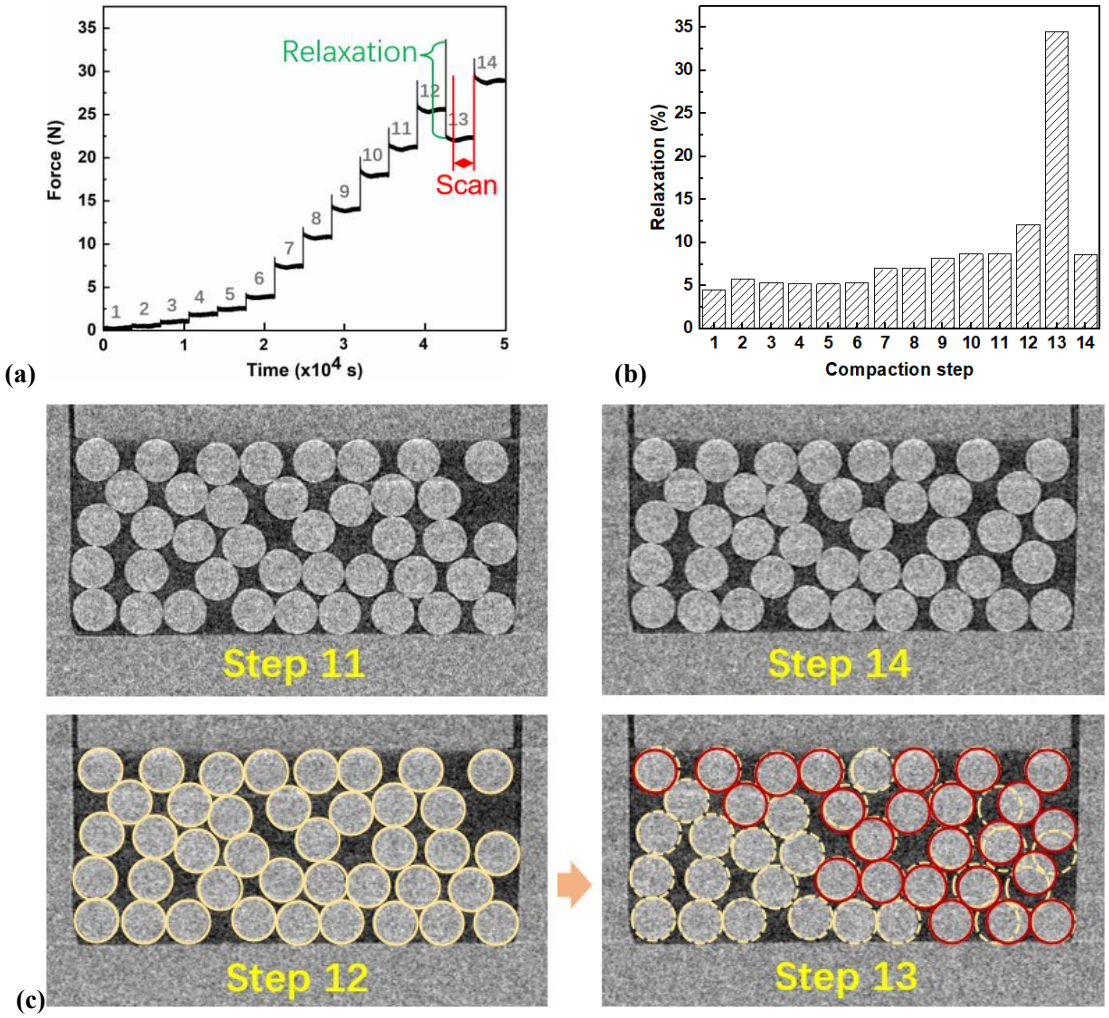

Figure 4.7 The relaxation step in the compaction experiment (a) the relationship between time and compaction force, (b) the percent of force decrease in the relaxation effect for each compaction step.

The compaction curves of the fiber bundles, and the microstructures at different compaction steps are shown in Figure 4.8. The curves of the relationship between the compaction force F (N) and the compaction displacement U (mm) are represented by a power function.

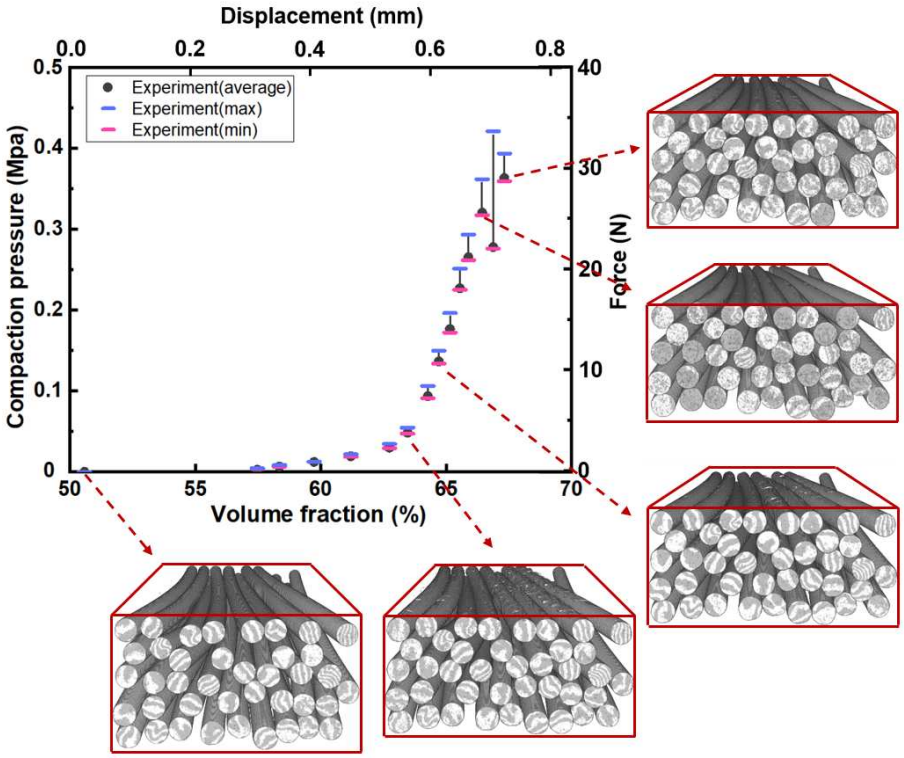

Figure 4.8 The relationship of compaction force F (N) / compaction pressure (Mpa) and compaction displacement U (mm) / volume fraction (%), and the geometry of different step.

4.4 Conclusion

This section described how the tomography scanner enables to obtain the microstructure in function of the compaction state and how the fiber samples are prepared. In addition, it described the process of tomography experiment with sample 2 as an example and discussed briefly the results of the fiber bundle micro-compaction experiment. The next step has then to propose a strategy to rebuild the tested microstructure within the simulation tool in order to perform the virtual compaction of the same sample.

Section 5 Reconstruction fiber bundle with virtual numerical estimator

5.1 Reconstruction

As mentioned in chapter one, the main difficulty as regards the extraction of the fibers form the scans for our application, is that the contacts zones between the fibers have to be very accurately described because it has a first order influence on the compaction behavior.

5.1.1 Extract the centerline of the fiber bundle

The method of extracting the centerline of the fiber bundle is shown in Figure 5.1 and includes pre-processing of the image by FIJI software and digital processing of the image by MATLAB software.

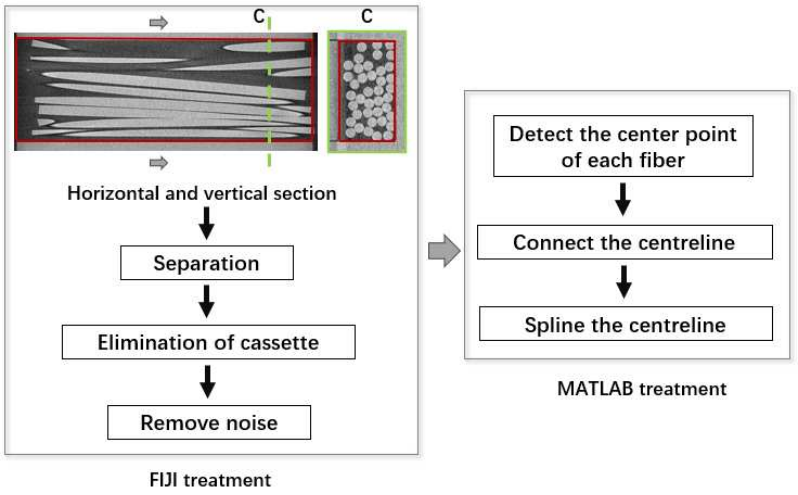

Figure 5.1 Flow chart for extraction of fiber bundle centerline.

a) X-ray tomography images pre-treatment with FIJI

i. Separation of fibers and voids

First, the sample scanned part has a cylindric volume of 7× 3.7 × 15.6 mm^3. From the circular section of this volume, a square zone including all fibers sections was selected (red zone in Figure 5.1). This square section contains 778 × 411 pixels. Following the images reconstruction by Xact software, a 16-bit grayscale image was reached. Then, the reconstructed image underwent post-processing, transforming the images grayscale to 8-bit format in order to reduce its size and facilitate the images post-treatment processing.

The X-ray CT scan image is represented in Figure 5.2 (a), manifesting as an aggregation of

pixel points. It can be seen that fibers and pores are composed of these distinct pixel points, and each one is characterized by varying the grayscale values. Significantly, the grayscale distribution along the boundaries of fibers, illustrated in Figure 5.2 (c), exhibits nonuniformity. Moreover, it is also a challenge to distinguish between the boundaries of the voids as they are not clearly demarcated. To solve this problem and achieve a precise segmentation of fibers and voids, a requisite grayscale adjustment is performed to prepare for the segmentation process. Figure 5.2 (b) show the histogram which details the mean and the standard deviation of the pixel brightness across the Figure 5.2 (a). Subsequently, a specific analysis of the brightness intensity distribution of individual fiber sections is conducted, as depicted in Figure 5.2 (d). Remarkably, the spectrum of intensity values within fiber sections can change from a minimum of 0 ADU (Analog-to-Digital Unit or the “gray level”) to a maximum of 65535 ADU. This insight informs the subsequent application of a brightness-contrast adjustment, confining the interval to 20711-65535 ADU, and effectuating brightness enhancement of the slice. The effectuating brightness enhancement was determined by comparing the accuracy of the MATLAB program's identification of circles (fiber cross sections) for different choices of different grayscale spectral ranges, shown in Figure 5.2 (c). The resultant adjusted slice is illustrated in Figure 5.2 (e). Next, the image that has been adjusted for brightness contrast will be thresholded (Figure 5.2 (f)).

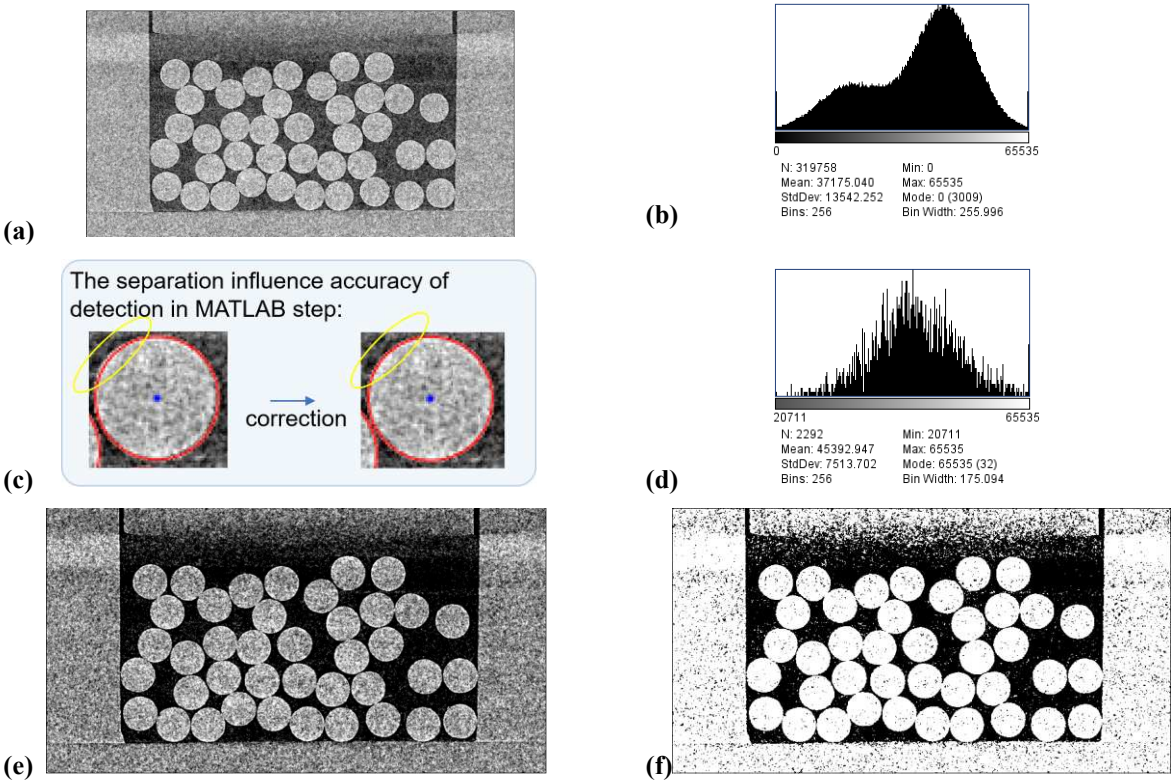

Figure 5.2 Separation of fibers and voids according to greyscale spectral. (a) Initial slice of fiber's section, (b), (d) the brightness intensity distribution of the slice. (c) The separation influence accuracy of detection in MATLAB step. (e), (f) Different treatment with threshold parameter.

ii. Elimination of compaction channel/plates

Elimination of box boundaries allows an accurate definition of the cross-section of fibers with MATLAB, as shown in Figure 5.3. In fact, the boundaries of the box can lead to inaccuracies in the definition of the circles especially for the fibers in contact with the box.

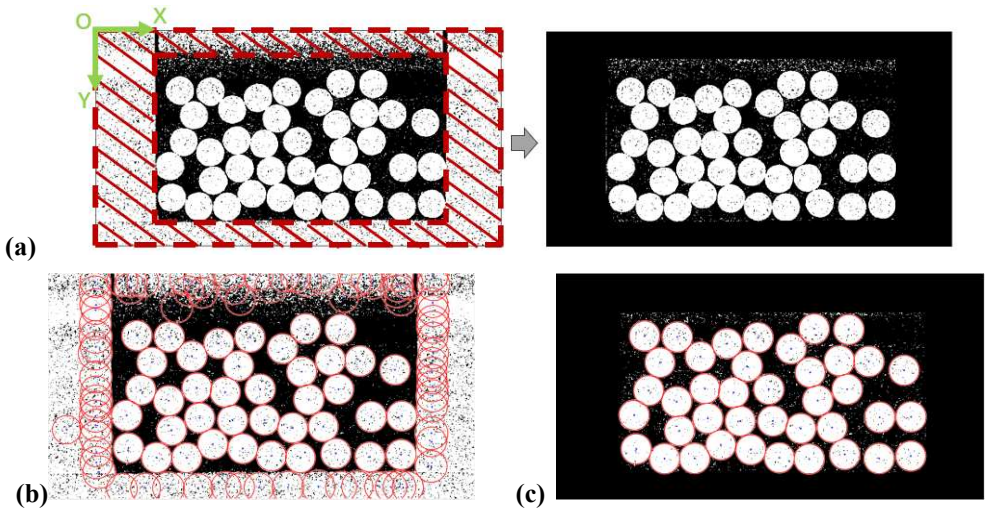

Figure 5.3 Elimination of sample cassette (compaction plates/ channel). (a) Remove the compaction plates. (b), (c) With and eliminate the errors of the detection influenced by compaction plates, respectively.

iii. Remove noise

The noise elimination is performed on the slices, where the noise radius is 2 pixels, and the threshold is 50. Subsequently, Figure 5.4 is obtained after removing noise. It can be seen that the fibers cross-section are almost perfect circles, and it can be further processed by the MATLAB program to extract the fiber center point.

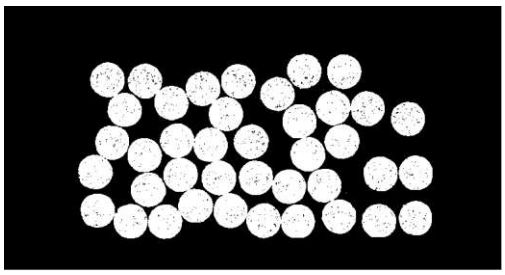

Figure 5.4 Remove the noise of the slice.

b) Extract the centerline of the fiber bundle with MATLAB

The fiber bundle centerline is extracted by detecting the center of the fiber cross-section based on the FIJI preprocessed image, and then connecting the center points of the same fiber.

i. Extract the center point

The fiber cross-section in each X-ray tomography slice can be approximated as a circle, and the center of this circle can be a pixel point coordinate. Therefore, the radius and the center of each circle can be defined by the "Imfindcircles" function in MATLAB. The principle used in this function for definition of the circle is the “Circle Hoff Transform (CHT)”, as shown in Figure 5.5 (a). Each pixel point in the image corresponds to a polar coordinate point of (x, y):

$$x = a + R\cos\theta$$

$$y = b + R\sin\theta$$

Where a and b represent the polar coordinates of the circle center while R is the radius of the fiber, $\theta \in [0° - 360°]$. The CHT finds an edge pixel in the region with the largest intensity gradient, which forms a circle (Figure 5.5 (a-left)). After estimating the radius R, the value of θ is computed by extrapolating from 0°to 360°in steps of 1° to produce each (a, b) coordinate point. The algorithm is performed for each pixel point on the image, resulting in the circles represented by the dotted lines shown in Figure 5.5 (a-right). Their intersections are accumulated, and the place with the highest number of intersections is determined to be the center of the circle (red point in Figure 5.5 (a-right)).

Figure 5.5(b) shows the detected circle after projecting them on the original tomographic image.

Subsequently, the detected circles and the fibers sections boundaries are almost exactly coincided. In addition, by changing the parameters in the function, such as the radius range, the sensitivity, etc., the circle can be defined more precisely.

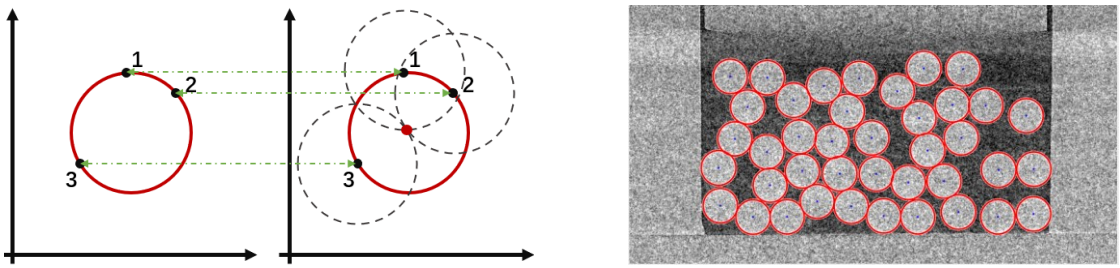

(a) (b)

Figure 5.5 Detection of fiber cross-section by Circles Hough Transform (CHT) method and projected onto the initial tomography image. (a) CHT principle. (b) Detection of the fibers section in one slice.

ii. Connect the center point

The coordinates of the center point and the radius of each fiber cross-section are obtained by the CHT algorithm, but MATLAB cannot automatically determine which circles of different slices belong to the same fiber. Therefore, the determination method is shown in Figure 5.6, for center point $\boldsymbol{C_{ij}}$ in slice $\boldsymbol{j}$ and the center point $\boldsymbol{C_{ij+1}}$ in slice $\boldsymbol{j+1}$ belonging to the same fiber **i**, the distance between the projection of $\boldsymbol{C_{ij}}$ and $\boldsymbol{C_{ij+1}}$ should be less than the diameter of fiber:

$$\left|\boldsymbol{C_{ij+1}} - \boldsymbol{C_{ij}}\right| < \emptyset \tag{5.1}$$

In this study, the distance between the two slices was d = 9 µm, which is enough small compared to the fiber's diameter $\emptyset$ = 500 µm. The 9µm present the voxel dimensions, which depends on the distance between the X-Ray source and the scanned object. In addition, through Figure 5.6 it can be seen that the fibers are slightly entangled, which means the curvature is very small and the distance between adjacent slices of the same fiber L satisfies the condition: $d \leq L < \sqrt{d^2 + \emptyset^2}$. And so on, connecting all center points of each fiber (Figure 5.6).

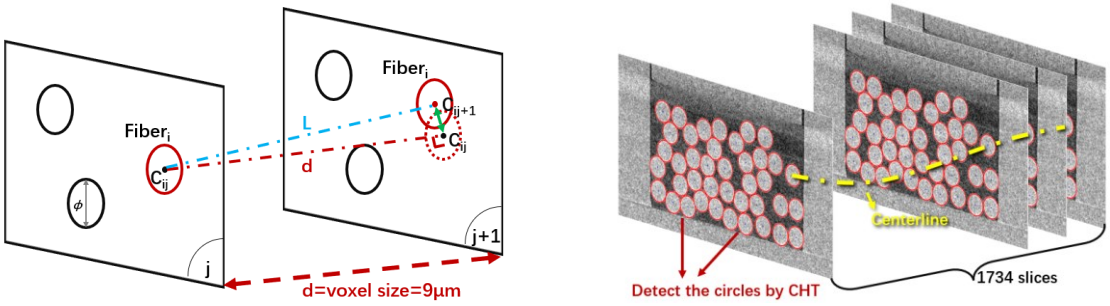

(a) (b)

Figure 5.6 Principle of connecting center points of the same fiber.

iii. Spline the centerline

As mentioned earlier, the tomography images are composed of thousands of pixel points. As shown in Figure 5.7, when defining a circle, the position of the center coordinates in the slice calculated using the CHT algorithm can be divided into two cases:

Case 1, the center of the circle is not on the pixel point and the actual center point is offset to the nearest pixel point when defining the center of the circle; Case 2, the center of the circle is on the pixel point and no offset occurs.

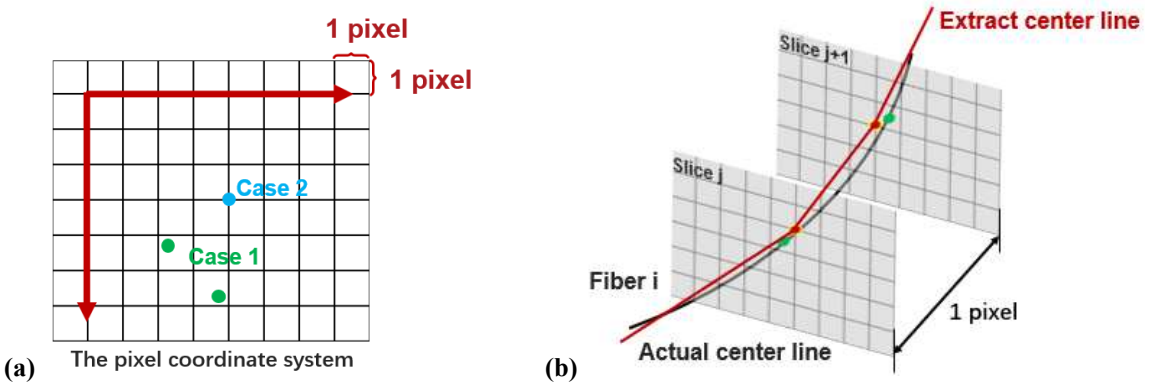

Figure 5.7 Distribution of fiber's center point in the pixel coordinate system. (a) The pixel coordinate system in MATLAB. (b) The connect fiber's centerline.

Therefore, when the center coordinates of fibers are connected, the form of the "folded" line (extracted line) in Figure 5.7(b) and Figure 5.8 (before smooth centerline) is obtained, which does not correspond to the actual fiber morphology due to the uncertainty of 1 pixel on the center position. The oscillations amplitude depicted Figure 5.8 are, indeed verified to be lower than 1 pixel. A smoothing step has then to be performed on them to obtain the consistent trajectory Figure 5.8.

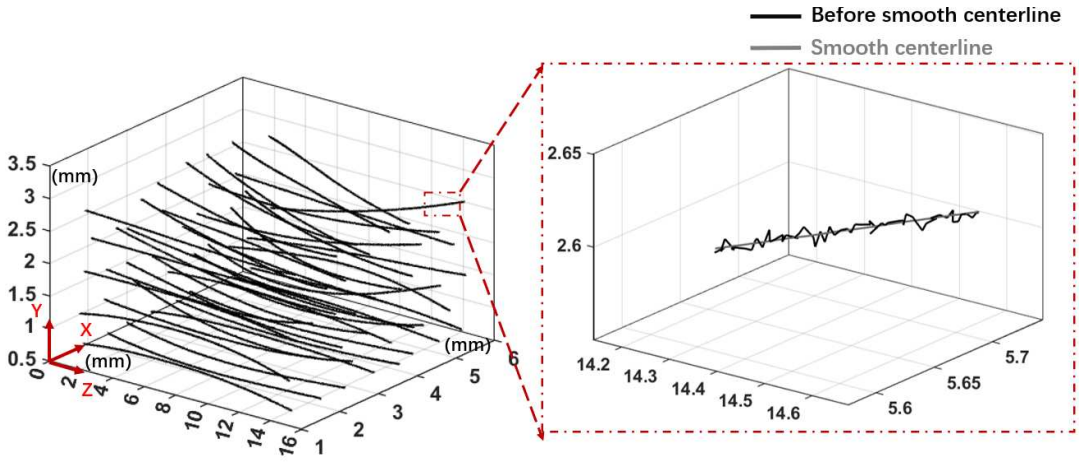

Figure 5.8 The centerline before smooth and after smooth of the fiber bundle.

c) Impose the cassette to ABAQUS®/CAE

Due to the processing accuracy of the cassette (the support of fibers bundle), the inner wall of the cassette used to compress the fiber bundle might be not completely vertical, and the horizontal axis of the cassette is not completely coincident and parallel to the axis of the X-ray source due to human error when placing the cassette in the micro-compressor. Creating a flat surface directly in ABAQUS® for the compaction simulation would result in inaccurate contact between the fibers and the cassette, leading to errors in the compaction simulation. Therefore, the position of the cassette (inner wall) / compaction channel needs to be imported as accurately as possible. Similarly, the location of the compaction channel will be obtained from the original tomography image. Its cloud points will be obtained by marking its boundaries by FIJI, imported into CATIA V5 to automatically create planes, and then imported into ABAQUS® /CAE, as shown Figure 5.9.

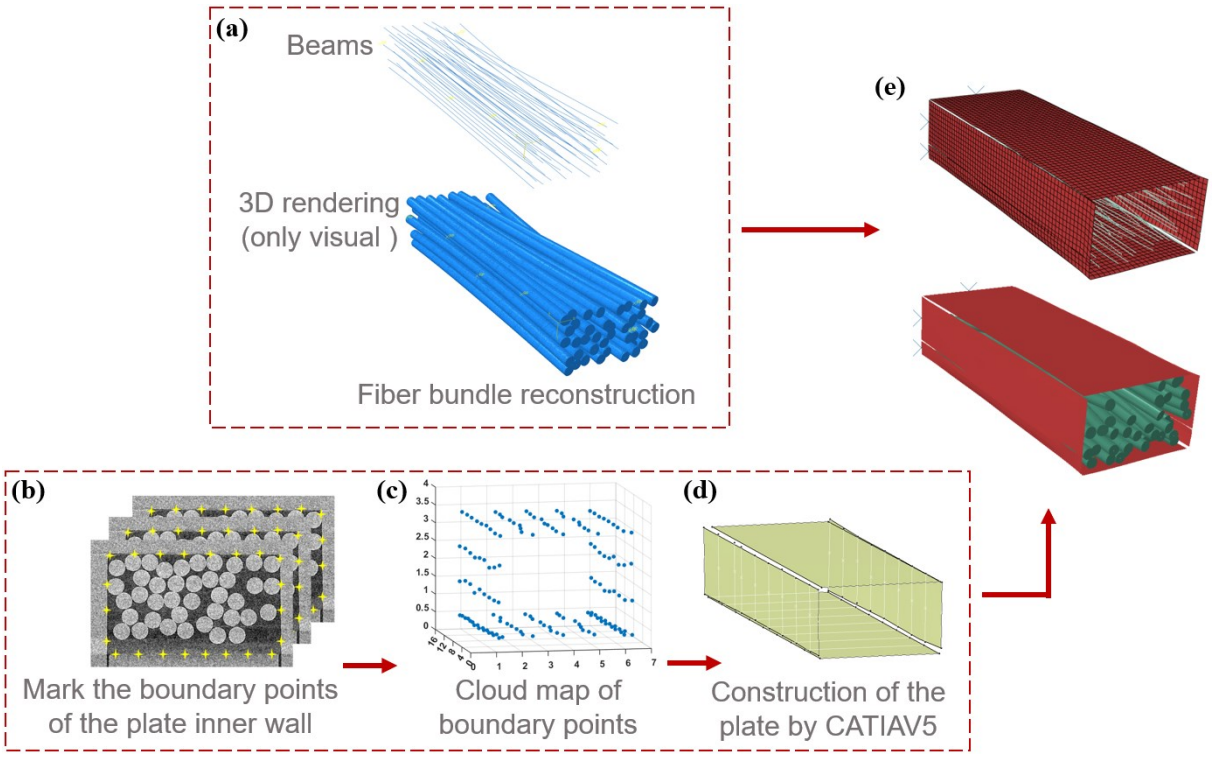

Figure 5.9 Introduced into the inner wall of the cassette (the compaction channel in contact with the fiber bundle), using Sample 2 as an example: (a) the numerical fiber beams, (b)mark the boundary points of the cassette's inner wall, (c)the cloud map of the boundary points of (b), (d)construction the compaction channel, (e)import the compaction channel to ABAQUS® with fiber bundle.

5.2 Numerical strategy

This study develops and enhances an existing simulation strategy (developed by Dr. Haji (Haji et al., 2023; Haji Oussama, 2018). The simulation strategy, which is executed in ABAQUS®/EXPLICIT, shows that Explicit method can be used for quasi-static dynamics simulations under many contact conditions and that selection of appropriate simulation parameters can optimize the computational time. Haji has tested (i) the finite element type for fiber (Haji Oussama, 2018), by testing the compaction simulation of two fibers, and it has been determined that the element B31(Timoshenko beam) is more stable compared to the element B32. And there are numerous contact in the fiber bundle model, the B31 is more efficient deal with the contact problem; (ii) Haji has also tested the dynamic/explicit simulation parameters, by the case of rearrangement of three fibers, under the condition of ensuring the quasi-static loading experiments, it has been obtained that the material damping coefficient $\alpha = 10^5$ and a compaction loading speed of $v = 10^3$ mm/min, can optimize the calculation time and avoid the inertia effect of the fibers, and the kinetic energy were checked.

In addition, for this simulation, other parameters were chosen to be consistent with the simulation strategy in Dr. Haji's thesis: (i) the tangential contact was modeled by the Coulomb's friction law, where the friction coefficient was used with an average value of $\mu = 0.2$ according to (Gassara, 2016); (ii) the adhesion coefficient was assumed to be equal to the coefficient of friction; and (iii) the diameter of the beam elements of the single fibers was the same (0.5mm) and constant.

For the selection of the size of the mesh elements of the fibers and the compaction channels (sample cassettes), the correction of initial penetration between the fiber bundles was set in next part.

5.2.1 Elements' size

In fiber bundle compaction simulations, the mesh size of beam elements and flat plates can influence the simulation results. Elements that are too large lead to inaccurate simulation results, and elements that are too small lead to long calculation times. The best way is to test mesh sensitivity.

When the mesh size is small enough, the accuracy of the calculation does not change significantly as the mesh continues to decrease. Therefore, the value is set here as the threshold value L_b. Figure 5.10 shows this test case for choosing the suitable element size, which is a

compaction test on an analytical rigid plate with three total parallel and straight fibers, using B31 elements. This case is suitable since the local curvature of the fibers in the targeted modeling is low and consequently does not challenge that much the number of elements. The mesh sensitivity of the model is tested to obtain the threshold value of mesh size L_b, with the change of mesh size the simulation results are almost unchanged, so the simulation with this mesh size L_b will get accurate the simulation results and shorten the calculation time.

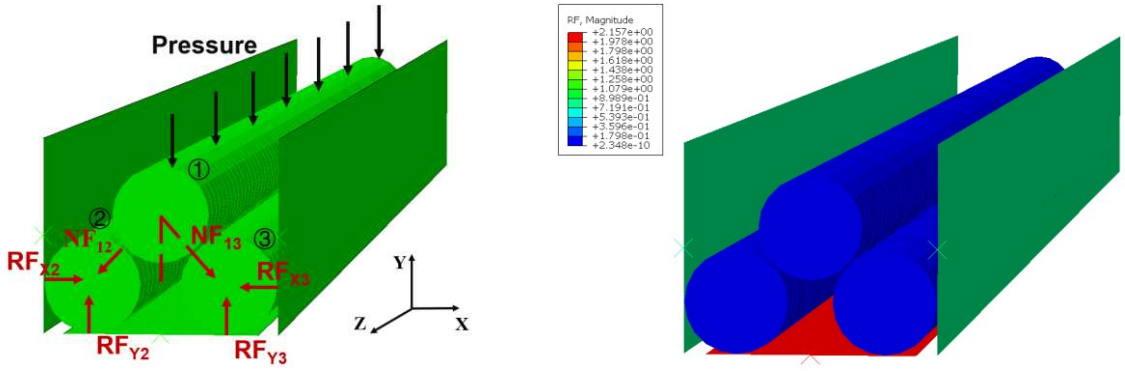

(a) **(b)**

Figure 5.10 Mesh sensitivity test case. (a) compaction of 3 parallel straight fiber, (b) the results of test mesh sensitivity of beam

For this preliminary testing the plates of Figure 5.10 are defined as analytical rigid body, but this choice must be questioned for the future simulation. Indeed, the difference between analytical rigid and discrete rigid is the following: (i) Analytical rigid is defined by the analytic formula, which only enables geometries explicitly described by an equation. Discrete rigid is controlled by the mesh node, which deal with any shape or description of the geometry. (ii) the computational cost of analytical rigid is smaller than discrete rigid. (iii) the discrete rigid should be mesh before calculation ("ABAQUS Documentation (6.5-1)," n.d.), as a consequence, the obtained solid is discretized. In the reconstruction of the fiber bundle model, the sample cassette as mentioned above is not a perfectly flat plane, and in order to obtain an accurate plane, CATIA V5® was used to import the sample inner plane into ABAQUS®. Such a plane can only be described by a discrete rigid part. If only rigid surface contact is provided for contact analysis, analytic rigid body can be considered, which can effectively reduce calculation time. So, the analytical rigid will be used here as a reference for the beam mesh size study in order to save calculation time and enhance the accuracy (no discretization).

The reaction force of the plane is shown in Figure 5.11 (a), when the element size of the fibers is L_b=0.3 mm (a single beam contains 50 elements), the reaction force stabilizes and reaches a critical value for the mesh sensitivity. Since, the discrete rigid solid will have to considered for

the real compaction case, the mesh sensitivity of the discrete rigid is tested with a beam with a mesh size of 0.3mm and the same case. The reaction force results are basically the same as the reference with analytical rigid part (Figure 5.11 (a)) when the mesh size of the discrete rigid part is 0.2mm.

Thanks to this sensitivity analysis the good range the for the mesh sizes is defined and will then be used for the calculations.

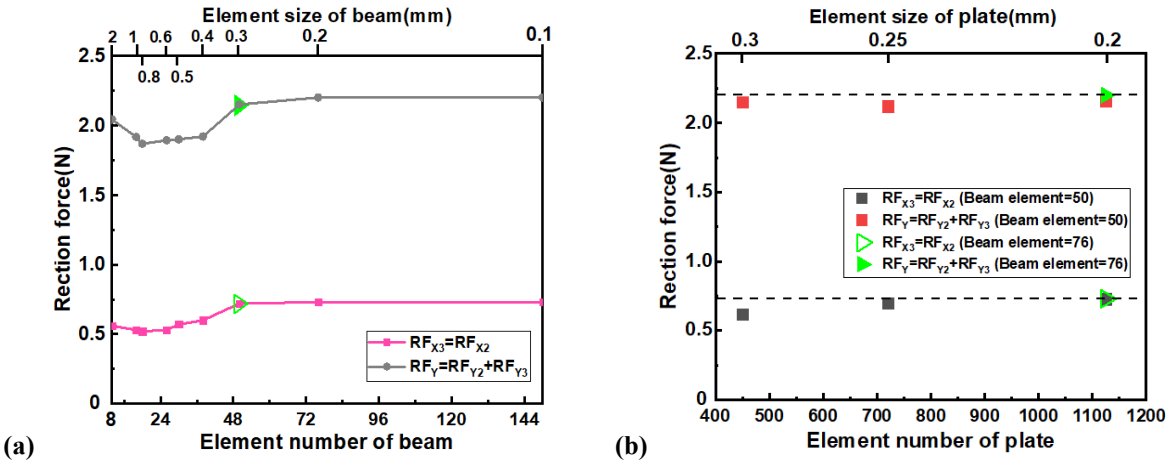

Figure 5.11 The reaction force in mesh sensitivity test case. (a) the rection force of test mesh sensitivity of beam, (b) the reaction force of test mesh sensitivity of discrete rigid part.

5.2.2 Young's modulus of fibers

In order to verify the reliability of the Young's modulus of single PE fiber, tensile experiments were processed.

a) Samples material

The considered Polyester fibers (Poisson's ratio = 0.25 (Haji Oussama, 2018)) for the validation experiments have a diameter of 500 µm and a density of 1.38×10^{-09} T/mm^3. In order to implement the as accurate as possible mechanical behavior for the fibers, mechanical tests have been conducted.

b) Tensile test of single PE fiber

The cyclic loading method was used to obtain the elastic and plastic deformation of polyester fibers under tensile testing. The tested sample was bounded in two fixtures or jaws as shown in Figure 5.12 (a). Many marks were placed on the fibers in order to measure the real material

strains, it enables also to verify the strain homogeneity and to verify the boundary conditions using the comparison with the device displacement. Experimental strains are consequently obtained measuring the displacement of the marker points during the tensile test with a camera. A pre-charge force was of 2 N was applied on the fiber loaded for 8 cycles, and increased by 5 N for each time the force was loaded. The tensile displacement speed was fixed at T_{ensile} =10 mm/min. Five tests were done to ensure the accuracy of tensile experiments, the results are shown in Figure 5.12(b, c), in which Hencky strain is defined by:

$$Hecky\ strain = \ln\left(1 + \frac{\Delta L}{L_0}\right)$$

where $\Delta\mathbf{L}$ is the displacement of the tensile machine upper fixture, L_0 is the initial length of fiber between fixtures. In the first three cyclic loading experiments (Figure 5.12 (d)), the fibers undergo elastic deformation, and the slope of the curve represents the Young's modulus of the polyester fiber. In addition, the relationship between Hencky strain and stress obtained by FIJI from displacements of markers of filaments is in general agreement with the experiment data. This agreement indicates that there is no slip of fibers inside the fixtures during tensile testing. The different strains measurements on the different marker couples didn't exhibit any significant difference (less than 2%) the homogeneity of the strain can then be confirmed. The resulted average Young's modulus is 6 ± 0.2 Gpa, and the average value of this parameter will be used in the simulation:

$$E_{average} = \frac{Elastic\ strain}{Elastic\ stress} = 6\ Gpa$$

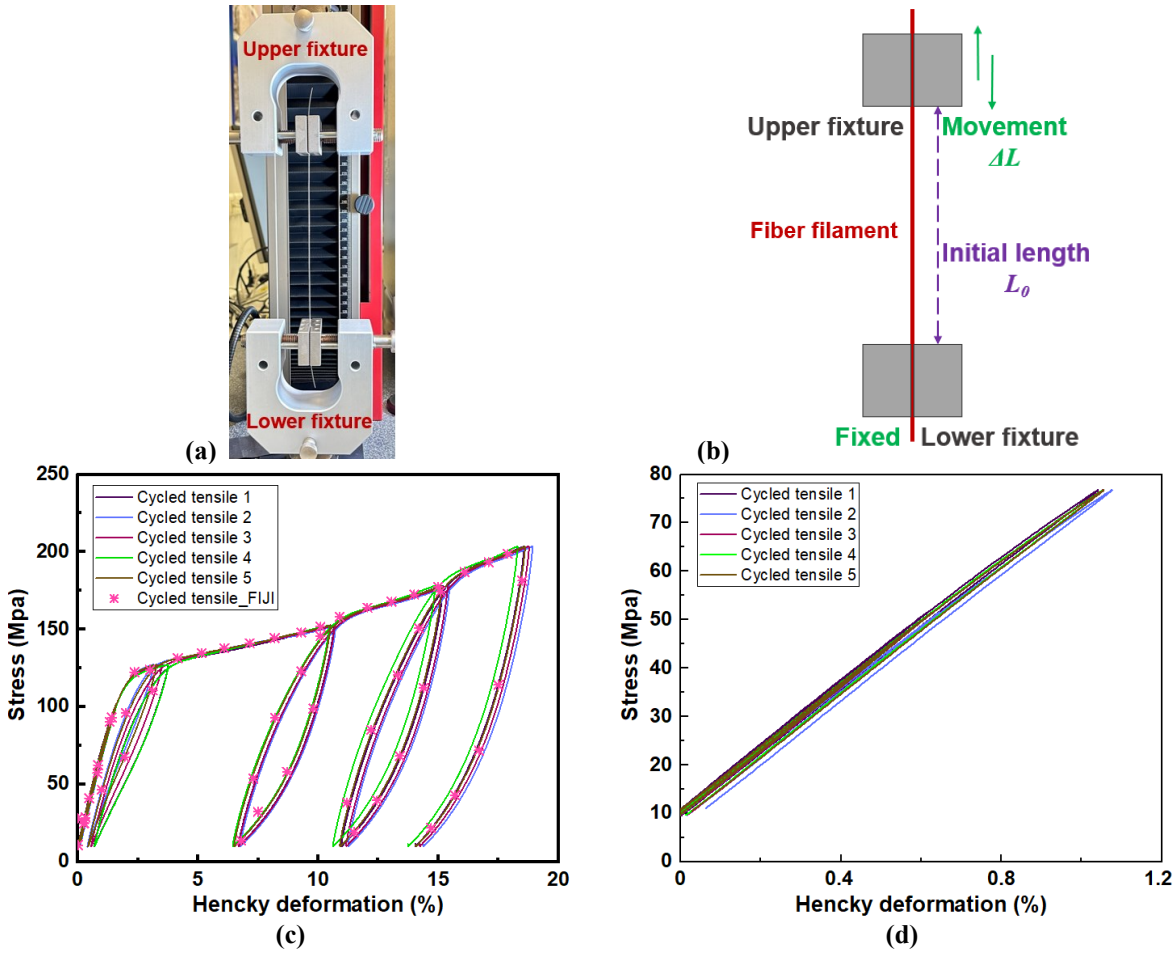

Figure 5.12 Cycled tensile test of polyester fiber. (a, b) tensile machine and principle, (c) 5 cycled tensile test, (d) the first three cycles of the 5 tests.

These cycled tests enabled then to obtain elastoplastic mechanical behavior that has to be implemented in the simulation, it also enables to determine the maximum Hencky strain for which the fiber is consistently assumed to be elastic. However, since it might be useful for future simulations to characterize the tensile strength, a monotonous tensile test until the breakage of the fiber was performed. Using the tensile jaws of Figure 5.12 (a), the breakage of the fiber was located within the jaws which obviously doesn't lead to a consistent value of the fiber strength. A capstan equipment was consequently tried. The loading speed $V_{tensile}$ = 10 mm/min and the results are shown in Figure 5.13. The maximum Hencky strain reached 22.5% to 30%.

However, a sliding was noticed within the capstan and the breakage could not be obtained in the central part of the fiber for none of the three tests. Since there is no risk of reaching the breakage during the compaction loading, no further investigation was made, but, in the future, it might be interesting to improve the boundary conditions and repeat a higher number of tests in order to obtain the tensile strength.

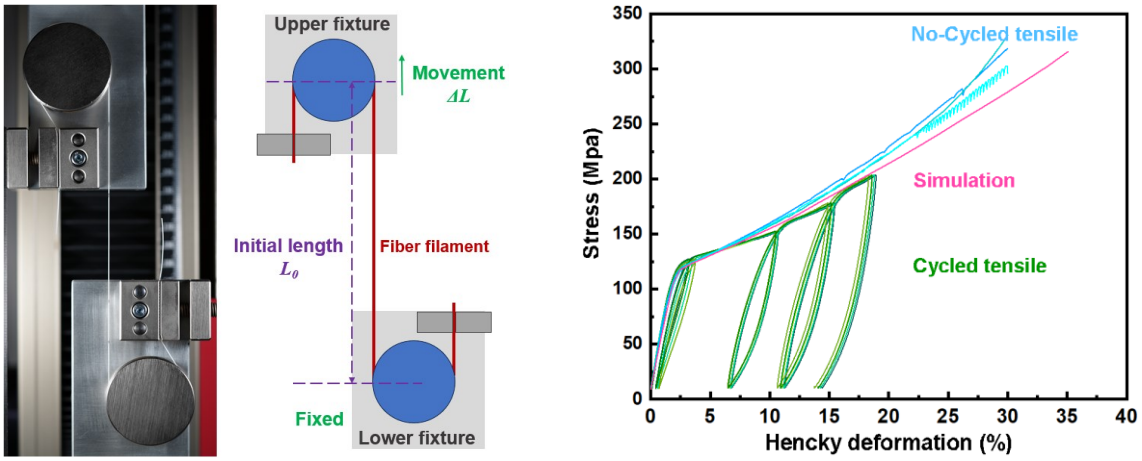

(a) (b)

Figure 5.13 No cycled tensile test of polyester single filament. (a) the equipment, (b) the experiment results.

A virtual tensile test has then been performed in Abaqus using the mesh parameters defined previously so has to validate the implementation. The simulation results were as expected close to the experimental ones.

5.2.3 Initial penetration and contact control

a) Initial penetration

As mentioned above, the reconstruction of the geometric model of the fiber bundle is based on detecting the center point of the fiber section. The fiber cross-section consists of approximately 2420 pixel points. Whereas the actual center point of the fiber may not be on the pixel points (as shown in Figure 5.15) resulting in the offset (approximately 1pixel) of the position of the detected circle. In addition, the real fiber's section is not strictly a regular circle, but it will be detected as a circle with different radius (r_{MATLAB}) in MATLAB (CHT circle detect program). The offset of the detected circle and the radius ($r_{ABAQUS®}$) of the individual fibers remains constant when importing the fiber bundle numerical geometry into ABAQUS®, will result in slight initial penetration between the fibers. In addition, the diameter of the same fiber is chosen to be constant in the ABAQUS® model, so that the contact points between fibers differs from the actual centerline.

The radius and midline point coordinates of the fibers are extracted when the fiber cross section is identified through MATLAB, therefore the detection of the circles using MATLAB has been analyzed. Since the "*Imfindcircles*" function (CHT circles detect) in the MATLAB program has

errors in the identification, the identification of the fiber radius and the errors in the original image are discussed here. In Figure 5.14, the diameters of the fiber cross sections in the tomographic images were manually detected with a mean value of 0.483 mm, as well as the diameters of the fiber cross sections detected by MATLAB were statistically counted with a mean value of 0.49 mm. As mentioned before, part of the error in the simulation strategy comes from the detection of the fiber cross section and the setting of the diameter of the fibers in the model. However, this error still reasonable since it represents 2% of the measured diameter.

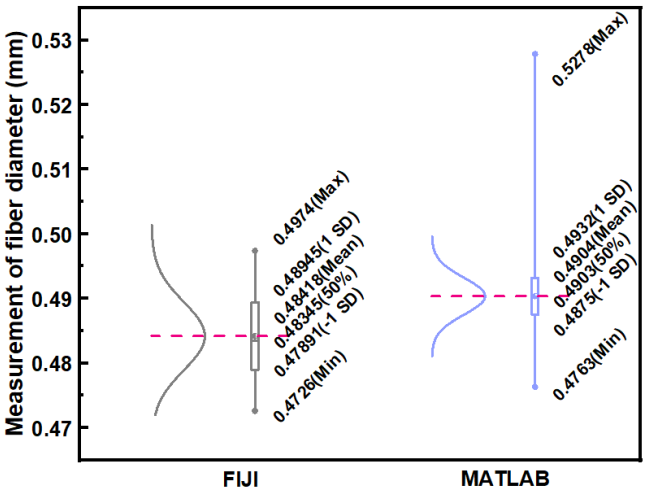

Figure 5.14 Measurement of fiber diameter by FIJI (manually operated) and MATLAB (automatically)

This problem of spurious voids or interpenetration is classically encountered while modeling and importing multi-solids structures in finite element codes.

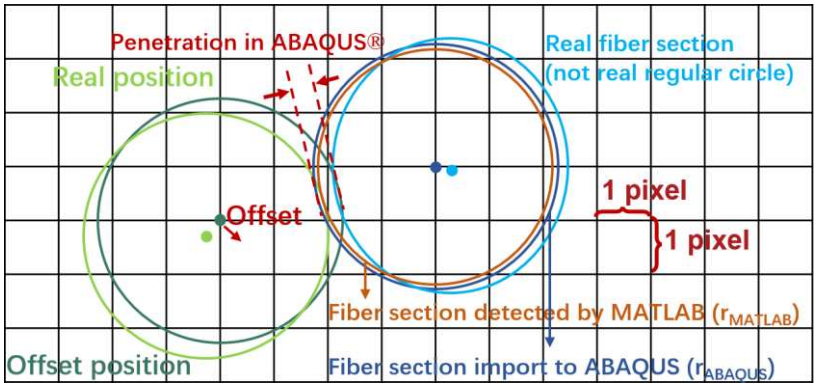

Figure 5.15 Penetration principle between fibers in ABAQUS®.

In order to study the best way to deal with this issue, 5 curved beams were simulated with initial penetration under gravity loading. These 5 beams were reconstructed by real tomography slices (micro-compaction experiment 1), and the random 4 fibers of fiber bundle were selected and rearranged to have initial penetration between the fibers, and also between the fibers and the

plate (Figure 5.16). Two methods can initially be considered to avoid the initial penetration in the first step of the calculation:

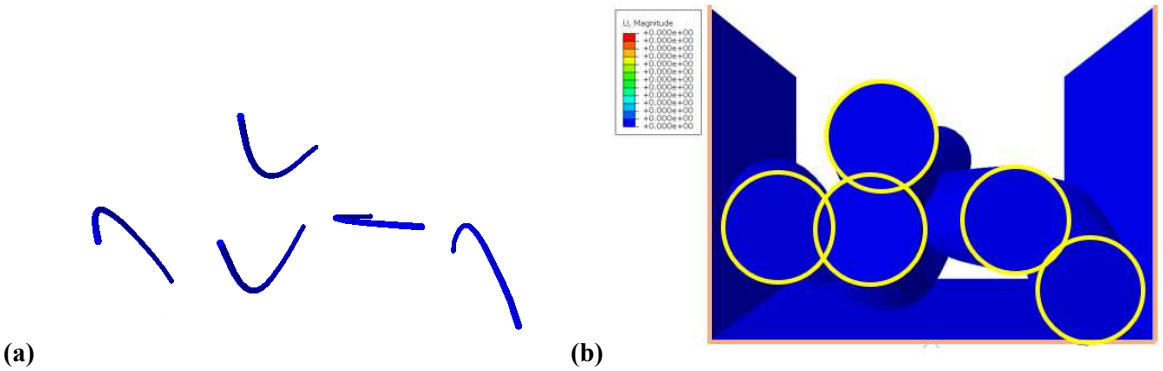

(a) (b)

Figure 5.16 Initial penetration test case, (a) centerline, (b) numerical geometry.

(i) The ABAQUS® auto-correction by moving nodes (default):

Abaqus®/Explicit automatically adjusts the positions of surfaces to remove the small initial overclosures that exist in the general contact domain in the first step of a simulation. Initial overclosures that are not resolved by repositioning nodes are stored as initial contact offsets to avoid large contact forces at the beginning of an analysis ("ABAQUS Documentation (6.5-1)," n.d.). So, the nodes will offset to avoid the initial penetration, as shown in Figure 5.17(a-d). After the first calculation, the nodes of the beam offset, and the smooth centerline becomes locally highly curved (Figure 5.17(a)), which is unrealistic, leads to high local strains and will affect the fiber microstructure (Figure 5.17(c)).

(ii) The contact control (manual):

To solve the initial penetration problem (Figure 5.16), contact control is manually proposed in the *".inp"* file for the contact pairs between fibers. The separation of the initial penetration after first calculation by ABAQUS® shown in Figure 5.17 (e), and the morphography of fibers after gravity calculation shown in Figure 5.17(e). The contact control of this strategy were manually proposed in the *".inp"* file for the contact pairs, for example, the fiber I and fiber are initial penetration in the initial geometry model, the initial penetration contact control were performed in "*.inp*" file:

"Beam i, Beam j, STORE OFFSETS",

With this "AUTOMATIC OVERCLOSURE" control, include this parameter to store offsets instead of adjusting nodes during initial overclosure resolution between surface pairs in the general contact domain("ABAQUS Documentation (6.5-1)," n.d.).

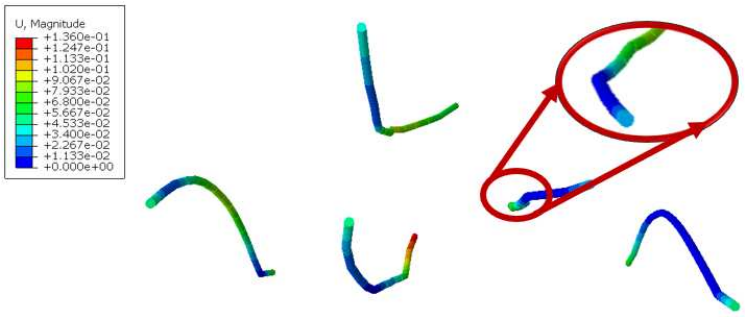

(a) Centerline after first calculation with ABAQUS®

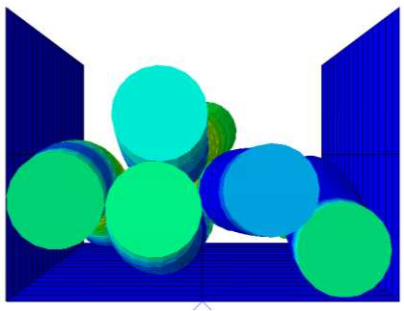

(b)

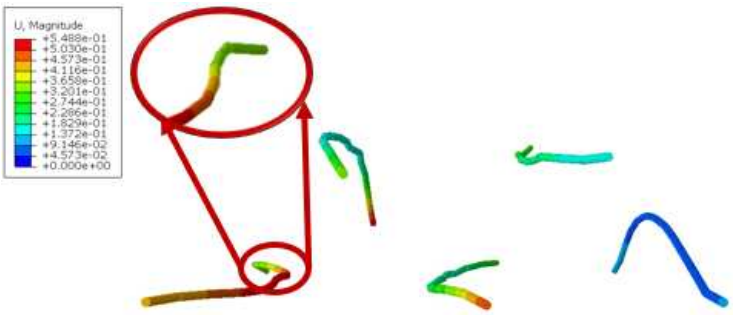

(c) centerline after gravity calculation with ABAQUS®

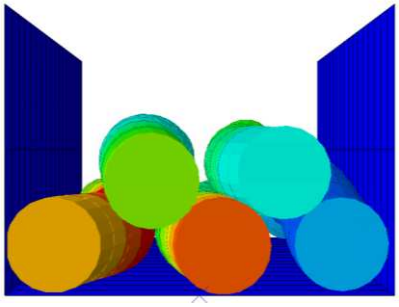

(d)

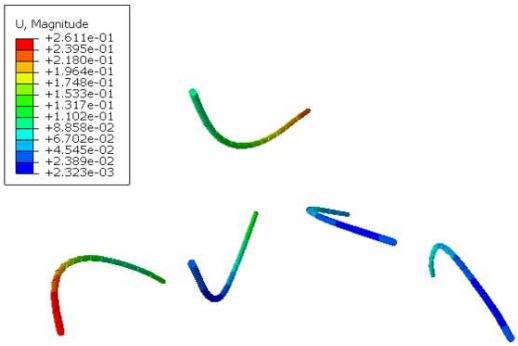

(e) centerline after first calculation with ABAQUS®

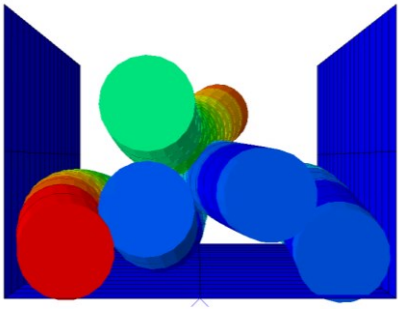

(f)

(g) centerline after gravity calculation with ABAQUS®

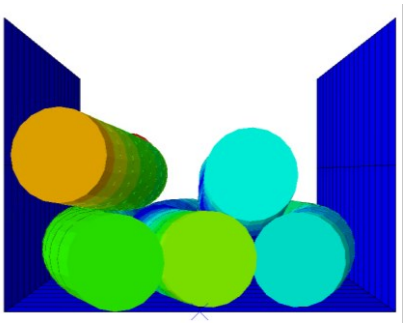

(h)

Figure 5.17 Initial penetration test case. (a, b) after first calculation, (c, d) after gravity calculation with ABAQUS auto-correction; (e, f) after first calculation, (g, h) after gravity calculation with ABAQUS contact control.

In order to analyses the results of each simulation from the energy point of view, the Figure

5.18 (b) presents the variation of the three energies of the initial penetration model: contact energy (penalty energy ($\mathbf{P_e}$)), kinetic energy ($\mathbf{K_e}$), and strain energy ($\mathbf{S_e}$). The $\mathbf{P_e}$ denotes the contact energy, which is the contact penalty work, $\mathbf{K_e}$ indicates the fiber rearrangement, and $\mathbf{S_e}$ indicates the deformation of the fibers, which is also the energy of the fiber bending in this case. As shown in Figure 5.18, in method (i) (method of auto-correction), the deformation energy $\mathbf{S_e}$ is greater than the $\mathbf{K_e}$ at the initial stage of the simulation, which is consistent with the movement of the fiber nodes shown in Figure 5.17 (a). Before the calculation time of 60 s, the values of $\mathbf{S_e}$ and $\mathbf{K_e}$ are basically the same, and the fibers are undergoing deformation as they move significantly under gravity. Finally, the fibers maintain a large deformation. In the method (ii), the kinetic energy is much lower but always larger than the deformation energy. The fiber undergoes small strains at the same time as the gravity calculation, and this deformation is entirely due to gravity. The highest strain energy value of method (i) is 10^3 times higher than that of method (ii), and from the energy perspective, "contact control" avoids the over-deformation of fibers in case of no applied force. And the difference in contact energy between the two method is not significant. In addition, the fibers spurious movements are significantly reduced a show the much lower Kinetic energy.

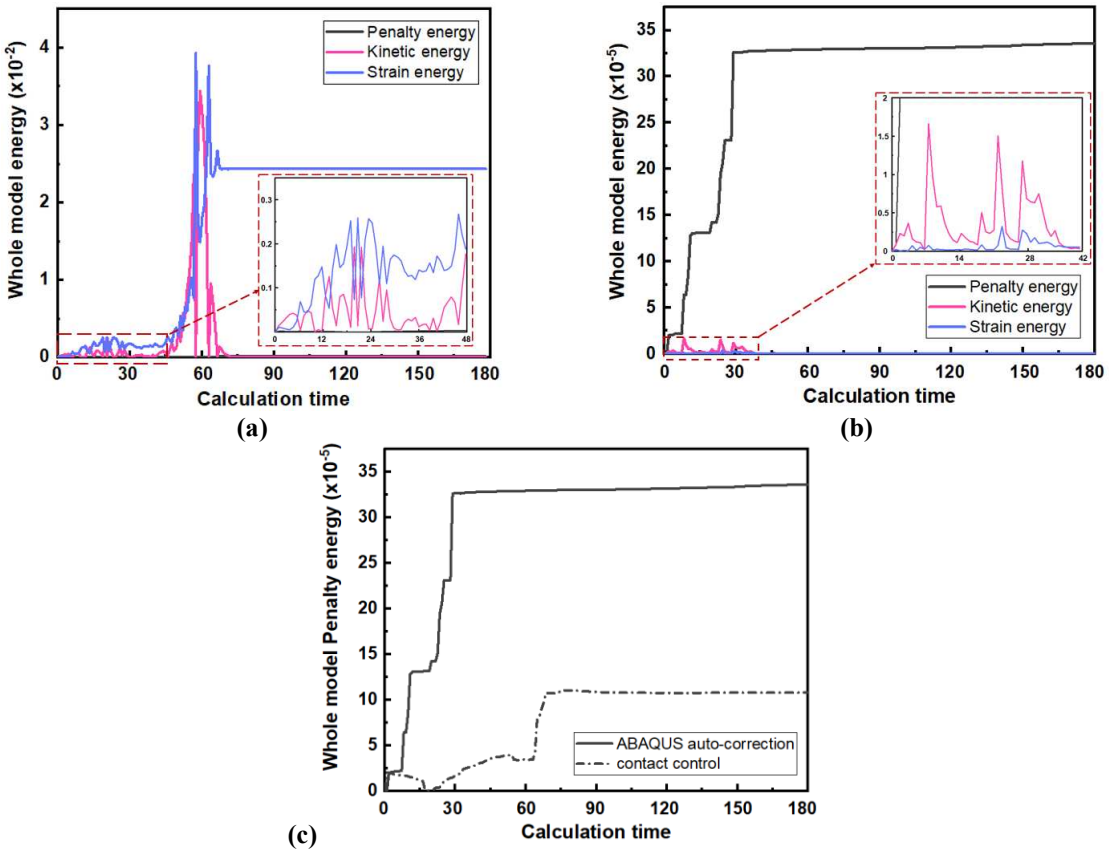

Figure 5.18 The contact, kinetic and strain energy in the initial penetration case with (a) ABAQUS® auto-correction, (b) manually contact control. (c) Penalty energy of this two-method penetration correction.

Thanks to this analysis the manual contact control method is chosen and has to used in the next steps.

b) Avoid the self-contact

By default, for calculations, self-contact occurs between the fibers, which means the fibers penetrate each other up to the centerline of the fibers, in addition, the compaction plate were penetrated with fibers firstly during compaction process, as shown in Figure 5.19 (a). To solve this problem, the *".inp"* file is modified manually:

"Contact controls assignment, contact thickness reduction=self",

This manually control could limit automatic contact thickness reductions to only regions of potential self-contact and the perimeters of shell surfaces ("ABAQUS Documentation (6.5-1)," n.d.). The self-contact between fibers, fibers and plates were eliminated, shown in Figure 5.19 (b).

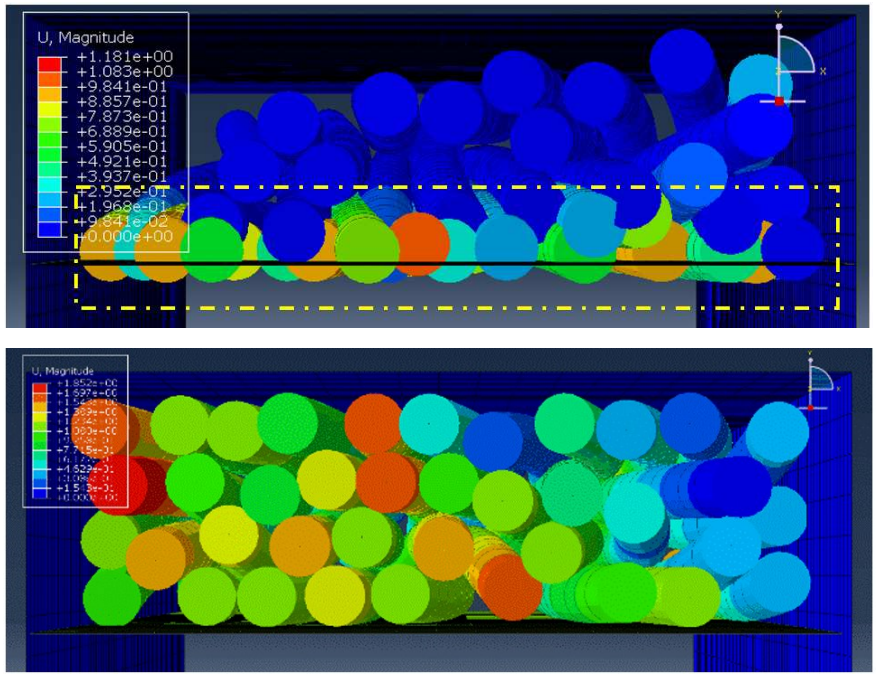

Figure 5.19 The contact control of avoid self-contact between fibers, fibers and compaction plates.

5.3 Conclusion

This section presented the numerical model reconstruction process of the fiber bundle. It includes (i) the post-treatment procedure of the tomography image (i.e. extraction of the fiber centerline, smoothing, etc.), the way of importing the fiber bundle compaction channel; and (ii) the strategy for the numerical modeling: selection of the element sizes, mechanical behavior of the fiber, and solving the problem of the penetration between fibers. In section 6 after dealing with the remaining uncertainties of the reconstructed model, in order to get a as consistent as possible initial geometry, indicators of the microstructure are proposed and coded. This step is of a main importance to characterize and understand the evolution with the compaction but also in order to define parameters that might be considered in the mechanical behavior of a fiber bundle.

Section 6 Analysis tools creation

6.1 Sources errors of simulation

For the reconstructed model of the numerical fiber bundles, small errors may remain on the positions of the reconstructed experimental fiber bundles which are analyzed from the experimental and modeling points of view in this simulation strategy. Here Sample 2 is used to investigate the errors.

Error from comparison of the fiber position of simulation and experiment:

The position error of the fiber centerline after importing the fiber geometry numerical model into ABAQUS® for "mesh" processing is considered here. The initial fiber geometry model after "mesh"(element size of fiber L_e= 0.3mm) is compared with the fiber centerline extracted from tomography experiments, and they are look in perfect agreement (Figure 6.1).

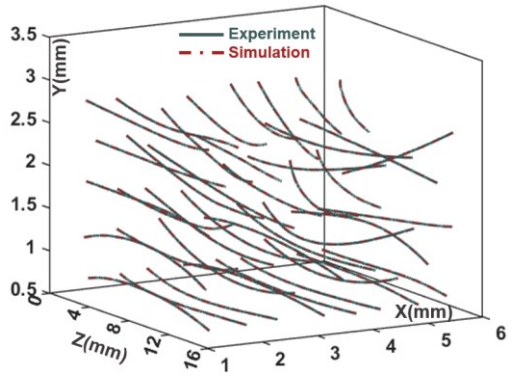

Figure 6.1 Comparison of the initial fiber centerline of experiment and after mesh (sample 2).

However, more than the overall position of the fibers the microstructure indicators of fiber bundle has to be challenged. As shown in the Figure 6.2, each individual fiber consists of about 1500 voxel points in the tomography experiment stack, the voxel size is 0.009 mm. And the element size of fiber is 0.3 mm in the ABAQUS® model, thus a modeled single fiber consists of about 50 points (elements).

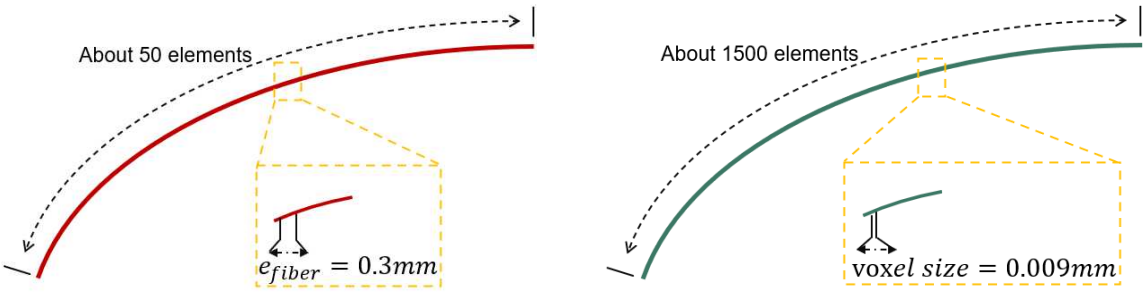

(a) (b)

Figure 6.2 Principle of individual fiber elements in experiment and simulation model. (a) Simulation, (b) Experiment.

In order to compare the microstructure indicators of fiber bundle, it's important to keep the points number of simulation consistent with the results of the tomography experiments ones. It might have been possible to use only the 50 simulation points, but, it would have been a shame not to consider all the information given by the pictures. Thus, the post-treatment of the Abaqus configuration will be submitted to an interpolation in order to solve this problem, as shown in Figure 6.3, where the **Interpolated point number by MATLAB programmer + simulation points number = tomography points number**.

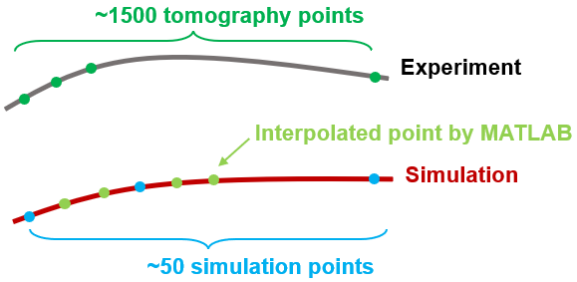

Figure 6.3 Interpolate points into the simulated fibers.

The interpolated points then represent at the initial step and during loading the position the intermediate points would have without the linearization imposed by B31 elements, which is very interesting as matter of comparison with the real microstructure.

6.2 Creation of the micro-structure indicator tools

6.2.1 Fiber position error

The goal of this long tuning step for the virtual fiber bundle estimator is to determine the most efficient strategies in order to obtain the compaction behavior as consistent as possible with the experimental results. The error requires then to be quantified. The absolute distance between

the simulated and real position of a fiber is an obvious but not so interesting information. Indeed, the latter has to be considered relatively to the fiber displacement, size and even to its possible movements (a fiber that is strongly kinematically constrained will be subjected to less errors). As consequence, the Figure 6.4 show 4 error proposed indicators to quantify the fiber position between simulation and experiment:

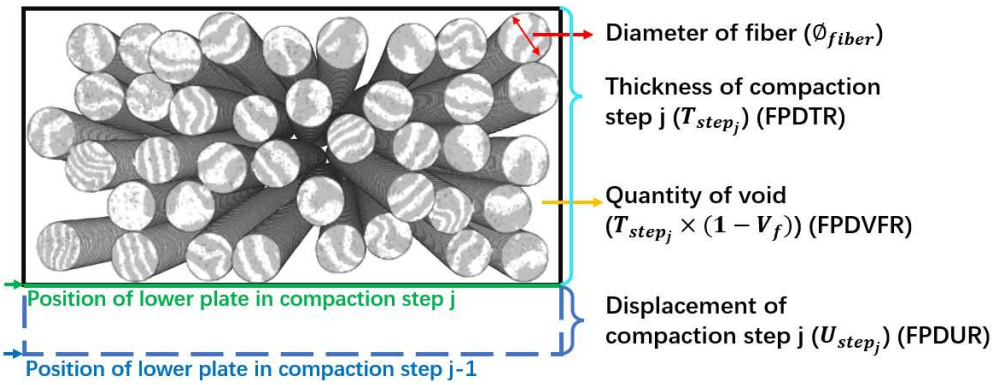

Figure 6.4 Indicators used to represent fiber position errors in experimental and simulation results.

a) According to thickness of fiber bundle

Fiber Position Deviation Thickness Ratio (FPDTR) which measures the ratio of the average deviation of the fiber position to the fiber bundle thickness in simulations and experiments:

$$\overline{FPDTR_{iJ}} = \frac{d_{fiber_i}}{T_{step_j}} \tag{6.1}$$

Where the $\overline{FPDTR_{iJ}}$ is the *FPDTR* for a single fiber i in the compaction step j.

$$\overline{FPDTR_J} = \frac{\sum_{i=1}^{i=N} \overline{FPDTR_{iJ}}}{N} \tag{6.2}$$

$$\sigma_{FPDTR_j} = \sqrt{\frac{\sum_{i=1}^{i=N} (\overline{FPDTR_{iJ}} - \overline{FPDTR_J})^2}{N}} \tag{6.3}$$

$\overline{FPDTR_J}$ and σ_{FPDTR_j} are the average value and standard value of the *FPDTR* for the total fiber (number N) in the compaction step j.

d_{fiber_i} is the average distance between simulation and experimental fiber position for fiber i, T_{step_j} is the thickness in the compaction step j of the fiber bundle.

b) According to quantity of void of fiber bundle

Fiber Position Deviation Volume-Fraction Ratio (FPDVFR). This indicator considers the average distance of the position of fiber between the experiment and simulation relative to the

quantity of voids in the fiber bundle.

$$\overline{FPDVFR_i} = \frac{d_{fiber_i}}{T_{step_j} \times (1 - V_f)} \tag{6.4}$$

Where the $\overline{FPDVFR_{ij}}$ is the *FPDVFR* for the single fiber i in the compaction step j.

$$\overline{FPDVFR_j} = \frac{\sum_{i=1}^{i=N} \overline{FPDVFR_{ij}}}{N} \tag{6.5}$$

$$\sigma_{FPDVFR_j} = \sqrt{\frac{\sum_{i=1}^{i=N} (\overline{FPDVFR_{ij}} - \overline{FPDVFR_j})^2}{N}} \tag{6.6}$$

Where the V_f is the volume fraction of the fiber bundle. $\overline{FPDVFR_j}$ and σ_{FPDVFR_j} are average value and standard value of the *FPDTR* for the total fiber (number N) in the compaction step j.

Fiber Position Deviation Diameter Ratio (FPDDR) is the ratio of the average of the fiber position distance relative to the fiber diameter in the experiments and simulations.

c) According to the fiber diameter

$$\overline{FPDDR_i} = \frac{d_{fiber_i}}{\emptyset_{fiber}} \tag{6.7}$$

Where the $\overline{FPDDR_{ij}}$ is the *FPDDR* for the single fiber i in the compaction step j.

$$\overline{FPDDR_j} = \frac{\sum_{i=1}^{i=N} \overline{FPDDR_{ij}}}{N} \tag{6.8}$$

$$\sigma_{FPDDR_j} = \sqrt{\frac{\sum_{i=1}^{i=N} (\overline{FPDDR_{ij}} - \overline{FPDDR_j})^2}{N}} \tag{6.9}$$

Where the $\emptyset_{fiber}$ is the diameter of fiber.

d) According to the compaction displacement

$$\overline{FPDUR_{ij}} = \frac{d_{fiber_i}}{U_{step_j}} \tag{6.10}$$

Where the U_{step_j} is the displacement of compaction j, $\overline{FPDUR_{ij}}$ is the *FPDUR* for the single fiber i in the compaction step j.

$$\overline{FPDUR_j} = \frac{\sum_{i=1}^{i=N} \overline{FPDUR_{ij}}}{N} \tag{6.11}$$

$$\sigma_{FPDUR_j} = \sqrt{\frac{\sum_{i=1}^{i=N} (\overline{FPDUR_{ij}} - \overline{FPDUR_j})^2}{N}} \tag{6.12}$$

These four indicators have been implemented so as to be automatically calculated for any

compaction level.

6.2.2 Contact

According to what was mentioned in the previous sections (section 4 and 5), the basic aspect of the reconstruction process of a fiber bundle is the extraction of the fiber cross-section from the tomographic image. Here the fibers are treated as regular circles. Therefore, the contact between the numerically reconstructed fiber bundles might deviate a little from the actual.

As discussed in the bibliography chapter, the contact forces transmitted by the contact points between the fibers significantly affect the compaction behavior, thus the fiber motion. Here, the different cases we have to face up to, are discussed in Figure 6.5. The contact is tackled considering two fibers in the same slice. Let's remember that the fiber section was detected as a regular circle by MATLAB with different radius.

The contact detected by program can be divided into two cases, for each one, the center shift might lead to an inconsistent determination of the contact reality.

(a) The two fibers are in contact in the real situation.

1. If the center position is not on the pixel coordinate point, the circle's center position will be shifted, causing the two circles to separate (case (a.1)) or intersect (case (a.2)), which leads to an inconsistency of the contact determination.
2. If the circle center position is on the pixel coordinate point, the circle center position does not shift and the circle center position remains unchanged (case (a.3)), the contact is correctly modeled.

(b) The two fibers are not in contact in the real situation.

After defining the circle and the center point, the two circles might contact after the circle center is shifted (case (b.1)).

Since the circle center will be offset to the nearest pixel, the deviation of the circle center position is $0 < \varepsilon_1 \leqq 0.5$ pixel and the deviation of the contact is $0 < \varepsilon_2 \leqq 1$ pixel. Therefore, when determining whether the two fibers are in contact, the distance between the fiber centroids being d_{ij}, if $\emptyset \leqq d_{ij} < \emptyset + 1$ pixel, then it means that fiber i and fiber j in that slice are considered in contact. Only if the real distance between the two fibers is less than one pixel and the centers aligned with a pixel, this might lead to a wrong detection of the contact. But this case is rare enough to be neglected, and in the few happening cases, will be regularized considering the previous and next slice (see next).

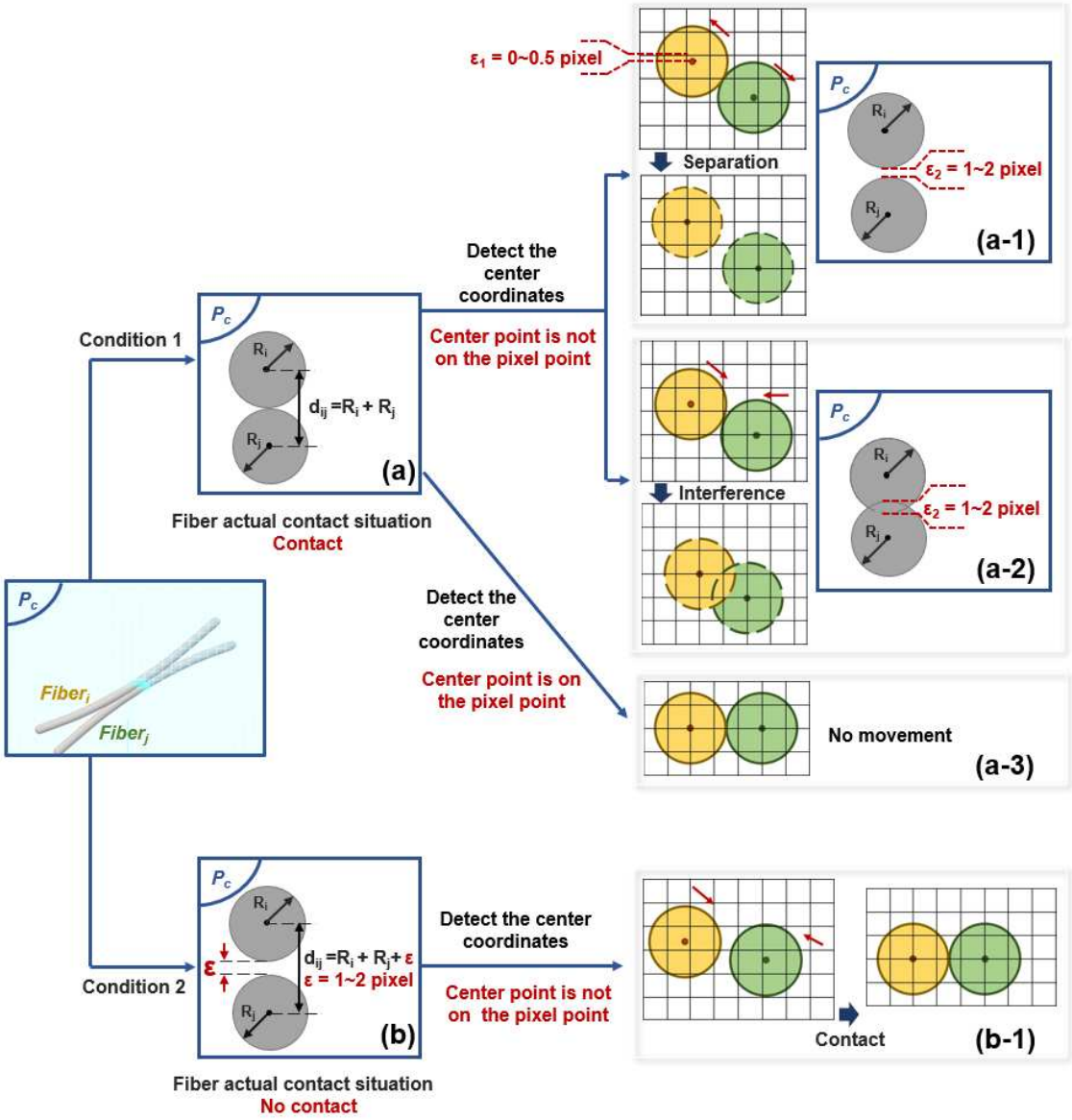

Figure 6.5 Principles of contact analysis.

a) Contact times in the model – "continuous" contact

As previously mentioned, the contact points transmit the stresses that affect the compaction behavior of the fiber bundle. So, it's important to localize accurately the contacts.

In the contact times calculation, the contact points of all fibers in each slice are considered. However, due to the errors discussed previously, the contact between the fibers detected by MATLAB might be different from real one. Here, the contacts in the Figure 6.5 are classified, the case (a-1): there is actually contact between fibers, but it is lost, define it as "lost-contact"; case (a-2, 3): it actually agrees with the real contact determined by MATLAB, defined as "correct-contact"; case (b-1): there is actually no contact, but it is determined to be contact,

defined as “incorrect-contact”.

Identifying and quantifying a continuous contact between two fibers is not obvious, because it requires to determine how many individual slices of a fiber are in contact as one continuous contact. For example, two individual continuous contacts may be incorrectly considered as one continuous contact.

A simplification of the contact model for two fibers is shown in Figure 6.6; Fiber (i) and Fiber (j) are in contact in space, and there are 2 times continuous real contact, however, this could be detected as 6 real continuous contacts by MATLAB.

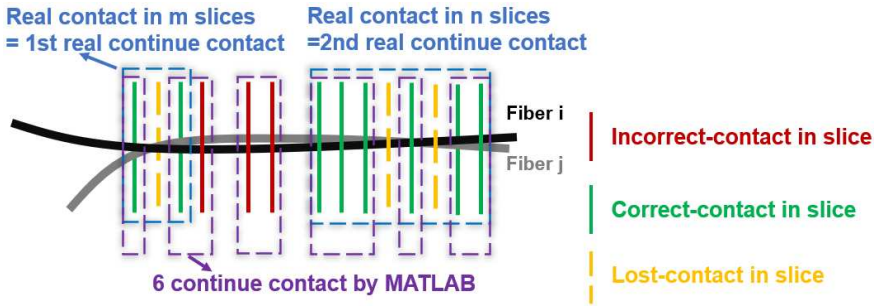

Figure 6.6 Simplified model of the number of contacts between the two fibers.

Thus, contact between fibers will be described by the number of contacts between fibers in each slice, this “contact number”, which describes the trend of the contact points between the fibers during the compaction process.

b) Contact angle in the fiber section and fiber length direction

As shown in Figure 6.7, the contact angle is presented in two aspects, the contact angle between the fiber cross sections (θ), and the contact angle between the fiber length directions (γ). During compaction of the fiber bundle, the contact angle between the fibers also changes when the number of contacts between the fibers is increased. In these two hypothetical cases of compaction of fiber bundles, the fibers transmit contact forces to each other and α changes as the fibers move. Also, after a certain amount of contact is reached, the fibers deform, causing them to continue to move and (γ) to change. Thus, the contact angles are also interesting descriptors of the microstructure since they are of a main importance in the load transmission, α for instance plays major role in the relationship between compaction and transverse load.

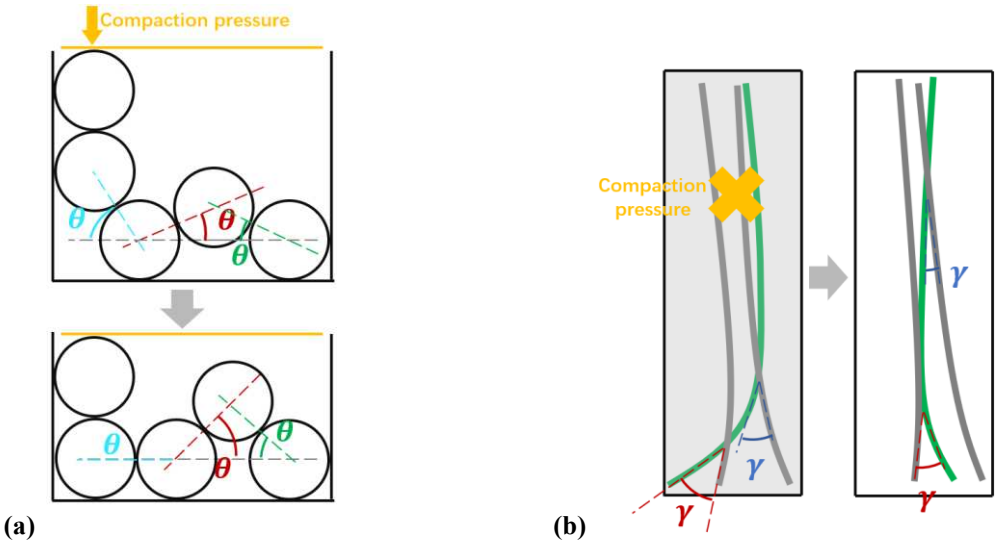

Figure 6.7 Principle of contact angle in fiber bundle. (a) Contact angle between each two fibers in the section (θ), (b) Contact angle between each two fibers in the fiber length direction (γ).

For the contact angle θ of the fiber cross-section (in the slice), there are three cases (Figure 6.8 (c)), acute (case1), obtuse (case2), and negative (case3). In case 2, when the detected angle is obtuse, it is calculated to an acute angle. In case three, when the detected pinch angle is negative, it is converted to positive. At the time of detection, it is not possible to determine which fiber cross-section serves as the vertex of the θ-angle, and the probability of these three cases occurring is not discussable. Therefore, in the α calculation, the detected values are converted to positive acute angles. This avoids the deviation of the mean value due to the occurrence of these three cases in the detection of the θ-angle. Similarly, the angle γ in the direction of the fiber length is always keep positive acute.

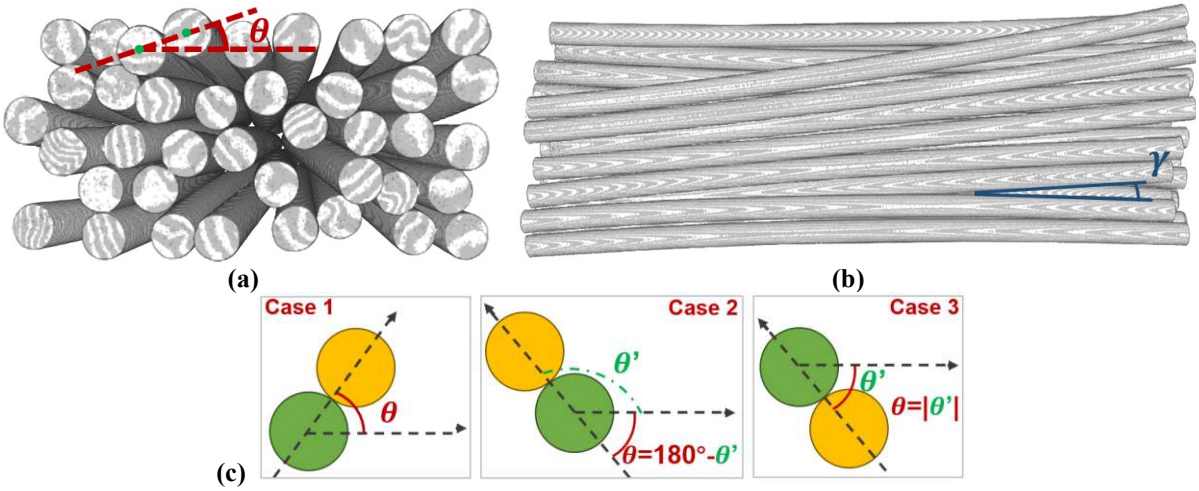

Figure 6.8 Contact angle in the fiber section and fiber length direction. (a) Contact angle in the fiber section, (b) contact angle in the fiber length direction.

6.2.3 Undulation of fibers

Compaction changes the microstructure of the fiber bundle, not only in terms of contact between fibers but also in terms of fiber curvature. Indeed, the bending compliance enables the fibers to fill in local gaps, and to follow 3D trajectory. On the opposite, the in-plane bending tends to increase the entanglement increasing the overall compaction stiffness.

The global undulation of fiber bundles will here be measured using the commonly used crimp of the projected curve in XZ and YZ plane. Discussion of the variation of fiber curvature in the XZ and YZ planes indeed helps to analyze the effect of compaction on the microstructure of the fibers in the horizontal and vertical directions. In addition, the orientation tensor of the fibers allows the analysis of the distribution of the fibers in space.

a) Crimp

In this case, the crimp of a single fiber is discussed. The crimp of single fiber is considered as the degree to which the non-straight fibers deviate from linearity:

$$Crimp\ (\%) = \frac{L_c - L_0}{L_0} \times 100\%$$

Where L_0 is the single fiber length in fiber bundle, L_c is the length of fiber in straighten form (Figure 6.9).

It has to be noticed that it is a global indicator that does not account of the curvature distribution along the fiber. Many different configurations lead to the same crimp.

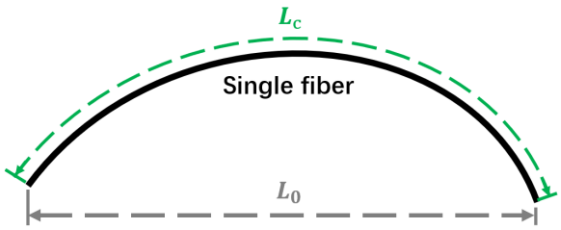

Figure 6.9 The principle of crimp of a single fiber.

b) Projected curvature of single fiber

Figure 6.10 shows the principle of analyze projected curvature of single fiber. The projected curvature of a single fiber in the fiber length direction in the XZ plane as well as in the YZ plane is discussed here to analyze the change in fiber tortuosity in both directions during fiber compaction.

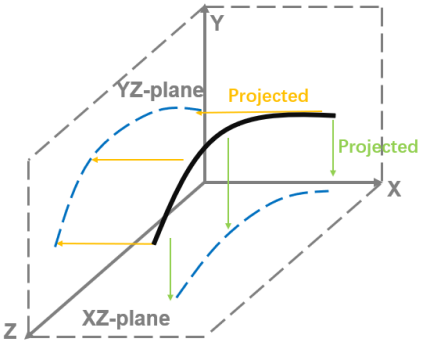

Figure 6.10 Principle of the projected curvature of a single fiber in the XZ-plane and YZ-plane.

6.2.4 Fiber orientation

a) Fiber mis-orientation distribution

Rovings considered in this thesis are supposed to be a network of quasi parallel fibers, which means not strictly parallel, this is one of the main difficulties when dealing with rovings because fibers are neither randomly nor periodically organized. The fiber misalignment has then to be tracked for a consistent characterization of the bundle microstructure. In addition, it might also have a significant influence on the compaction behavior.

The fiber orientation distribution in a fibers bundle microstructure is performed by computing the angle α and β, which measure misorientation of single fiber relative to the global Z-axis and Y-axis. As shown in Figure 6.11, to simplify this calculation, the fiber is considered as a straight line that connect the benign point (point B) and the end point (point E) of the fiber.

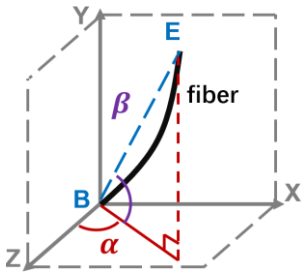

Figure 6.11 Single fiber orientation distribution of mis-orientation.

b) Fiber orientation tensor

The orientation vectors describe the orientation distribution properties of the fibers in a fiber bundle. The Second-order orientation tensor can be used to quantify the orientation distribution of fibers, i.e $\boldsymbol{A_j}$:

$$\boldsymbol{A_j} = \frac{1}{N}\sum_{i=1}^{N} \bar{\boldsymbol{q}}_i \otimes \bar{\boldsymbol{q}}_i \tag{6.13}$$

Where $\bar{\boldsymbol{q}}_i$ is the orientation tensor of single fiber i in the compaction step j.

This section presented all the indicators implemented for the description of the microstructure. They have been coded so as to be useable and automatically computed both for the analyses of experimental and simulation results. Each of them brings a different point of view and will be helpful for the understanding of the reorganization of the fibers within a bundle during compaction.

The following table serves as a summary of indicator tools:

Analyze Tools of Microstructure of fiber bundle for experiment and simulation			
Analyze the errors between experiment and simulation of fiber position		Fiber Position Deviation Thickness Ratio (FPDTR)	Measures the ratio of the average deviation of the fiber position to the fiber bundle thickness in simulations and experiments
		Fiber Position Deviation Volume-Fraction Ratio (FPDVFR)	Takes into account the average distance of the position of fiber between the experiment and simulation relative to the quantity of voids in the fiber bundle.
		Fiber Position Deviation Diameter Ratio (FPDDR)	The ratio of the average of the fiber position distance relative to the fiber diameter in the experiments and simulations
		Fiber Position Deviation Displacement Ratio (FPDUR)	The ratio of the average of the fiber position distance relative to the compaction displacement in the experiments and simulations
Contact	Contact number	Contact number between fibers	
		Contact between fibers and compaction channel	
	Contact angle between fibers	Contact angle between fibers in the cross section of the fiber $(\theta)(°)$	
		Contact angle between fibers in the fiber length direction $(\gamma)(°)$	
Undulation	Crimp		
	Curvature	Projected curvature of fiber in XZ and YZ plane	
Fiber orientation	Orientation tensor		
	Mis-orientation of fiber		

6.3 Analysis the micro-structure of the fiber bundle geometries

Previously, section 4 presented the procedures and results of tomography combined with micro-compaction experiments, and section 5 described the fiber bundle reconstruction method and the improvement of the simulation strategy. For the sample 2, 3, which are performed by micro-compaction experiments, reconstruction of fiber bundle tomography images, then the microstructural analysis of fiber bundles will be analyzed here. These fiber bundle samples containing 40 fibers (fiber diameter = 500 μm, length $\approx$ 14-15 mm). The XCT spatial resolution of these 2 samples is 9 $\mu m/voxel$. Due to a different fibers initial organization during the manufacturing step, the initial fiber volume fraction differs between the tree samples especially for sample 2 (50.5 % of sample 2, 37.9 % and 38.9 % of samples 0 and 3).

This thesis also performed fiber bundle numerical model reconstruction, and compaction simulations on a fiber bundles composed of the same polyester fibers initially used to demonstrate the feasibility of the strategy in a previous thesis (sample 0) (39 fibers, dimensional diameter = 500 μm, length $\approx$ 15 mm) (Haji et al., 2023; Haji Oussama, 2018). The tomography and micro-compaction machine was provided by 3SR laboratory in Grenoble University, the XCT spatial resolution = 15 $\mu m/voxel$, compaction speed is 0.08 mm/s. Here, the same microstructural analysis is performed for this sample 0.

6.3.1 Impose gravity to fiber bundle geometries

The mentioned approximation and inaccuracy of numerical geometry generation lead to an increase in the accumulation of small errors in the position of the fibers compared to the actual. The fiber bundle which is, in actual fact, in a static equilibrium, is at the beginning of the simulation in an unstable state. Indeed, the initial fiber's section penetrated a little before calculation or miss the point of contact that exists in the real bundle geometry. After the introducing of the gravity force, the fibers move towards each other until their contact are each an equilibrium. The first gravity step in then very useful to bring back the sample to the static equilibrium but above all is a very good indicator of the quality of the modeling: the less the fibers move during this step, the most accurate the bundle reconstruction is. And the "initial contact stability check" process for the each initial reconstruction fiber bundle model (sample). The spatial resolution used during the XCT is actually one of the main parameters to be considered since it enables a more or less description of the fibers section and position. A lower spatial resolution may result in the loss of surface details of the fibers, especially in the contact

region between the fibers. Inaccuracies in the contact analysis will enlarge the loss of details introduced by resolution limitations, leading to even more inaccurate predictions of the structure of the fiber bundle after simulation. The superposition of such errors during compaction simulations may lead to systematic errors in the prediction of compaction behavior of the fiber bundle.

The effect of the gravity field in the fiber bundles is considered here to consider whether the contact points of the bundles are stable or not. As introduced previously, under the effect of the gravitational field, the inaccurate contact between the fibers leads to a slight slippage of the fibers due to their own gravity. This micro-adjustment of the internal structure of the fiber bundle leads to a statically equilibrated structure.

The geometries of sample 0, 2, 3 is reconstructed and performed gravity with ABAQUS®, firstly. The simulation parameters were validated with section 5.2 in this thesis and Haji's work (Haji Oussama, 2018), shown in Table 6.1.

Table 6.1 Computational parameters of the gravity simulation of fiber bundle sample 0, 2, 3.

Young's Module (E)	6 Gpa	**Beam element size (L_b)**	0.3
Poisson ratio (γ)	0.25	**Discrete rigid element size (L_d)**	0.2
Density (ρ)	1.38e-09 T/mm^3	**Coefficient of friction (μ)**	0.2

After the gravity imposed to fiber bundle geometry, the centerline of fiber bundle sample 0, 2, 3 shown in Figure 6.12.

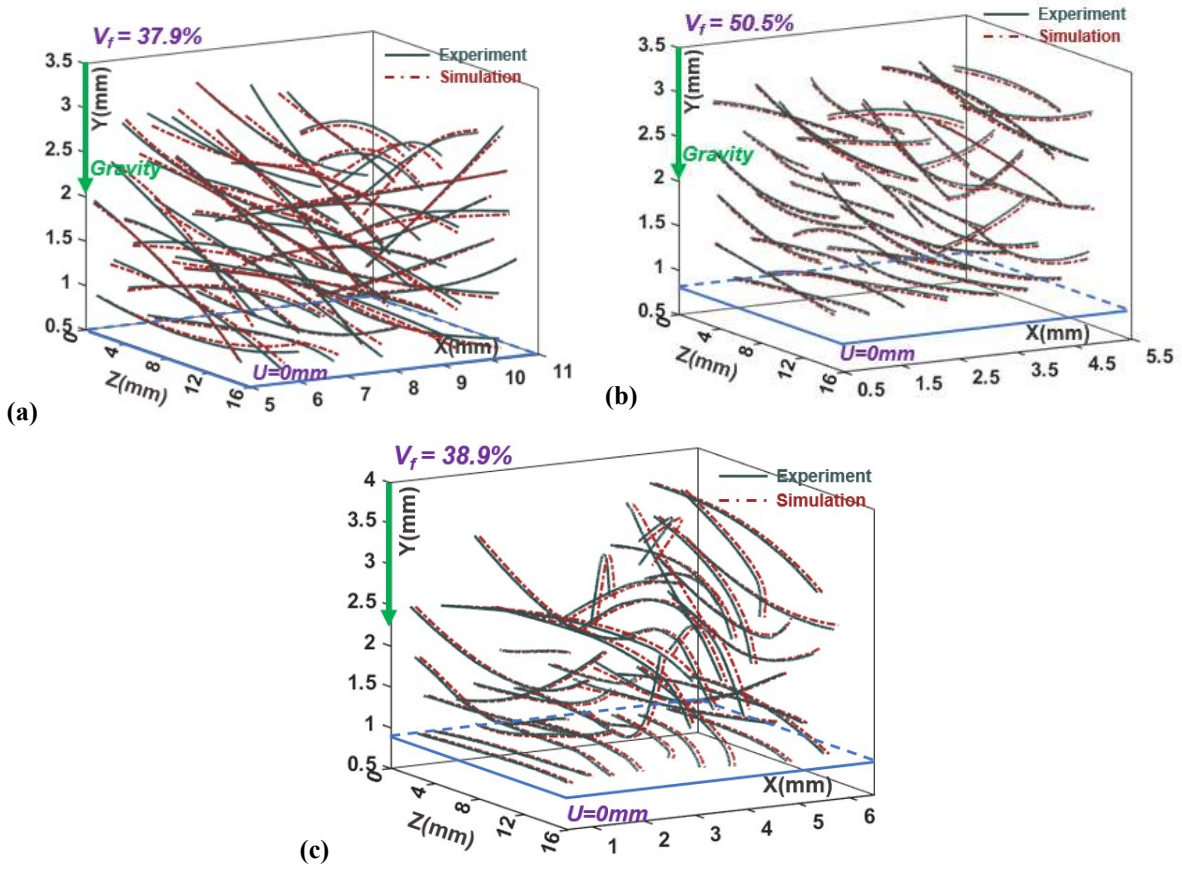

Figure 6.12 The centerline of fiber bundle after imposing the gravity field. (a) Sample 0 (Dr. Haji's sample), (b) Sample 2, (c) Sample 3.

The fibers displacements (d_{fiber_i}: the distance between simulation and experiment for fiber i) between gravity simulation and initial experiment geometry were quantified using the indicators developed previously (the description of this indicators shown in section 6.2). This shows clearly the influence of the voxel size but also that the initial modeling obtained for sample 2 and 3 is accurate since very small changes and the indicators are observed.

Table 6.2 The position errors of fibers between experiment and simulation.

	Sample 0		**Sample 2**		**Sample 3**	
Spatial resolution (μm)	**15**		**9**		**9**	
Diameter of fibers ($\emptyset_{fiber}$) (mm)	**0.5**					
Thickness of fiber bundle (mm)	**3**		**3**		**3.24**	
Indicators (%)	μ	σ	μ	σ	μ	σ
FPDTR (according to the thickness of fiber bundle)	2.66	0.92	0.86	0.26	1.28	0.40
FPDVFR (according to the V_f)	4.25	1.47	1.75	0.40	2.09	0.62
FPDDR (according to the diameter of fiber)	15.83	5.50	5.20	1.20	8.30	2.45

6.3.2 Analyze of the sample's microstructure

In the section 6.2, the microstructure indicators tools are developed, these tools could be used to analyze the orientation, contact between fibers, curvature of fibers after compaction test. The compaction experiments were performed for sample 0, 2, 3, and the compaction pressure function in volume fraction shown in Figure 6.13.

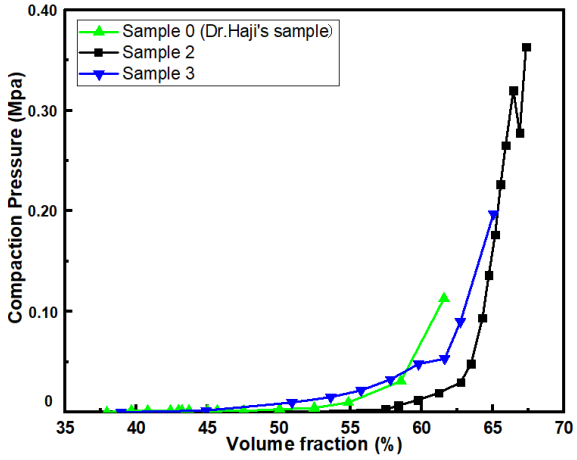

Figure 6.13 Compaction pressure function in volume fraction for sample 0, 2, 3.

The analysis of the internal structure of fibers by the orientation tensor of the fibers is able to quantitatively describe the orientation distribution of the fibers and provides a mathematical tool for understanding the mechanical behavior of fiber bundles. This approach can reveal the uniformity and orientation of the fiber arrangement.

a) Orientation and mis-orientation

The orientation unit spheres and orientation tensor A_{33} of the sample 0, 2, 3 shown in Figure 6.14 and Figure 6.15, respectively. A_{33} reflects the orientation intensity of the fibers in the $\boldsymbol{e_3}$ direction in the orientation unit spheres. The A_{33} is closer to 1.000, it means that the distribution of fibers in the plane perpendicular (XY plane/$\boldsymbol{e_1 e_2}$ plane) to the fiber length (Z-axis/$\boldsymbol{e_3}$) is more ordered and denser so that the unit orientation tensor distribution closer to $\boldsymbol{e_3}$. Here since rovings are targeted, in the three cases the privileged $\boldsymbol{e_3}$ orientation of the fibers is noticed.

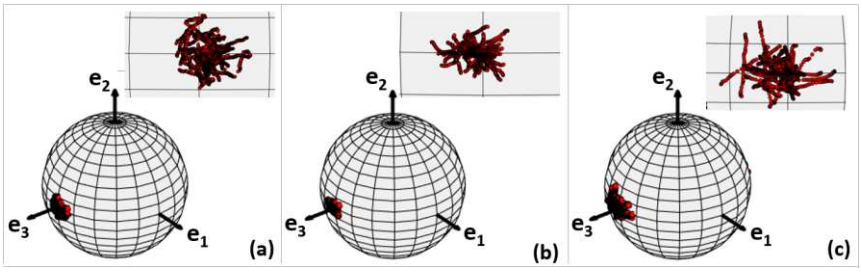

Figure 6.14 The orientation unit spheres of sample 0, 2,3.

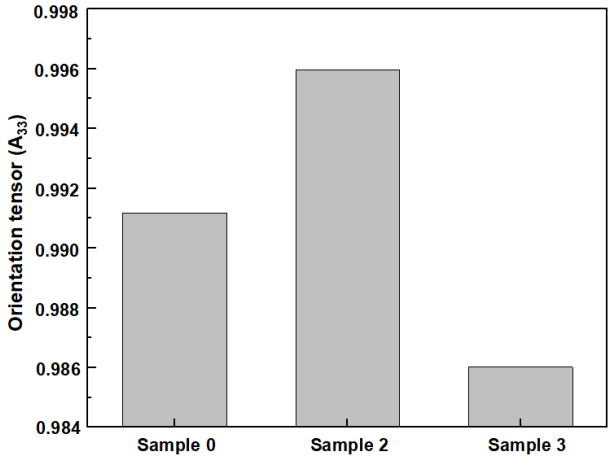

Figure 6.15 The orientation tensor A_{33} of sample 0, 2, 3.

In addition, the mis-orientation degree of fibers offset direction from Z-axis/$\boldsymbol{e_3}$ were analyzed here, to understand the global orientation of fibers. The mis-orientation indiacotors show the begin-end of fiber offset direction from Z-axis/$\boldsymbol{e_3}$, as described in section 5. The global orientation of fibers offest from Z-axis to X-axis named α, and offest from Z-axis to Y-axis named β. The boxplot of mis-orientation degree of fibers offset direction from Z-axis/$\boldsymbol{e_3}$ shown in Figure 6.16, the "Box-Normal Plot" is used to represent the average value μ, standard value σ, the normal distribution of data, and the data, shown in Figure 6.16. The α of sample 0, sample 2, and sample 3 are distributed in [-5,11] (°), [-8,2] (°), and [-15,8] (°), respectively. It indicates that samples 0 and 3 have a large offset angle from the Z-axis to the X-axis, which means that the fibers are crossing each other. The β of sample 0, sample 2, and sample 3 are distributed in [-7,8] (°), [-5,2] (°), and [-5,7] (°), respectively. For samples 0 and 3 (V_f=37.9 % and 38.9 %), the initial volume fraction was low compared to sample 2 (V_f=50.5 %). Combined with the centerlines of the fibers Figure 6.12 and the 3D reconstructed figure of the fiber bundle samples (sample 0: Figure 6.23, sample 2: Figure 6.26, sample 3: Figure 6.34), the initial positions of the different samples are random and different. Higher volume fractions/densities, indicate that the fibers in the fiber bundle have smaller gaps between each other, and exhibit a

tighter and more ordered arrangement. This ordination is mainly shown in the arrangement of the fibers along the Z-axis direction.

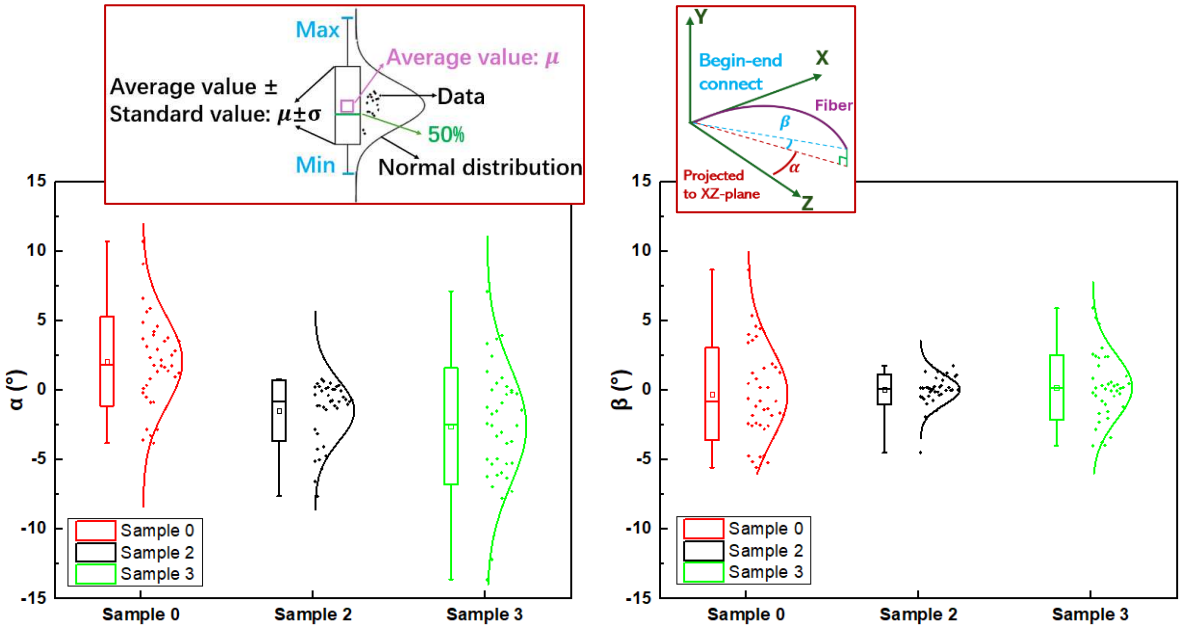

Figure 6.16 The boxplot of mis-orientation angle of fibers for sample 0, 2, 3. (a) α, (b) β (°).

b) Contact

The contact principle between fibers is discussed in section 6.2. The contact number between the fibers, contact number between fibers and plates, total contact number of sample 0, sample 2 and sample 3 shown in Figure 6.17. The fibers in the higher V_{f_0} of fiber bundles (sample 2) are closer to each other, therefore, the number of contacts between the fibers is high compared to samples 0 and 3.

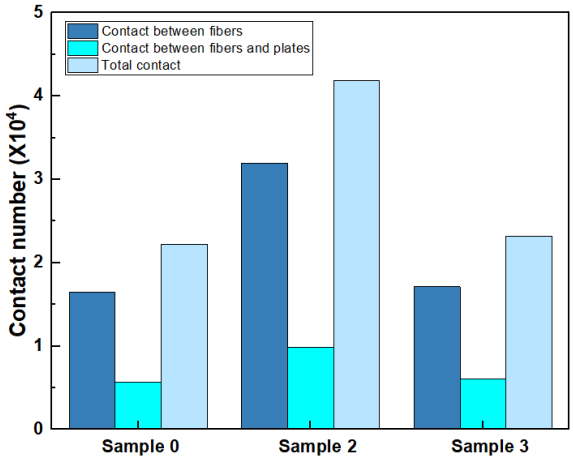

Figure 6.17 Contact number of sample 0, 2, 3.

The contact angle between fibers in fiber's section is θ and the contact angle between fibers in fiber's length direction is γ. The distribution of θ and the Boxplot of γ for sample 0, sample 2 and sample 3 are depicted in Figure 6.18 (a) and (b), respectively, and the average (μ) and standard value (σ) of γ are presented in Table 6.3. From Figure 6.18, the distribution value of θ and γ of sample 0 and sample 3 is larger, the larger contact angles usually reflect the presence of larger spaces between the fibers, implying that the fibers are in less contact with each other, and the alignment of fibers deviate more from the Z-axis direction than for sample 2.

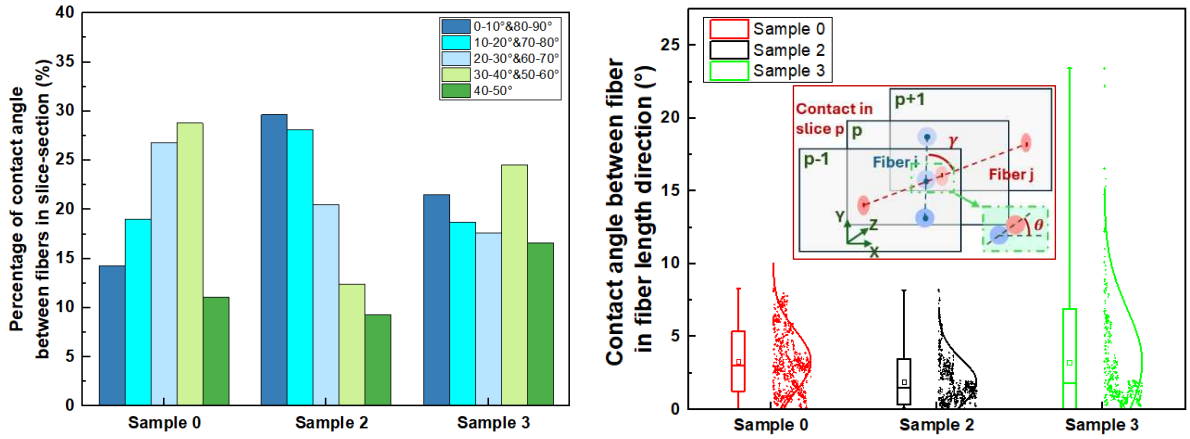

Figure 6.18 The contact angle between fibers. (a) in the fiber section (θ), (b) in the fiber length direction (γ) (°).

Table 6.3 The contact angle between fibers in fiber length direction of sample 0, 2, 3 (γ) (°).

	Sample 0		Sample 2		Sample 3	
	μ	σ	μ	σ	μ	σ
γ (°)	3.88	2.05	2.79	1.02	4.11	3.23

c) Crimp and curvature

The crimp describes the wavy or curved character of the fiber. The Boxplot of sample 0, sample 2 and sample 3 shown in Figure 6.19, and the μ, σ of crimp shown in Table 6.4. In addition, the Boxplot and μ, σ of projected curvature radius of these sample shown in Figure 6.20 and Table 6.5, respectively. The crimp and projected curvature of sample 3, shown the fibers have a higher average crimp compared to the sample 0 and sample 2. It is also logical to notice that the sample 2 has the lowest average value and the narrowest distribution which is consistent with the straighter and better organization leading to the highest initial volume fraction in fiber bundles. The curvatures illustrate also the morphology of the fibers, indeed the highest values

for sample two shows straighter trajectory, consistently with realignment with the increase in the volume fraction. The differences between the sample 0 and 3 are reflecting the higher tortuosity the XZ plane.

Sample 3 has also the widest crimp distribution shown by the highest standard deviation. On the overall the two values indicate some fibers are widely curved and crimped in both planes (YZ and XZ), however, all the more in the XZ plane showing a stronger disorganization in this plane.

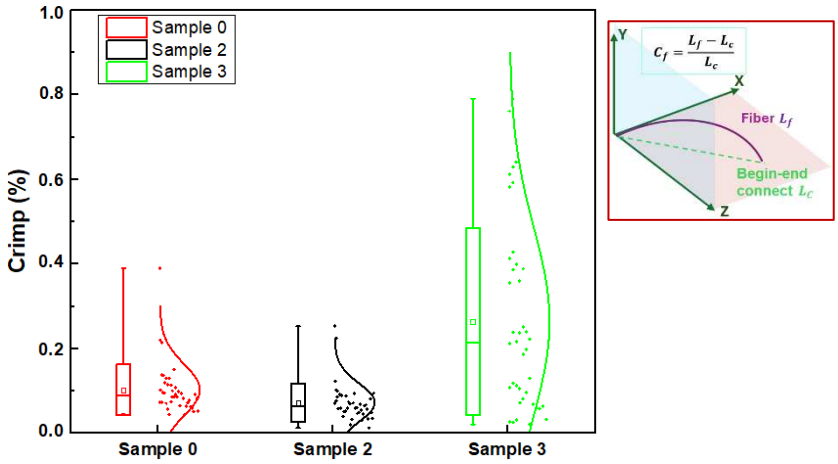

Figure 6.19 The boxplot of crimp for sample 0, 2, 3 (%).

Table 6.4 The crimp of sample 0, 2, 3 (%).

	Sample 0		Sample 2		Sample 3	
	μ	***σ***	***μ***	***σ***	***μ***	***σ***
Crimp (%)	0.110	0.061	0.072	0.045	0.264	0.191

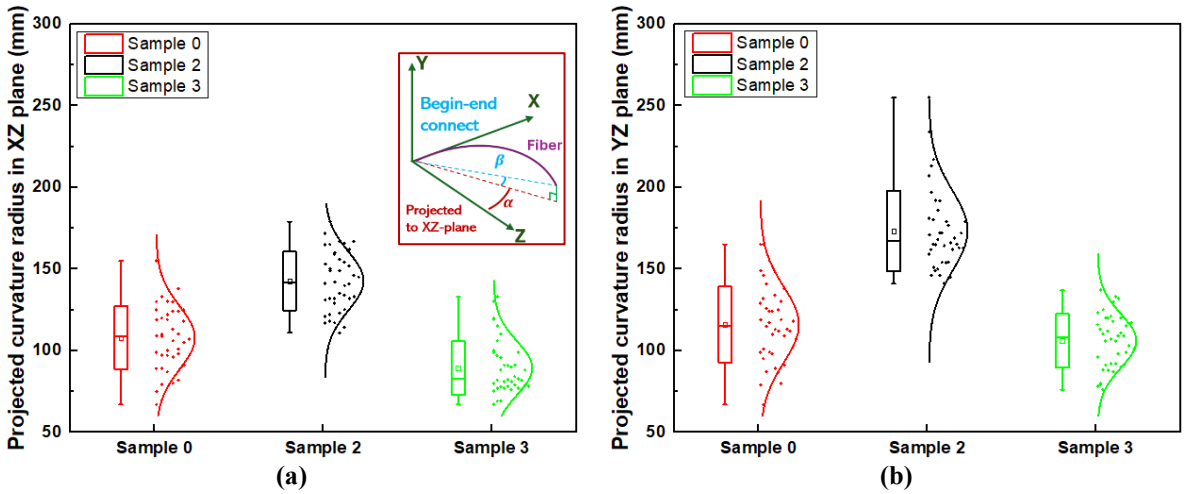

Figure 6.20 The boxplot of projected curvature radii (mm) of sample 0, 2, 3 (a) In XZ plane, (b) In YZ plane.

Table 6.5 The projected curvature radius of sample 0, 2, 3 (mm).

	Sample 0		Sample 2		Sample 3	
	μ	σ	μ	σ	μ	σ
In XZ plane (R_{XZ})	109	20	141	15	87	16
In YZ plane (R_{YZ})	118	23	174	19	111	13

6.3.3 Compaction simulation

The compaction simulation of sample 0, 2 and 3 were performed here, the simulation strategy is discussed in section 5.2.

a) Sample 0

The compaction pressure in function of volume fraction shown in Figure 6.21. The simulation and experimental results are compared. In addition, the fiber position and 3D morphology of fibers after experiment and simulation compaction also analyzed here. The centerline of sample 0 before and after compaction shown in Figure 6.22, and the Table 6.6 show the errors of fiber position between experiment and simulation according to thickness of fiber bundle (FPDTR), V_f (FPDVFR), the diameter of fiber (FPDDR), and the displacement of compaction plate (FPDUR). The consistency between the simulated and experimental values is interesting and acceptable. However, in step 9 of the compaction step of sample 0, the positional error of fibers between the simulated and experimental is large, and this error is due to the accumulation of initial errors in the fibers (discussed in section 6.1). During the compaction step of the fiber bundle, the fibers deform or move by transferring compaction force between them through the contact points. The accumulation of the initial error is finally displayed in the contact error between the fibers. However, as compaction proceeds (step 12, 13 and 14), the positional errors of the fibers in the simulation and experimental results gradually decrease. This is due to the fact that quasi-static compaction is a slow compaction process in which the movement and adjustment of the fibers is gradual, thus allowing the fibers to better adapt to the alignment of their neighboring fibers and the overall structure. For the initial model, the contact and force transfer between the fibers is less than optimal as the initial contact error of the fibers may be large. However, as the compaction process proceeds, the fibers tend to move to more stable positions as they are progressively subjected to forces, reducing the positional deviations due to initial errors.

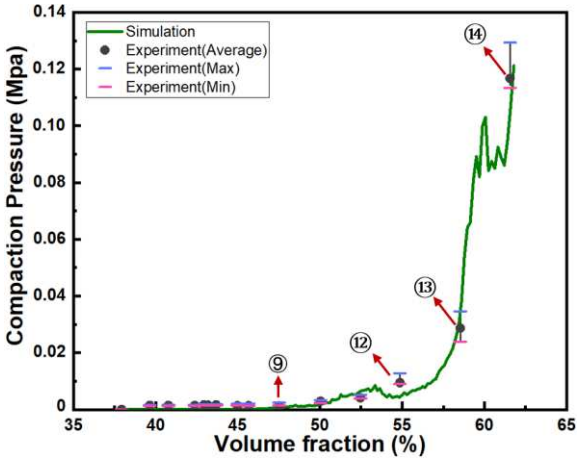

Figure 6.21 The compaction pressure function in volume fraction of sample 0.

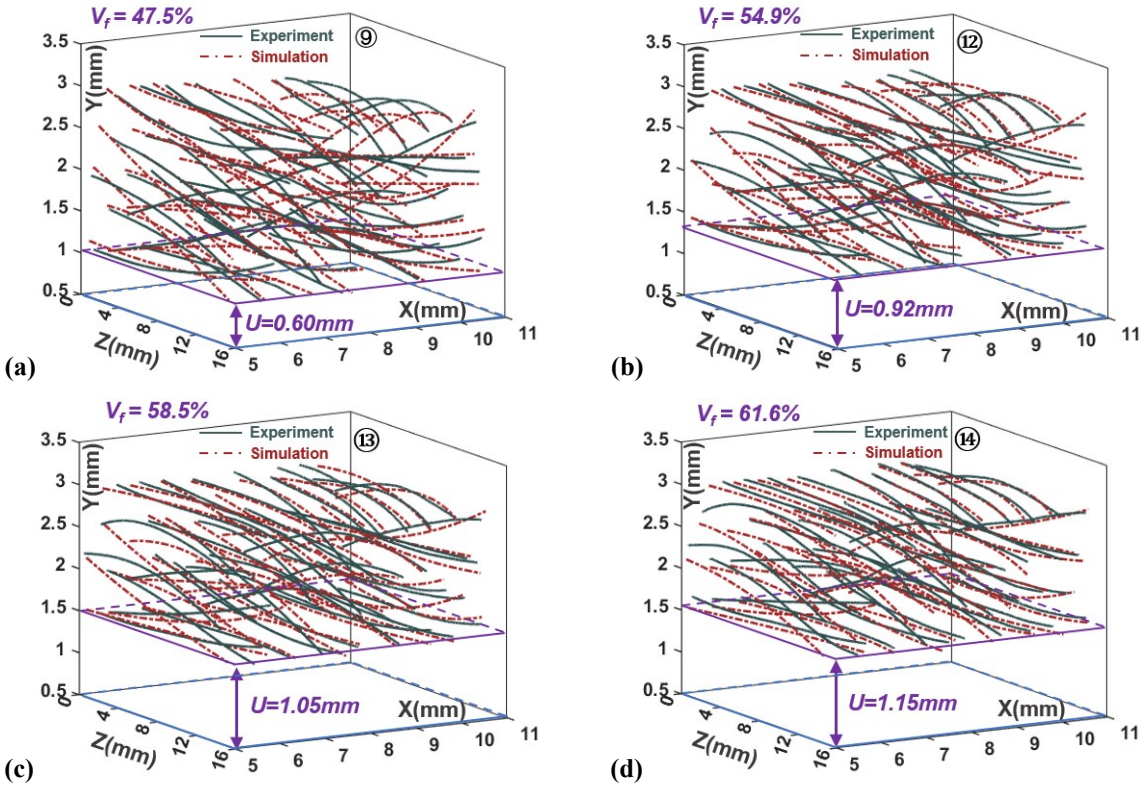

Figure 6.22 The centerline of sample 0 after simulation and experiment compaction. (a) Step 9, (b) Step 12, (c) Step 13, Step 14.

Table 6.6 The position errors of fibers between experiment and simulation of sample 0 for compaction step 9, 12, 13, 14.

Indicators (%)	Step 9		Step 12		Step 13		Step 14	
	μ	σ	μ	σ	μ	σ	μ	σ
FPDTR (according to the thickness of fiber bundle)	7.84	1.68	8.13	2.49	7.76	2.40	7.55	2.85
FPDVFR (according to the V_f)	13.67	2.94	15.99	4.42	16.33	5.05	16.79	6.42
FPDDR (according to the diameter of fiber)	37.66	8.09	33.80	9.35	30.26	9.36	27.95	10.56
FPDUR (according to the displacement of compaction plate)	31.38	6.73	18.37	5.08	14.41	4.46	12.15	2.59

The 3D rendering simulation numerical geometry and 3D experiment reconstrued geometries of sample 0 after compaction step shown in Figure 6.23, the fiber morphology of fibers after compaction is almost same. This sample 0 exhibit the importance of an accurate description of the initial geometry to be able to validate the proposed strategy.

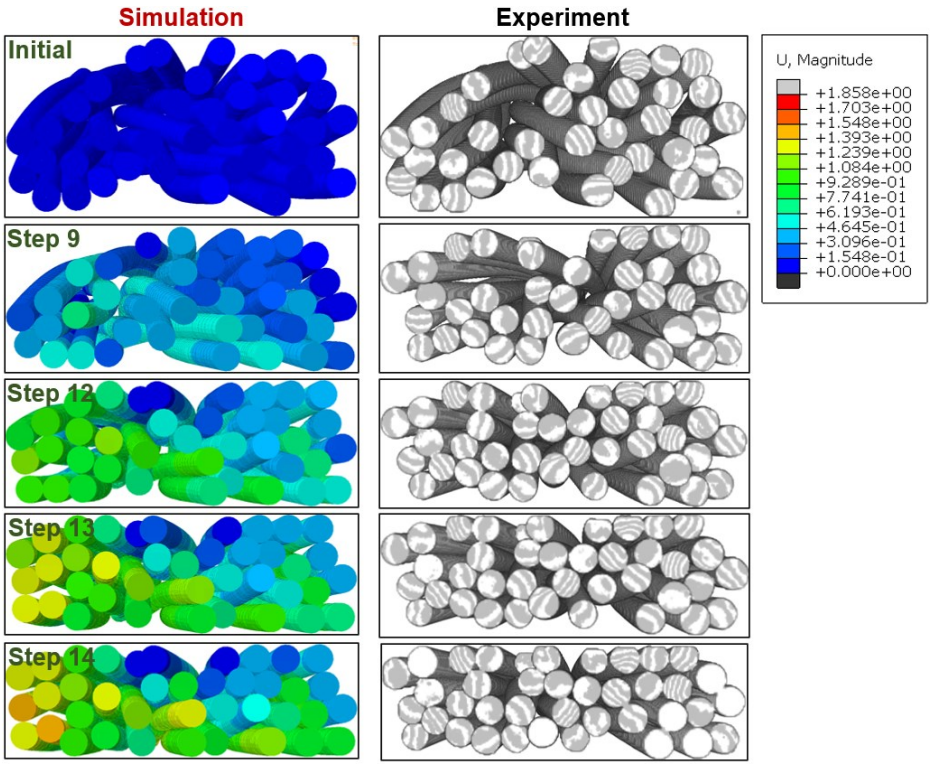

Figure 6.23 The 3D rendering geometry of sample 0 after compaction for step initial, 9, 12, 13, 14.

b) Sample 2

The Figure 6.24 (a) show the compaction pressure in function of volume fraction of sample 2 , and the strain, penalty and kinetic energy in the compaction process shown in Figure 6.24 (b).

The simulation curves are essentially in agreement with the experiment results. It is especially noticeable that the drop of the compaction curve at step 13 has been captured by the simulation which is a very good indicator for the consistency of the proposed strategy. In addition, as mentioned in the above section, it is also meaningful to analyze the simulation results through kinetic energy ($\mathbf{K_e}$), contact energy ($\mathbf{P_e}$), and deformation energy ($\mathbf{S_e}$). In contrast to the model in which fibers fall freely by gravity, in the compaction model the kinetic energy is not only that of the rearrangement of the fibers, but also that of the movement of the sample compaction channel. The contact energy contains the energy of the contact between the fibers and the contact between the fibers and the sample compaction channel. The strain energy contains only the deformation energy of the fibers, since the sample compaction channel is simulated as a rigid body in the model and does not undergo deformation.

At the initial stage of compaction ($V_f \in [50, 55]$ (%)), there is space for the fibers to move (initial volume fraction of 50.5%), so the deformation and contact energies of the model are about 10^{-5} times of kinetic energy. The number of contact points between the fibers and between the fibers and the rigid plate increase rapidly with the beginning of the compaction simulation, and the contact between the fibers increases and slight movement occurs due to slippage. The contact between the fibers and the rigid plate leads to a small deformation of the fibers, which can also be obtained through the energy curves, a rapid increase in the contact energy, with an increase in the kinetic energy and a low deformation energy at the beginning of the compaction. At V_f = 55 %, the energy of the model reaches almost the same level ($\mathbf{S_e}$=$\mathbf{K_e}$=$\mathbf{P_e}$), and the kinetic and contact energies increase significantly, indicating that the rigid movement of the fibers reaches a threshold, the contact points between the fibers increase, and deformation begins to occur. At $V_f \in [55, 62]$ (%), the contact energy is higher than the deformation energy of the model, which is due to the fact that the fibers, with the compaction experiments, undergo contact firstly, and then transfer compressive forces through the contact points thereby deforming the fibers. After V_f = 62 %, the energy of the model is dominated by the deformation energy of the fibers.

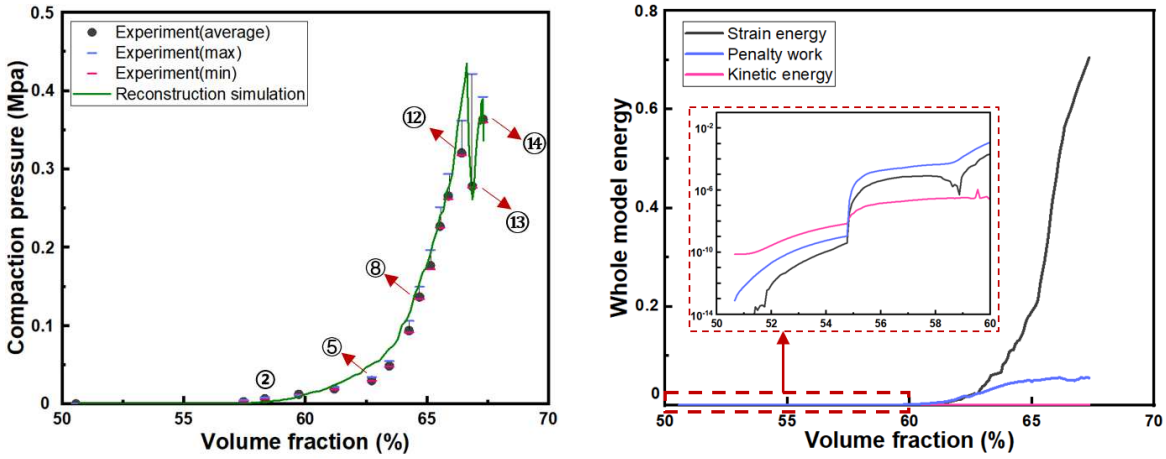

(a) (b)

Figure 6.24 The compaction simulation for sample 2. (a) The compaction pressure function in volume fraction. (b) The energy evolution during compaction.

The centerline of sample 2 before and after compaction shown in Figure 6.25, and the Table 6.7 show the errors of fiber position between experiment and simulation according to thickness of fiber bundle (FPDTR), V_f (FPDVFR), the diameter of fiber (FPDDR), and the displacement of compaction plate (FPDUR). From the centerline of the fibers, the fibers show the different positions between simulation and experiment, but, the position are closed. It is noticeable that, as expected the results are significantly regarding the microstructure than the ones of sample 0 thanks to a better resolution of the pictures and then definition of the initial microstructure.

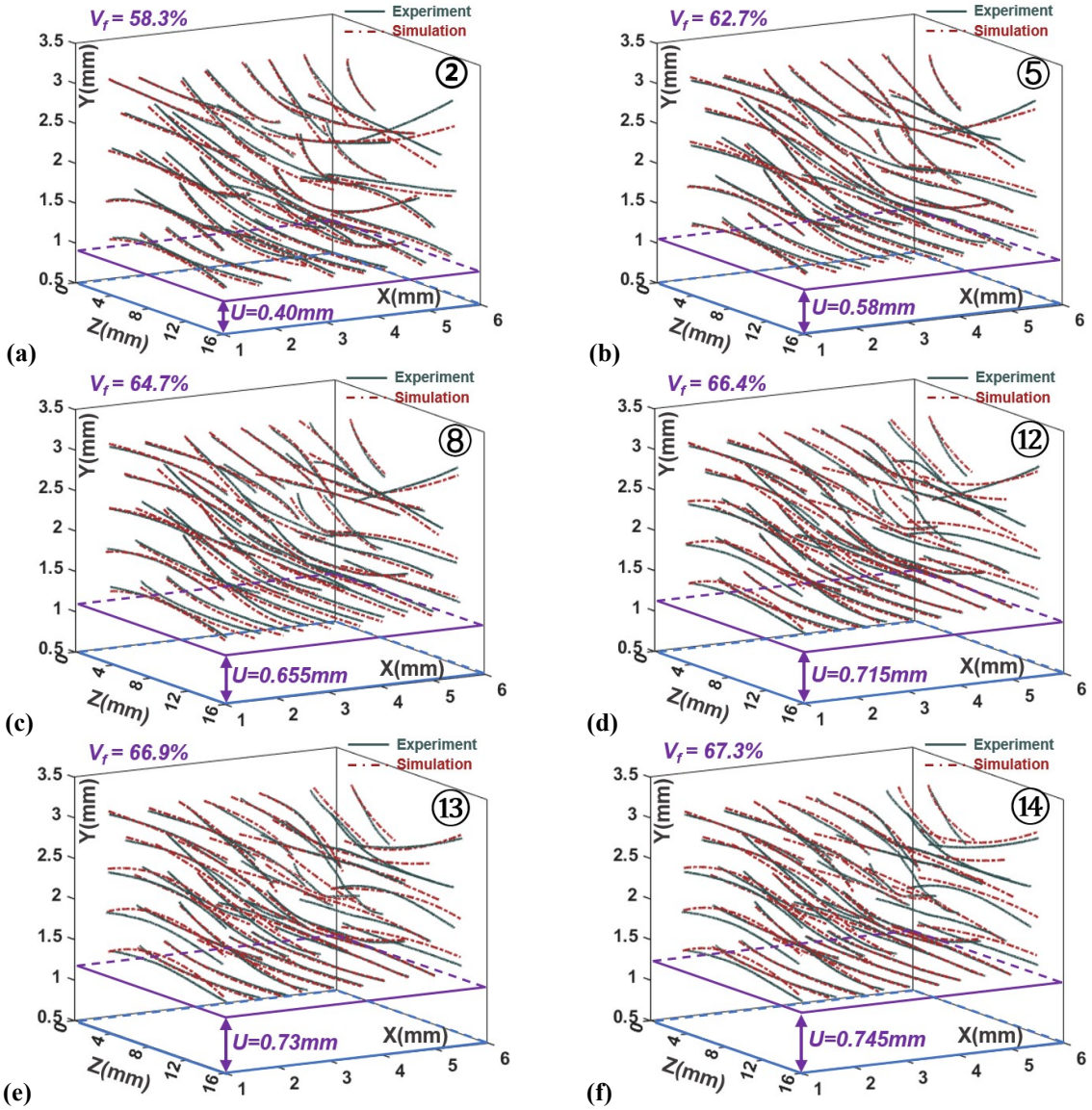

Figure 6.25 The centerline of sample 2 after simulation and experiment compaction. (a) Step 2, (b) Step 5, (c) Step 8, (d) Step 12, (e) Step 13, (f) Step 14.

Table 6.7 The position errors of fibers between experiment and simulation of sample 2 for compaction step 5, 12, 13, 14.

Indicators (%)	Step 5		Step 12		Step 13		Step 14	
	μ	σ	μ	σ	μ	σ	μ	σ
FPDTR (according to the thickness of fiber bundle)	2.25	0.59	3.72	2.12	3.19	1.71	3.12	1.75
FPDVFR (according to the V_f)	6.43	1.67	11.88	6.78	10.35	5.55	10.30	5.78
FPDDR (according to the diameter of fiber)	10.95	2.74	17.00	9.70	14.48	7.76	14.07	7.89
FPDUR (according to the displacement of compaction plate)	9.41	2.45	11.89	6.78	9.92	5.32	9.44	5.40

The Figure 6.26 show the 3D rendering fiber bundle of simulation and 3D reconstrued geometry of experiment. The morphology of fiber bundle after compaction step is almost same. The compaction curve of sample 2 of simulation and experiment in Figure 6.24 (a) shown the compaction pressure was drop down at compaction step 13 (V_f=66.9 %), the fibers in step 12 (marked in red circle) displaced as the compaction continue to step 13 (marked in green circle), so, the microstructure of fiber bundle of step 12, 13 and 14 were analyzed here.

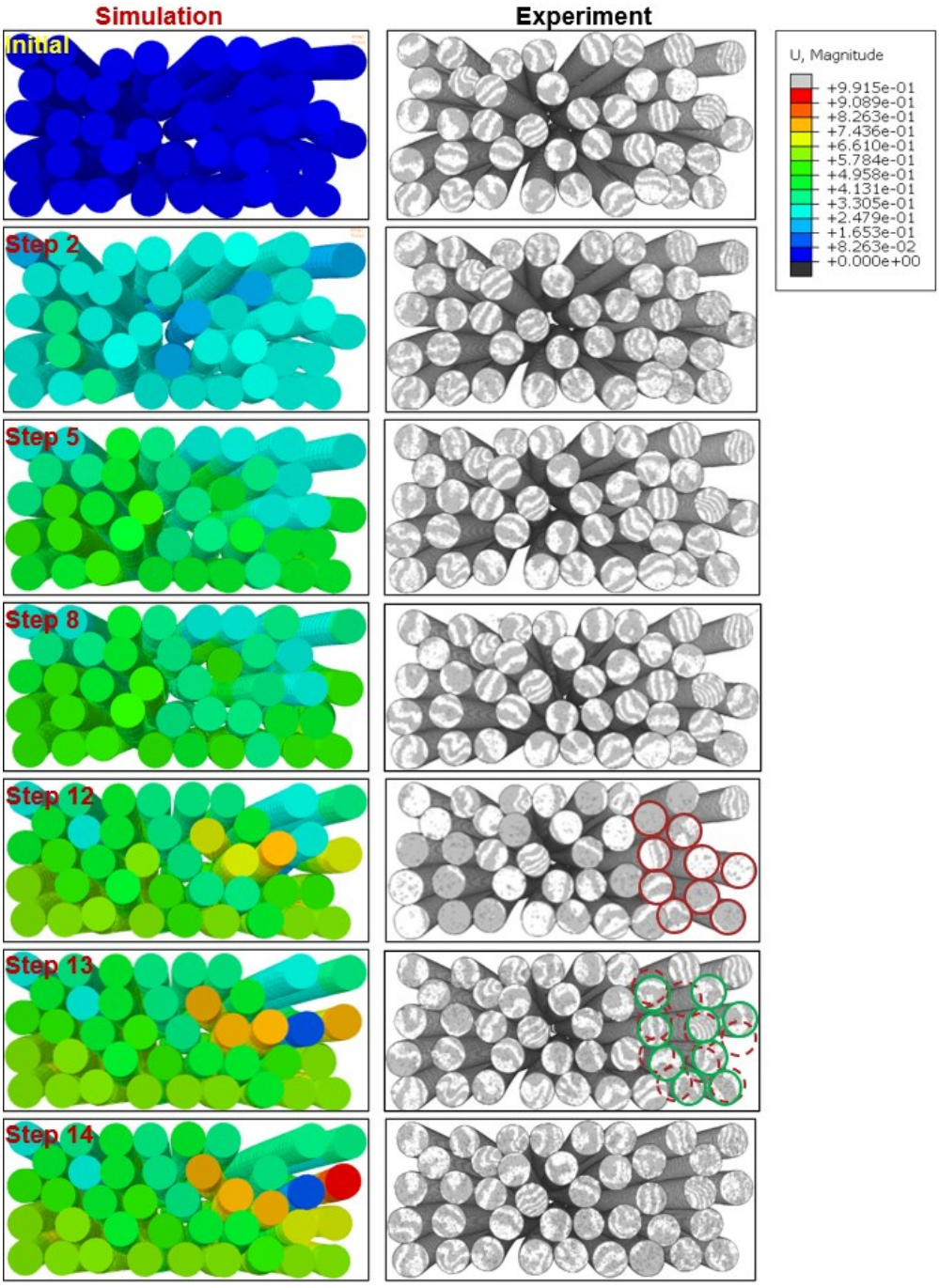

Figure 6.26 The 3D rendering geometry of sample 2 after simulation and experiment compaction for step initial, 2, 5, 8, 12, 13, 14.

For the sample 2, the compaction pressure is drop down in the V_f = 66.9 %, the indicator tools were used to understand the evolution of fiber bundle structure from step 12 to 14.

i) Orientation and mis-orientation

Here, the orientation tensor A_{33} of the fibers in sample 2 with compaction step 12, 13, 14 shown in Figure 6.27, and the orientation unit spheres of fibers shown in Figure 6.28. The A_{33} increased from step 12 to step 13, but after step 13, the A_{33} and unit orientation tensor distribution in $\boldsymbol{e_1 e_2}$ plane were almost same. The fibers are slipped from step12 to step 13, and after compaction step 13, the fibers keep to fill the space, which created by the slipped between fibers in step 13.

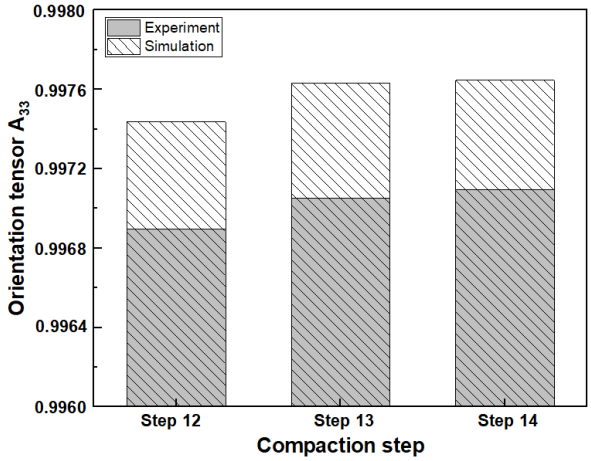

Figure 6.27 The orientation tensor A_{33} after simulation and experiment compaction step 12, 13, 14 (sample 2).

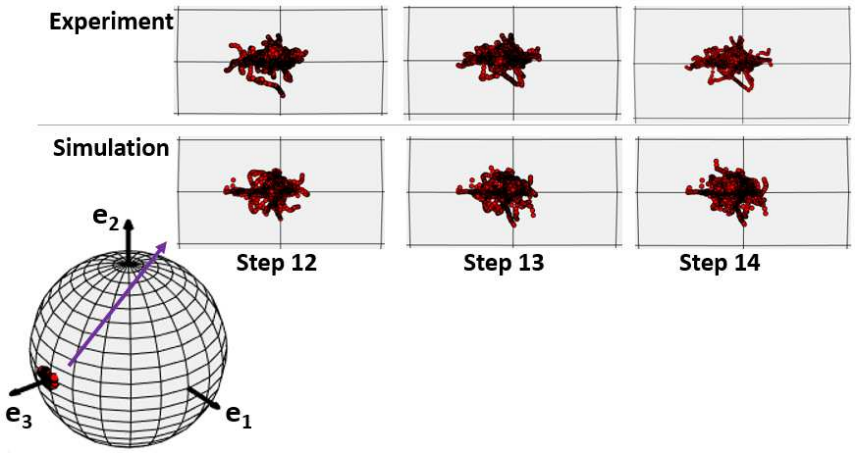

Figure 6.28 The orientation unit spheres of fibers with simulation and experiment compaction step 12, 13, 14 (sample 2).

ii) Contact

The contact between fiber, between fibers and plates, total contact number shown in Figure

6.29, the total contact number in the compaction step 13 is dropped compared to the total number in step 12. The total contact number is influenced by contact number between fibers, that's means the fibers slipped in step 13 changed the contact point and numbers at same time.

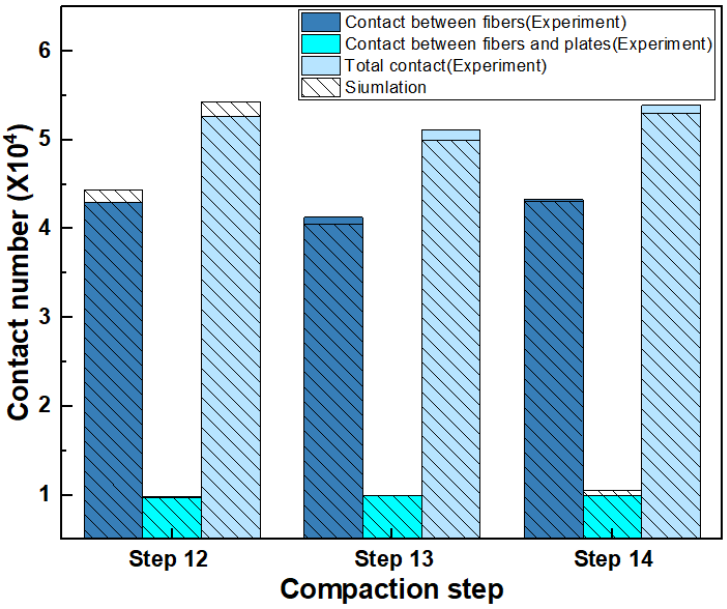

Figure 6.29 The contact number between fibers, between fibers and compaction plates, total contact of simulation and experiment compaction step 12, 13, 14 (sample 2).

From the distribution of contact angle between fiber in the fiber's section (θ) and between fiber length direction (γ) (Figure 6.30), the distribution of contact angle between fiber keep almost same and are in good agreement.

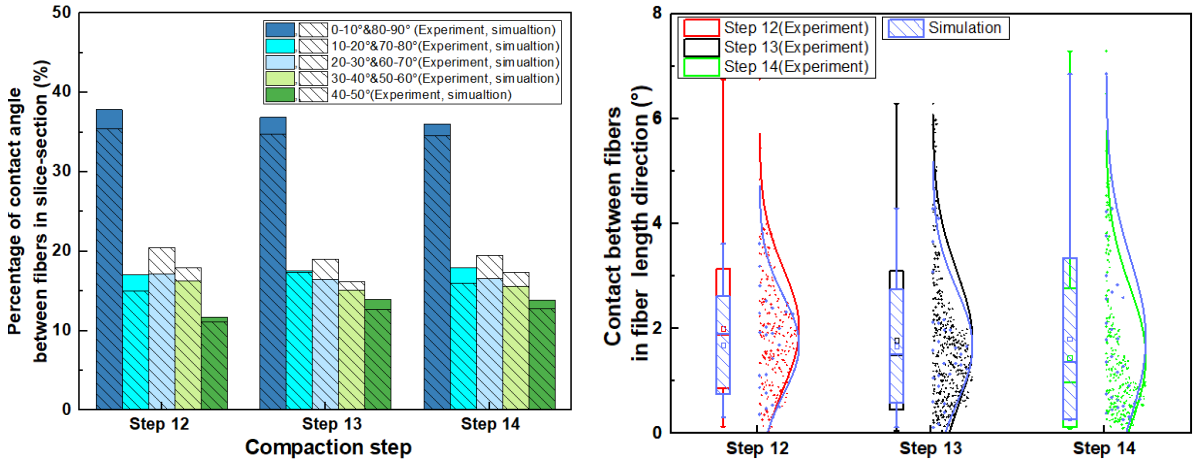

(a) **(b)**

Figure 6.30 The contact angle (a) between fiber in fiber's section (θ), (b) between fiber length direction (γ) (°) (sample 2).

iii) Crimp

The boxplot of crimp of fibers after compaction step 12, 13, 14 show in Figure 6.31, here again the consistency between calculated and experimental values is noticeable. The distribution of crimp shows the undulation didn't change that much according to the contact angle and the fiber position, even if a slight drop in crimp exist in Step 13, these shows that the drop in step 13 is not due to a global reorganization of the structure but to an instability and the drop of one or few fibers.

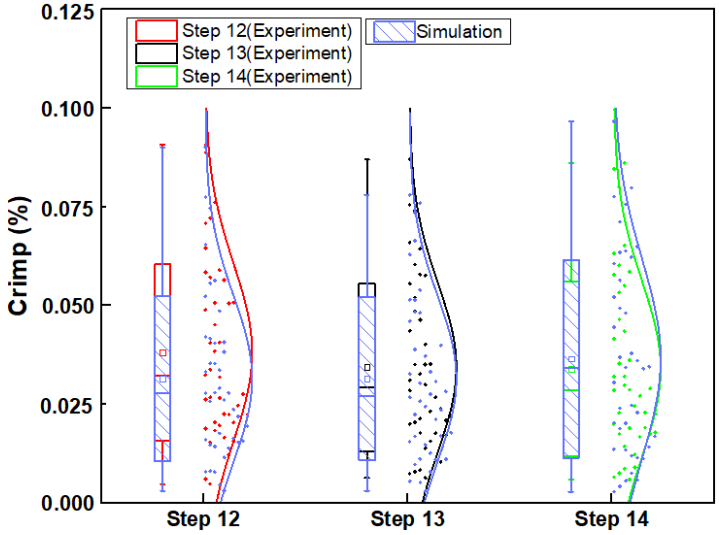

Figure 6.31 The boxplot of crimp of fibers in the simulation and experiment compaction step 12, 13, 14 (sample 2).

The consistency between the simulated and experimental results appears to be very promising, it has then to be confirmed on the sample 3.

c) Sample 3

It won't be entered into so much detail than for the previous sample, since the phenomenon involved and the analysis would be the same. However, since the goal of this chapter is to validate the proposed strategy as representative of a real bundle, the consistency between the experimental and numerical results has to be confirmed. The Figure 6.32 show the compaction pressure in function of volume fraction of sample 3. The compaction curve of simulation shows in this case also a good constancy according to experimental one. The centerline of fibers in the different compaction step of simulation and experiment shown in Figure 6.33, Table 6.8 show the errors of fiber position between experiment and simulation according to thickness of fiber bundle (FPDTR), V_f (FPDVFR), the diameter of fiber (FPDDR), and the displacement of

compaction plate (FPDUR).

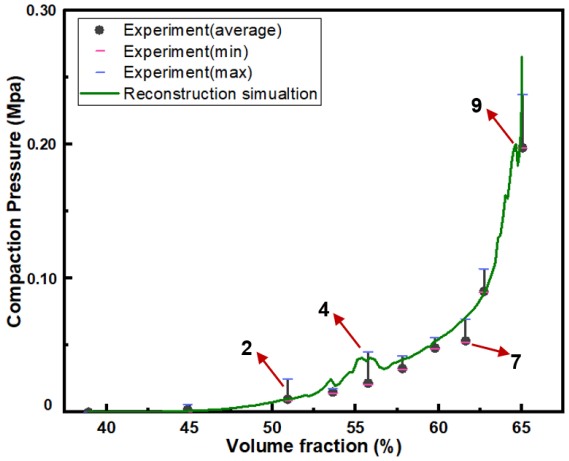

Figure 6.32 The compaction pressure function in volume fraction of sample 3.

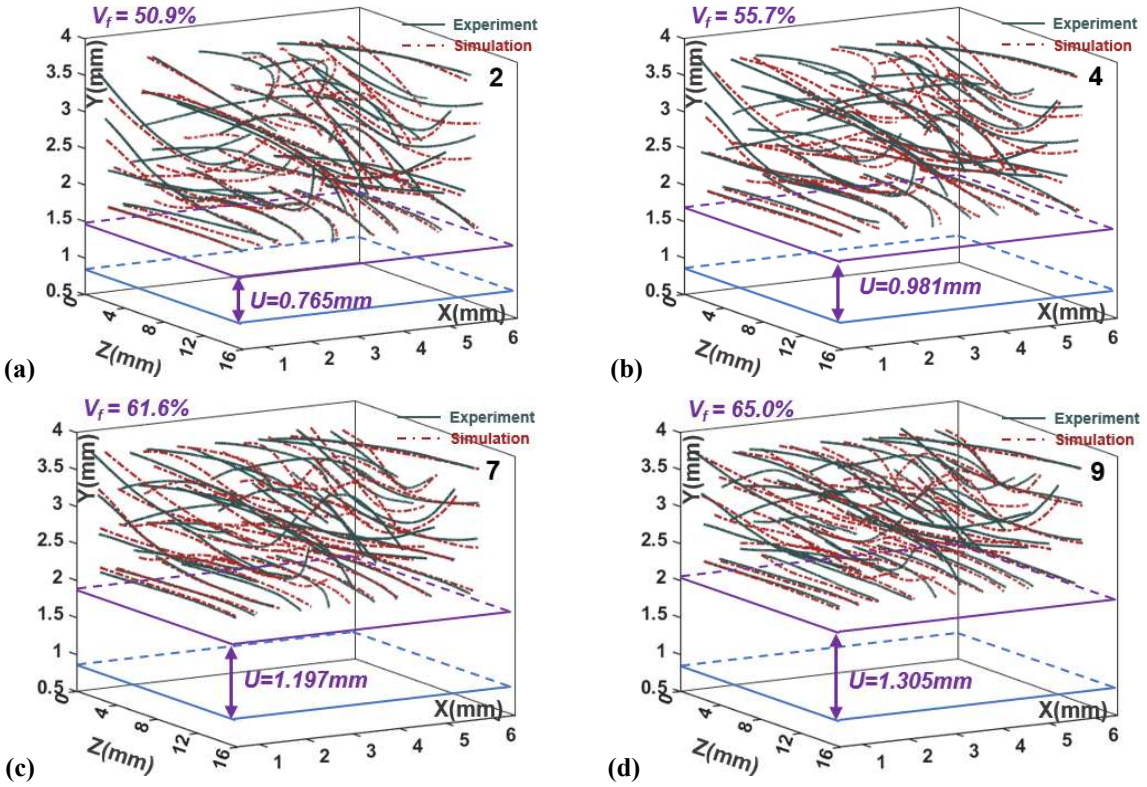

Figure 6.33 The centerline of sample 3 after simulation and experiment compaction. (a) Step 2, (b) Step 4, (c) Step 7, (d) Step 9.

Table 6.8 The position errors of fibers between experiment and simulation of sample 3 for compaction step 2, 4, 7, 9.

Indicators (%)	Step 2		Step 4		Step 7		Step 9	
	μ	σ	μ	σ	μ	σ	μ	σ
FPDTR (according to the thickness of fiber bundle)	6.14	2.63	5.27	2.88	5.43	2.57	5.06	3.00
FPDVFR (according to the V_f)	12.51	5.35	11.19	6.50	14.15	6.69	14.47	8.56
FPDDR (according to the diameter of fiber)	30.40	13.00	23.80	11.00	22.20	20.50	19.60	11.60
FPDUR (according to the displacement of compaction plate)	19.89	8.50	12.13	6.26	9.27	4.39	7.51	4.45

In Figure 6.34, the 3D rendering fiber bundle of simulation and 3D reconstrued geometry of experiment of different compaction step were performed. The morphology of fibers in simulation and experiment are closely related. Even if the sample 3 results are not as accurate as for the sample 2, experimental and simulated results is good remains in good agreement which enables to confirm the potential of the strategy to model consistently the deformation of a fiber bundle during compaction. It is important to notice and confirm here that the initial errors of the reconstructed microstructure from the experimental one are of a main importance for the general consistency which is definitely a very good thing for the use of the strategy as a virtual estimator because this step does not exist for such simulations.

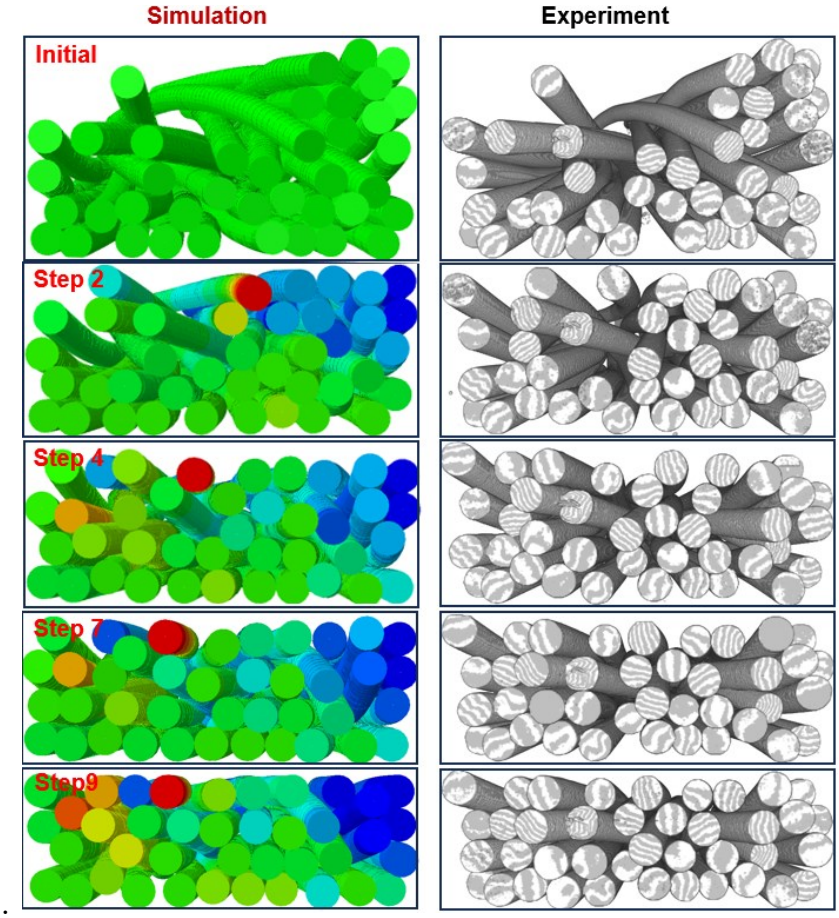

Figure 6.34 The 3D rendering geometry of sample 3 after simulation and experiment compaction for step initial, 2, 4,7, 9.

6.4 Conclusion

Compaction experiments were carried out on two new samples and simulations were carried out on three samples using the simulation strategy described above, and the initial volume fraction is 37.9 %, 50.5 %, 38.9 %, respectively. The accuracy of the initial model was verified by imposing a gravity simulation. The contact position detected by post-treatment strategy could be verified by imposing the gravity filed to the fiber bundle geometry: the fibers move until the static equilibrium and the differences consequently point out the uncertainties of the reconstruction process. The average error (FPDDR: the error according to the fiber diameter) of the fiber position under imposing gravity simulation and one extracted by tomography experiment for the three samples was 16 %, 5 %, and 8 % of the fiber diameter, respectively. As expected, the increase in the XCT resolution enables obtain a more accurate initial consistency which is very promising for the proposed strategy. This means the initial contact introduced by the post-treatment strategy achieve the goal, with a very satisfying accuracy even

if the errors couldn’t be completely eliminated due to the necessary simplification of the modeling.

The microstructure indicators were analyzed also, different samples with different orientation, crimp and contact number, so that the samples present different macroscopic compaction behavior (the compaction pressure in function of volume fraction). The fiber position from simulation and tomography experiment at same compaction step are in good agreement, and the position errors of results with high resolution sample are smaller.

Even though, there is potential for improvement, the comparison between the simulated and experimental, in terms of macroscopic compaction behavior, and the position of the fibers after compaction is interesting and promising and enables to validate that the virtual numerical estimator, as well as the developed microstructural analysis tools are effective for the current work.

In order to use the previously validated strategy as a virtual estimator, fiber bundles with controlled parameters have to be created. It is then necessary to create stochastic near-realistic models of fiber bundles in order to explore the mechanical response of the fiber material at the microscopic level. Therefore, a methodology for creating a virtual numerical random fiber bundle generator is presented in next Chapter.

Chapter III Random Fiber Bundle Generator and analyze the influence of creation parameters

This chapter contains section 7, 8 and 9. The effect of microstructural parameters in the fiber bundle on the behavior of fiber compaction is discussed by creating a virtual numerical random fiber bundle generator, the parameters of which being controlled failing to be perfectly imposed.

In section 7, the strategy of creating virtual numerical random fiber bundle generator is presented and its feasibility verified.

Based on the virtual numerical random fiber bundle generator in section 7, Section 8 investigates the effect of microstructural parameters in the fiber bundle on the compaction behavior. Finally, section 9 study the effect of different parameters on the compaction behavior, like the loading path, friction coefficient, etc.

Section 7 Virtual numerical random fiber bundle generator

This section develops a virtual numerical random fiber bundle generator based on the principle of the tomography experiments of fiber bundles as presented in Chapter II. The generator allows the control of the microstructural parameters of the fibers bundle, including the number of fibers, the length-diameter ratio, the undulation, and so on. In this way, fiber bundle models with different microstructures can be generated.

The feasibility and the reliability of this strategy is verified by a compaction simulation comparison with the fiber bundle sample II from the tomography experiment in Chapter II.

This method does not require extensive experimentation and saves time and cost. It provides a reliable and fast method to discuss the effect of the microstructure of the fiber bundle on the compression behavior.

7.1 The basic hypothesis

The principle of the numerical generator is based on the principles of tomography scan in-situ image of fibers bundles and the 3D reconstruction of fiber bundles, as described in Chapter II. Tomography slices of a fiber bundle consisting of cross-sections spaced in voxel size intervals. The numerical model reconstruction of the fiber bundle is based on the connection of the fiber centerlines. In this case, the fiber cross-section is treated as a regular circle and the fiber bundle is divided into n equal parts, where n is the number of slices, determined by the fiber bundle length L_{fiber} and resolution v, as shown in Figure 7.1. The centerlines of the n equal parts of the fiber bundle are connected to obtain the 3D numerical geometry model. But it's difficult to create the virtual numerical random fiber bundle basic on this principle of tomography scan in-situ image and 3D reconstruction of fiber bundles. Since fiber cross sections are created in slices and then joined, penetration between fibers is unavoidable with high volume fraction (> 45%).

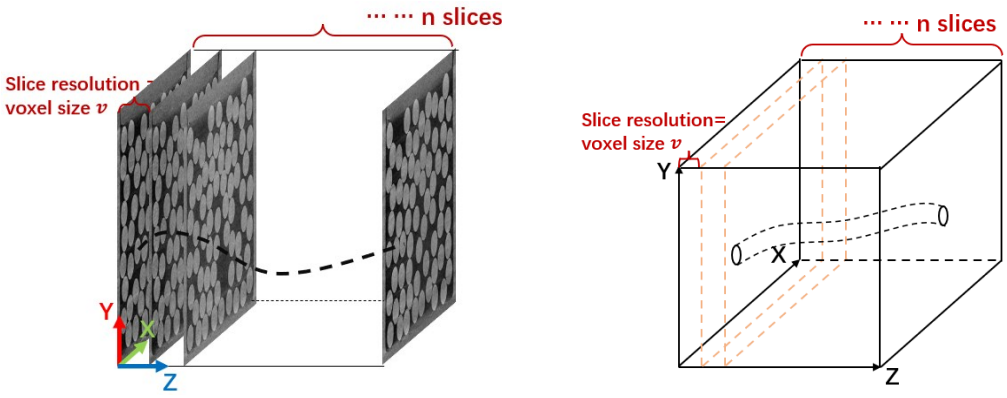

Figure 7.1 Generation of fiber according to tomography principle: the fiber bundle consists of n tomographic slices spaced by v (resolution).

So that, the basic hypothesis of virtual numerical random fiber bundle generator involves three steps, as shown in Figure 7.2; the first two steps concern the geometrical modeling of each fiber with a MATLAB code and the third one imposes gravity with Abaqus® software to generate the final fiber bundle.

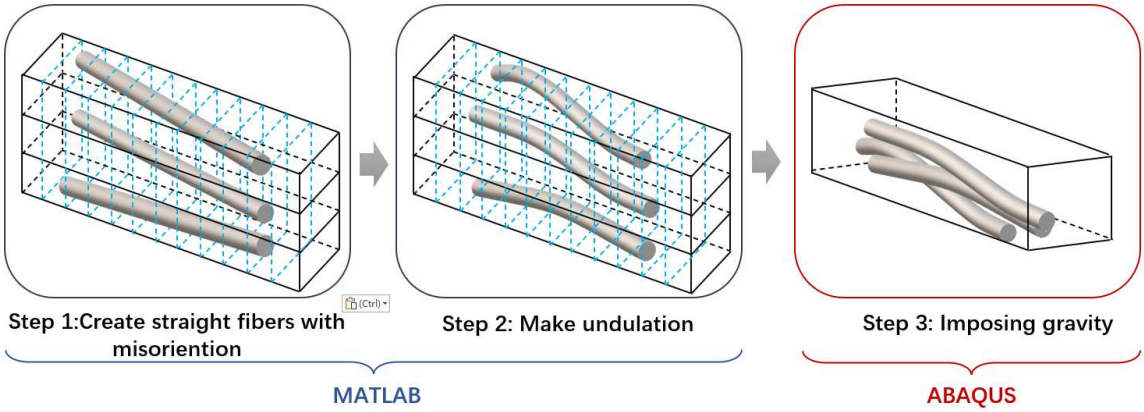

Figure 7.2 Main steps of a virtual numerical random fiber bundle generator.

Each step will be detailed in section 7.2 but can be resumed as follow:

(i) Step 1: create straight fibers with misorientation:

In this creation strategy, we consider the fiber cross section as regular and uniform in size. As shown in Figure 7.3, with the fiber length controlled by the number of slices n and the resolution of the slices (voxel size v), $L_{fiber} = v \times (n-1)$. In this step, the mis-orientation of fibers is created, and it discussed in the section 7.2.

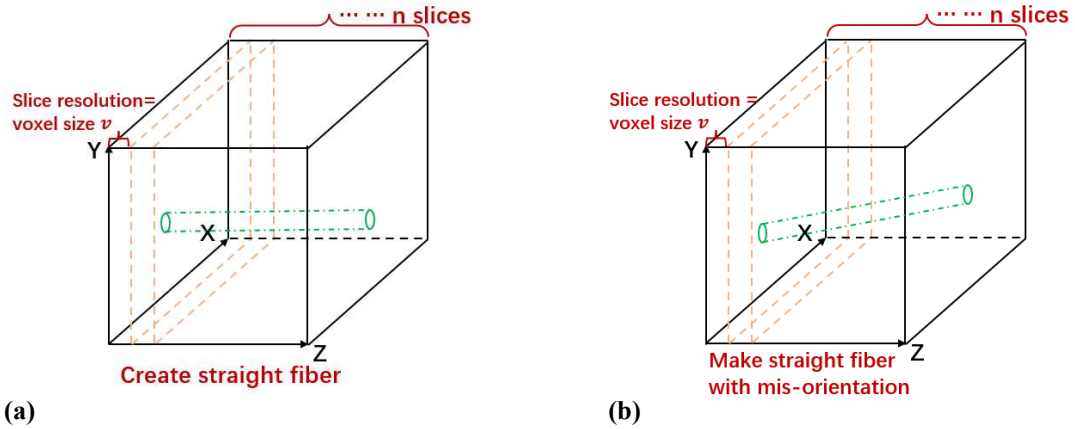

Figure 7.3 Principle of a virtual numerical fiber bundle generator to create straight fibers with misorientation. (a) Create straight fiber, (b) Make straight fiber with mis-orientation.

(ii) Step 2: impose undulation

The misorientation being imposed, the undulation has to considered. Therefore, the number of undulations, which means the number of inflection points (1 for the two bottom fibers, 2 for the upper one in Figure 7.2), and the intensity of the curvature are introduced to indirectly control the microstructure of the fibers.

(iii) Step 3: impose gravity

The natural fibers bundle in the real case are arranged in contact with each other. Under the condition of controlling the parameters in (ii), each fiber is curved and orientated. In MATLAB programming. Therefore, the denser the media the most difficult it is to avoid interpenetration between the newly created fibers and the existing ones. This might lead to infinite calculation so as to obtain the targeted volume fraction with the targeted geometrical statistics. This problem is easily solved for 2D microstructures since the number of configurations is an order of magnitude lower, however, to our knowledge, it remains an issue for 3D modeling and no efficient perfect solutions have been found for this issue.

In order to avoid this problem, the creation of single fibers is distributed in a separate area to ensure that the fibers are not affected by fiber undulation and deflection. This method makes the fibers impenetrable to each other. Then, a model of the fiber bundle arranged in contact with each other is obtained by gravity field simulation in ABAQUS®, as shown in Figure 7.4. This will consequently lead to small changes in the microstructure parameters explaining why they are defined as controlled whether than imposed.

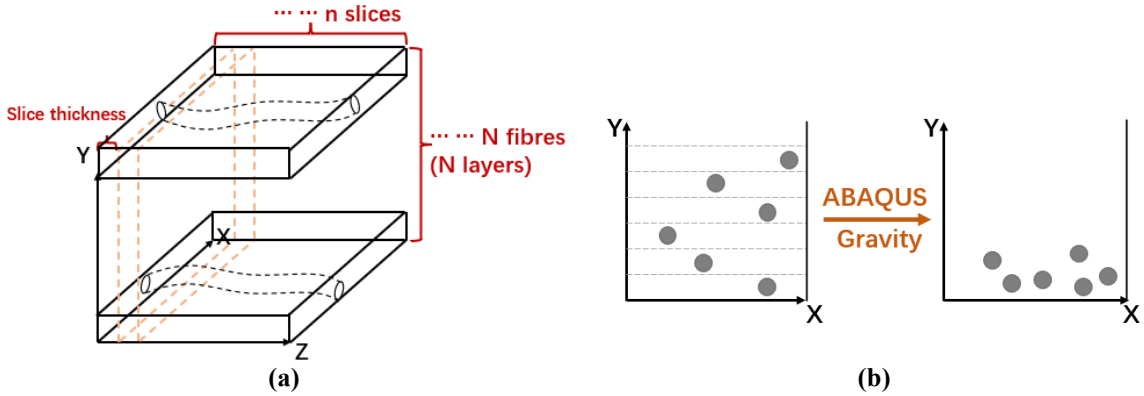

Figure 7.4 Principle of avoiding penetration between fibers. (a) Create a single fiber in a separate layer, (b) impose gravity by ABAQUS®.

7.2 Numerical generation step

The numerical generation step for random fiber bundle geometry is shown with a flowchart in Figure 7.5. It is important now to specify that the word "random" means randomly chosen through a normal distribution. The two imposed parameters (average value and standard deviation value) of the normal distribution are the parameters that drive the targeted microstructure. In addition to this statistical approach some control rules have to be verified and ensured, and lead to an iterative creation for each fiber.

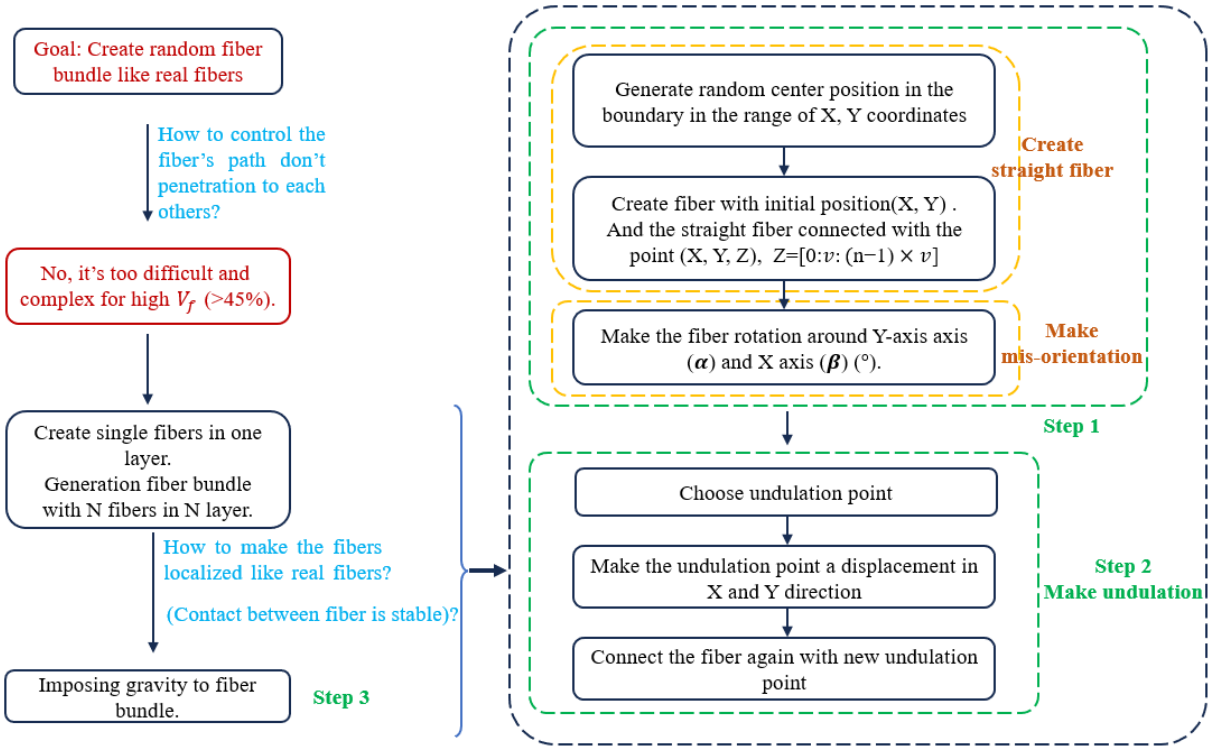

Figure 7.5 The flowchart of numerical generation step for random fiber bundle geometry.

In order to implement this method, the following steps have been done:

a. Randomly generate the center position of the fibers in each layer (the single fiber located in one layer in Figure 7.4). The fiber i is generated in layer i, in this way, N fibers are generated in N layer (N∈[0: 1: N]).

For a single fiber the location of the center point in the layer is shown in Figure 7.6. In this first step, the first center point of the fiber is randomly selected within a range (the red dot range). After that, the fiber centerline is extended in the Z-axis direction with a spacing of v to $(n-1)\times v$ to the end of the fiber, where n is the slice number, v is the voxel size. In order leave space for a single fiber to make a deflection in the Y direction, the Y coordinate is located on the centerline of each layer ($Y_{N_{th}} = \frac{1}{2}d$). Considering the radius of the fibers, then the X coordinate is chosen in the range $X \in (r, X-2r)$ to make sure the entire 3D fiber remains in the box. Then the random coordinates of the Nth fiber are (X, Y), $X \in (r, X-2r), Y = \frac{1}{2}d + (N-1)d$.

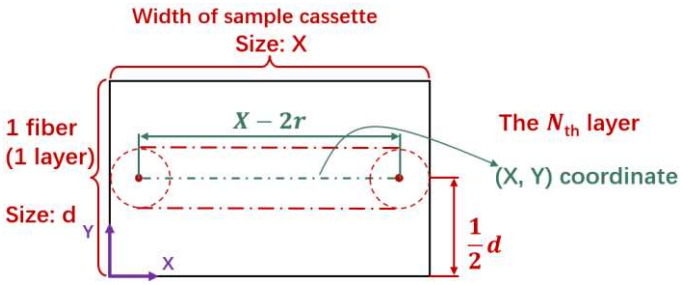

Figure 7.6 Principle of single fiber creation.

b. Control fiber misorientation (deflection)

The initial fiber position is selected randomly (step(a)), and the Euler angle system is introduced to control the fiber misorientation. As illustrated in Figure 7.7 (a-c), the arrow's direction (initial direction of fiber (step (a))) is controlled by adjusting the rotation angle of the arrow (α and β). In a similar manner, this principle is applied to manage the misorientation of the fibers.

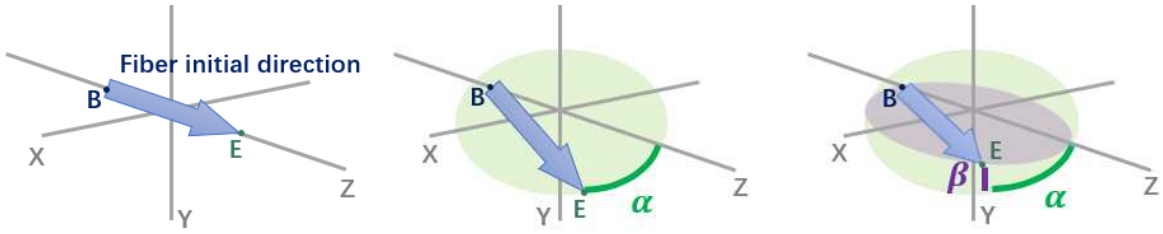

(a) **(b)** **(c)**

Figure 7.7 Principle of misorientation of single fiber, according to Euler's theory of rotation.

In the first slice, the circle's center point is randomly selected as the initial position of the fiber slice (step (a)). The misorientation is obtained by the rotation of the fiber around this point. Figure 7.8 (a) shows the establish a coordinate system (X-Y-Z) with the fiber centerline. This coordinate system direction is consistent with the global coordinate system. Following the Eulerian rotation principle, the initial fibers are rotated by an angle α around the Y-axis, and a new X_1-Y_1-Z_1 coordinate axis is obtained. Similarly, the fibers are rotated around the X_1 axis to acquire the X_2-Y_2-Z_2 coordinate axes, as shown in Figure 7.8 (b). Consequently, the orientation of the fibers can be controlled by the parameters α and β. No twist is considered in our modeling since it can be neglected as regards rovings and its manufacturing principles.

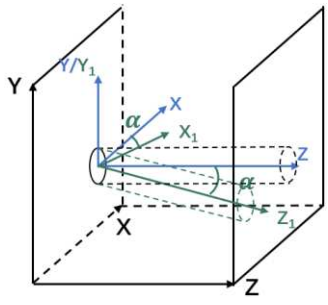

(a)

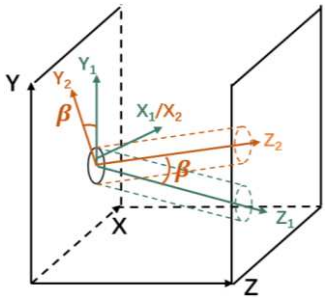

(b)

X_1: New X-axis after around Y-axis rotation
Z_1: New Z-axis after around Y-axis rotation
α: rotation angle around Y-axis

X_2: New X-axis after around X_1-axis rotation
Y_1: New Y-axis after around X_1-axis rotation
β: rotation angle around X_1-axis

Figure 7.8 Rotation of fibers according to Euler's theory of rotation. (a) Rotation of a single fiber in a separate layer around Y-axis (α) (°), (b) Rotation of a single fiber in a separate layer around X-axis (β) (°).

Furthermore, it's important to ensure that the spatial positioning of the fiber bundle remains inside the sample cassette inner wall (compaction channel). This concerns not only to the initial position of the fibers (Figure 7.6) but also to the positions of the deflected fibers. All the coordinates of fibers should be contained within the sample cassette inner wall boundaries. As such, it is essential to identify for which case the randomly generated initial fiber position in Figure 7.9 (a) aligns. For instance, it could be case 1, where the fiber can only deflect to one side (the right side), or case 2, where the fiber has the capability to deflect in both directions. Moreover, the angles α and β should never exceed the maximum allowable values, as shown in Figure 7.9 (b):

$$|\alpha| \leq \alpha_{max} = \arctan\left(\frac{\frac{d}{2}-r}{L}\right) = \arctan\left(\frac{\frac{d}{2}-r}{n\times v}\right) \tag{7.1}$$

$$|\beta| \leq \beta_{max} = \arctan\left(\frac{X-2r}{l}\right) = \arctan\left(\frac{X-2r}{n\times v}\right) \tag{7.2}$$

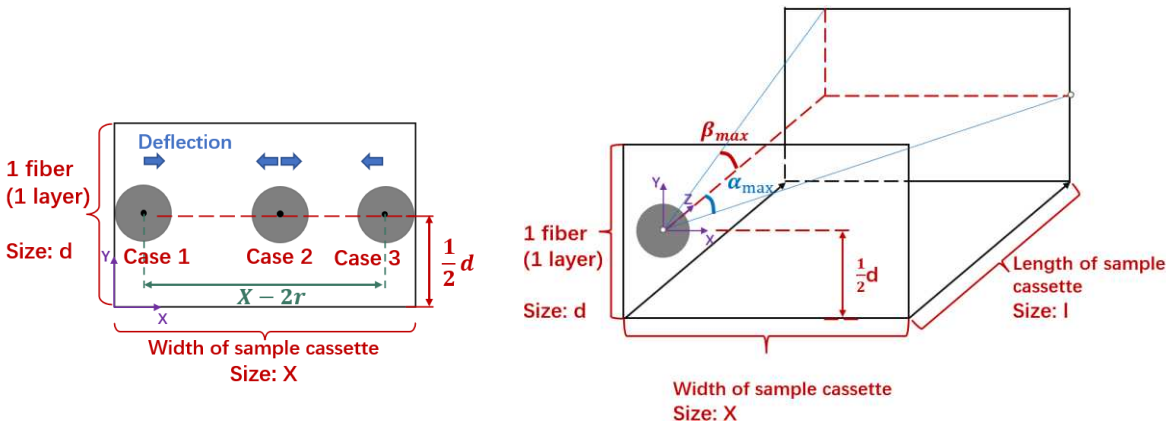

(a) (b)

Figure 7.9 Maximum misorientation angle of α and β. (a) Three different cases for deflection of fiber, (b) Scheme of max rotation angle α_{max} and β_{max}.

c. Undulation of single fiber.

Once the misorientation is generated, a random position fiber bundle is obtained with fiber of straight lines oriented according to three-directions of the space. For the real case, the fibers are bent at different degrees, so the number of undulations and the range of undulation positions of the parameters are introduced hereafter.

After step (b) of deflection, the morphology of fibers is shown in Figure 7.11 (a). An undulation point is inserted and, to illustrate this, an example is indicated in Figure 7.10. The final undulation point is obtained by displacing the selected points (black point) on the fiber in Z, X, Y direction. The new curved fiber (blue curved line) is obtained with one undulation point.

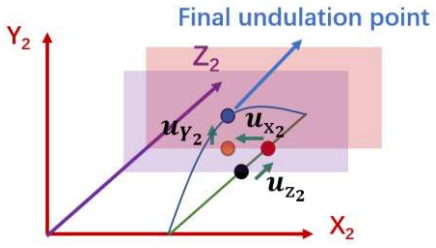

Figure 7.10 Insertion undulation point (example with only one undulation point).

The strategy used to insert undulation point is the following:

(i) Choose the initial insertion point (black point). Find the equipartition point of the fiber length (the undulation position in which slice (Z coordinate)), as shown in Figure 7.11 (a).

(ii) Make a displacement of that point in the longitudinal, thus Z direction. In Figure 7.11 (b), a slice is randomly selected by parameter σ_{u_z} with Gaussian probability distribution to insert the undulation point, the average value being the middle of the fiber.

(iii) Make a displacement in X and Y direction. In the randomly selected slice, the center

point of the fiber is shifted first in the X_2 direction and then in the Y_2 direction to obtain the final undulation point. The shift value is controlled by μ_{u_X}, σ_{u_X} and μ_{u_Y}, σ_{u_Y}, μ_{u_X}, σ_{u_X} is the average and standard value of the selected point shift in X direction, respectively; and μ_{u_Y}, σ_{u_Y} is average and standard value of the selected point shift in Y direction, respectively, as shown Figure 7.11 (c).

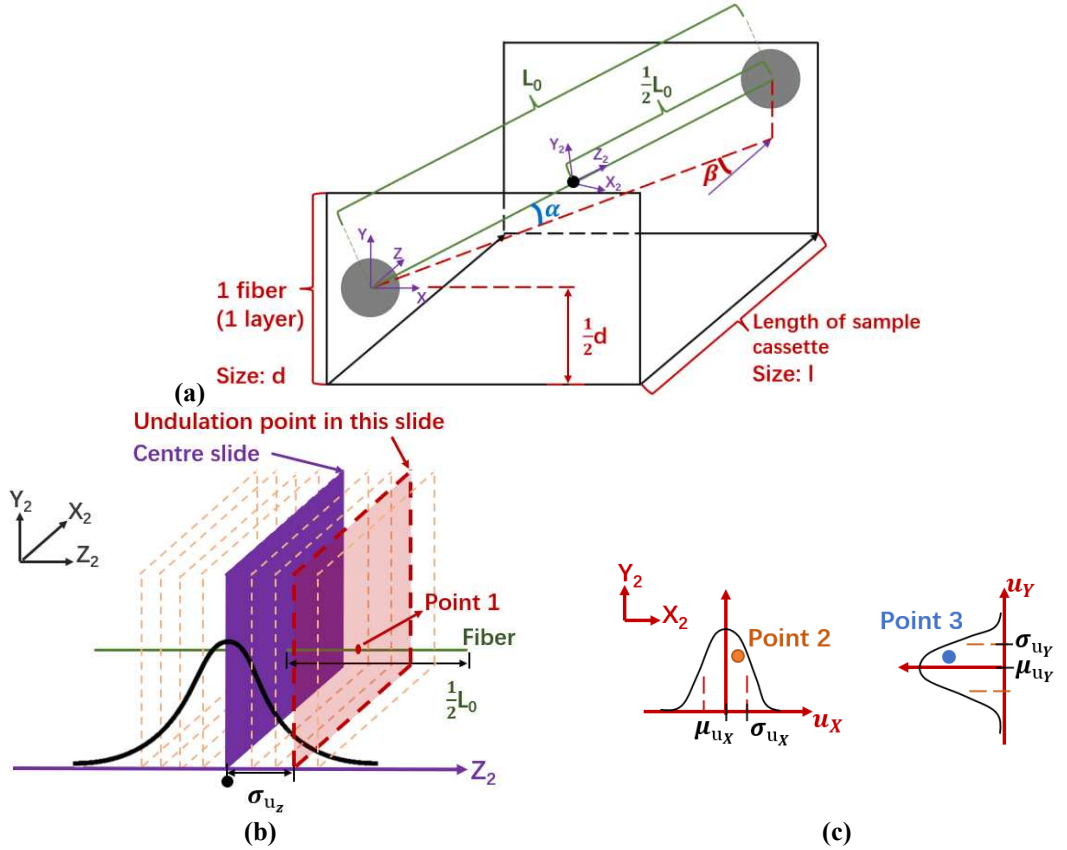

Figure 7.11 Principle of insertion of undulation point in single fiber (example with one undulation point).

7.3 Validate the fiber generator with experiment sample

7.3.1 Create geometry with same parameters of sample 2

In order to check the efficiency of the virtual numerical random fiber generator, the same compaction test was simulated for virtual numerical fiber bundles. 3 virtual numerical fiber bundle geometries (geometry 1-3) were created with the same parameters of the Table 7.1.

As an example, the creation step 3 (imposing the gravity on the fiber bundle) for geometry 1 is shown in Figure 7.12, the Figure 7.12 (a) show the centerline of the fiber bundle geometry 1 before step 3 (imposing the gravity), and Figure 7.12 (b) show the centerline of the fiber bundle

geometry 1 after imposing the gravity step by ABAQUS®. Next, the Figure 7.13 (a-b) show the 3D rendering fiber bundle geometry 1 before and after imposing gravity. The reconstruction fiber bundle geometry from tomography experiment is shown in Figure 7.13 (c1), and another 3D rendering virtual numerical fiber bundle geometries 2, 3 are shown in Figure 7.13 (e1, f1), which created with same parameters as geometry 1. After imposing gravity, the initial volume fraction of geometry 1-3 is 46.7%, 46.7% and 47.6% respectively which is in the range of what was obtained experimentally and of what is usually observed to real roving yarns.

Table 7.1 Creation parameters of geometry 1-3 created by virtual numerical random fiber generator.

Basic parameters of fiber bundle				
Fiber number		40		
Fiber radius (mm)		0.25		
The size of the box (width)(mm)		5		
Voxel size (mm)		0.009		
Slice number n		1522		
The size of layer for each fiber(mm)		2		
Misorientation				
Rotation angle (°)	μ_β	0.055	μ_α	-1.510
	σ_β	1.089	σ_α	2.294
Undulation				
Undulation point number		1		
X, Y, Z direction shift value (mm)	σ_{u_z}	110		
	μ_{u_X}	1.2	μ_{u_Y}	0.2
	σ_{u_X}	0.14	σ_{u_Y}	0.2

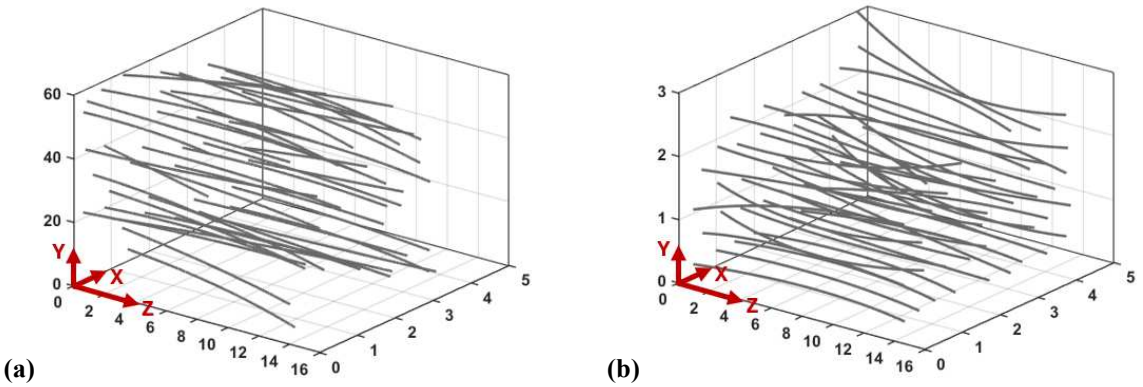

(a) (b)

Figure 7.12 The centerline of fiber bundle geometry 1 created by virtual numerical random fiber bundle generator. (a) Initial fiber bundle (before gravity simulation), (b) After gravity simulation by ABAQUS®.

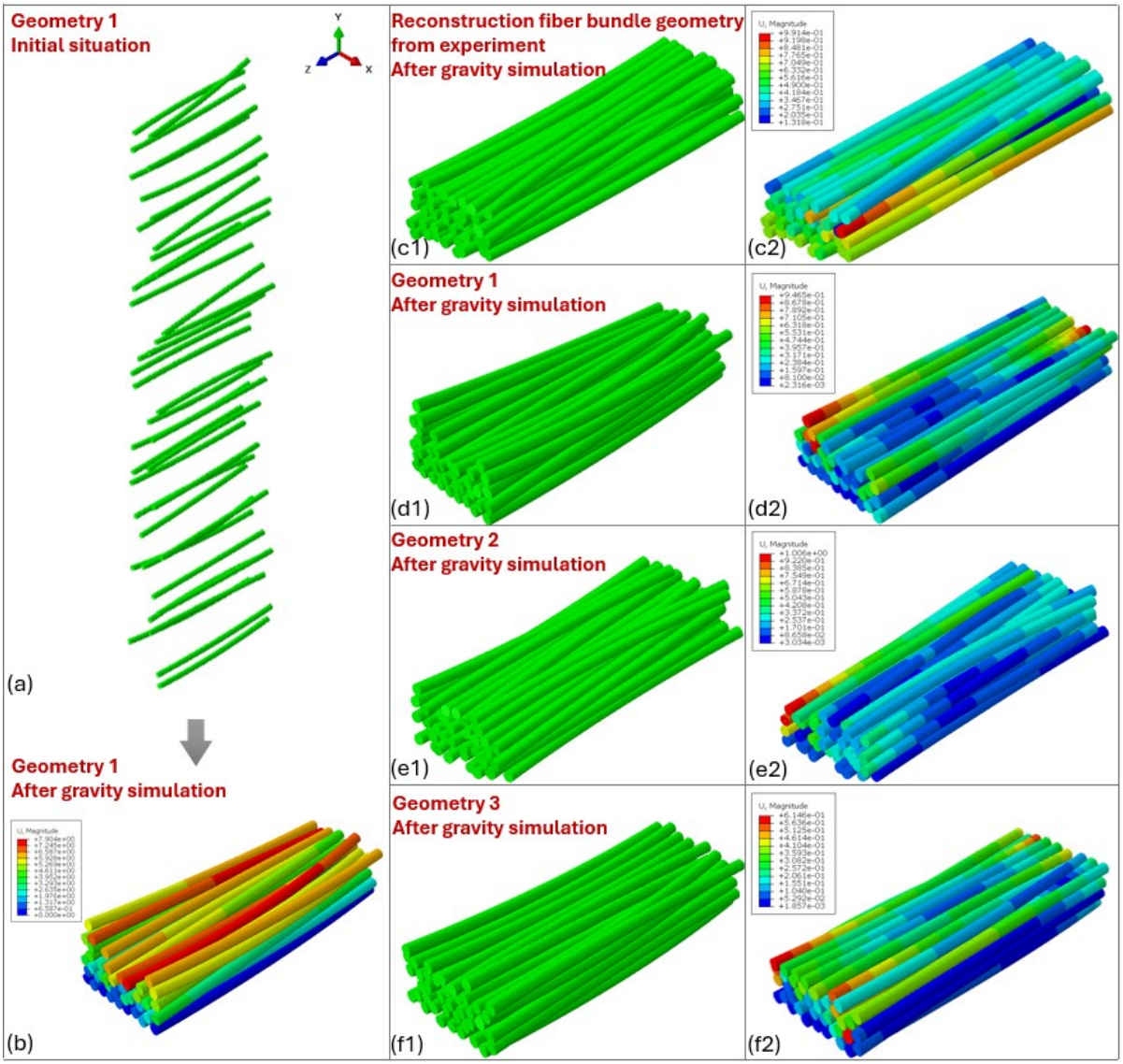

Figure 7.13 Numerical fiber bundle geometries. (a) The initial geometry 1 before imposing gravity. (b) geometry 1 after ABAQUS® gravity field simulation. (c1) Reconstruction fiber bundle geometry from tomography experiment. (d1-f1) Created geometries after ABAQUS® gravity field simulation, creation parameters same as Sample 2 indicators. (c2-f2) After compaction test with geometries (c1-f1).

As shown in Figure 7.14, there are three curves of the volume fraction-compaction pressure of fiber bundle geometries 1-3. And the 3D rendering of fiber bundle geometry 1-3 are respectively shown in Figure 7.13 (d2), (e2), (f2).

As expected, since the microstructure parameters are similar, these three fiber bundle geometries showed pressure trends consistent with the experimental and the reconstruction simulation results. It is however interesting and not so obvious, that the compaction pressure is decreased at around V_f = 67%, and continue increase again, this suggests that in the later steps of compaction, there was major sliding between all the fibers, resulting in a sudden drop in

compaction force. Obviously, this fluctuation varies in magnitude as well as slightly in position (V_f) but the phenomenon remains. Even if the internal structure parameters of different fiber bundle models are basically the same, the positions of the fibers are different, resulting in different slip between fibers at the late stage of compaction. This is due to the complex and random nature of the three-dimensional structure of fiber bundles, which makes tight structural differences produce significantly different deformation behaviors during compaction, even if the initial structures are similar. In the early stage of compaction, the sliding of the fibers against each other accounts for the major part. Thus, it is easier to adjust the relative position between fibers during this stage, so the compaction curve is basically the same. However, as the compaction continue, the relative movement between fibers becomes more difficult, and some fibers may bend or twist, which in turn affects the stress distribution within the fiber bundle. This difference becomes particularly pronounced in the later stages of compaction, where small changes in compaction may also lead to large stress or shape differences. In addition, with larger fiber diameters, the contact area between fibers increases, making the inter-fiber friction increase, further exacerbating the strain changes caused by slip.

The reliability of the virtual numerical random fiber generator was verified in terms of the consistency between the experiment, the reconstruction simulation, and the created fiber bundles compaction curves. The microstructural parameters after compaction are discussed in the next section.

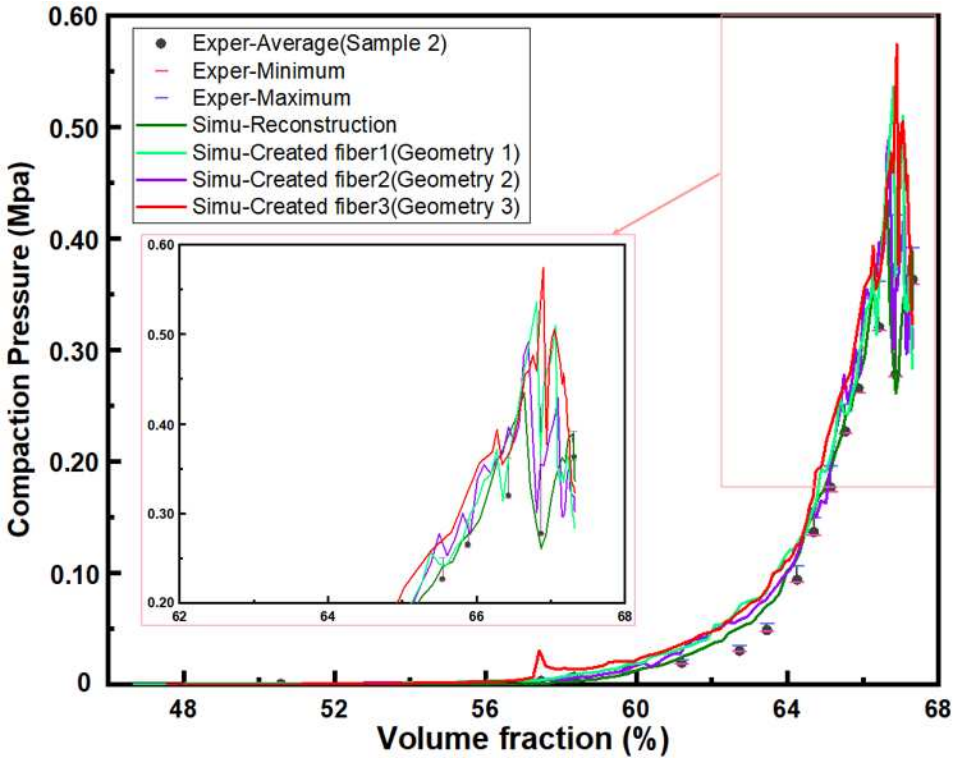

Figure 7.14 Compaction test with 3 numerical fiber bundle geometries, created by virtual numerical random fiber bundle generator.

7.3.2 Analyze the indicators of microstructure of geometry 1-3

a) Orientation and mis-orientation

As mentioned in section 5, the initial geometry of the fiber assembly is determined by several parameters, including the fiber orientation. The orientation parameter is usually characterized by the orientation tensor A, where the A_{33} component indicates the alignment of the fibers along the $\boldsymbol{e_3}$ direction. The A_{33} and orientation unit spheres of geometry 1-3 are shown in Figure 7.15 and Figure 7.16, respectively. A_{33} floats within 0.001 before and after compaction for geometry 1-3. The distribution of the orientation tensor over the unit sphere is closely related to A_{33}. Larger A_{33} indicates that its fibers are more directional after which mean that the fibers are distributed along the Z-axis ($\boldsymbol{e_3}$). This is logical since the volume fraction increases fibers tends to realign with each other along the Z direction.

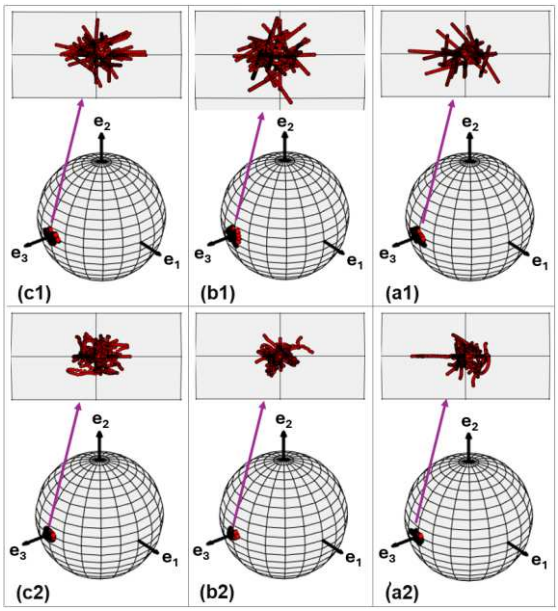

Figure 7.15 Orientation unit spheres, centerline of fiber. (a1-c1) Geometry 1-3 before compaction simulation (initial geometry), (a2-c2) Geometry 1-3 after compaction simulation.

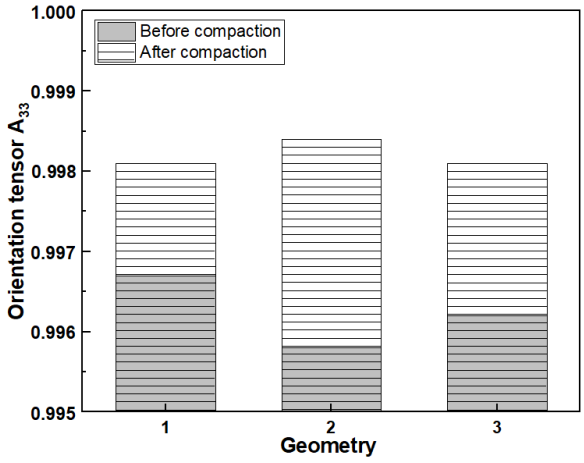

Figure 7.16 Orientation tensor A_{33} of geometry 1-3 before and after compaction.

Furthermore, mis-orientation indicates deviations of the fibers from the YZ and XZ planes, which are named α and β, respectively. Mis-orientation parameters shown the direction of fiber, the deviation of the fibers from the Z-axis. The boxplot of α and β of geometry 1-3 before and after compaction simulation shown in Figure 7.17.

Before the compaction simulation, the α of geometry 1-3 distribution is [-6, 5], [-6, 5] and [-5, 4] (°), respectively. The mean value of α of geometry 1-3 at -0.8°, 0.1° and -1.8°, respectively. The β of geometry 1-3 distribution in [-4, 4], [-5, 4] and [-4, 4] (°), respectively. And The mean value of β of these 3 geometries are around at 0°. The α and β distribution range of geometry 2 is wide, and the μ_α =-1.8 °, deviates more from 0° compare with

geometry 1 and 3. Correlates with the orientation tensor A_{33} of geometry 2 is 0.9958 small than geometry 1 (0.9967) and 3 (0.9962), which means the fibers in geometry 2 have more random orientation. The boxplot of mis-orientation indicators of fibers (α) also indicates the geometry 2 is a little directionally low compared to geometry 1 and 3 in the XZ plane.

After compaction, the average value of α and β of the geometry 1-3 get closer to 0°, and the distribution range are narrowed, especially for geometry 2 and 3. The A_{33} of geometry 1-3 increase to 0.9981, 0.9984 and 0.9981, respectively. As a conclusion, the mis-orientation distribution to 0°, and A_{33} close to 1.000, consistently indicate that the orientation of the fiber is distributed along $\boldsymbol{e_3}$/Z-axis. Here again this logically witnesses that the increase of the fiber volume fraction leads to a reorganization of the fibers toward the most compact one, that is to say, strictly straight and parallel fibers.

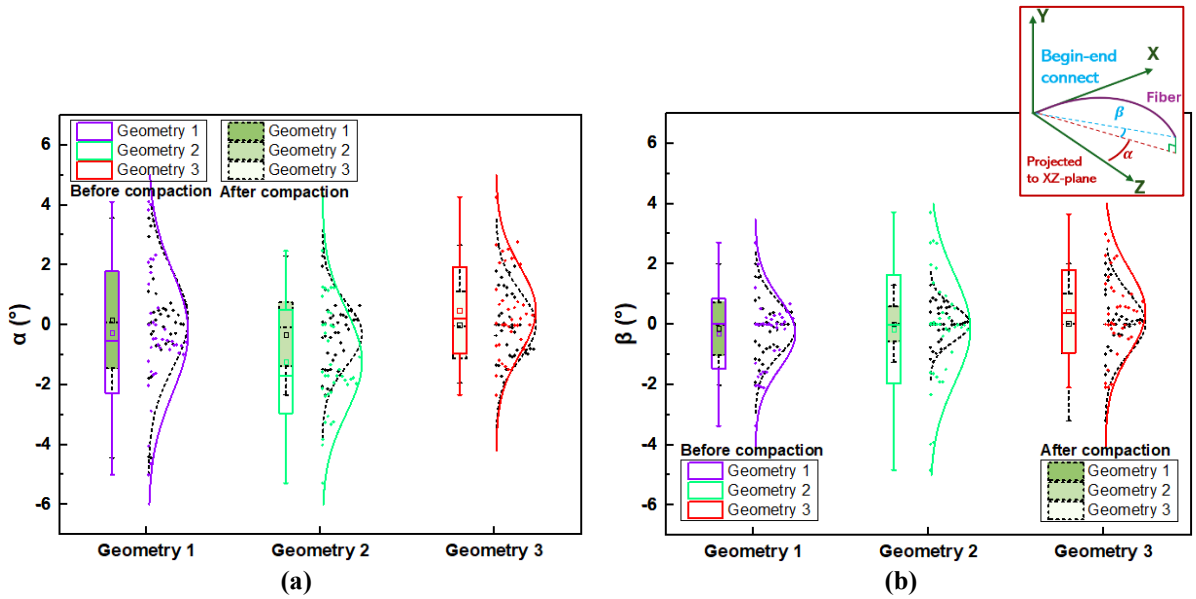

Figure 7.17 The boxplot of mis-orientation of fibers in the geometry 1-3. (a-c) α (°), (e-f) β (°).

b) Contact between fibers

The compaction forces are transferred between the fibers through the contact points. Here, we consider the number of contacts in created geometry 1-3: the contact between fibers, the contact between fibers and compaction plates, and total contact number (Figure 7.18).

In fiber bundle compaction test, the total contact consists mainly of the contact between fibers (C_{f-f}) and a smaller percentage of the contact between the fibers and the compaction channel/plates (C_{f-p}). This is because during the restricted compaction, the fibers are not free to displace freely in the X and Y directions, but due to their compression between each other. Therefore, the compaction leads to form new contact points continuously until the maximum

contact limit is reached. The C_{f-p} reaches a relatively stable value (for directional fibers) before compaction, and ΔC_{f-p} depends mainly on the contact between the top layer of fibers and the plate of compression. During compaction process, the number of C_{f-f} reaches saturation which witnesses the end of the available movements for the fibers and then the significant increase in the compression stiffness. The number of saturated C_{f-f} depends on fiber bundles with different microstructural characteristics of the fibers, such as curvature and aspect ratio and the fibers initial orientation. For example, under the same compaction conditions, even straight fibers and crimped fibers of the same material and dimensions (fiber diameter, number, length) can reach different maximum C_{f-f}.

The deviation of contact between the fibers, between fibers and plates, and the total contact before and after compaction are defined as ΔC_{f-f}, ΔC_{f-p}, ΔC_{sum}, respectively. Here again it is interesting to confirm that different microstructure with the same statistics lead to a very close evolution of the contacts. We however discuss the relationship between ΔC_{sum} and the variation of orientation tensor $\Delta A_{33} = A_{33_{after\ compcation}} - A_{33_{before\ compcation}}$. The ΔC_{sum} of geometry 1-3 is 4.39×10^4, 4.48×10^4 and 4.41×10^4, respectively; the ΔA_{33} is 0.0014, 0.0026, 0.0019, respectively. The orientation tensor A_{33} reflects the density of fiber orientation in the fiber length direction. When ΔA_{33} becomes larger, it means that the orientation of the fibers in this direction during compaction becomes denser. The density change affects the contact between the fibers, as the fibers tend to be more aligned along the fiber length direction, which makes it easier for them to contact each other.

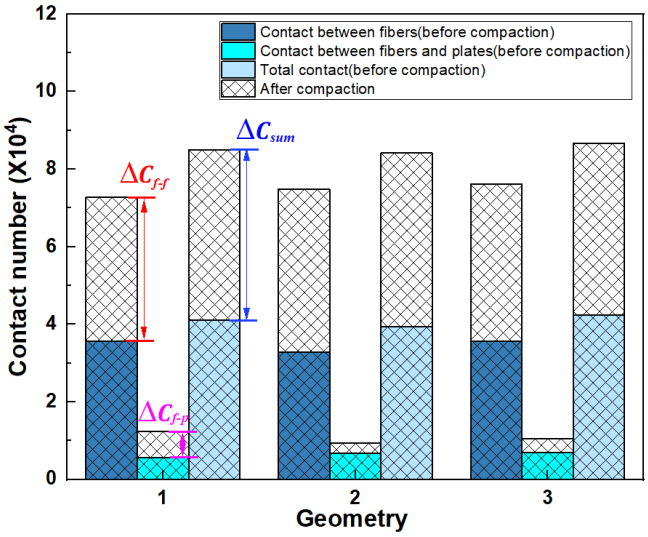

Figure 7.18 Contact number between fibers, fibers and compaction plates (compaction channel), total contact number.

Let's consider for geometry 1-3 the contact angle θ (°) which represents the angle between fibers in the direction of fiber's section and the contact angle γ (°) which is the angle between the fibers in the fiber's length direction, as presented in Figure 7.19 (a) and (b) respectively. The average and standard value are shown in Table 7.2. Before compaction, the angles θ and γ distribute in bigger value (standard deviation for γ) for geometry 2 compared to geometry 1 and 3, the large contact angle is likewise indicative of a relatively sparse distribution of fibers in geometry 2, related to a lower orientation tensor A_{33}. But the main conclusion is that the microstructure tends to converge from initially different configurations during the compaction.

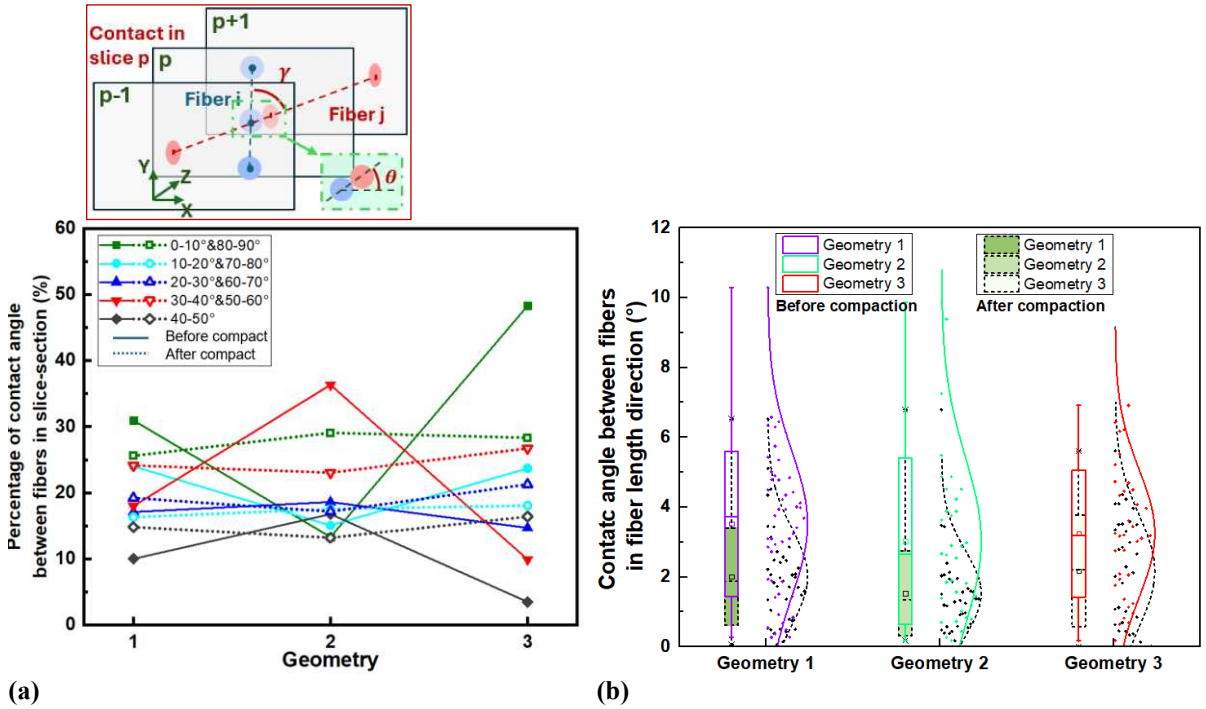

Figure 7.19 Contact angle. (a) Contact angle θ(°) between fibers in the fiber's section, (b) The boxplot of contact angle γ(°) between fibers in the fiber length direction.

Table 7.2 Contact angle γ(°) between fibers in the fiber length direction.

	μ	σ	μ	σ	μ	σ
	Geometry 1		**Geometry 2**		**Geometry 3**	
Before compact	3.55	2.235	3.03	2.66	3.21	2.11
After compact	1.90	1.86	1.13	1.24	1.35	1.30

c) Crimp and curvature

The boxplot of crimp of the fibers in geometry 1-3 is presented in Figure 7.20 and the average and standard value in Table 7.3. the curvature radii projected in XZ ($\overline{R_{XZ}}$) and YZ ($\overline{R_{YZ}}$) plane are illustrated in Figure 7.21 and Table 7.4. In geometry1-3, the change range of the crimp is

small (about 5%) but the trend is related to the projected curvature. However, it confirms the convergence of the three microstructures toward the closer and lower crimped one which was expected.

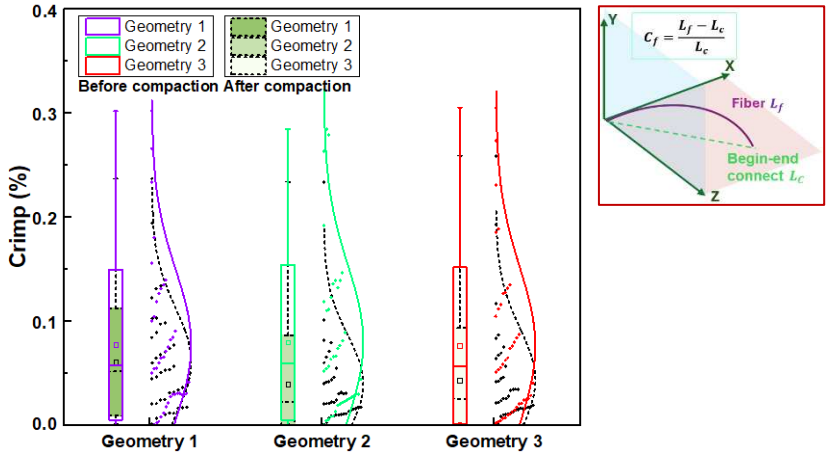

Figure 7.20 The boxplot of crimp of fiber for geometry 1-3 (%).

Table 7.3 Crimp of fiber for geometry 1-3 (%).

	μ	σ	μ	σ	μ	σ
	Geometry 1		**Geometry 2**		**Geometry 3**	
Before compact	0.078	0.072	0.080	0.074	0.077	0.075
After compact	0.060	0.051	0.043	0.047	0.046	0.050

The projected curvature radii of the fibers are significantly higher in the YZ plane than in the XZ plane. This phenomenon can be attributed to the gravity step which tends to foster the bending of the fiber in the YZ plane. The curvature in the YZ plane is more affected by this gravity step. This phenomenon has to be monitored and accounted and is one of the limits of the proposed strategy in the control of the microstructure parameters. It might be emphasized with fiber with a lower bending. The relative increase in $\overline{R_{XZ}}$ is higher than in $\overline{R_{YZ}}$ after compaction. In contrast, $\overline{R_{YZ}}$ value remains higher than $\overline{R_{XZ}}$ in the initial geometry, which means the fibers are more tightly arranged in the YZ plane. It limits the movement and deformation of the fibers in the Y direction, resulting in a smaller increase in $\overline{R_{YZ}}$ than $\overline{R_{XZ}}$. Consistently with the crimp, the global increase in curvature radii reflects here again, the microstructure convergence, the trend of realignment and the different responses of the fiber bundle to the external and internal forces acting in different directions, revealing the influence of the fiber microstructure on its macroscopic mechanical behavior.

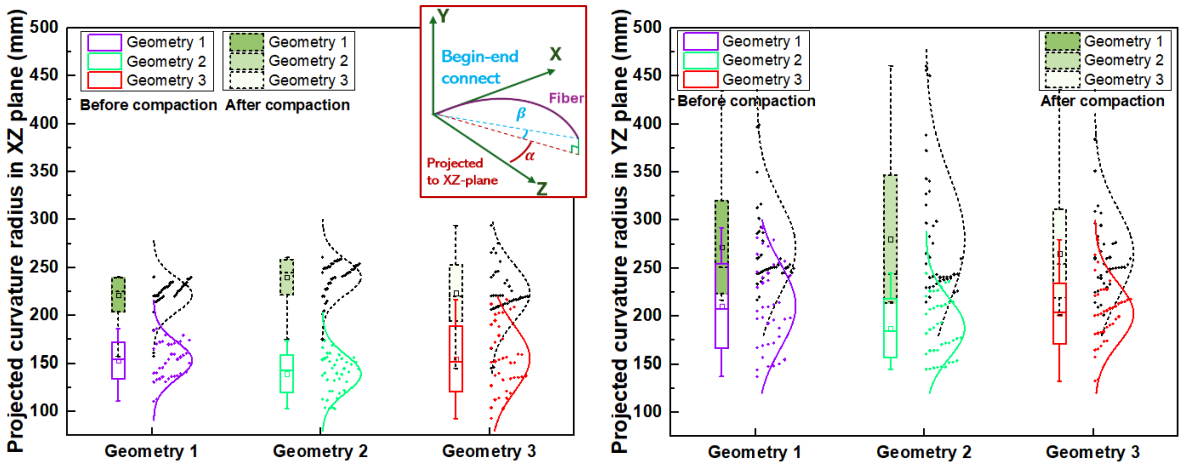

(a) (b)

Figure 7.21 The boxplot of projected curvature radii (mm) of fiber bundle geometry 1-3, (a) In XZ plane. (b) In YZ plane.

Table 7.4 Projected curvature radii in XZ plane and YZ plane of fiber bundle geometry 1-3 (mm).

	$\overline{R_{XZ}}$		$\overline{R_{YZ}}$		$\overline{R_{XZ}}$		$\overline{R_{YZ}}$		$\overline{R_{XZ}}$		$\overline{R_{YZ}}$	
	μ	σ	μ	σ	μ	σ	μ	σ	μ	σ	μ	σ
	Geometry 1				Geometry 2				Geometry 3			
Before compact	153	20	210	44	140	20	170	30	155	34	192	31
After compact	221	17	271	48	240	18	260	60	229	26	239	45

7.4 Conclusion

This section presented a strategy for a virtual numerical random fiber generator. The strategy is based on the principle of images reconstruction by XCT of fiber bundles and divided into two main parts: creation of the centerline coordinates of the fiber bundles, and introduction of the gravity field in the simulation during the compaction of the generated fiber bundles, to make the fiber's contact state close to the state of a real matrix-free fiber network.

Three geometrical models of fibers bundles were created by controlling the geometrical parameters statistics and their loading paths were simulated to be consistent with the micro-compaction experiments. The creation parameters were derived from the microstructural analysis of the micro-compaction experiment sample 2 (section 6). From the curves of the relationship between V_f and compaction pressure, the compaction results of the created fiber bundles seem to be in good agreement with the experimental.

The parameters of the geometrical model of the fiber bundle before and after compaction were

analyzed, and the fiber orientation distribution (A_{33} and mis-orientation) was closely related to the contact angle and curvature between fibers. Even though the structural parameters between the fiber bundles before compaction are different, they become close after the same compaction path. The monitoring of the microstructure evolution enables to show the convergence of the latter toward a close, better organized one with straighter fibers. This also verifies that, at the end of compaction, the compaction strengths are basically the same (0.28 MPa, 0.30 MPa and 0.32 MPa). However, even though the parameters of the internal structural of three fiber bundle geometries are consistent, there are differences in the distribution of fibers within them, and these small differences have an effect on the changes in the compaction curves at the late stages of compaction: the slip between the fibers leads to a different location of the compaction pressure drop. This illustrates the variability obtained and expected for the mechanical behavior of fibrous reinforcements.

After the compaction simulations of fiber bundle models with the same geometric parameters, the while reliability of the numerically created random fiber generator was verified. Therefore, the generator will be used to generate different fiber bundle models to investigate the effect of curvature on compaction performance in the next part. As well as discussing the effect of compaction path, slenderness of fibers, friction coefficient between fibers, and compaction speed on compaction behavior and micro-structure indicators.

Section 8 Analysis of internal structure factors affecting compaction behavior

This section focuses on the different compaction simulation of fiber bundles geometry and analyze the effect of the internal structural characteristics, like undulation, slenderness ratio and friction. The analysis of the simulation results highlights the important role of the internal structure of the fibers on the mechanical response of the fiber bundles during the compaction process. Finally, this section also provides a microscopic characterization of the compacted fiber bundles to further explore the effect of compaction behavior on the microstructure of fiber bundles and their mechanical properties. Now, we have validated the virtual estimator a wide range of use is opened, the two next sections illustrate with preliminary results how much the strategy will be helpful in the future for the understanding of the physics involved during the deformation of a fiber media. However, a greater number of simulations will have to be done to obtain an accurate and quantified parametric study.

8.1 Impact of undulation structure of fiber bundles

By setting different undulation parameters of virtual numerical random fiber bundle generator, a series of compaction simulations on fiber bundles is performed with the aim of exploring the influence of the undulation of the fibers on the compaction performance. In addition, the ideal straight fiber bundle geometry is performed here.

8.1.1 Create geometries with different parameters

In order to study the effect of misorientation and undulation of the fibers in the fiber bundle, multiple geometries of fiber bundles are created for compaction simulations. The compaction curves are compared, as well as their microstructural characters. Geometries 4-11 are all composed of 40 fibers, the basic parameters are same as Table 7.3 (the fiber diameter and so on), misorientation and undulation parameters shown in Table 8.1.

Table 8.1 Orientation parameters of the created geometries.

Geometry	Misorientation and undulation parameters		
Random straight fiber (geometry 4)	No misorientaion	No undulation	
Square distribution fiber (geometry 5)	No misorientaion	No undulation	
Compact distribution fiber (geometry 6)	No misorientaion	No undulation	
Random straight fiber2 (geometry 7)		Undulation point =0; $\sigma_{u_z} = 0$	
Random curved fiber1 (geometry 8)	μ_β = 0.055;	Undulation point =1; $\sigma_{u_z} = 110$	
Random curved fiber1 (geometry 9)	σ_β = 1.089;	Undulation point =2; $\sigma_{u_z} = 110$	μ_{u_X}= 0.12;
Random curved fiber2 (geometry 10)	μ_α = -1.510;		σ_{u_X}= 0.14;
Random curved fiber3 (geometry 11)	σ_α = 2.294;	Undulation point =3; $\sigma_{u_z} = 110$	μ_{u_Y}= 0.02;
		Undulation point =4; $\sigma_{u_z} = 110$	σ_{u_Y}=0.2;

In the creation of the geometries 4 to 7, the fibers are designed as straight line, and geometries 4 to 6 exhibit no mis-orientation and undulation characters. The idealized straight fiber bundle geometry is a simplified approach in the study of fiber bundles behavior. This approach allows the researcher to ignore complexities such as curvature, entanglement, and orientation within the fibers, thus focusing on the theoretical analyze of the mechanical behavior of the fiber bundle.

Figure 8.1 shows the of fiber bundle geometries 4 to 6 before imposing gravity, for which random fiber center point locations were generated by MATLAB programming. Then, the gravity field simulation was then performed by ABAQUS® to obtain a stable contact geometry model between the fibers. The initial volume fraction of geometries 4 to 6 are respectively 69.8 %, 78.5 % and 82.9 % after imposing gravity.

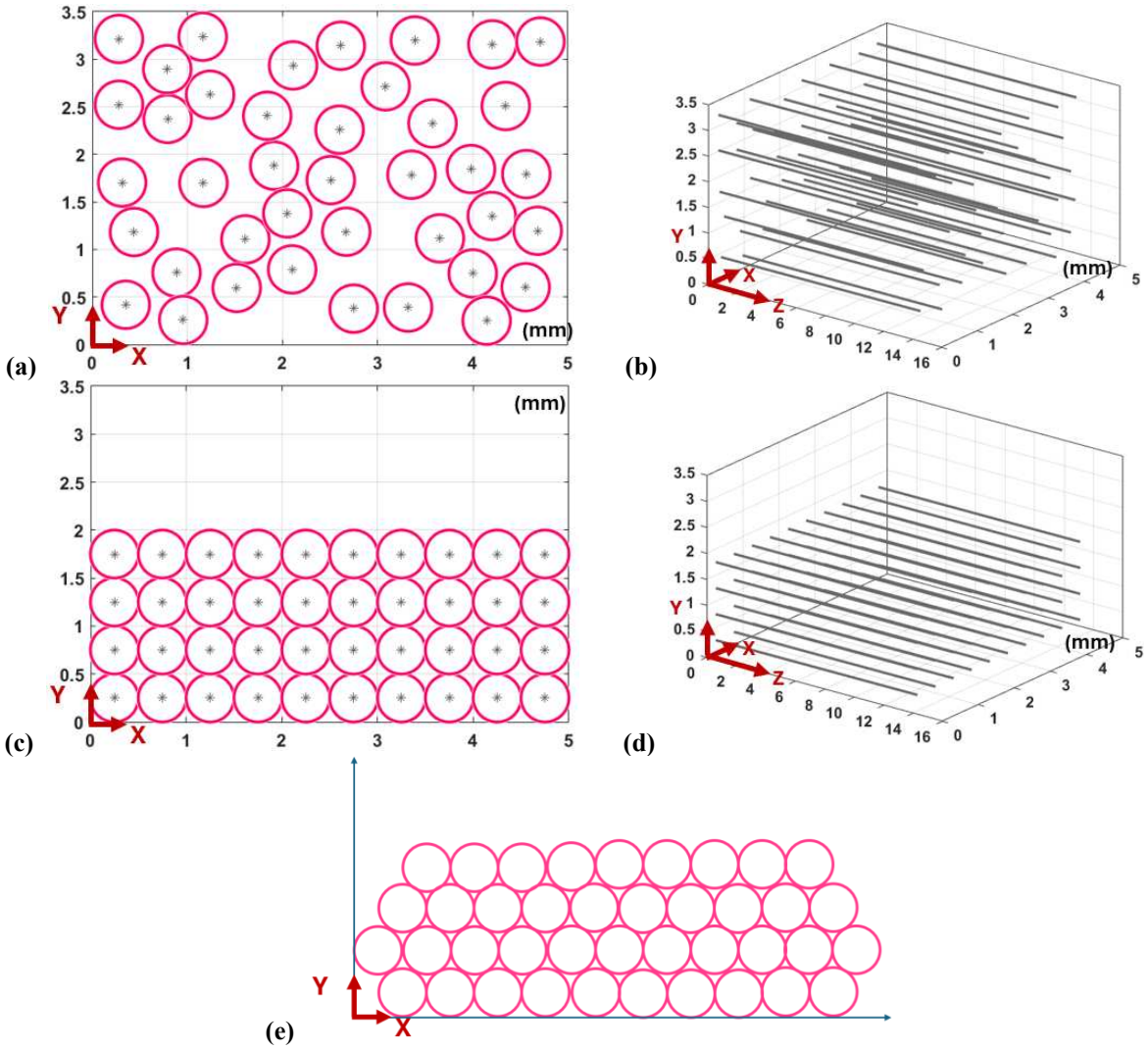

Figure 8.1 Created random straight fibers (mm). (a, b) Geometry 4, (c, d) Geometry 5, (e) Geometry 6: compact arrangement model $V_{f_0} = 82.95\%$.

Geometry 7 was created with mis-orientation parameters without undulation point in the fibers, the initial volume fraction is 62.8 %; geometries 8 to 11 are created with undulation parameters, to understand the effect of undulation of fibers on the compaction behavior. The initial volume fraction is 46.8 %, 43.5 %, 34 % and 27.8 %, respectively.

As mentioned above, the fiber's movement and the deformation in the fiber length direction account for the main part during the compaction, which changes the undulation and orientation of the fibers. So, in next part, the compaction simulation is performed for different fiber bundle structures, and the effect of their microstructural parameters (contact, directionality, curvature) is analyzed after compaction.

8.1.2 Compaction simulation with straight fiber geometries

The compaction simulation strategies used for compaction of straight shaped fiber bundles (geometries 4, 5 and 7) are the same that those presented in Table 6.1, i.e., to apply compaction until a volume fraction of 80% is reached (Figure 8.2 and Figure 8.9). Concerning geometry 6, the initial volume fraction is too high ($V_{f_0} = 82.9\ \%$) compared to the three others, so, the analyze concerns only the contact indicators.

For the randomly distributed linear fiber bundle model in geometries 4 and 7, the compaction force of the fibers is almost zero until V_f=72.8 %, where the movement of the fibers dominates. At V_f=72.8 %, the compaction force increases rapidly as the volume fraction increases. And at the position around V_f=74-75 %, there is a decrease in the compaction pressure for both models, which is again due to the slip between fibers, and at high volume fractions, even small slips of fibers can lead to large changes in pressure. This illustrates here again the difficulty induced by the stick-slip phenomenon between fiber which definitely a challenge for the modeling but above all will lead to instability phenomenon and then to an expected variability even for real structures. Compared to geometry 4, the fiber arrangement in geometry 7 is not completely parallel, and the gaps between fibers are relatively large, resulting in fibers that are more likely to slip during compaction. The position of pressure drop occurs at V_f=74 % earlier compared to geometry 4.

For geometry 5 the straight fibers are perfectly parallel, and their highly ordered arrangement makes the overall structure more stable and resistant to deformation under compression pressure. In the quasi-static compression process, the top layer of fibers suffers a uniform compression force (Figure 8.3), the quasi-static compression speed allows to finally obtain the ordered fiber structure as no slip will occur the fibers slip, so there is no fluctuation in the compaction curve.

The two steps compaction/compression of granular and fibrous media is then reduced to a pure compression step since almost no reorganization is possible. We then obtain the compressive stiffness induced by the fiber material stiffness and the fiber transverse strains. The slope consequently obtained, since we have only linear contact, is the highest stiffness that can be reached for such bundle, it then interesting as a matter of comparison.

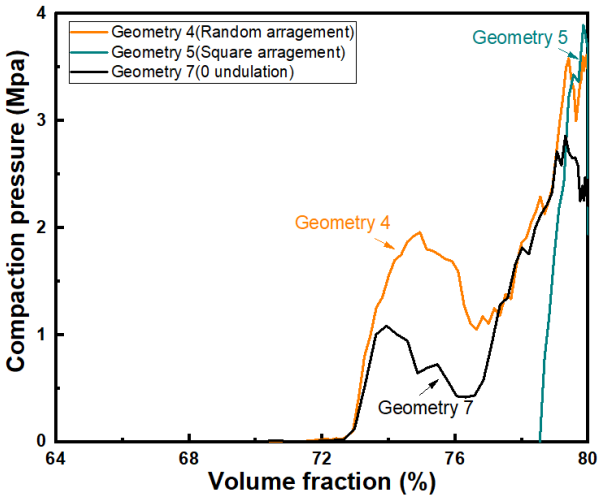

Figure 8.2 Relationship between volume fraction and compaction pressure: geometry 4, 5, 7 with straight fibers.

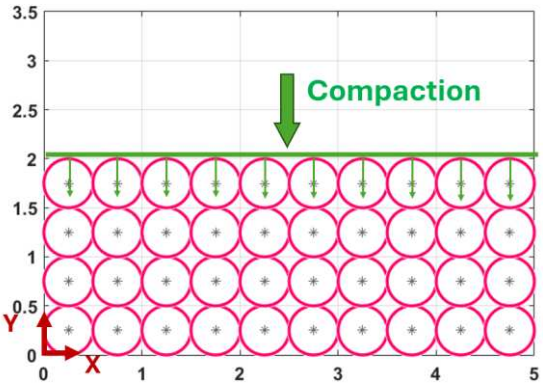

Figure 8.3 Compaction force transfer to fibers of geometry 5.

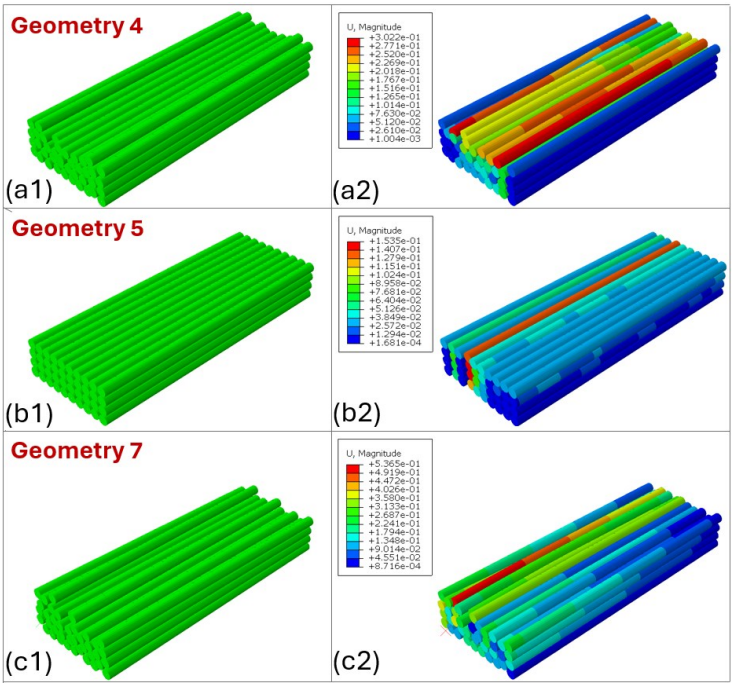

Figure 8.4 3D model before and after compaction: Geometry 4 ,5, 7 with straight fibers.

From the 3D geometry of the compacted fiber bundles (Figure 8.4), even parallel straight fibers showed deformation with displacement of fibers, so the microstructures of geometries 4-7 were discussed to analyze the changes in contact and other indicators.

a) Orientation and mis-orientation

The geometry 4-6 consists of perfectly parallel and closely spaced straight fibers, so their orientation tensor A_{33}=1, and for geometry 7, A_{33}=0.9999 (Figure 8.6). After compaction, the random aligned fibers are more likely to move towards each other and undergo bending deformation, as shown by the fiber centerline in Figure 8.5 and the orientation tensor in Figure 8.6. This illustrates that a unperfect organization lead the fibers to occupy locally the voids and then are subjected to bending. Therefore, the bending stiffness of the fibers due to material or entanglement might have an impact on the compression behavior.

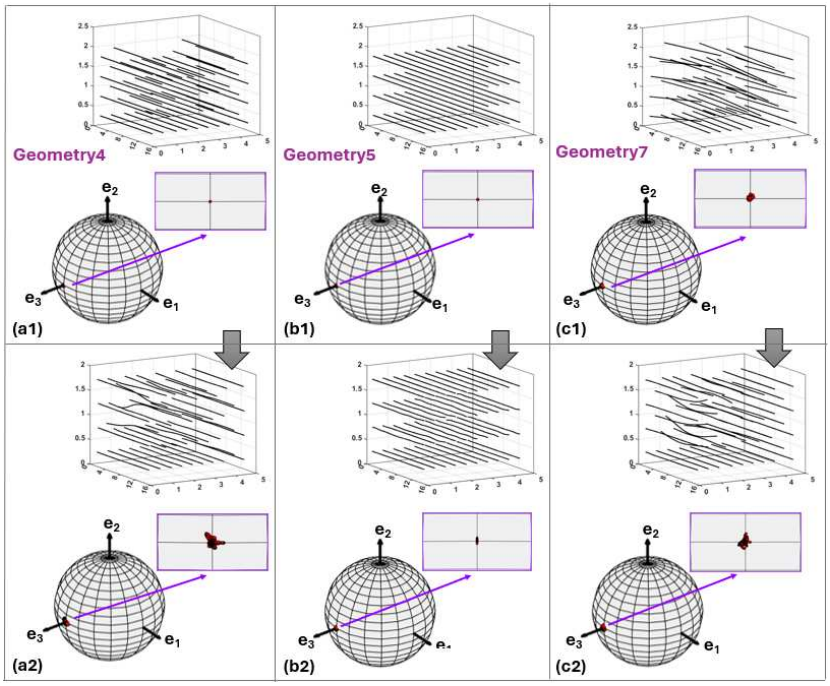

Figure 8.5 Orientation unit spheres of the centerline of fibers. (a1, b1 andc1) Orientation unit sphere for geometries 4, 5 and 7 before compaction simulation (initial geometry), (a2, b2 and c2) Orientation unit sphere for geometries 4, 5 and 7 after compaction simulation.

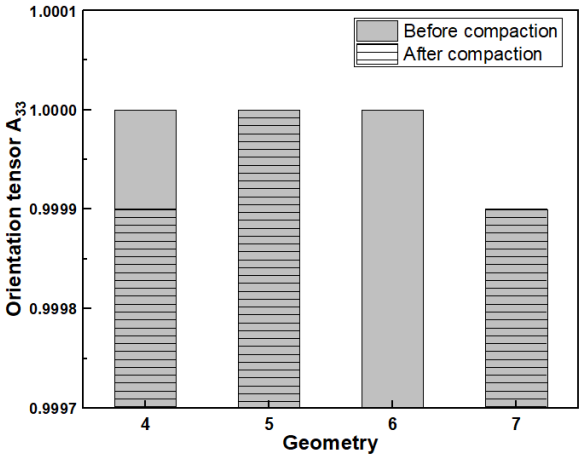

Figure 8.6 Orientation tensor A_{33} of geometries 4, 5 and 7 before and after compaction, and orientation tensor A_{33} of geometry 6 before compaction.

In addition, Figure 8.7 show the boxplot of the mis-orientation angle of fibers in geometry 4, 5, 7. Before the compaction, the fibers are almost parallel but straight, the α and β distributed in [-1.2, 1.5] (°) and [-1.1, 2] (°) respectively. The geometry 4 and 5 consist of totally parallel fibers, so that the α and β are $0°$ before compaction.

During compaction, for geometry 7, the fibers trend to rearrangement to fill the space between fibers and converge through a better orientated and straight configuration. The mis-orientation angle shown the global orientation of fibers, so the distribution of α and β close to 0°. On the opposite geometry 4, consistently with the A_{33} variation, exhibit a large increase in the mis-orientation distribution which means that the initial random distribution led the fibers to reorient in the XZ plane in order to fill in the gaps randomly distributed according the XZ plane. The same phenomenon is not observed for geometry 5 since the fibers are organized. Regarding β it is interesting to notice, in the direction of compaction, the reorganization and the convergence of the three initially different microstructure during compression, which explains the similar trends at the end of the compression curves for different but close initial microstructure.

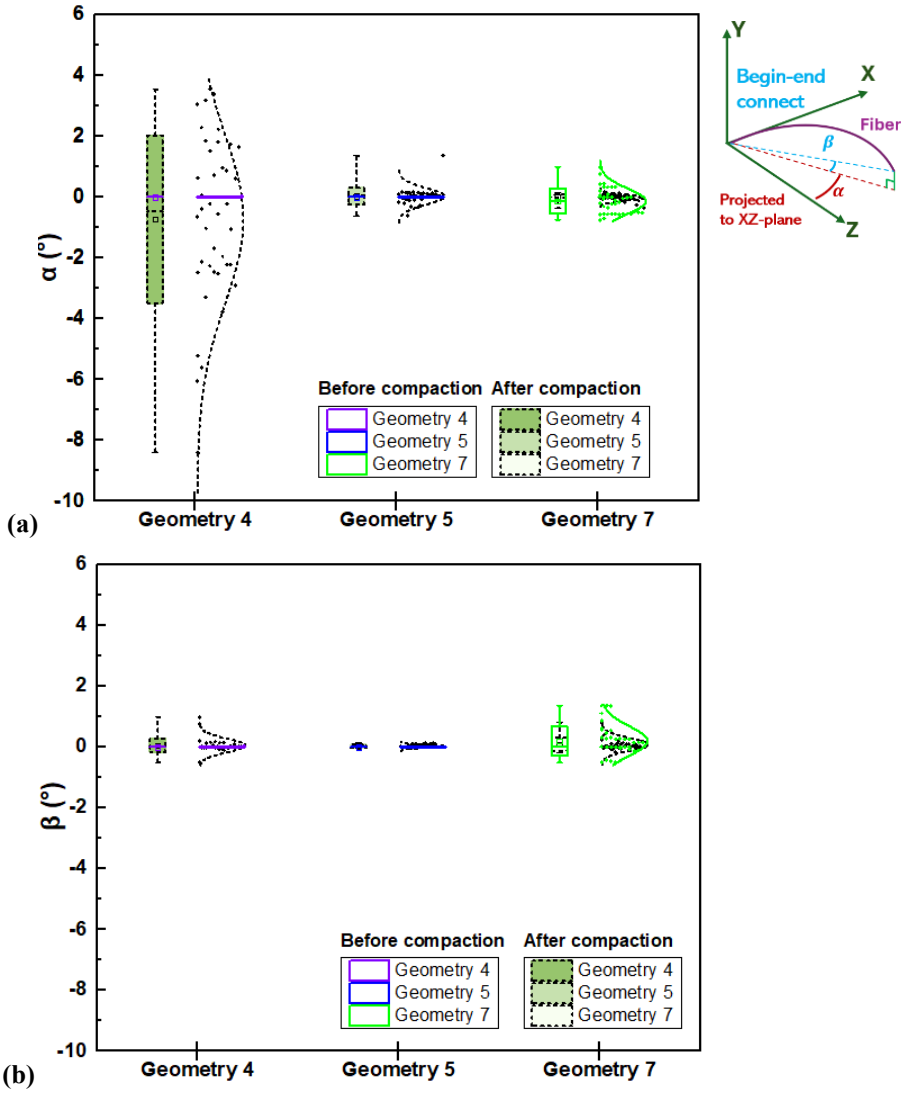

Figure 8.7 Boxplot of mis-orientation of fibers in geometries 4, 5, 7. (a) α (°), (b) β (°).

b) Contact and undulation of fibers

The total contact number and also contact between fibers and contact between fibers and compaction plates is shown in Figure 8.8 (a); the contact angle between fibers in the fiber's section shown in Figure 8.8 (b). The contact number of geometry 5 is almost same, because the fibers are parallel and tightly arranged, which are trend to small bending deformation under static compaction load. The crimp (Table 8.3) and projected curvature radii (Table 8.4) show the fibers are submitted to local very small bending deformation.

Compared to geometry 5, the fibers of geometry 4 and 7 are trend to bending deformation and rearrangement. After compaction, the total contact number increases, the undulation crimp and projected curvature radii change, the fibers bend.

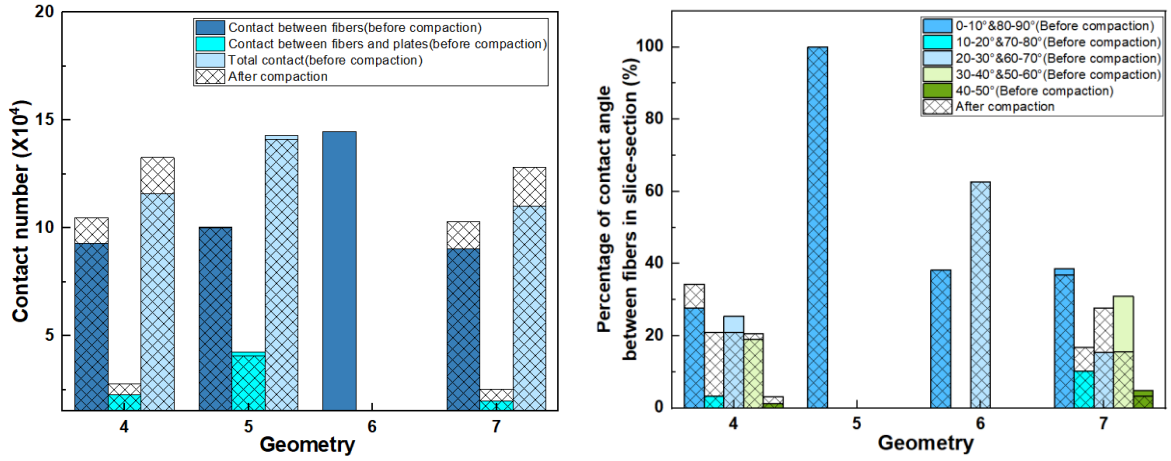

(a) (b)

Figure 8.8 (a) Contact number between fibers, fibers and compaction plates and total, (b) Contact angle between fibers in the fiber's section (θ (°)).

Table 8.2 Contact angle γ (°) between fibers in the fiber length direction.

Compact	μ	σ	μ	σ	μ	σ	μ	σ
	Geometry 4		Geometry 5		Geometry 6		Geometry 7	
Before	0	0	0	0	0	0	0.391	0.251
After	0.083	0.079	0.029	0.014			0.206	0.101

Table 8.3 Crimp of all the fibers in geometries 4 to 11 (%).

Compact	μ	σ	μ	σ	μ	σ	μ	σ
	Geometry 4		Geometry 5		Geometry 6		Geometry 7	
Before	0	0	0	0	0	0	0	0
After	0.003	0.007	≈0	≈0			0.004	0.008

Table 8.4 Projected curvature radii $\overline{R_{XZ}}$ and $\overline{R_{YZ}}$ (mm).

Compact	$\overline{R_{XZ}}$		$\overline{R_{YZ}}$		$\overline{R_{XZ}}$		$\overline{R_{YZ}}$		$\overline{R_{XZ}}$		$\overline{R_{YZ}}$		$\overline{R_{XZ}}$		$\overline{R_{YZ}}$	
	μ	σ	μ	σ	μ	σ	μ	σ	μ	σ	μ	σ	μ	σ	μ	σ
	Geometry 4				Geometry 5				Geometry 6				Geometry 7			
Before	∞	∞	∞	∞	∞	∞	∞	∞	∞	∞	∞	∞	∞	∞	∞	∞
After	1483	555	1078	337	55811	3352	10698	2234					1069	407	833	466

The orientation tensor A_{33}, mis-orientation (α, β) and undulation indicators show that, for the initial geometries 4 and 7, the fibers are rearranged and slightly bent, whereas fibers of geometry 5 are also more slightly bent. As the bending and rearrangement are easier to occur in geometries 4 and 7, the volume fraction increases more easily for lower pressure, as it can be seen on Figure 8.2 with a drop at V_f=74 % to 75 %.

The comparison between 4 and 7 is also interested because almost the same microstructure parameters are obtained at the end of the calculation.

8.1.3 Compaction simulation with undulated fibers geometries

Geometries 8 to 11 are created with the same initial parameters; besides undulation point number, the number of bending points increased from 1 to 4, and V_{f_0} are 46.7 %, 43.5 %, 34 % and 27.8 %, respectively. Figure 8.9 (a) shows the relationship between V_f and compaction pressure; at first, only gravity is imposed to the initial geometries 8 to 11. For more undulated and entangled fiber bundles compacted to the same volume fraction, more pressure is required. The undulation and entanglement of the fibers increases the contact number or length and thus, the interaction forces between the fibers. This avoids fibers to slip and rearrange and thus requires a greater external pressure to achieve the same compaction. In addition, bent and twisted fibers may spatially form more locked structures that are difficult to break during compaction, thus also increasing the force required for compaction. This phenomenon highlights the importance of structural intricacy within the fiber bundle on its compaction ability. One can notice, especially for the geometry 11 which is the most irregular, that as previously explained the increase of the compression stress led to instabilities especially at high volume fractions resulting by significant drops in the compaction curve. This phenomenon is also emphasized by the smooth step at the end of the dynamic explicit calculation as it will be tackled in section 9. Such instabilities are among the most interesting phenomenon to be analyzed in the future.

In order to exclude the effect of different initial volume fractions on compaction, geometries 9 to 11 were first compacted to V_f=46.8 % (Figure 8.9 (c)), and then its compacted fiber bundle geometry model was re-imported into ABAQUS® for the second compaction simulation (Figure 8.9 (b), shown with dot line). Compared to compaction from different initial fraction (Figure 8.9 (a)), the compaction pressure is lower at V_f=70-80 %, the final compaction pressure dropped by 0.8 Mpa, 0.4 Mpa and 0.3 Mpa respectively for geometries 9, 10 and 11. However this does not change the conclusion of the undulation influence on the compression behavior. During pre-compaction (compaction with low V_{f_0}), the fibers undergo predominantly ordered rearrangement, and this rearrangement may reduce the friction and resistance to each other during subsequent compaction. Moreover, pre-compaction results in fewer voids between fibers, and fiber bundles become tight and more structurally stable. Thus, lower pressures are required

to further increase the volume fraction. However, a kind of maximum volume fraction exists for compacted materials due to the locking the geometry imposed by friction. All samples, whether pre-compacted or not, may reach a similar state of structural locking, where all fibers are tightly packed and few possible movements for the fibers. Thus both pre-compacted and un-pre-compacted fiber bundles should exhibit similar physical confinement, and thus the end compaction pressures for both are in the same range consistently with Figure 8.9 (b) and Figure 8.10.

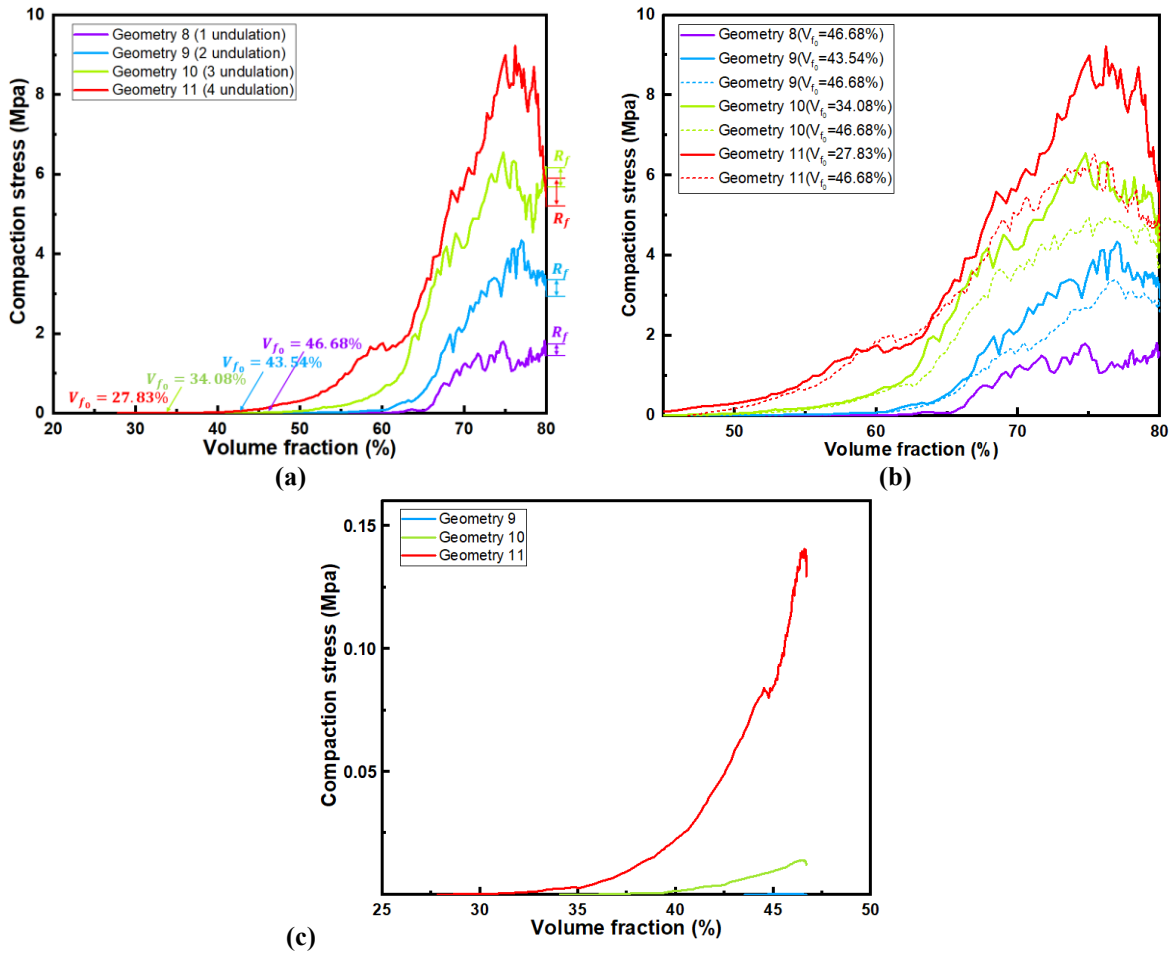

Figure 8.9 Relationship of Volume Fraction and Compaction Pressure: Geometries 8 to 11, created with different undulation parameters. (a) Compaction test with different V_{f_0}, (b) Compare the compaction test with (a) and (d), (c) Pre-compaction test with different V_{f_0}.

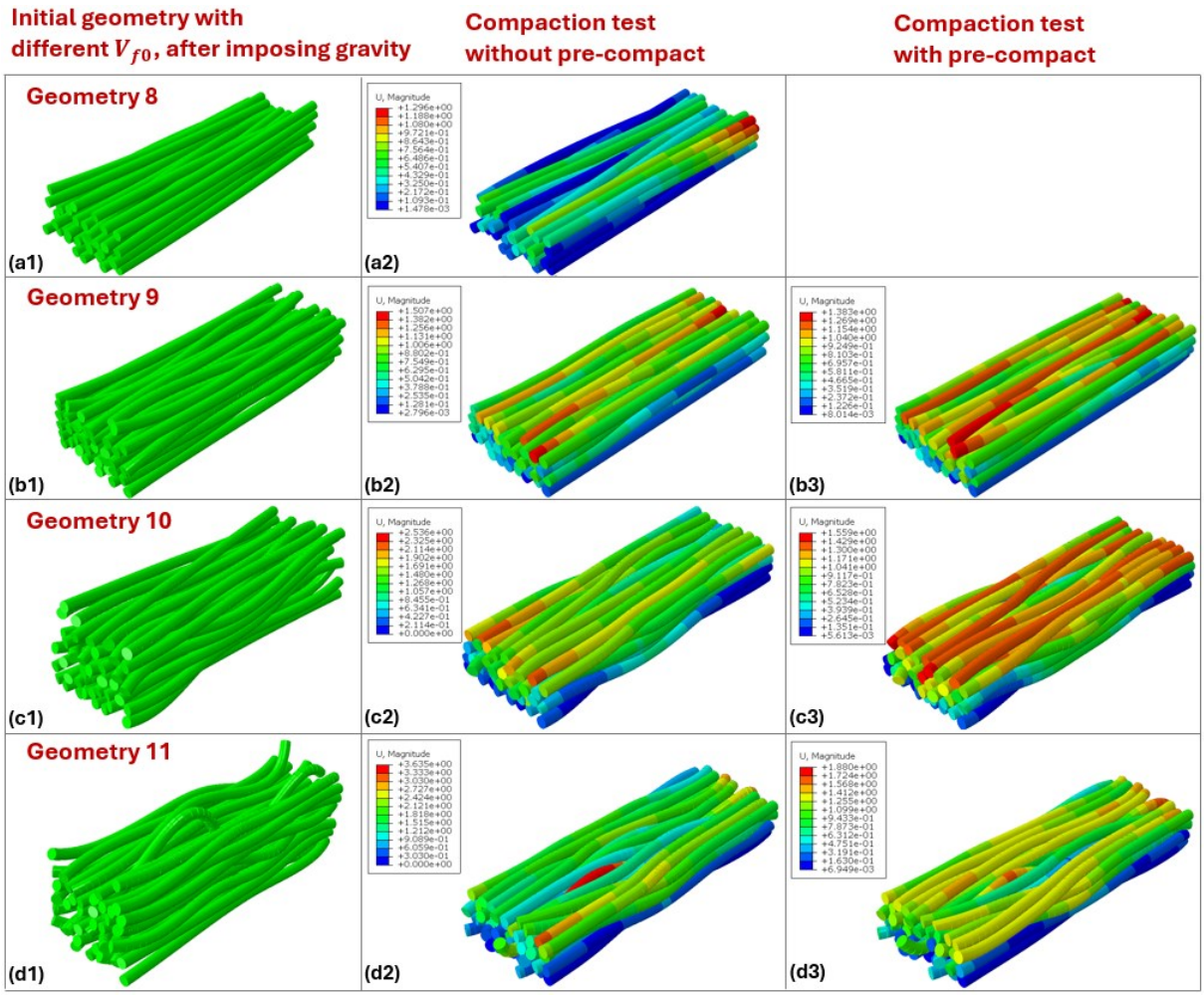

Figure 8.10 The 3D rendering of (a-d) geometry 8-11. (a2-d2) Compaction simulation without pre-compact with end $V_f = 80\%$, (b3-d3) Compaction simulation with pre-compact with end $V_f = 80\%$..

The microstructure indicators of geometries 8 to 11 were analyzed after the development of indicator tools, to understand the effect of undulation parameters in fiber bundle geometries before and after compaction.

a) Orientation and mis-orientation

The orientation unit spheres, centreline of fiber and orientation tensor A_{33} are shown in Figure 8.11 and Figure 8.12 respectively, the boxplot distribution of mis-orientation (α, β) of the fiber bundle is presented in Figure 8.14. It should be noted that the ΔA_{33} (the difference of orientation tensor A_{33} before and after compaction) gradually increases with the increase of fiber undulation points. The reason for the increase in the ΔA_{33} values due to the increase in fiber undulation points related to the effect of fiber curvature on inter-fiber voids and interactions. Bent or entangled fibers need to be rearranged to fit the spatial constraints during

compaction, a process that led to more complex contact and force transfer between fibers, that compacts the overall directionality of the fiber bundle. This effect is more pronounced when the number of fibers undulation points increases, leading to more complex changes in compaction effects and fiber alignment directionality, which are reflected in changes in A_{33}. However, the reorganization cannot lead to the sale final values, that is to say, it leads to a realignment and straightening of the fibers until the locking of the geometry occurs. The locking configuration is all the more entangled that the initial configuration is.

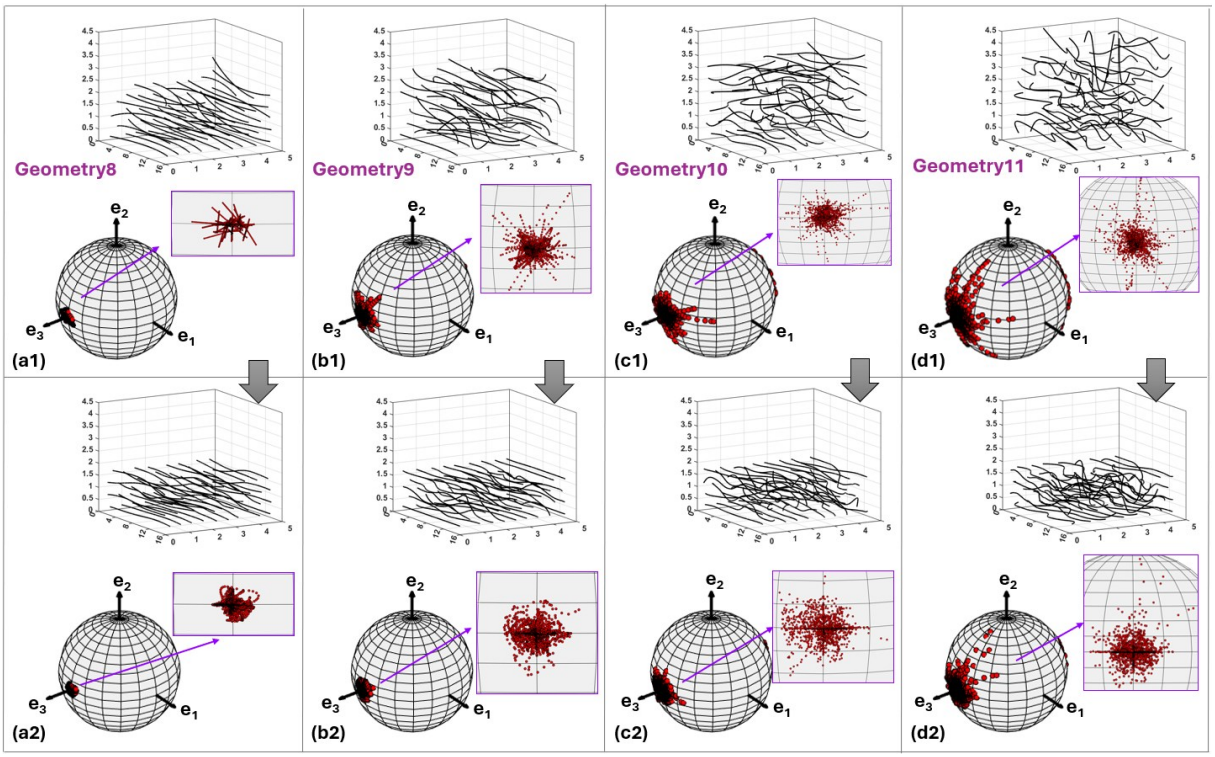

Figure 8.11 Orientation unit spheres of centerline of fiber. (a1-d1) Geometries 8 to11 before compaction simulation (initial geometry), (a2-d2) Geometries 8 to 11 after compaction simulation.

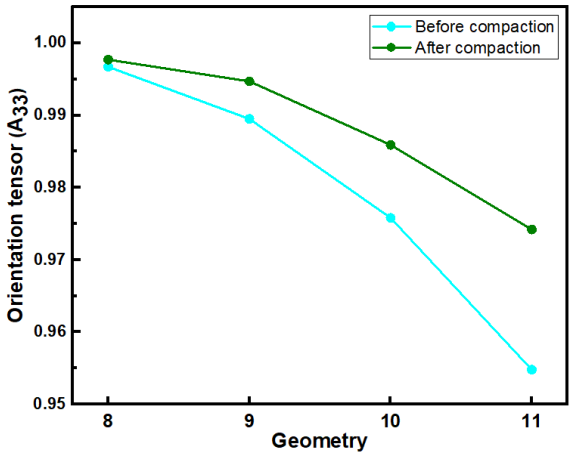

Figure 8.12 Orientation A_{33} of Geometries 8 to 11 before and after compaction.

First, the influence of the creation step is tackled regarding α and β angle. Here, the effect of the gravity field imposed during the fall down of fibers for the initially separated state is analyzed. Introducing a gravity field in the simulation models the free-fall effect on fibers. This aims to reflect the alignment and contact state of fibers under gravity more realistically. However, this method cannot avoid the possible displacements and rotations of the fibers due to gravity during the free fall process. One can notice that even if the values remain in the same order of magnitude, the initially equal distribution for all the geometry is not kept. The gravity step leads to an increase of the angle dispersion, which can be different for the different configurations. This has to be accounted in the analysis but also this explains why we talk about controlled parameters and not imposed ones. As shown in Figure 8.13, the α angle is less affected by the gravity field probably because it represents the deflection of the fibers relative to the Z-axis towards the X-axis. In contrast, when a gravity field is introduced, gravity acts along the Y-axis. Therefore, the motion and alignment of the fibers in the Z-X plane is less affected by gravity. In contrast, the β angle as deflection in the Z-Y plane is more directly affected by gravity. Here this leads much wider distribution of β angle concentrated with a little change in the average value. Anyway, this reveals the impact and the anisotropy of the effect of gravity on fiber alignment in different directions we have to deal with and account on.

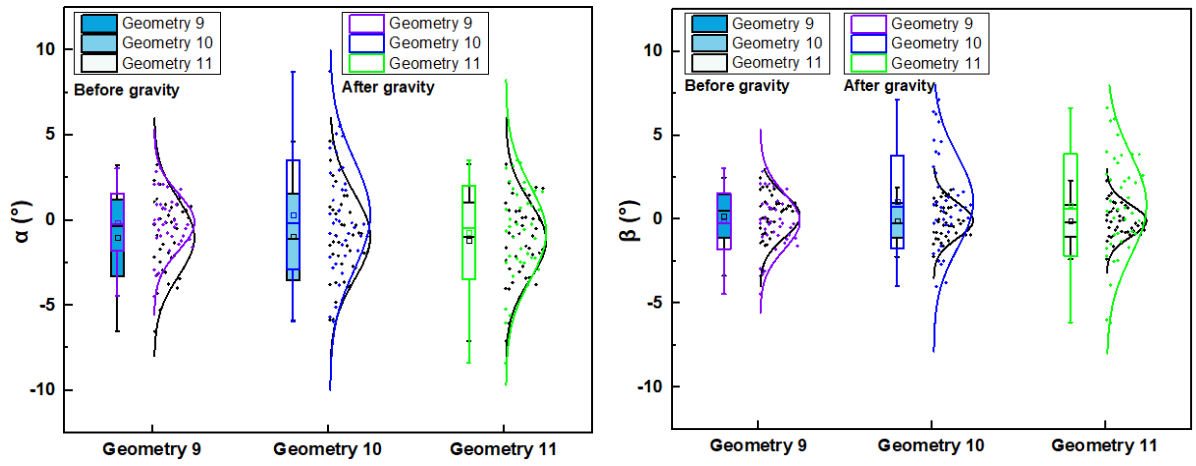

Figure 8.13 The boxplot of mis-orientation of fibers in geometries 9 to 11 before and after gravity. (a) α (°), (b) β (°).

After compaction, for the geometrical model of fiber bundle with linear structure, the fibers mainly changed the offset direction and the fiber deflection decreased during the compaction process. For the geometrical model of fibers (geometry 8-11) with entangled bends, the change in the β angle before and after compaction is more pronounced (Figure 8.14). Before

compaction, the boxplot is much wider for beta angle, implying a wide range of deflection angles and a high directional diversity of fibers. The compaction using a parallel flat plane causes the fibers to adjust toward a more parallel state. Thus, achieving a more stable structural configuration during compaction. direction. The β angle distribution is concentrated around 0 degrees, reflecting the tendency of the fiber bundles towards a quasi-parallel stable state during compaction.

Although the compaction process will prompt the fiber rearrangement and tends to reduce the directional dispersion, due to the interaction and friction between the curved fibers, these fibers are not as easy to align in the XZ plane, as straight fibers, and therefore still show a wider distribution after compaction. The deflection distribution (α) of the fibers follows the same trend as the distribution of the directional tensor spherical units (Figure 8.11).

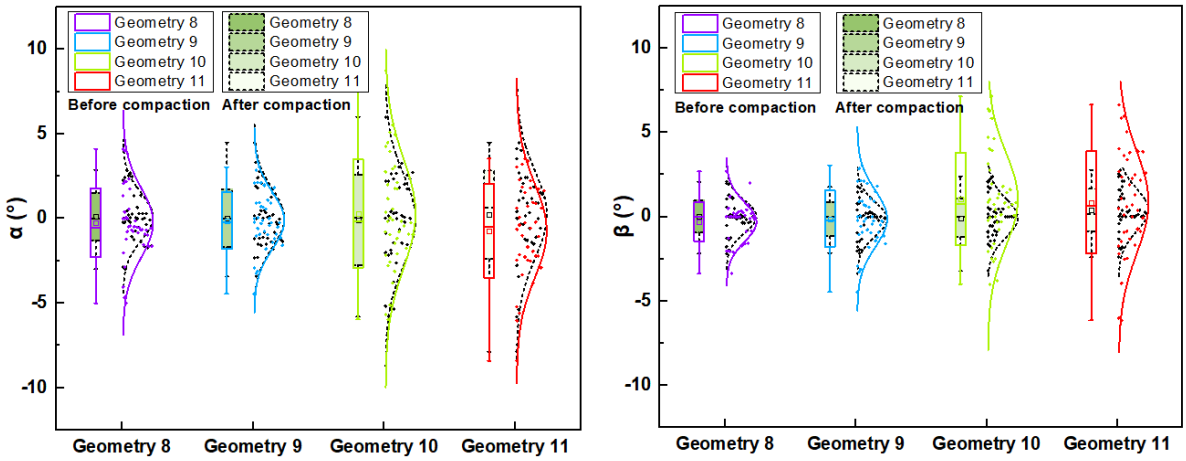

Figure 8.14 Boxplot of mis-orientation of fibers in geometries 8 to 11. (a) α (°). (b) β (°).

b) Contact

Figure 8.15 shows the contact number between fibers, fibers and compaction plates and total contact number of geometries 9 to 11, Figure 8.16 presents the boxplot of contact angle between fibers (θ and γ). The average and standard values of γ are presented in Table 8.5. The bent and entangled fiber bundle geometries 8 to 11 have less total contact with each other in the uncompacted state. The undulation provides the fibers with more freedom of spatial deformation, which keeps the fibers widely spaced from each other. As a result, the initial volume fraction of bent and twisted fiber bundles is low for the same number of fibers. That is, the volume occupied in space is relatively large. When external pressure is applied to the fiber

bundles, these fibers are more likely to be rearranged and densified during the deformation. After compaction the trend is inverted showing an increase of the contact numbers with the undulation, shown in Figure 8.15. This is logical because the entanglement requires more fibers to be in contact in order to reach the same volume fraction, however, the small differences of the values after compaction also shows that the number of contacts is not the unique parameter that drives the compression stiffness which was not so obvious and has to be kept in mind for the analysis of the compression behavior of fibrous media.

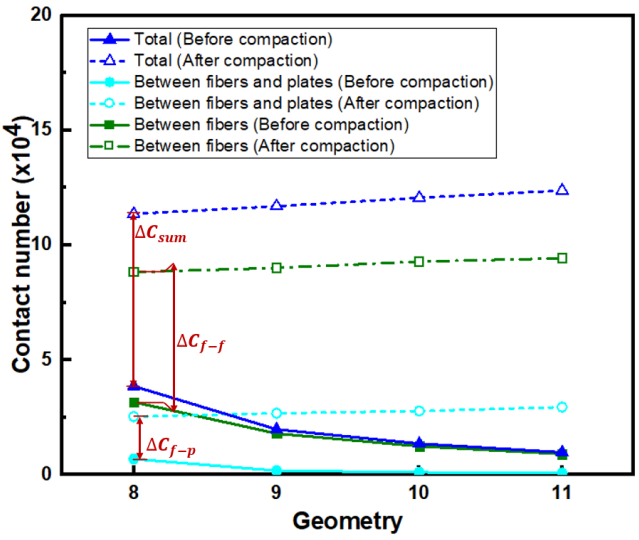

Figure 8.15 Contact number between fibers, fibers and compaction plates and total.

The contact angles are also very interesting to study (Figure 8.16). Considering γ, before compaction, as the undulation of the fiber increased (from geometry 8 to 11), the fibers are more dispersed and the interaction between them is relatively weak, so the contact angle is distributed in a relatively wider range with a higher average value. After compaction, the contact number increase slightly, the contact angles of the fibers in the cross-section are mainly concentrated in the range of smaller angles, which indicates that the interaction and constraints between the fibers are enhanced, and the alignment of the fibers is more consistent. However, it is very interesting to notice here again that the realignment is all the more possible that the initial curvature is low. The increase in fiber undulation implies the presence of interlocking phenomena between the fibers in the form of entanglement which cannot permit the realignment. The relative decrease in the average value and standard deviation is significantly lowered as the undulation increased.

At the end of the compaction, the contact angles distribution is then significantly different whereas the contact number was not that much. This is confirmed by the values of θ, a

concentration of contact angle (θ) in the range of [10-20° & 70-80°] for geometry 11 is noticed while it decreases for configuration 8 and 9. For the geometry 8 and 9 increase concerns the [0-10° & 80-90°] range so a better organized configuration. Indeed, the [10-20° & 70-80°] contacts are more easily transformed to concerns the [0-10° & 80-90°] as the reorganization occurs for less undulated configuration. The realignment is then possible for low angles and is almost locked for higher angles which explains their relative stability. For more undulated configuration such as geometry 11, the locking for [10-20° & 70-80°] occurs and the realignment is not possible.

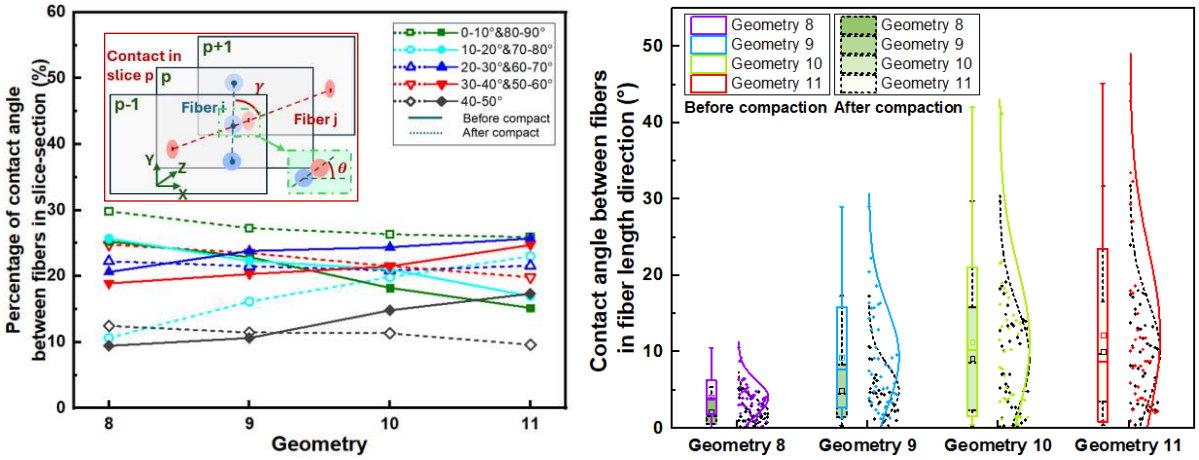

(a) (b)

Figure 8.16 Contact angle. (a) Contact angle between fibers in the fiber's section (θ(°)), (b) Contact angle between fibers in the fiber's length direction (γ(°)).

Table 8.5 Contact angle γ (°) between fibers in the fiber length direction.

Compact	μ	σ	μ	σ	μ	σ	μ	σ
	Geometry 8		Geometry 9		Geometry 10		Geometry 11	
Before	3.059	2.235	8.102	6.896	11.276	9.823	10.078	11.295
After	1.920	1.515	3.529	3.650	8.340	6.923	9.626	6.706

c) Crimp and curvature

The crimp boxplot, average and standard values of fiber bundle geometries 8 to 11 are presented in Figure 8.17 and Table 8.6 respectively and the projected curvature radii in XZ ($\overline{R_{XZ}}$) and YZ plane ($\overline{R_{YZ}}$) in Figure 8.18 and Table 8.7. They confirm the previous analysis.

The crimp of the fibers in geometries 8 to 11 increases, which was likewise responded to by increased creation undulation point number. This phenomenon exists before and after compaction. This is related to the previously mentioned, entanglement within the fiber bundle.

Fibers partially straighten during compaction. However, due they do not straighten completely all the less than the locking configuration imposed by entanglement is disordered. This is the reason why fibers remain curved, and thus the crimp is higher and projected radii is smaller. Combine the compaction curve (Figure 8.9) and the crimp of the fiber bundle geometries, the geometry with high crimp requires more pressure to rearrange and movement to achieve the same volume fraction than fibers with low crimp.

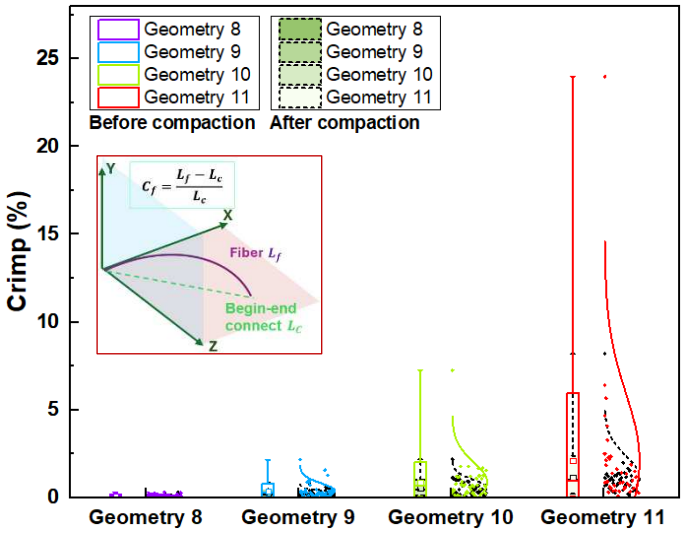

Figure 8.17 Boxplot of crimp of geometries 8, 9, 10 and11 (%).

Table 8.6 Crimp of all the fibers in geometries 8 to 11 (%).

Compact	μ	σ	μ	σ	μ	σ	μ	σ
	Geometry 8		Geometry 9		Geometry 10		Geometry 11	
Before	0.077	0.075	0.317	0.433	0.833	1.154	2.115	3.840
After	0.072	0.006	0.202	0.170	0.570	0.449	1.147	1.238

The analysis of the radii are interesting witnesses of the fibers transformation. As shown in Figure 8.18, before compaction simulaion, the the $\overline{R_{XZ}}$ and $\overline{R_{YZ}}$ of geometry 8 to 11 gradually decrease, consistently with the undulation from geometry 8 to 11. After compaction the difference remains and in order to achieve the goal V_f, the curvature radius $\overline{R_{YZ}}$ shows the fibers become straighter in YZ plane, because the compaction force acts on the fibers, forcing them to adjust their shape to take up less space. Fibers tend to align in the direction of fiber length, so crimped fibers will partially straighten under pressure. However, due to the initial microstructure undulation properties (entanglement structure) of the fibers in geometry 9 to 11, the fibers are interlocked to each other, they cannot straighten so maintain certain curved structure. One can also notice that there is a small decrease of $\overline{R_{XZ}}$ for the undulated

configuration which here again shows the ability of the fibers to bend locally to occupy gaps.

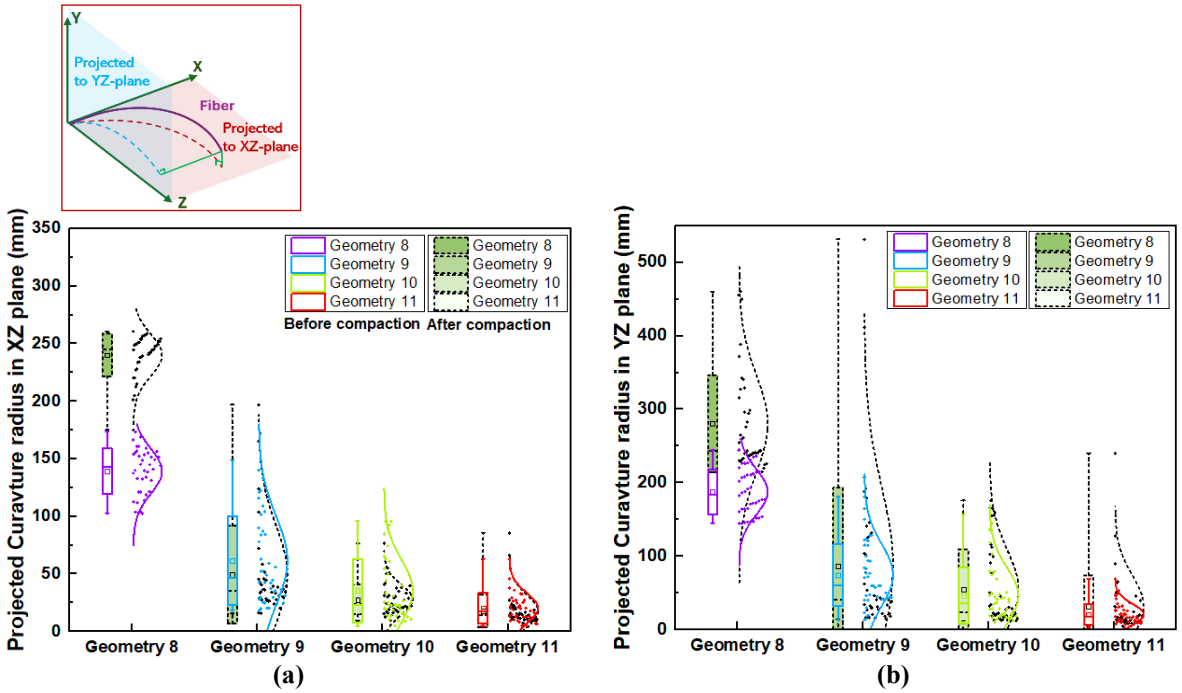

Figure 8.18 Boxplot of projected curvature radii (mm) (a) in XZ plane, (b) in YZ plane.

Table 8.7 Projected curvature radii $\overline{R_{XZ}}$ and $\overline{R_{YZ}}$ (mm).

Compact	$\overline{R_{XZ}}$		$\overline{R_{YZ}}$		$\overline{R_{XZ}}$		$\overline{R_{YZ}}$		$\overline{R_{XZ}}$		$\overline{R_{YZ}}$		$\overline{R_{XZ}}$		$\overline{R_{YZ}}$	
	μ	σ	μ	σ	μ	σ	μ	σ	μ	σ	μ	σ	μ	σ	μ	σ
	Geometry 8				Geometry 9				Geometry 10				Geometry 11			
Before	139	19	187	30	61	38	74	42	35	29	46	38	21	13	21	14
After	240	18	280	66	50	42	86	106	27	13	54	54	17	14	31	41

This section enabled to demonstrate the influence of the fibers undulation on the compaction behavior, even for the same volume fraction, which already indicates that neither the volume fraction, neither the contact number might only drive the compaction behavior. The increase of the undulation leads to an increase of the compression stiffness, within the range of study, which was the searched answer. This illustrates how the virtual estimator can enable to tackle the influence of a parameter on the mechanical response, here, compression. In addition, since we have microstructure indicators explanations have been proposed and commented. This description reflects the microscopic behavior and structural changes of fiber bundles during compaction. Straight parallel fibers adapt to spatial constraints mainly through deformation during compaction with high V_{f_0}, while curved fibers reduce their size mainly through rearrangement at the early stage of compaction, which suggests that in fiber bundles of different geometries, deformation and rearrangement act together to achieve ideal V_f. Especially in the last stage of compaction, when the space between fibers becomes extremely limited, even the

originally straight fibers may undergo small deformation to further compaction. During compaction, the interaction between fibers involves rearrangement and also mechanical interactions. Undulated fibers, because of their complex shape, lead to the formation of a tangled structure between fibers, a structure that increases compaction resistance.

Pre-compaction can be regarded as a pre-treatment process, which changes the initial state between fibers by compacting the fiber bundles to a defined V_f. Pre-compacted fiber bundles require less compaction force to reach the same volume fraction, probably because pre-compaction has already adapted the fiber structure to the compression state, reducing the internal resistance that needs to be overcome in the subsequent compaction process. The final compaction strength of both pre-compacted and un-pre-compacted fiber bundles converged after compaction to a same volume fraction. This indicates that the structure of the fiber bundle tends to reach a steady state during compaction, and the close contact between fibers makes further deformation or rearrangement difficult.

8.2 Influence of slenderness ratio

8.2.1 Different slenderness ratio geometry

The slenderness ratio (*S*) affects the arrangement and deformation of fibers during the loading process, because the slenderness ratio affects the bending stiffness of fibers. The value of that bending stiffness B can be set by changing either the Young's modulus E or the beam element diameter which defines its second moment of inertia I (Daelemans et al., 2021). So, the bending stiffness of beam element was set as follow:

$$B = EI,\ I = \frac{\pi d^4}{64} \tag{8.1}$$

In order to understand the influence of different slenderness ratio, models with different radius of fiber have been created:

$$S = \frac{d_{fiber}}{\mu_{L_{fiber}}} = \frac{1}{m} S_0 \tag{8.2}$$

Where $\mu_{L_{fiber}}$ is the average length of fiber, which will keep same for different geometries, d_{fiber} is the diameter of fiber in the fiber bundle geometry, m is the number scaling multiplier of the *S*, S_o shown in Table 8.8. The fiber bundle geometry is created with parameters in Table 8.8 , but with different radius of fiber. In this study, the used polyester filaments have a diameter of 0.5 mm but, in real fiber bundles, fibers are closer to 0.05 mm $(i.e.\frac{1}{10}S_0)$ and carbon fibers

have a diameter of 0.005-0.01 mm ($\frac{1}{50}S_0$), so the values of diameter d are chosen to represent the diameters of real fibers, i.e. $d = 0.05$ and 0.01mm as presented in Table 8.8:

Table 8.8 Parameters of different slenderness ratio (S).

Diameter of fiber	Slenderness ratio (S)
0.5mm	3.64% (S_o)
0.05mm	0.36% ($\frac{1}{10}S_0$)
0.01mm	0.07% ($\frac{1}{50}S_0$)

In order to understand the influence of S ratio parameter of the fiber structure, the initial geometry parameters are constant: the length of the fibers, structure of the fibers (curvature, contact and so on), as well as the dimensional ratio of the X and Y directions of the compaction channel.

The creation principle of geometries with different slenderness ratio is illustrated in Figure 8.19. First, the dimensions of the compaction channel in the X and Y directions vary in equal proportions, keeping the dimensions in the Z direction (fiber length direction) constant:

$$d_{X_{S_0}} \times d_{Y_{S_0}} = 5 \times 3.22mm, \tag{8.3}$$

$$d_{X_{\frac{1}{10}S_0}} \times d_{Y_{\frac{1}{10}S_0}} = 0.5 \times 0.322mm, \tag{8.4}$$

$$d_{X_{\frac{1}{50}S_0}} \times d_{Y_{\frac{1}{50}S_0}} = 0.1 \times 0.0644mm, \tag{8.5}$$

$$d_Z = 16mm \tag{8.6}$$

Where the $d_{X_{\frac{1}{m}S_0}}$, $d_{Y_{\frac{1}{m}S_0}}$ is the dimension of the X and Y direction of geometry, respectively. d_Z is the dimension of the Z direction of geometry. Secondly, the fiber center point position is scaled to keep the structural parameters inside the fiber bundle unchanged. The creation of the fiber model is based on treating the fibers as regular circles and generating their centerlines. Therefore, the fiber centerline coordinates are still scaled here based on that principle. Figure 8.19 (b) shows an example of the scaling principle with a cross-section of a fiber i in the slice p. The (X, Y) coordinates of the fiber are simultaneously reduced by a factor *m*, and the Z coordinates remain unchanged:

$$X_{\frac{1}{m}S_0} = \frac{1}{m}X_{S_0},\ Y_{\frac{1}{m}S_0} = \frac{1}{m}Y_{S_0} \tag{8.7}$$

And the diameter of fiber i reduced by a factor *m* also:

$$R_{\frac{1}{m}S_0} = \frac{1}{m}R_0 \rightarrow S_{\frac{1}{m}S_0} = \frac{1}{m}S_0 \tag{8.8}$$

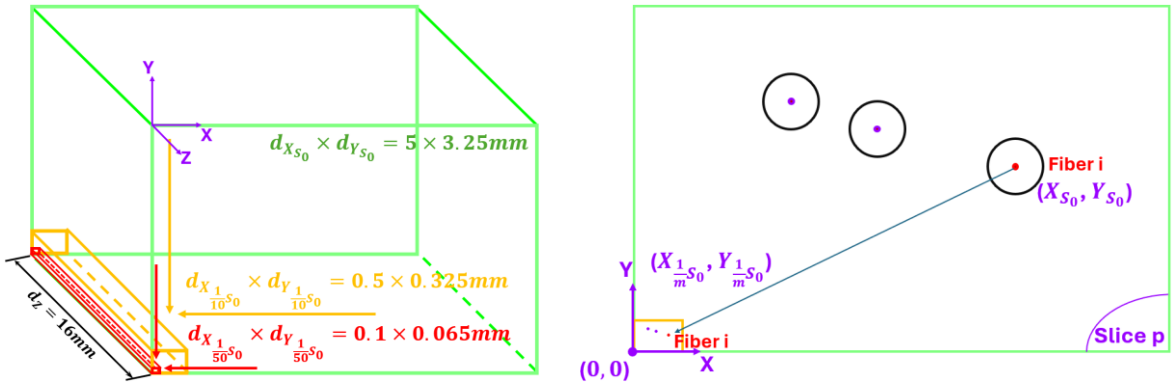

Figure 8.19 Principle of creation of geometries with different slenderness ratio. (a) Equally scaled down compaction channel, (b) Maintain the coordinate position of the fibers relative to the compaction channel ($S = \frac{1}{10}S_0$ as an example).

Finally, the initial structures (contact, undulation, fiber position) of the fiber bundle geometries with different slenderness ratio are totally same, as shown in Figure 8.20.

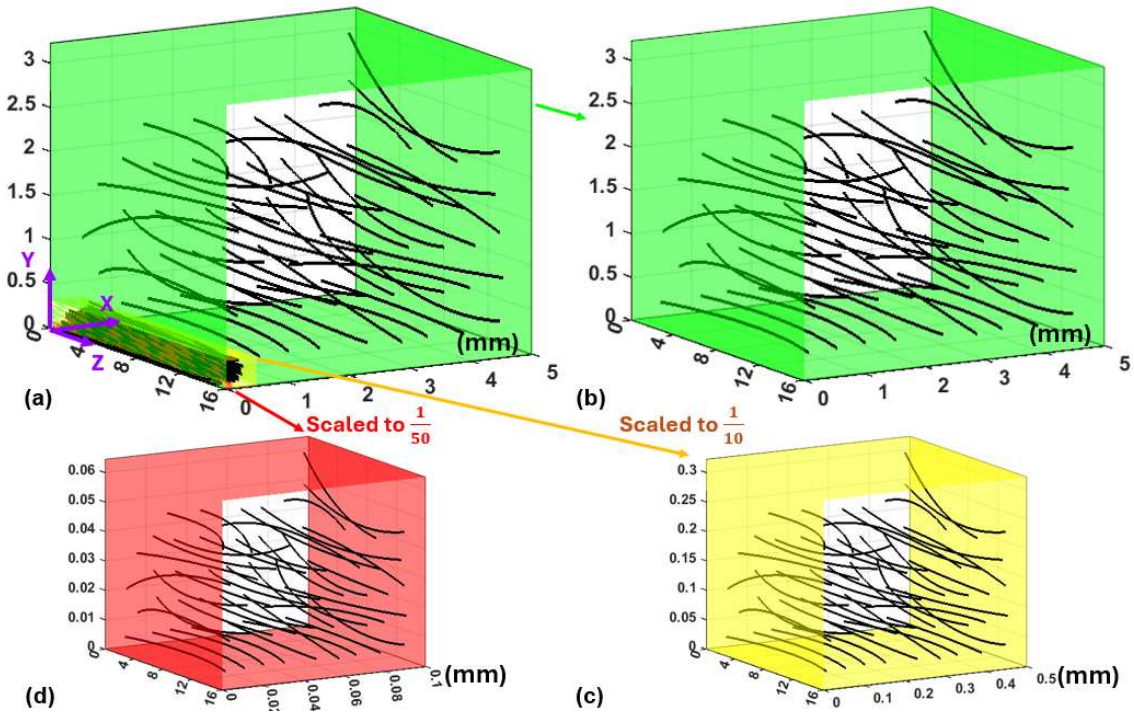

Figure 8.20 Create the geometry of fiber bundle and compaction channel with different slenderness ratio (S). (a) Comparison of the geometry with different ratio S. (b) S_o. (c) $\frac{1}{10}S_o$. (d) $\frac{1}{50}S_o$.

The same compaction simulation was carried out for fiber bundle models with different slenderness ratios, to compare their compaction behavior and microstructure. Figure 8.21

presents the compression pressure in function of volume fraction shown and Figure 8.22 presents the 3D geometry rendering, the initial volume fraction is 43.6 %.

Figure 8.21 shows that, at the beginning of the compaction test, the volume fraction increases under low pressure, in the three cases. As the V_f increases, the gaps between fibers decrease, leading to increased friction and constraints among fibers. Therefore, the pressure rises more sharply. In addition, as S decreases, the compaction pressure also decreases when the $V_f = 80\%$. The final compaction pressures corresponding to the model with parameter S_0, $\frac{1}{10} S_0$ and $\frac{1}{50} S_0$ are 1.18 Mpa, 0.56 Mpa, and 0.045 Mpa respectively. In the final stage of compaction, the fiber bundles experienced significant relaxation of compaction pressure. As the S ratio decreases, the end compaction pressure of the same V_f and the relaxation pressure R_f decrease. According to the equation 8.1 and 8.2, the small S corresponds to small bending stiffness. Therefore, those fibers with smaller S ratio can more easily bend and thus it is easier for these fibers to move locally to fill the voids in the later stages of compaction and need less compaction pressure. This can be validated by Figure 8.22, on which the geometry with $\frac{1}{50} S_0$ presents almost 0 deformation of fiber's section compared to geometries with S_0 and $\frac{1}{10} S_0$ (Figure 8.22 (a-c2)), the fiber's section deformation show in contact penetration between rendering fibers in the ABAQUS® (real case: fiber's deformation), as shown in Figure 8.22 (d). With decreasing S, the compacted fibers are more tightly packed, and their arrangement tends to stabilize the triangular structure (Figure 8.22 (e)). Concerning the compaction pressure of the geometry with different S at same V_f, the pressure of geometry with different S_0 is higher, this indicates that the fiber bundle geometry with bigger S, the more resistance increase is encountered at same V_f. So, these results show two different ways to adjust/accommodate in the microstructure: material deformation with high load and local reorganisation with low load.

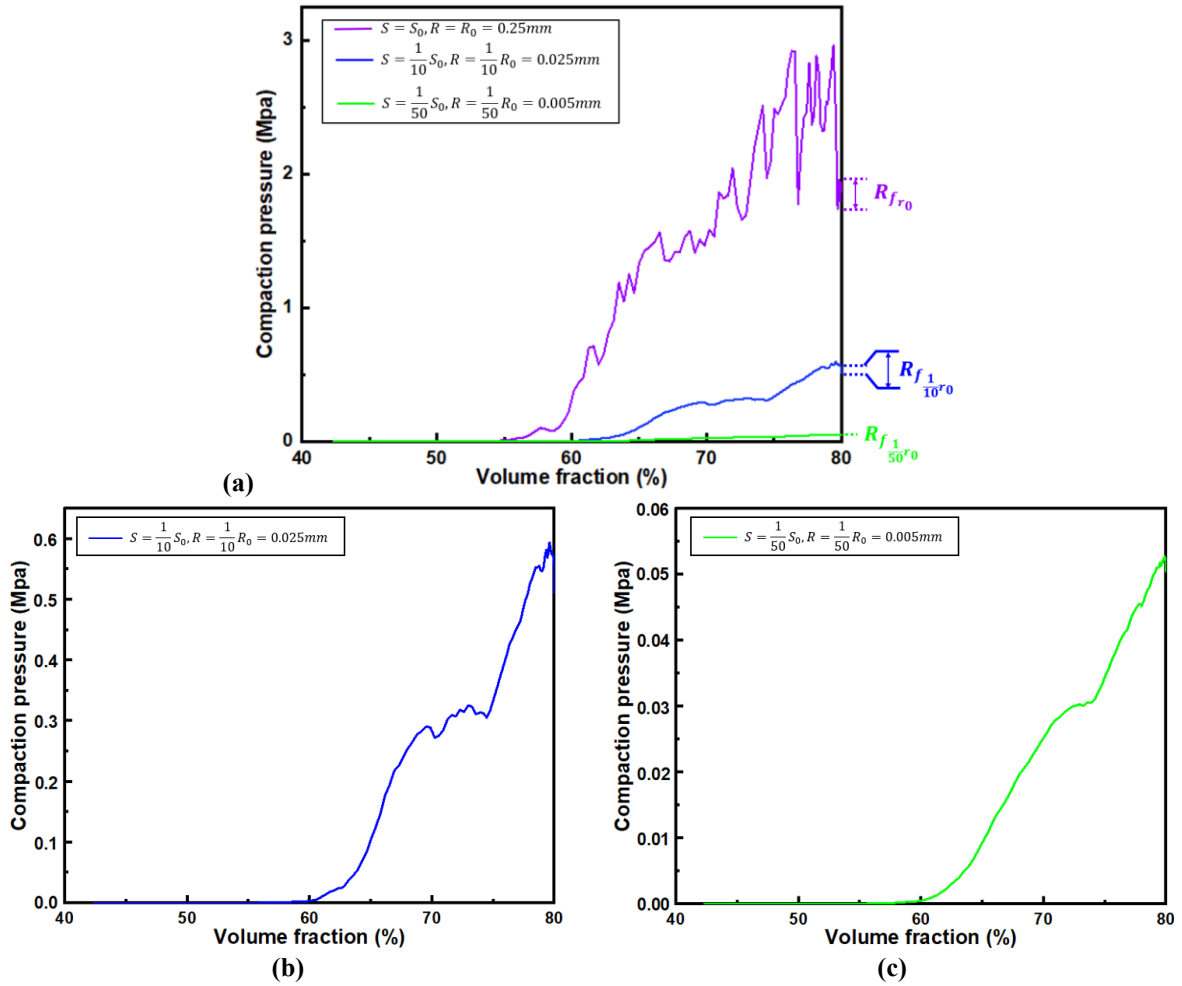

Figure 8.21 Relationship between Volume-fraction and Compact pressure of different fiber length-radius ratio (S). (a) S_0, $\frac{1}{10}S_0$ and $\frac{1}{50}S_0$. (b) Zoom of (a), $\frac{1}{10}S_0$. (c) Zoom of (a), $\frac{1}{50}S_0$.

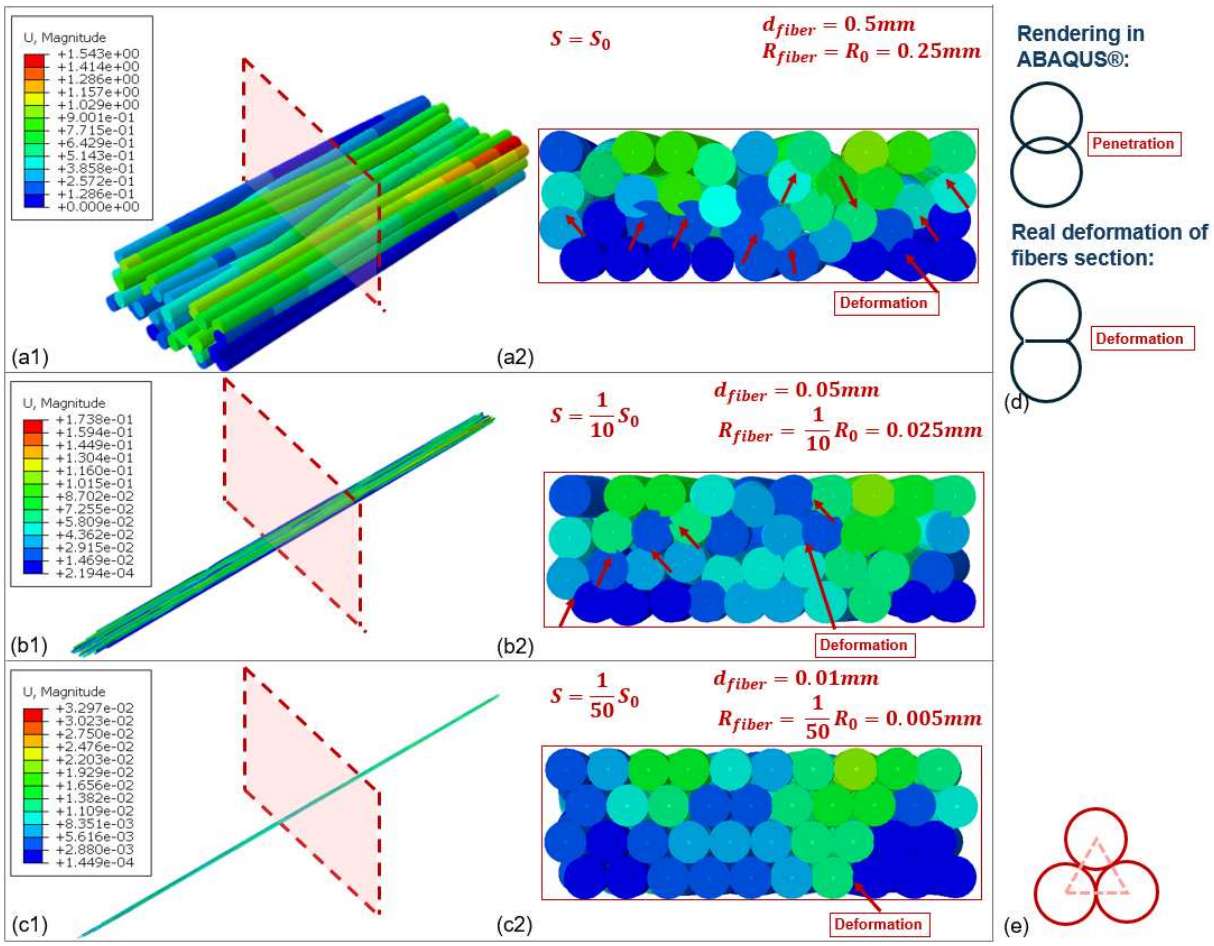

Figure 8.22 Compaction simulations on geometries with different fiber S ratio. (a1-2) S_o, (b1-2) $\frac{1}{10}S_o$, (c1-2) $\frac{1}{50}S_o$, (a-c 1) 3D rendering fiber bundle geometries, (a-c 2) Cross-section of fiber bundle and, (d) principle of contact penetration between fibers with rendering beam and real case of fiber's section deformation, (e) fibers stabilize the triangular structure.

8.2.2 Indicators analysis of geometries with different S

a) Orientation and mis-orientation

The orientation unit spheres of fiber bundle geometries with different S ratio are presented in Figure 8.23, and the orientation tensor A_{33} in Figure 8.24. The geometry with different S ratio created are equal scaling, the microstructure of them is total same before compaction. From the distribution of the orientation tensor in orientation unit spheres, the previous conclusion is verified: smaller S lead to a tight alignment, the value of the orientation tensor A_{33} of the fibers is then close to 1.000.

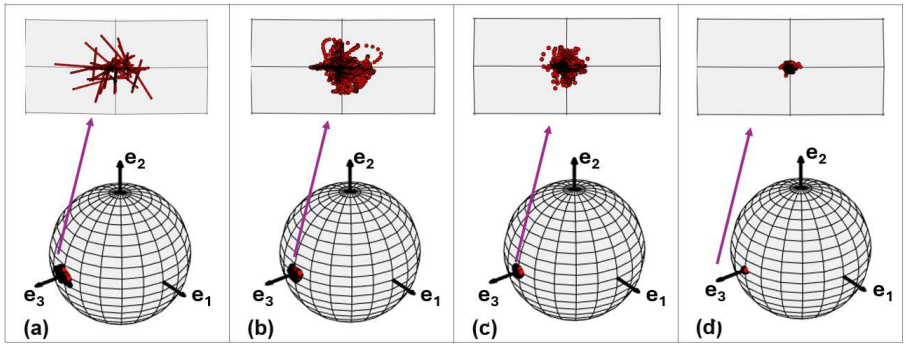

Figure 8.23 Orientation unit spheres of fiber bundle geometries with different slenderness ratio of fiber. (a) Before compaction simualtion for different S ratio geometry. The geometry with (b) S_0, (c) $\frac{1}{10}S_0$ and (d) $\frac{1}{50}S_0$ after compaction simulation.

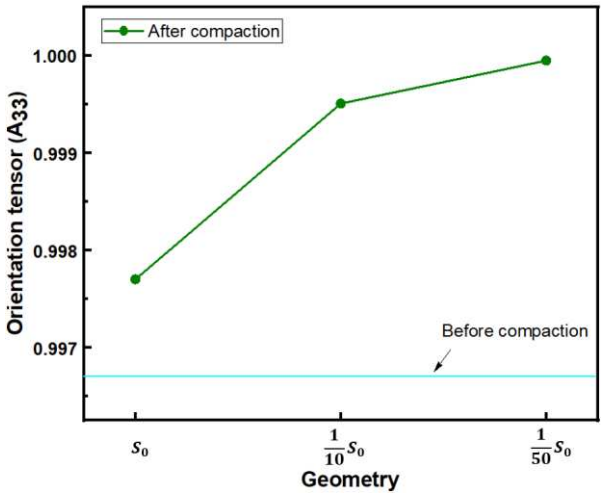

Figure 8.24 Orientation tensor A_{33} with different slenderness ratio of fiber: S_0, $\frac{1}{10}S_0$ and $\frac{1}{50}S_0$.

The mis-orientation of the fibers in geometries with different S ratio is shown in Figure 8.25. The distribution of fiber mis-orientation angles is influenced by fiber diameter. Before compaction, the mis-orientation (α) of the initial geometry is distributed in [-6, 5] (°). As mentioned before, the fibers with small S have lower bending stiffness, and can then rearrange more easily to fill in voids between fibers. Therefore, the deflection of the fibers from the Z-axis (direction of the fiber length) is angularly distributed at 0°, either α or β.

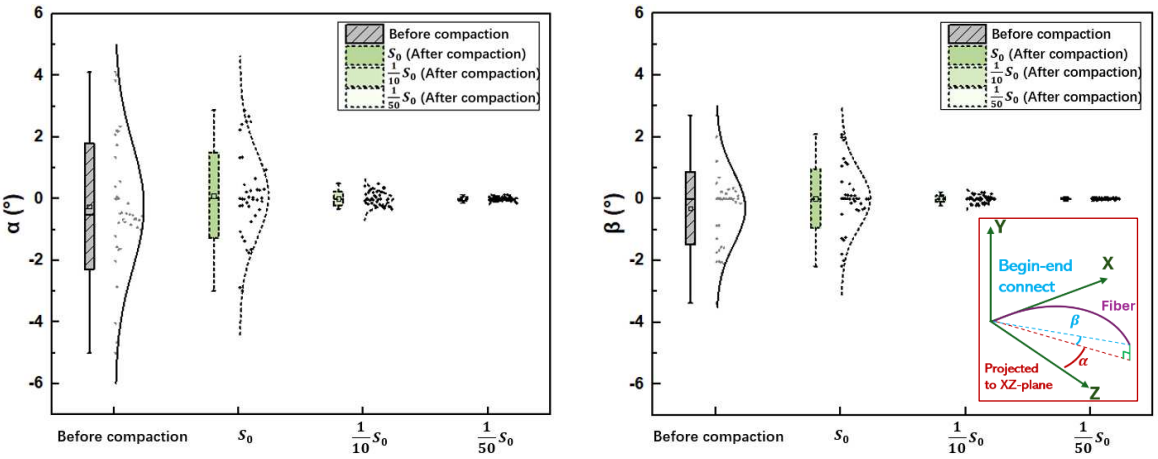

(a) (b)

Figure 8.25 Boxplot of mis-orientation of fibers in geometries with different slenderness ratio of fiber: S_0, $\frac{1}{10}S_0$ and $\frac{1}{50}S_0$. (a) α (°). (b) β (°).

b) Contact

The contact number of geometry with different S is presented in Figure 8.26. The total initial contact number increases for the geometry with r_0, $\frac{1}{10}r_0$ and $\frac{1}{50}r_0$. This indicates here again that the number of contacts is not directly related to the compaction stiffness and even is not so easy to relate to the fibers organisation. Here it seems to demonstrate a more compact structure for the smaller fibers.

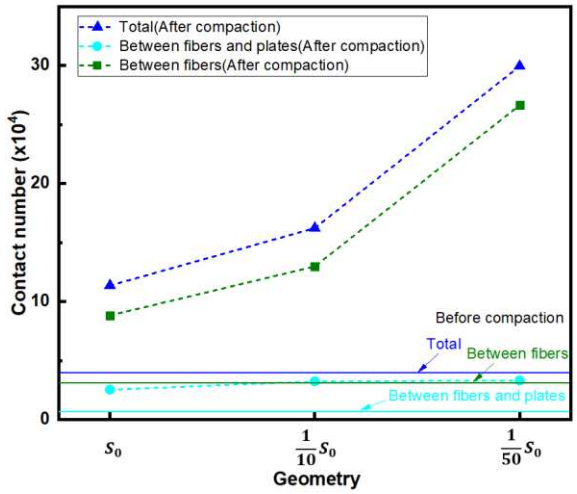

Figure 8.26 Contact number of fiber bundle geometries with different slenderness ratio of fiber: S_0, $\frac{1}{10}S_0$ and $\frac{1}{50}S_0$.

Here again the distribution of contact angle between fibers is more interesting. In the fiber's section (θ (°)) is presented in Figure 8.27 (a), the distribution of contact angle between fibers

in the fiber's length direction (γ (°)) in Figure 8.27 (b) and the average and standard values in Table 8.9 . After compaction, the contact angle θ is mainly distributed in [0-10° & 80-90°, 20-30° & 60-70°], all the more with the decrease of S ratio. In addition, the contact angle (γ) between fibers in fiber's length direction is also shifted toward 0°, more quickly when S decreases. These phenomena validate the same result: when S decreases, at the same state of compaction, the fibers tend to be arranged in a stable triangular structure within the fiber cross-section.

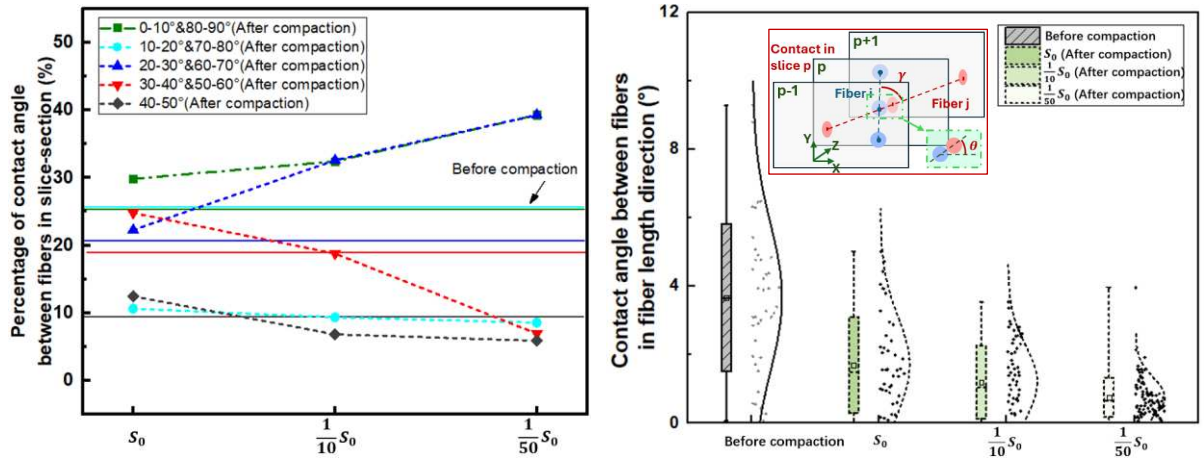

Figure 8.27 Contact angle of geometries with different slenderness ratio of fiber: S_0, $\frac{1}{10}S_0$ and $\frac{1}{50}S_0$. (a) θ (°) in the fiber section, (b) γ (°) in the fiber length direction.

Table 8.9 Contact angle between fibers γ (°) in the fiber length direction.

Before compact	μ			σ		
	3.552			2.235		
After compact	μ	σ	μ	σ	μ	σ
	S_0		$\frac{1}{10}S_0$		$\frac{1}{50}S_0$	
	1.862	1.514	1.00	0.987	0.652	0.589

c) Crimp and projected curvature radii

The crimp boxplot of different geometries with S_0, $\frac{1}{10}S_0$ and $\frac{1}{50}S_0$ can be seen in Figure 8.28 and the average and standard values in Table 8.10. For models whith smaller S, the decrease in the curvature radius indicates that more local bends are formed in the fibers after compaction. But crimp decreases after compaction. That means that small local bends appear and these bends increase the overall curvature of the fiber. The increase in the orientation tensor A_{33} likewise

indicates that the fiber bundles tend to align in the Z-axis direction. By combining the observation of the fiber bundle centerline deformation with the variation of its microscopic parameters, a schematic diagram of the fiber morphology after compaction is presented in Figure 8.30. Fiber bundle with $\frac{1}{50}S_0$ parameter have a lower bending stiffness, enbaling high local curvature and leading them to deform easyer during the compaction process, and then ot occupy more easily the spaces leading to a better organisation and then a global realignment. As a result, fiber bundles with S-parameter of $\frac{1}{50}S_0$ have locally reduced curvature radius but also a large number of straight part zones along it, which leads to a very sharp crimp curve. The fiber bundle geometry with different S are scaling with coefficient m (equation 8.2), the fiber length (L_f) is same in these three models, but the begin-end connect length of fiber (L_c) is higher for $\frac{1}{50}S_0$ parameter, so the crimp is small for $\frac{1}{50}S_0$ parameter.

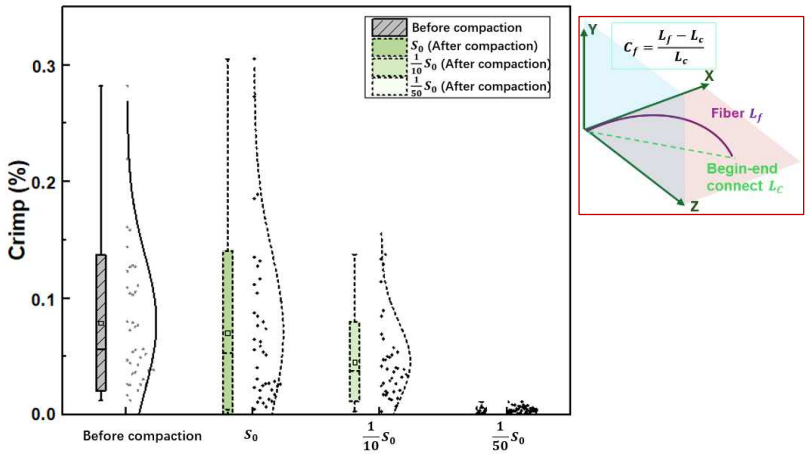

Figure 8.28 The crimp boxplot for different S.

Table 8.10 The crimp of different S(%).

Before compact	μ				σ	
	0.079				0.058	
After compact	μ	σ	μ	σ	μ	σ
	S_0		$\frac{1}{10}S_0$		$\frac{1}{50}S_0$	
	0.070	0.045	0.046	0.034	0.009	0.008

In contrast, larger diameter fibers, due to their greater stiffness, may slide more easily in the direction of the fiber axis before deforming and coming in contact with each other. As a result, the value of the change in their average curvature radius, which is decreased while the standard deviation increases, which means a smoother but still misaligned microstruture.

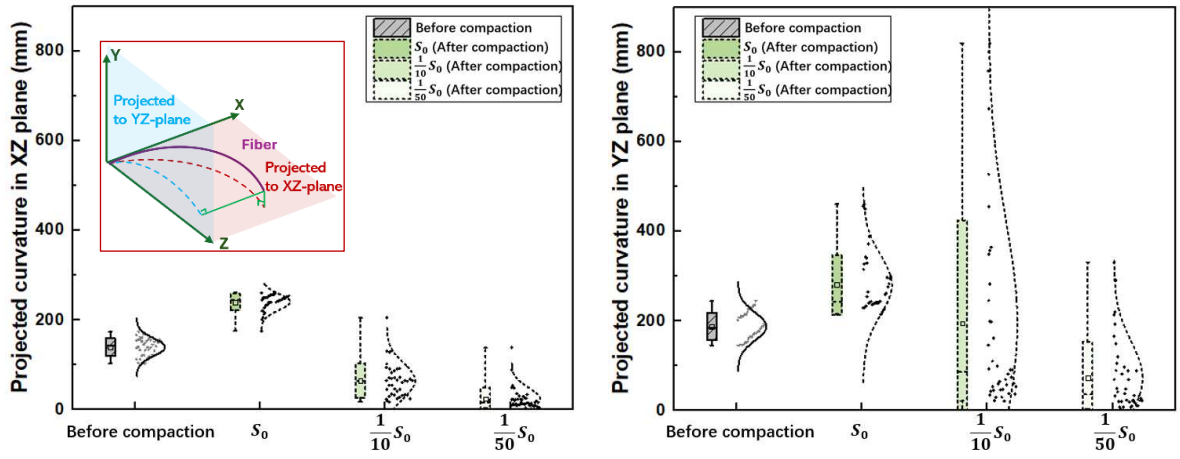

Figure 8.29 Boxplot of projected curvature radii of different S geometry. (a) in XZ plane, (b) in YZ plane.

Table 8.11 Projected curvature radii of fiber bundle geometry with different S ratio (mm).

Before compact	$\overline{R_{XZ}}$						$\overline{R_{YZ}}$					
	μ			σ			μ			σ		
	139			19			187			31		
After compact	$\overline{R_{XZ}}$		$\overline{R_{YZ}}$		$\overline{R_{XZ}}$		$\overline{R_{YZ}}$		$\overline{R_{XZ}}$		$\overline{R_{YZ}}$	
	μ	σ	μ	σ	μ	σ	μ	σ	μ	σ	μ	σ
	S_0				$\frac{1}{10}S_0$				$\frac{1}{50}S_0$			
	240	18	280	60	64	38	194	120	24	24	73	60

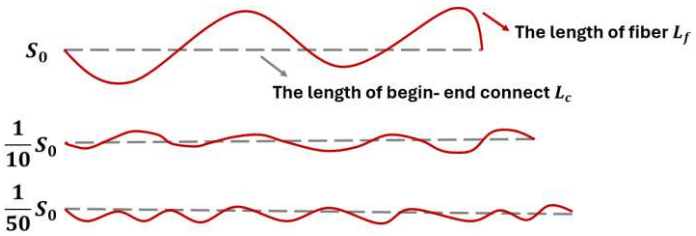

Figure 8.30 Schematic diagram of the fiber's morphology after compaction.

This section discussed the compaction behavior of the same fiber structure with different slenderness S ratios. The compaction pressure for the slenderest fibers was significantly lower. This is determined by the bending stiffness of the fibers, which is related to the diameter of the fibers. During compaction, fibers need to rearrange and deform to reduce volume and increase density. Fibers with lower bending stiffness are more subjected to bending and deformation, which allows them to fill spaces and gaps more efficiently, thereby reducing the required compaction pressure. In addition, fibers that bend more easily also adapt more easily to the position of surrounding fibers during rearrangement, promoting a tighter inter-fiber

arrangement. This tighter structure is also indicated by the microstructural parameters of the compacted fibers, such as A_{33}.

8.3 Friction between fibers

During compaction of fiber bundles, the friction coefficient is a parameter of the interaction between the fibers, which depends on the characteristics of the fiber surface as well as the contact between the fibers, and influences the interaction between the fibers. Compaction simulations of fiber bundle geometry with different friction between fibers ($\mu = 0.2, 0.4, 0.6, 0.8$) are performed and the relationship between V_f and compaction pressure is presented in Figure 8.31. The simulations are performed with compaction in the X direction and compaction in the Y direction independently and the results are analyzed in both directions for each simulation.

As shown in Figure 8.31 (a, b), the compaction simulation at final V_f = 67 % is strongly influenced by the friction coefficient, and the final compaction pressure gradually increases as the friction coefficient increases. However, when the final compaction V_f increases to 87 %, at this point, the final compaction pressure basically converges for each friction coefficient.

At lower V_f, more space exists between the fibers, and the fibers can move and rearrangement relatively freely. In this case, a higher friction coefficient means that the resistance between fibers increases, leading to an increase in compaction pressure. This is because a higher friction coefficient reduces the relative sliding of the fibers, making the rearrangement more difficult, thus it requires a greater external force to change the position of the fibers and to achieve the ideal compaction state. With the higher end V_f, which means the fiber bundle becomes denser, the space between the fibers decreases and there is less freedom for fibers rearrangement. In this case, even with a higher friction coefficient, the movement of the fibers is greatly restricted and therefore the increase in compaction force becomes less sensitive to changes in the friction coefficient. After reaching a critical volume fraction, the difference in compaction forces starts to decrease until eventually it is no longer significantly affected by the friction coefficient. The locking configuration is the more a question of geometry than of friction. The conclusion is then interesting since not uniform with the volume fraction. The higher volume fraction the lower influence of the friction coefficient.

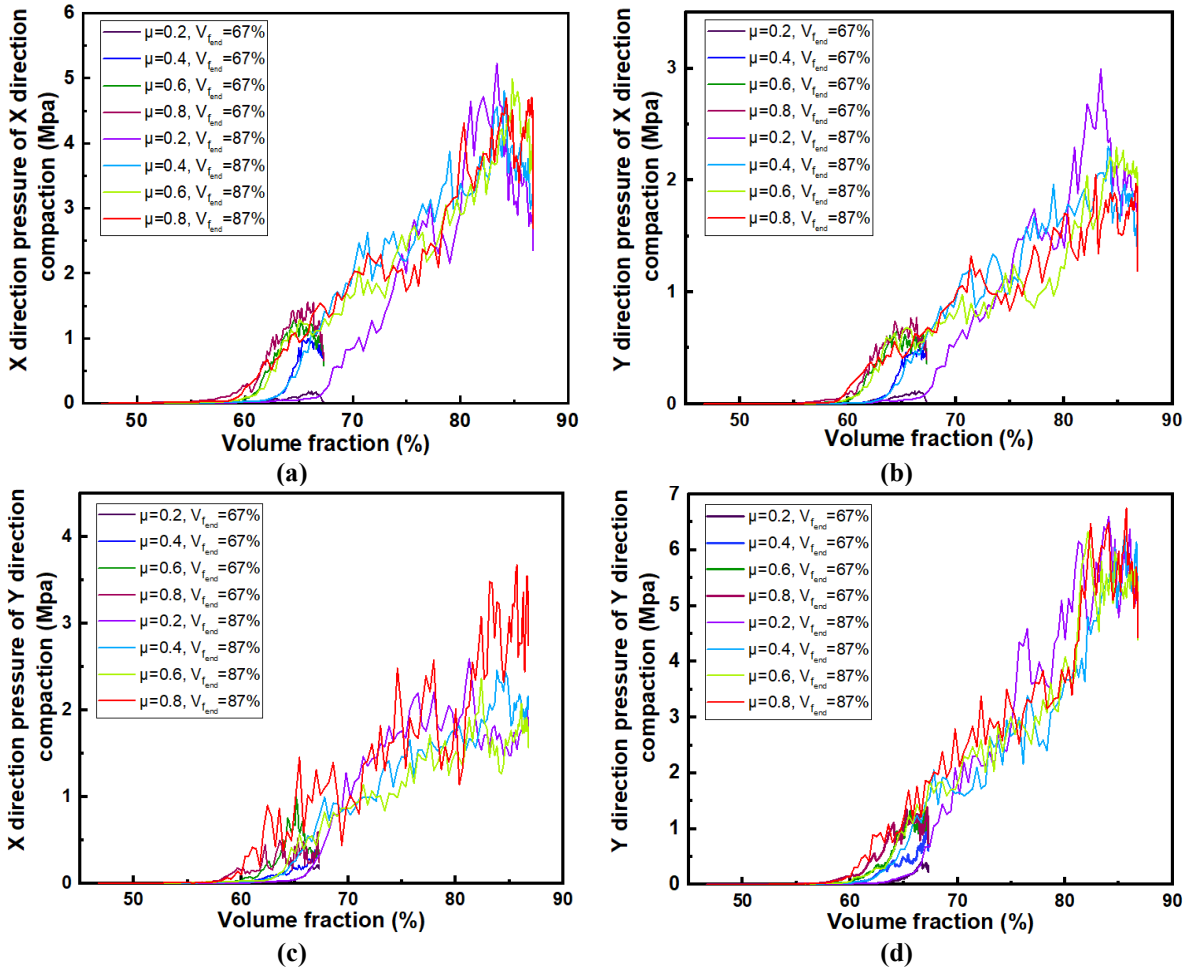

Figure 8.31 Relationship between volume fraction and compaction pressure of fiber bundle geometry with different friction ($\mu = 0.2, 0.4, 0.6, 0.8$) between fibers, with end volume fraction V_f=67%, 87%. (a) X and (b) Y direction pressure with compaction performed in X direction, (c) X and (d) Y direction pressure with compaction performed in Y direction.

From the 3D rendering of the fiber bundles after compaction, there is little difference in the morphology of the fibers, as shown in Figure 8.32 and Figure 8.33. However, any small movement of the fibers under high compaction state could cause changes in compaction pressure. Therefore, the microstructure of the fibers is discussed next.

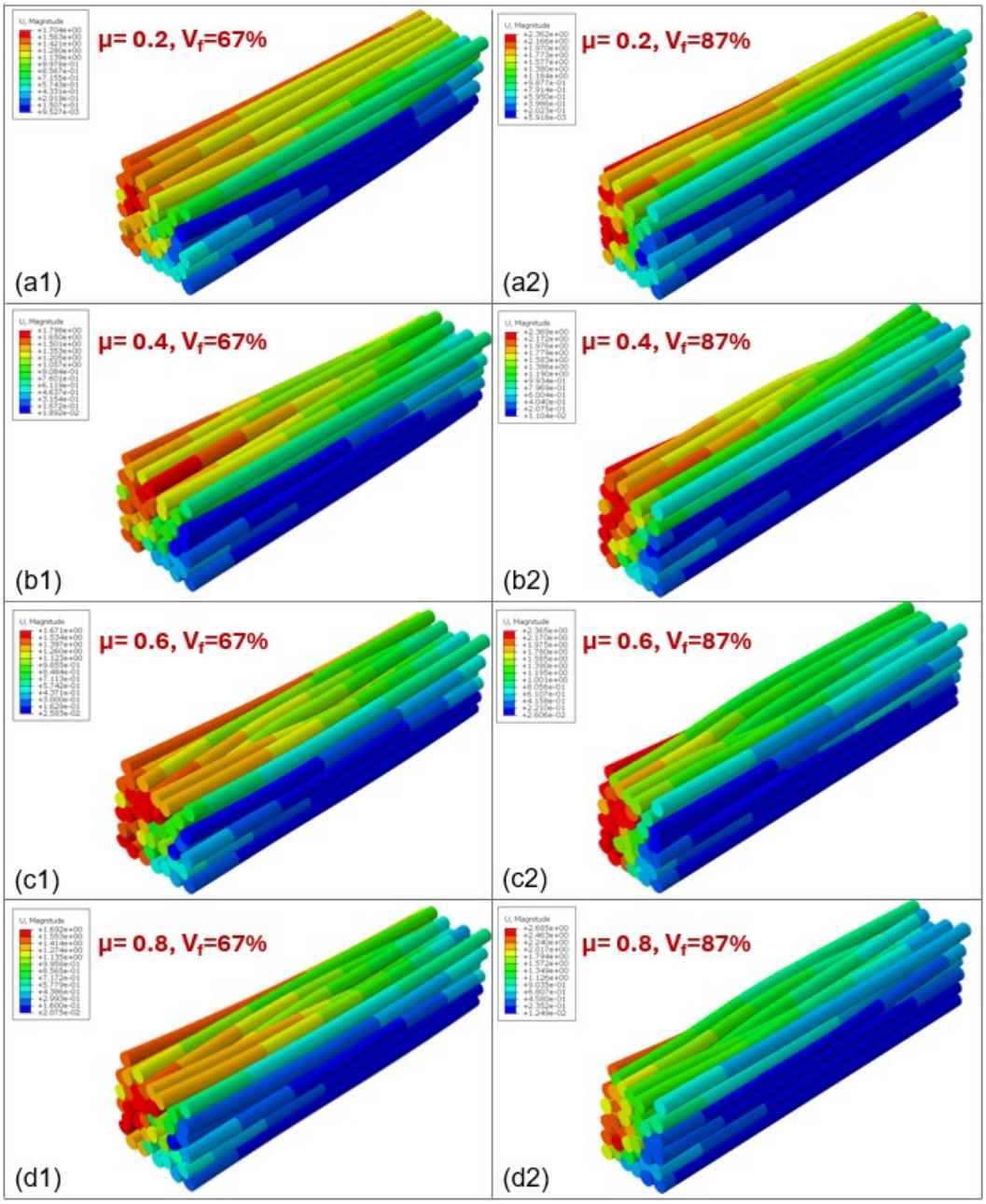

Figure 8.32 3D rending of fiber bundle geometry with different friction coefficient ($\mu = 0.2, 0.4, 0.6, 0.8$) between fibers, with end volume fraction V_f=67% and V_f=87%, with compaction performed in X direction.

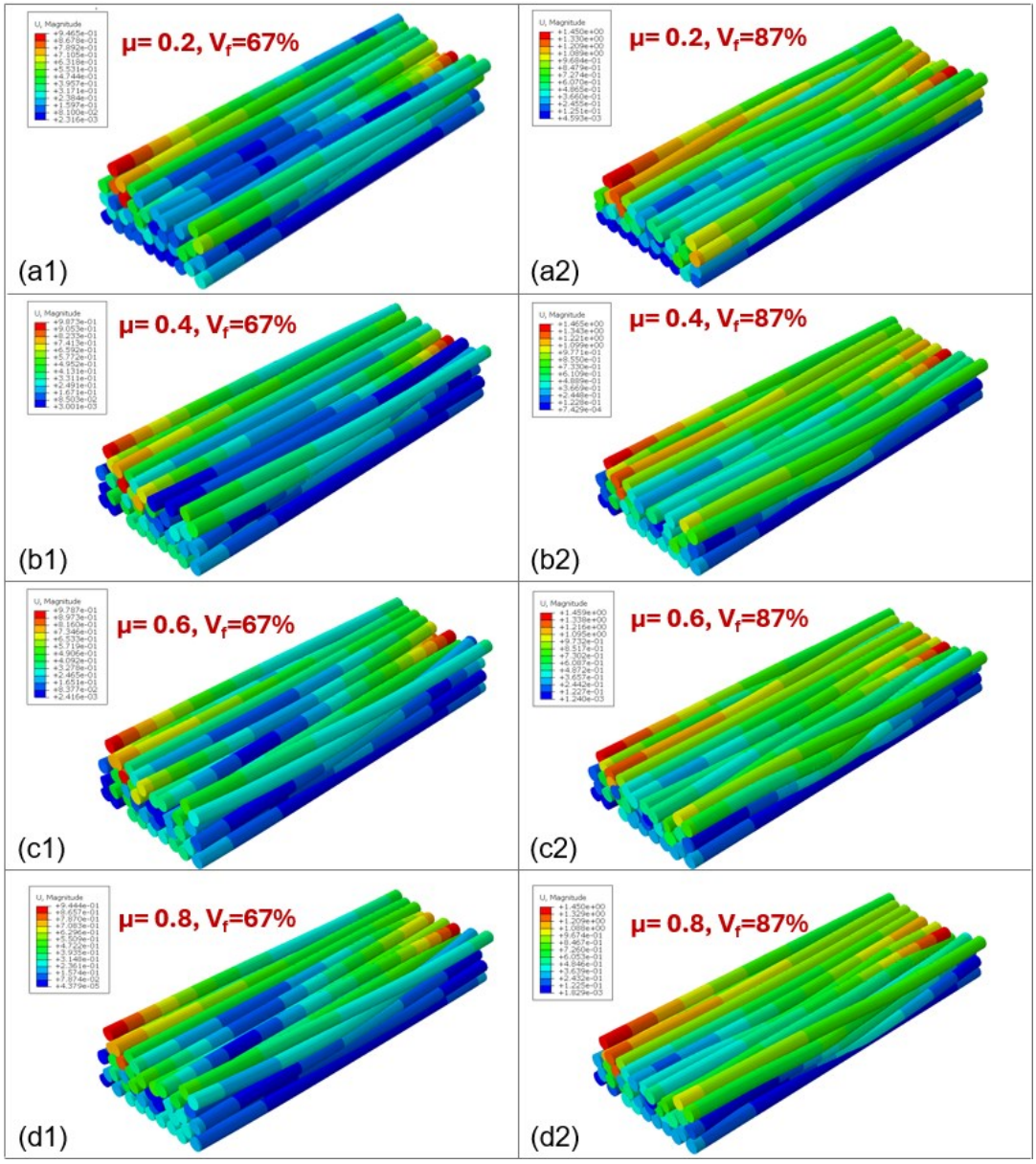

Figure 8.33 3D rending of fiber bundle geometry with different friction coefficient ($\mu = 0.2, 0.4, 0.6, 0.8$) between fibers, with end volume fraction V_f=67% and V_f=87%, with compaction performed in Y direction.

8.3.1 Microstructures analyze

The centerline of the fiber bundle geometry after compaction in X and Y direction at V_f=67 % and 87 % is presented in Figure 8.34. Concerning the position of the fiber centerlines, any change in friction coefficient between the fibers results in a shift of the fibers for the same compaction pressure. This means that the coefficient of friction influences the interaction between the fibers and thus the rearrangement.

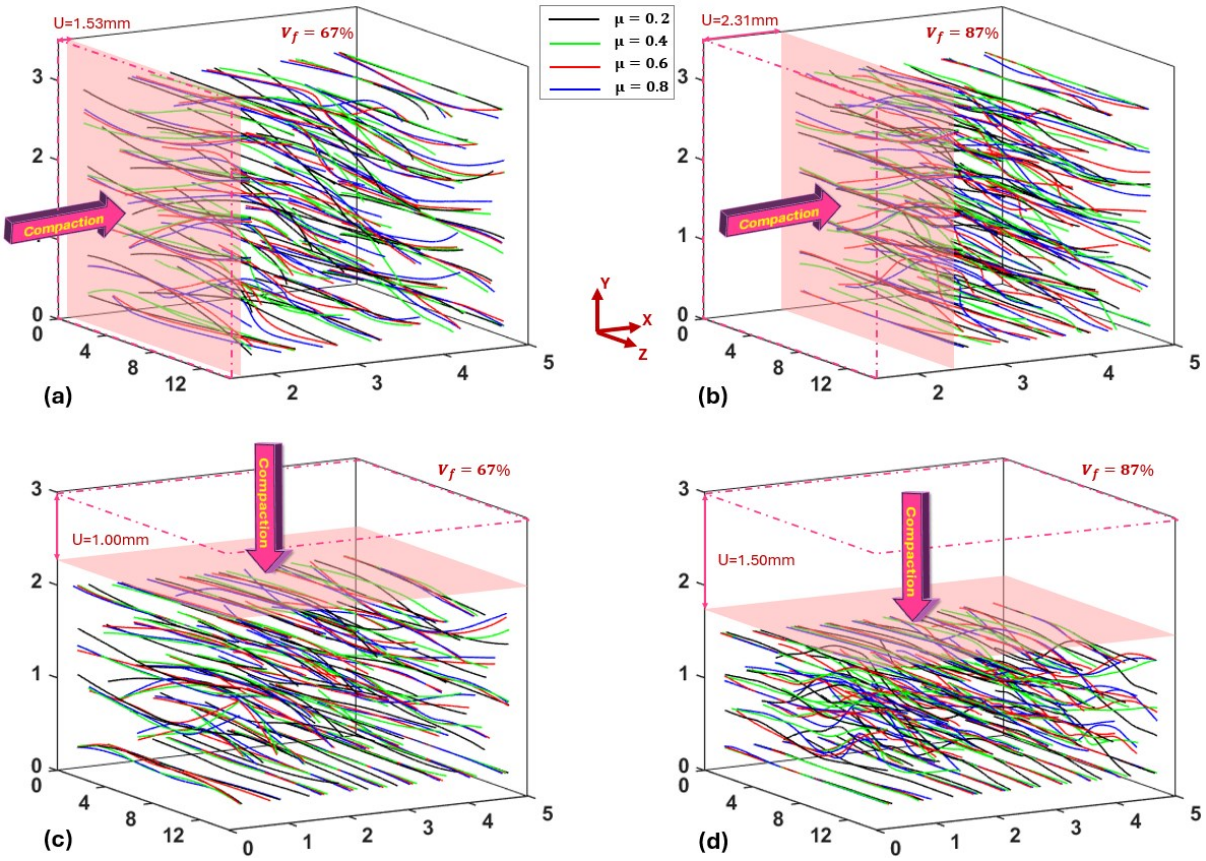

Figure 8.34 Centerline of fiber bundle after X direction compaction at (a) V_f=67%, (b) V_f=87%; and after Y direction compaction at (c) V_f=67%, at (d) V_f=87%.

The difference between the compaction paths will be studied in detail in the next section, in addition, the conclusion for the microstructure analysis regarding the friction coefficient are the same for both direction of compaction thus only the X axis compaction will be tackled for the microstructure analysis.

a) Orientation of the fibers

The orientation unit spheres of fiber bundle geometry with μ=0.2 and μ=0.8 between fibers at V_f=87 % with X direction compaction is presented in Figure 8.35. These cases correspond to an orientation tensor A_{33}=0.999 and A_{33}=0.998, respectively. The higher coefficient of friction (μ = 0.8) implies greater friction between fibers, which can prevent fiber movement and rearrangement during compaction. Due to the restricted sliding of the fibers against each other, the fibers cannot effectively rearrange themselves into a more ordered structure, resulting in reduced directionality. Higher coefficients of friction may lead to higher shear stresses near the fiber contact points, which may affect the local rearrangement and directionality of the fibers.

This means that the local structure within the fiber bundle may be more stable at high friction coefficients, and this stability may lead to differences in overall directionality even when the final compaction pressures are similar.

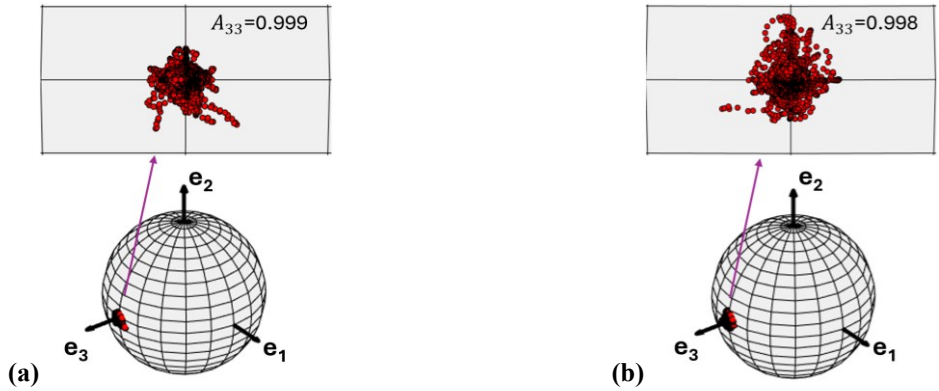

Figure 8.35 Orientation unit spheres of fiber bundle geometry with different μ between fibers at V_f=87% with X direction compaction. (a) μ=0.2, (b) μ=0.8.

Figure 8.36 presents the Boxplot of the mis-orientation of fibers with μ=0.2 and μ=0.8 at V_f=87 % with X direction compaction. Similarly, the offsets of the fibers with respect to the Z-axis, in the direction of the X-axis (α) and in the direction of the Y-axis (β), exhibit very small differences. The narrowest distribution around the 0 value indicates that the high friction coefficient of the fibers, slightly leads to the distribution of the fibers (lengthwise) more away from the Z-axis direction after the same compaction test. This conclusion is consistent with the fiber orientation tensor conclusion. A lower coefficient of friction leads to a more directional fiber distribution after compaction. However, the differences observed are very small to conclude with high degree of certainty.

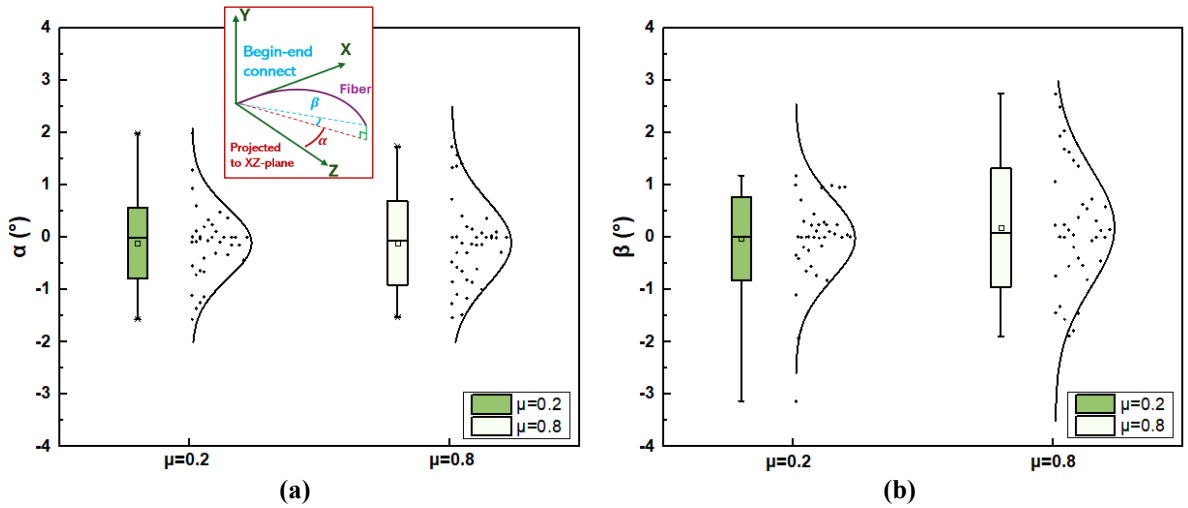

Figure 8.36 Boxplot of mis-orientation of fibers bundle geometry with μ=0.2 and 0.8 at V_f=87% with X direction compaction. (a) α, (b) β.

b) Contact

Figure 8.37 shows the contact number between fibers, fibers and compaction plates, and total contact number of fiber bundle geometry with μ=0.2 and μ=0.8 at V_f=87 % with X direction compaction. Fiber bundles with higher friction coefficients result in the fewer interfiber contacts after compaction, which can be explained by the fact that it is more difficult to rearrange the fibers to be in close contact with each other. The difference in the total number of contacts within the fiber bundle at different friction coefficients is about 20 %, this difference can still be considered significant. The friction coefficient directly affects the amount of contact between fibers in a fiber bundle during compaction, as well as the contact between fibers and the compaction channel. A higher friction coefficient usually leads to a weaker orientation of the fiber bundle because the high frictional resistance between the fibers prevents the movement and rearrangement of the fibers, resulting in the formation of fewer points of contact between the fibers relative to a more oriented fiber bundle with a low friction coefficient. However, the final compaction pressure were essentially the same, suggesting that the determination of the compaction load, it seems then that even though there is a difference in the number of contact points, the sliding inside the fiber bundles decrease due to the high friction coefficient, resulting in a similar pressure being required to achieve compaction.

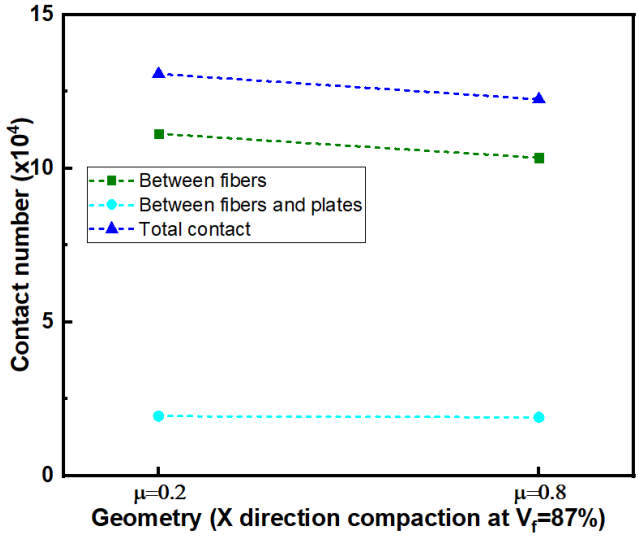

Figure 8.37 Contact number of fiber bundle geometries with μ=0.2 and μ=0.8 at end V_f=87% with X direction compaction.

The contact angles in the section (θ) and in the length direction (γ) between fibers and the boxplot of θ and γ are considered in Figure 8.38. The contact angle between fibers is larger

with higher μ. This confirms the previous analysis. Since high μ prevents relative movement of the fibers, the relative arrangement structure of the fibers formed during the initial compaction step remains relatively stable during subsequent compaction. This stability limits the ability of the fibers to rearrange themselves in later steps of compaction, resulting in the maintenance of high contact angles, not only for θ, but also for γ.

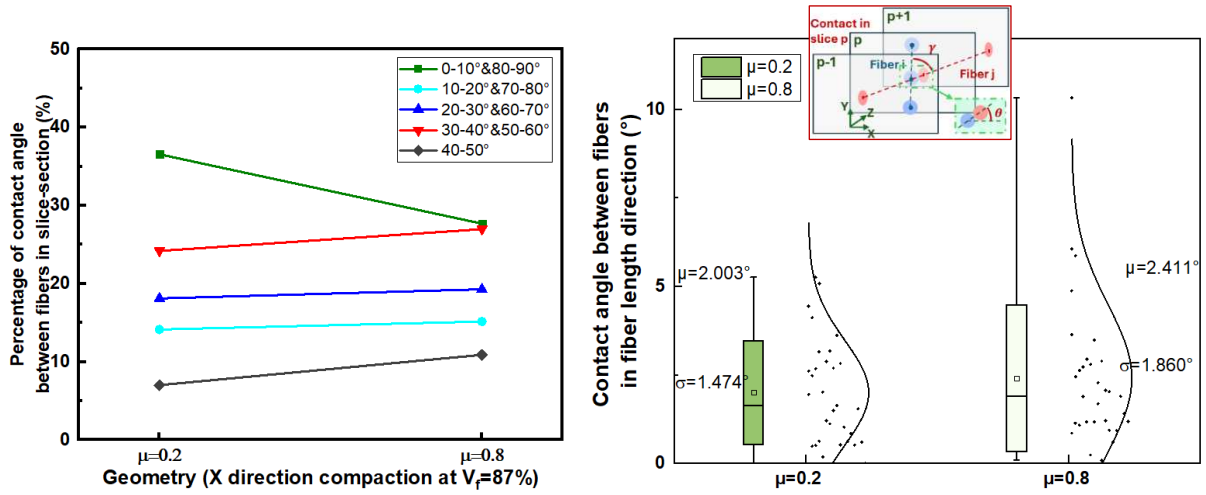

Figure 8.38 Contact angle of geometry with μ=0.2 and μ=0.8 at V_f=87% with X direction compaction.

(a) θ (°) in the fiber section, (b) γ (°) in the fiber length direction.

c) Undulation

The crimp Boxplot and the projected curvature radius of fiber bundle geometry with μ=0.2 and μ=0.8 at V_f=87 % with X direction compaction is presented in Figure 8.39 and Figure 8.40, respectively. The crimp and the projected curvature radius of geometry with μ=0.8 and one with μ=0.2 exhibit small differences which globally confirms the results of the angles: a lower coefficient of friction leads to a little more directional fiber distribution after compaction.

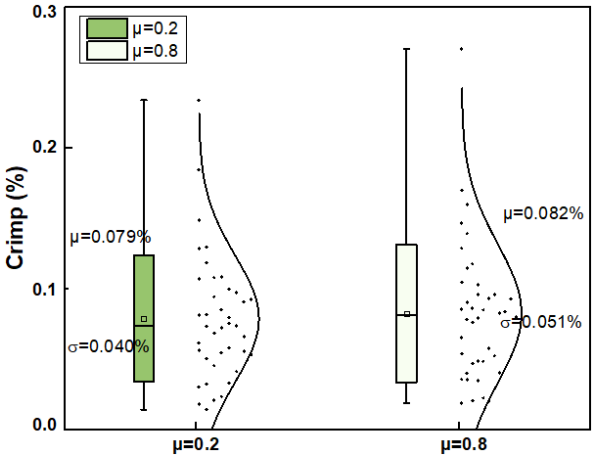

Figure 8.39 The crimp Boxplot of geometry with μ=0.2 and μ=0.8 at V_f=87% with X direction compaction.

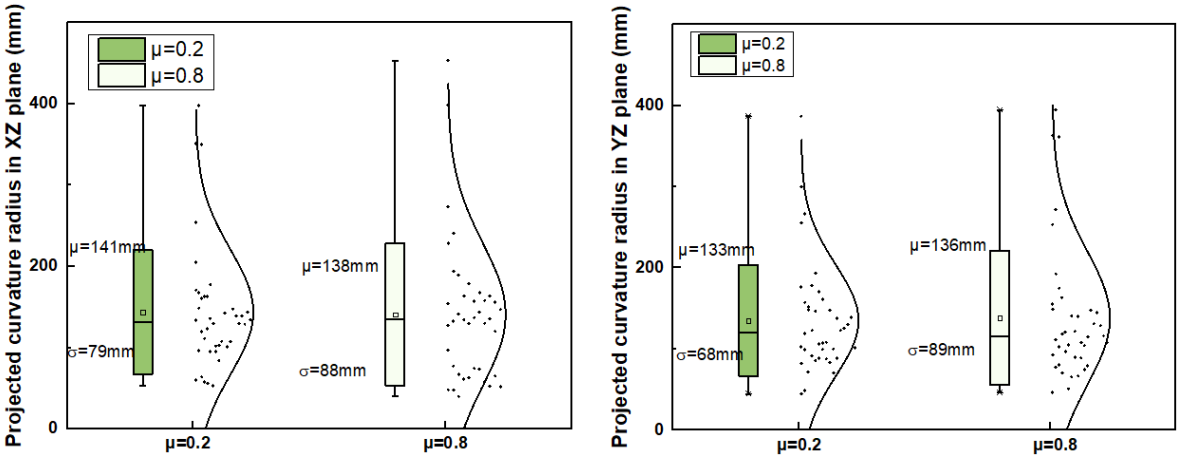

Figure 8.40 Boxplot of projected curvature radii of geometry with μ=0.2 and μ=0.8 at V_f=87% with X direction compaction. (a) in XZ plane, (b) in YZ plane.

The effect of the friction coefficient has been analyzed in this section. The influence of the friction coefficient is different depending on the fiber volume fraction. Indeed, the shape of the compaction curve is different. Indeed, at low volume fractions the increase in the friction coefficient induces a significant increase in the compression load, preventing the fibers movements when the latter are more easily possible. At higher volume fraction, the influence decrease until becoming negligible to reach almost the same compression load. Indeed, even if a small modification in the compacted microstructure is noticed and inherited from the differences in the early stage of reorganization, it seems not to affect significantly the stiffness.

8.4 Conclusion

In this section, the influence of the internal structure of the fibers on the compaction simulation was analyzed: the undulation of the fibers, the slenderness ratio (S), and the friction coefficient between fibers (μ). In addition, the microstructure (position) of the compacted fibers was also analyzed by the definition of microstructural parameters: the orientation tensor (A_{33}) of the fibers, angle of deviation from the Z-axis (α, β), number of contacts between the fibers, angle of contact between the fibers (within the fiber cross-section (θ), in the direction of the fiber length (γ)), crimp of the fibers, and the projected curvature of the fibers (in the XZ (R_{XZ}) and YZ planes (R_{YZ}))).

The initial alignment of the fibers is an important factor in determining their subsequent deformation and rearrangement behavior when exploring fiber bundle compaction simulations. For perfectly parallel and thoroughly aligned straight fiber bundles, during quasi-static compaction, there is no space for the fibers to move due to their close alignment. Therefore, under external forces, these fibers adapt to the compaction process mainly through axial lightly bending deformation. In contrast, arbitrary aligned linear fiber bundles exhibit rearrangements and deformations during compaction. Since there is no strict alignment between fibers, more interactions between fibers occur when compaction pressure is applied, including sliding and bending. These interactions result in deformation of the fibers in the lengthwise direction and may produce localized rearrangements and bending. Microstructural parameters indicate that these bending deformations remain relatively large. The non-uniform distribution of the fibers leads to a non-uniform distribution of compaction forces between the fibers, resulting in stress concentrations between the fibers, which in turn cause fine deformations locally.

The undulation of the fibers increases the ability of the fibers to interact with each other. This not only affects the density and stiffness of the material on a macroscopic level, but also changes the stress transfer and distribution between fibers on a microscopic level. When fibers have a high degree of undulation, they are more inclined to form complex structures such as tangles and locks during compaction. These structures increase the friction and entanglement of the fibers with each other, resulting in the need for greater pressure to reposition the fibers or further compact the material. Comparatively, fibers with low crimp are easier to rearrange and slide during compaction, resulting in a relatively low compaction pressure required to achieve the same volume fraction. Fiber bundle models with a high degree of undulation (4 undulation

points) have low initial volume fractions (low density), and to exclude the effect of initial density on compaction, pre-compaction simulation of fiber bundles is a strategy. At a later stage of the compaction process, the final compaction strengths were essentially the same. Furthermore, although the number of contacts inside the fiber bundle differed between with and without pre-compaction (different in 20%), the overall increase was not significant, especially when considering the complexity of the high crimp fibers. The compaction strength of the fiber bundle is not linearly related to the number of physical contacts between fibers, but is more influenced by the morphology of the fibers themselves. Fibers with a high degree of undulation create more resistance in space through entanglement and interlocking; this structure is more difficult to be changed under same pressure, and therefore exhibits higher resistance during compaction.

In addition, the microstructural parameters such as diameter, have a significant effect on the behavior during compaction. The slenderness of fibers with S_o(with fiber's diameter=0.5 mm), $\frac{1}{10}S_o$(with fiber's diameter=0.05 mm), $\frac{1}{50}S_o$(with fiber's diameter=0.01 mm) were analyzed with compaction simulations. The slenderness is an important factor affecting the bending stiffness of fibers. Therefore, the geometric model of small-diameter fiber bundles demonstrated low compaction pressures, compared to the large-diameter fiber bundle model. Small diameter fibers are more subjected to deformation under external forces because of their lower bending stiffness that enables local high curvature and then ability to fill-in gaps. This deformation is not only bending or compression at the level of individual fibers, but also includes rearrangement behavior under the interaction of multiple fibers. When the fibers are compacted, the arrangement in the cross-section shows a stable triangular structure, which is typically the most compact way of filling the space.

Friction coefficient directly affect the ability of fibers to rearrange and move during compaction, thus affecting the compaction behavior. Compaction simulations were performed for fiber bundle models with different friction coefficients. At low fiber bundle densities (V_f), higher friction coefficient requires higher compaction pressure. However, for geometries with high density, the effect of friction coefficient on compaction pressure almost disappears. This indicates that the friction coefficient is an important factor affecting the compaction pressure at the early step of compaction. As the compaction process continues, the density of the fiber bundles increases and the space between the fibers decreases until there is no additional space

for fiber movements and rearrangements. In the high-density compaction state, although the friction between fibers still exists, its effect on the compaction pressure is relatively weak. This is because at the locking configuration is mostly a geometrical phenomenon rather than a friction one (even if both may cohabit). As a result, the effect of the friction coefficient on the compaction pressure almost disappears under high-density compaction.

Even if an intensive work remains to do, and much more calculations have to be done to provide a real parametric and sensitivity study this section gave a first overview of the potentiality of the developed tool to analyze the influence of the initial microstructure parameters on the compression behavior which is of a main importance to build a consistent constitutive law. But there is another important issue that has to be addressed, especially because hyperplastic and hypoplastic approaches are currently used for the fiber bundles modeling: what is the influence of the loading path on the microstructure and forces, and consequently as regards continuous modeling, what is the relationship between the strain history and the stresses. This question is addressed in the next section.

Section 9 Influence of compaction parameters

9.1 Impact of compaction loading Path

This section investigates the effect of compaction path on the fiber bundle. Such investigation can reveal how different compression strategies affect the tuning of the internal structure of the fiber bundle, the inter-fiber interactions, the density and mechanical properties after compression. It is also of a main importance for the homogenized mechanical modelling at the mesoscale.

9.1.1 Simulation of different compact paths

The compaction simulation described above is single vertical direction compaction. In addition, biaxial compaction is a loading method to further investigate the effect of fiber rearrangement on compaction performance.

Here, biaxial constrained compaction simulations of fiber bundles with different compaction paths are performed, and the initial model is shown in Figure 9.1. Six different compaction paths were tested for two different final strains: 12 % and 6 %, as presented in Figure 9.2. The compaction paths are written 1 to 6 for the strain 12 %, and 1* to 6* for the strain 6 %. The compaction channel where the fiber bundle is located is rectangular, the length in X direction (5 mm) is higher than the height in Y direction (3.22 mm), the paths 1 to 5 and 1* to 5* follow the same compaction speed in X and Y directions; paths 6 and 6* follow the same deformation (strain) in X and Y directions at the same time, so the compaction speed in X and Y directions is not the same. However, the differences in strain velocity are small enough to be neglected. The other simulation parameters for all the compaction paths are the same, previously presented in Table 6.1. Even if 12 % could be considered as a relatively high value for the small strains assumption, the linearized strain in X and Y directions are used and calculated for multiple compaction paths. Indeed, the goal here is not to obtain the constitutive equation of the continuous homogenized media but to analyze the influence of the path on the response.

$$\varepsilon_{XX} = \frac{\Delta X}{X},\ \varepsilon_{YY} = \frac{\Delta Y}{Y} \tag{9.1}$$

$$\varepsilon_{XX} = \varepsilon_{YY}=12\%,\ \frac{1}{2}\varepsilon_{XX} = \frac{1}{2}\varepsilon_{YY} = 6\% \tag{9.2}$$

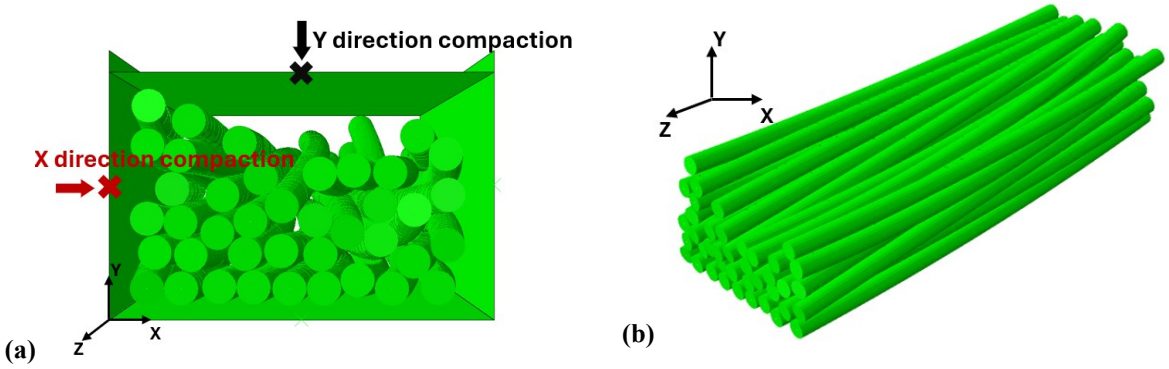

Figure 9.1 Fiber bundle model of different compaction paths.

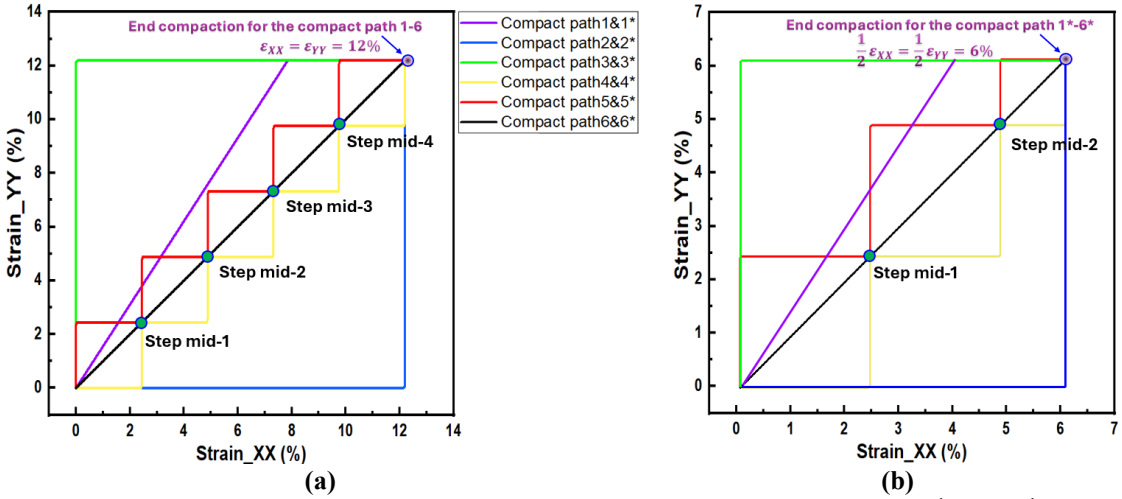

Figure 9.2 Compaction paths (a) 1 to 6 with $\varepsilon_{XX} = \varepsilon_{YY} = 12\%$, and (b) 1* to 6* with $\frac{1}{2}\varepsilon_{XX} = \frac{1}{2}\varepsilon_{YY} = 6\%$.

a) $\varepsilon_{XX} = \varepsilon_{YY} = 12\%$

Figure 9.3 presents the relationship between strain and compaction pressure in X and Y directions, at during the compaction (a, b) but also at the same final strain field (c, d), and the Figure 9.4 shown the compaction pressure at the same strain ($\varepsilon_{XX} = \varepsilon_{YY}$) point (step mid-1 to step mid-4 point) in Figure 9.5. Figure 9.5 presents the 3D compaction deformed geometry of compaction path 1 to 6.

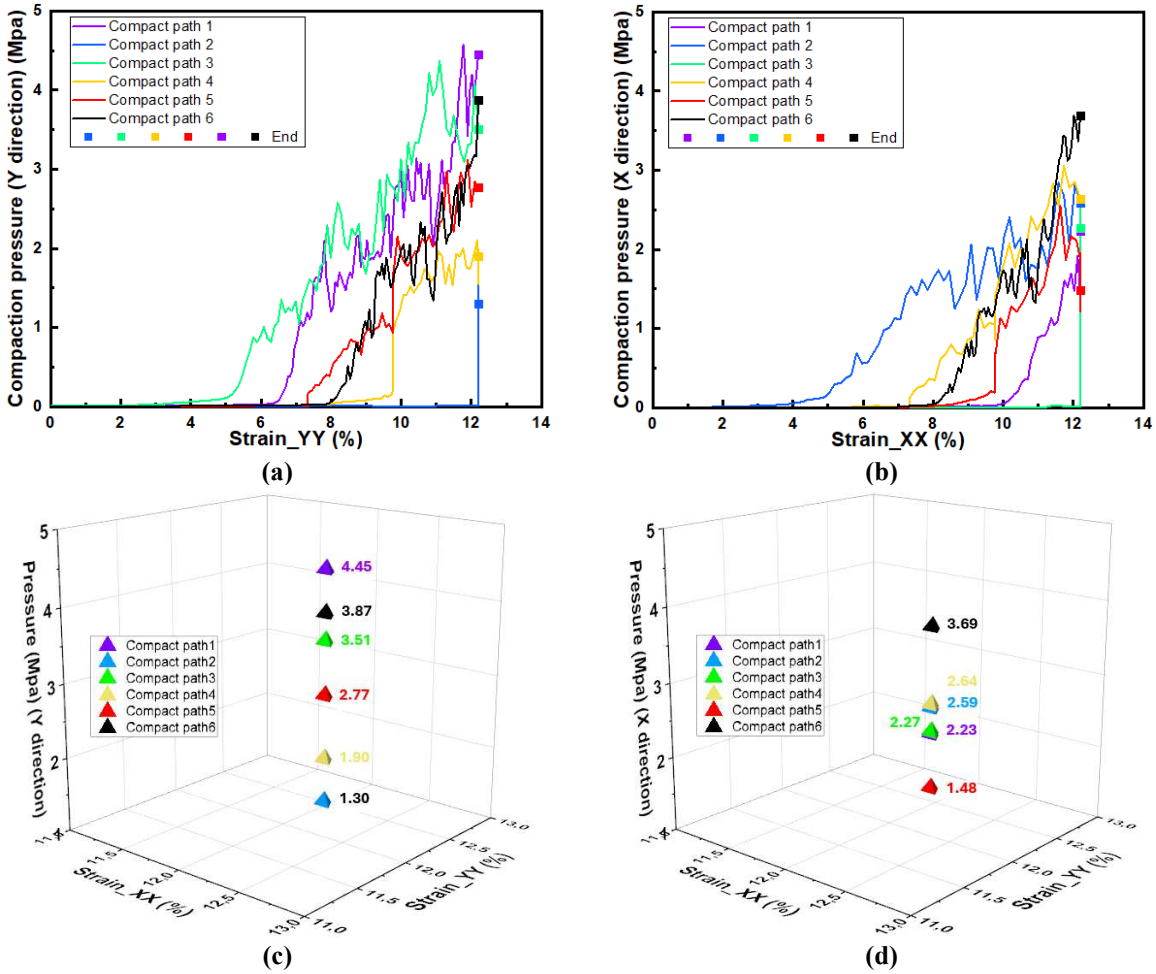

Figure 9.3 Geometry with different compaction paths 1 to 6, $\varepsilon_{XX} = \varepsilon_{YY} = 12\%$. (a) Relationship between Strain YY (ε_{YY}) and Pressure of Y direction, (b) relationship between Strain XX (ε_{XX}) and Pressure of X direction, (c) end of compaction pressure in Y direction, (d) end of compaction pressure in X direction.

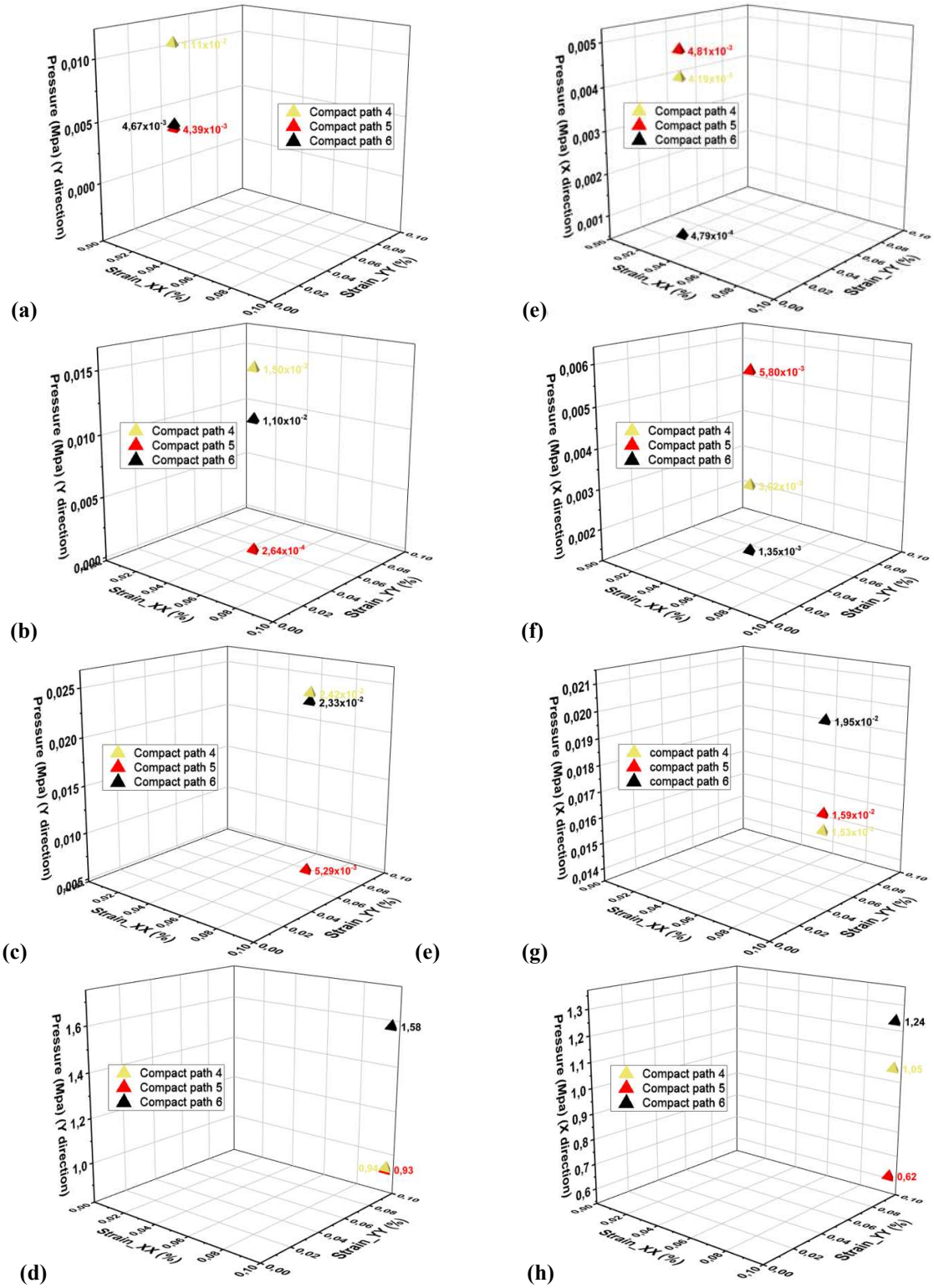

Figure 9.4 The compaction pressure of geometry with different compaction paths 4 to 6. (a-d) The Y direction pressure at the compaction step mid-1 to step mid-4 point of compact path in Figure 9.2 (a). (e-h) the X direction pressure at the compaction step mid-1 to step mid-4 point of compact path in Figure 9.2 (b).

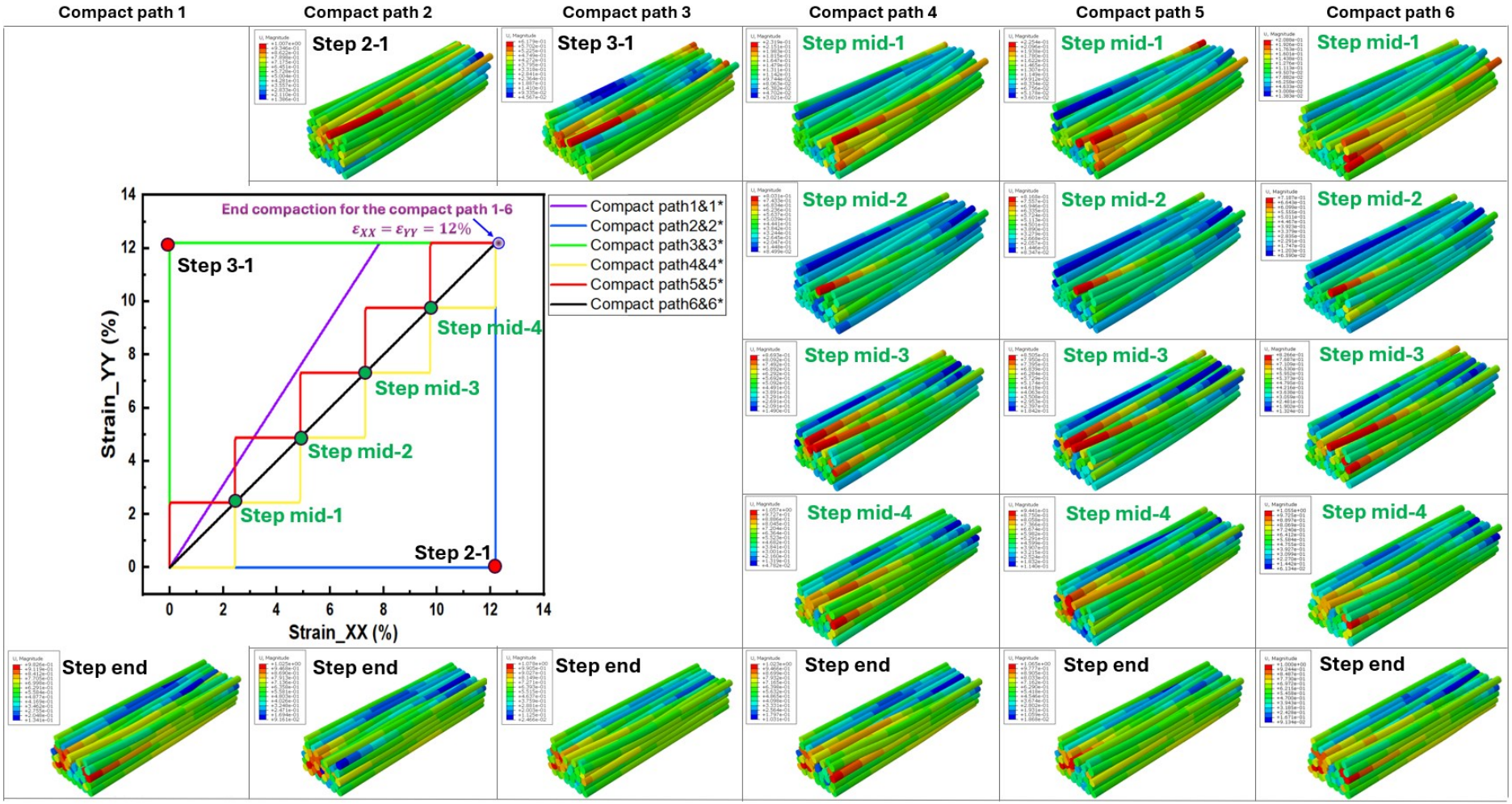

Figure 9.5 Simulation with 6 different compaction paths 1 to 6, $\varepsilon_{XX} = \varepsilon_{YY} = 12\%$.

The compaction behavior of the fiber bundle model through different compaction paths is significantly different. This is a first answer to the asked question; the strain path seems to lead to different forces. More than that the order in the loading direction seems to drive the ratio between the pressure. The first strain direction inducing higher pressure in the same direction. Consequently, it is concluded that the final strain state and the stress state are not directly related. The curves shapes are the expected ones, which is explained hereafter, but the different final forces are the relevant point. Looking at path 2 and path 3, where path 2 is compaction in the X-direction followed by compaction in the Y-direction, and path 3 is the opposite. The trend of the compaction pressure is as expected almost the opposite. The upward trend of the pressure from the fibers in the X and Y direction when the X direction is compacted first is the same as the upward trend of the pressure from the fibers in the Y and X direction when the Y direction is compacted first. Let's then consider the fiber bundle which is first compacted in the X-direction because the dimensions in the Y-direction are fixed, the fibers cannot expand in the Y-direction to accommodate compression in the X-direction. The reorganization has then to occur within a lower space. This leads as already seen to an increase of the X pressure, however, the pressure is not transmitted by the fiber network to the Y sides of the box, the Y pressure does not increase or only slightly. This can be explained by the contact path and the friction forces between the fibers, the contact angles between the fibers makes the loads to be transferred toward X direction and not toward Y direction. This was already observed in the work of Latil (Latil et al., 2011). He had indeed noticed that when the volume fraction increases the confined and free compaction behavior were converging, meaning the confinement had no influence, in other words, the compression inducing no movements in the transverse direction even not blocked. Here it the fact must wait for a higher volume fraction might be explained by the presence of oil that reduces the friction coefficient. This specific loading transfer which is also encountered in the granular media is undoubtedly the reason why the strain path influences the load configuration. It appears then clearly that since the loads are not transferred from one direction to the other, the first strain direction will keep a higher pressure than the transverse one.

The same phenomenon is observed to a lower extend for paths 4, 5, 6 and 1 exhibiting consistent trend and values regarding the previous analysis. Thus, more than the comparison of two strain paths which could be questioned since instabilities and uncertainties exist, the 6 consistent and different results for the 6 paths enables confirm the analysis and the conclusion. In order to validate it further and see the influence of the strain, the less deformed paths are analyzed

hereafter.

b) $\frac{1}{2}\varepsilon_{XX} = \frac{1}{2}\varepsilon_{YY} = 6\%$

The relationship between strain and compaction pressure of X and Y direction with a strain of 6 % is presented in in Figure 9.6 and 3D compaction strain geometry of compaction path 1* to 6* in Figure 9.8. Similarly, different compaction paths influence the compaction behavior with a final strain of 6 %. During compaction, the X and Y directions responded differently to the compaction pressure. Even if some instabilities are noticed during the calculation, this enables to confirm the previous analysis and conclusion.

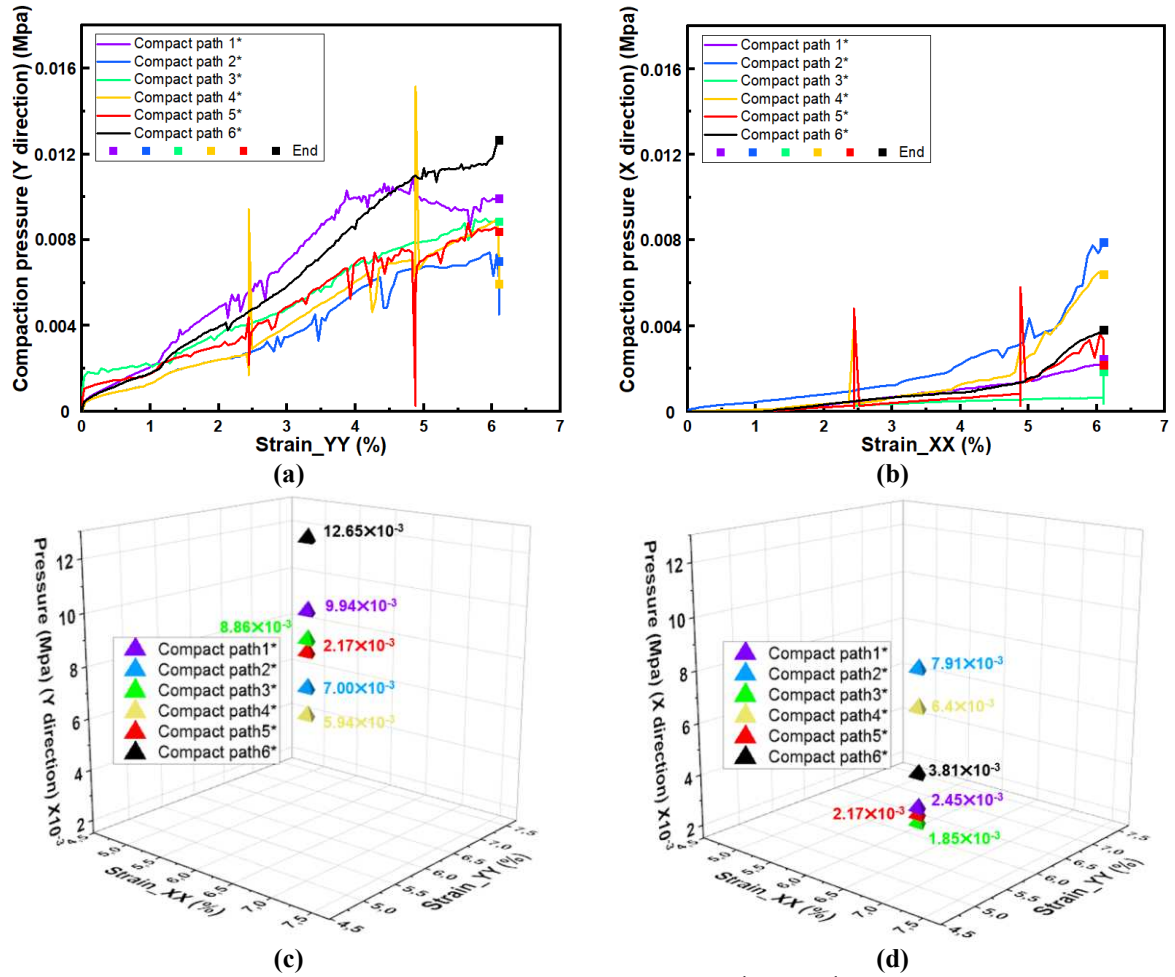

Figure 9.6 Geometry with different compaction path 1* to 6*, $\frac{1}{2}\varepsilon_{XX} = \frac{1}{2}\varepsilon_{YY} = 6\%$. (a) Relationship between Strain YY (ε_{YY}) and Pressure of Y direction, (b) relationship between Strain XX (ε_{XX}) and Pressure of X direction, (c) end of compaction pressure in Y direction, (d) end of compaction pressure in X direction.

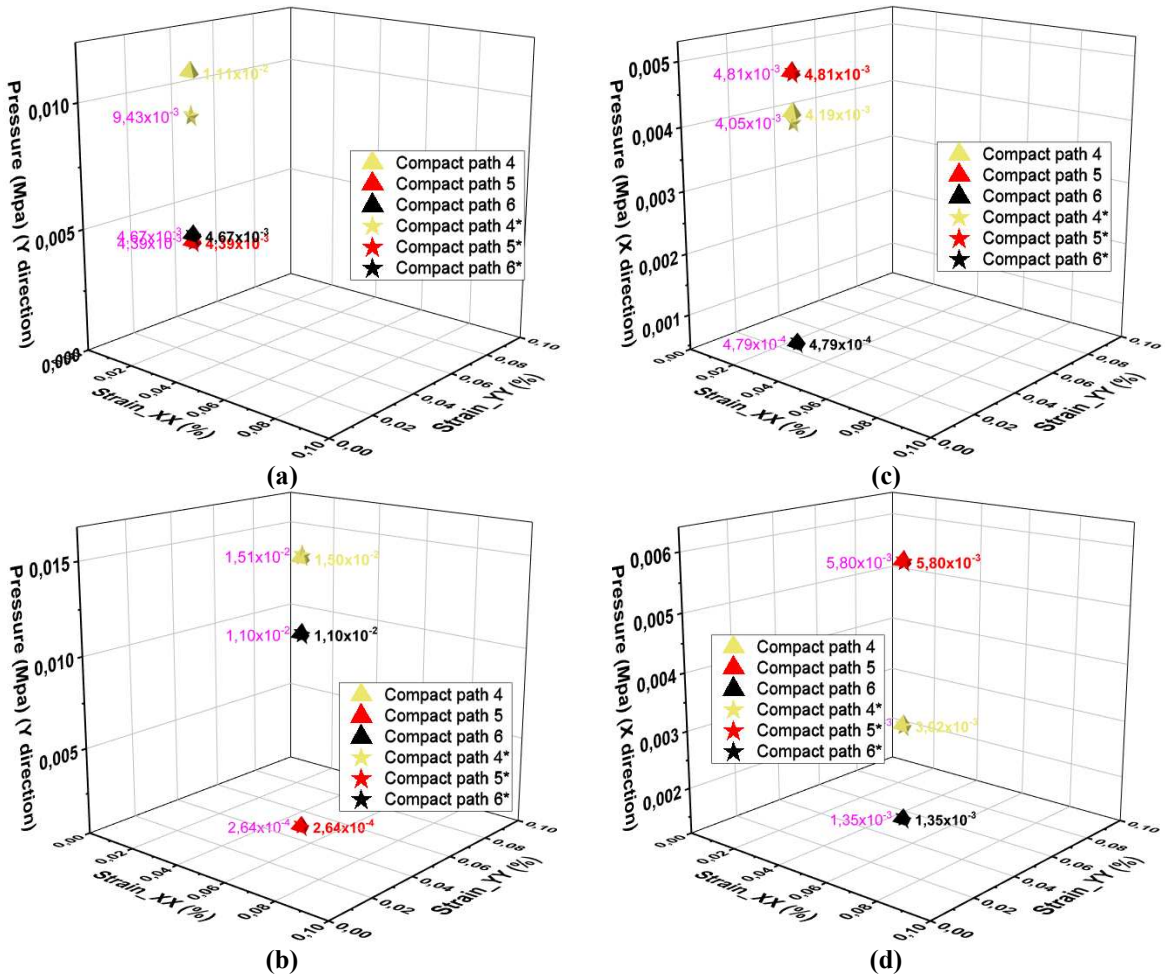

Figure 9.7 The compaction pressure of geometry with different compaction paths 4 to 6 and path 4* to 6*. (a, b) The Y direction pressure at the compaction step mid-1 and step mid-2 point of compact path in Figure 9.2 **(a, b). (e-h) the X direction pressure at the compaction step mid-1 and step mid-2 point of compact path in Figure** 9.2 **(a, b).**

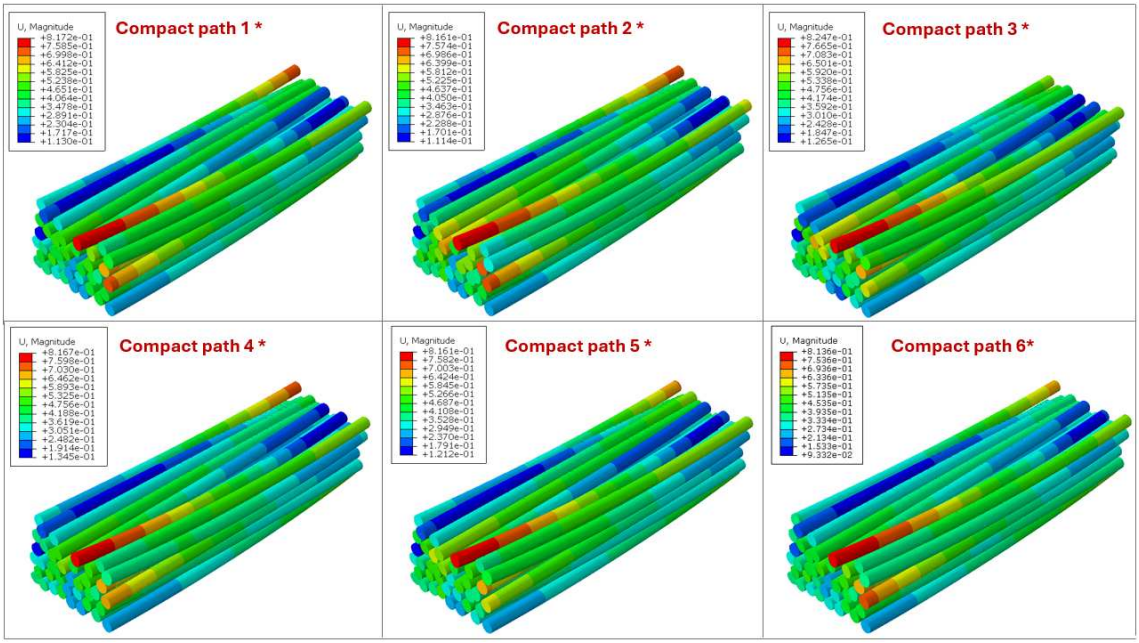

Figure 9.8 Simulation with 6 different compaction path 1* to 6*, $\frac{1}{2}\varepsilon_{XX} = \frac{1}{2}\varepsilon_{YY} = 6\%$.

9.1.2 Analyze of the indicators of microstructure of fiber bundle

The compaction curves comparing the deformation of 12 % to 6 % are shown in Figure 9.9. The compaction pressure in X and Y direction are shown in Figure 9.9 (a) and (b), respectively. In addition, the centerline positions of the fibers with deformation of 12 % and 6 % are shown in Figure 9.9 (c) and (d), respectively.

It is reasonable that the position of the fibers is related to the compaction pressure. This is because the position of the fibers determines the mutual contact and interaction between the fibers. In addition, the fiber position of compact 1 is considered as the reference, the distance between the fibers of compact path 1, 2 and 1, 3 are presented in Table 9.1; the same analyze for compact path 1*, 2* and 1*, 3*, show in Table 9.2.

In addition, average and standard value of the distance of fibers position between compaction path 2, 3 (FPDDR (according to the diameter of fiber)) is shown in Table 9.3. As the compaction continue compact path with strain 12 %, the fiber arrangement is changed significantly compared to state with compact path with strain 6 %.

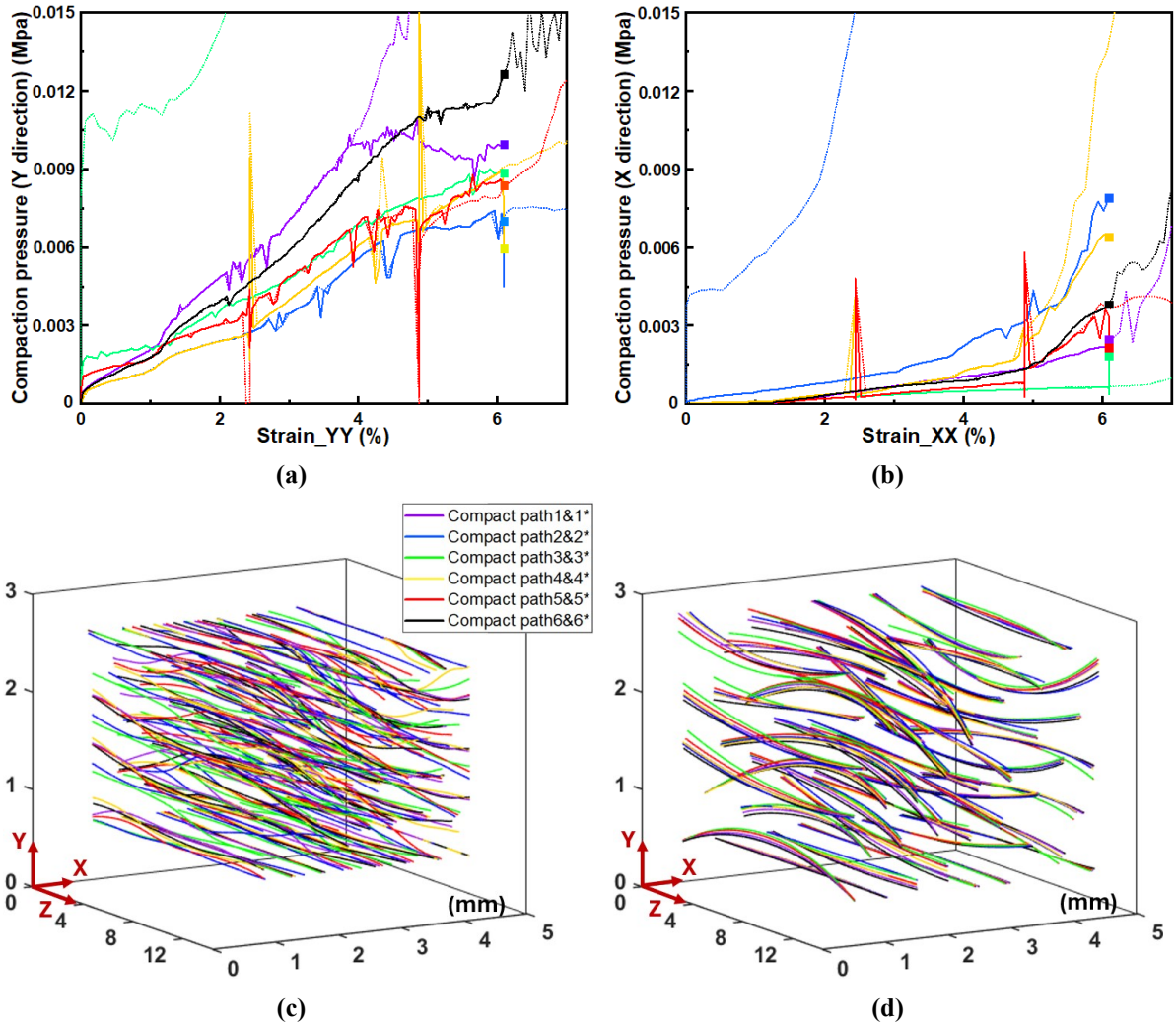

Figure 9.9 Compact pressure comparison between paths 1 to 6 and paths 1* to 6*. (a) Pressure of Y direction, (b) pressure of X direction, (c) centerline of fiber bundle after compaction path 1 to 6, (d) centerline of fiber bundle after compaction path 1* to 6*.

Table 9.1 The distance of fibers position between compaction path 2, 3 and 1.

	Compact path			
Indicators (%)	**2**		**3**	
	μ	***σ***	***μ***	***σ***
FPDDR (according to the diameter of fiber)	18.8	10.5	15.8	12.1

Table 9.2 The distance of fibers position between compaction path 2*, 3* and 1*.

	Compact path			
Indicators (%)	**2***		**3***	
	$\boldsymbol{\mu}$	$\boldsymbol{\sigma}$	$\boldsymbol{\mu}$	$\boldsymbol{\sigma}$
FPDDR (according to the diameter of fiber)	19.8	10.0	15.8	11.9

Table 9.3 The distance of fibers position between compaction path 2 and 3, and 2* and 3*.

	Compact path			
	3		**3***	
Indicators (%)	$\boldsymbol{\mu}$	$\boldsymbol{\sigma}$	$\boldsymbol{\mu}$	$\boldsymbol{\sigma}$
FPDDR (according to the diameter of fiber)	**25.6**	**11.2**	**27.1%**	**13.4**

a) Orientation and mis-orientation

The orientation unit spheres of fiber after compaction path 1, 2 and 3 and 1*,2* and 3* are presented in Figure 9.10, and the orientation tensor in Figure 9.11. The orientation A_{33} of compaction path 2, 3 and 2*, 3* is higher than 1 and 1*, which means the fibers arrangement are more directionally, which means the fibers distributed along the Z-axis/$\boldsymbol{e_3}$. In addition, the mis-orientation (α and β) is considered to indicate the orientation of fibers. The α angle converge consistently of all the paths toward 0 from 6 to 12 %, and the β dispersions are reduced consistently due to the convergence toward a better organize microstructure. However, no significant influence can be noticed on the angles depending on the strain path, especially because they converge toward 0.

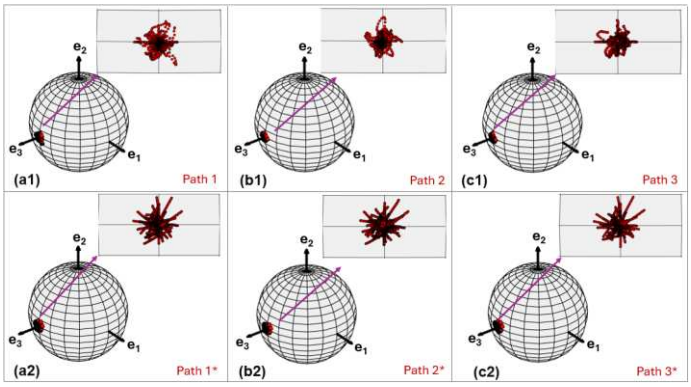

Figure 9.10 Orientation unit spheres of fiber. (a1-c1) Compact paths 1 to 3, (a2-c2) compact paths 1* to 3*.

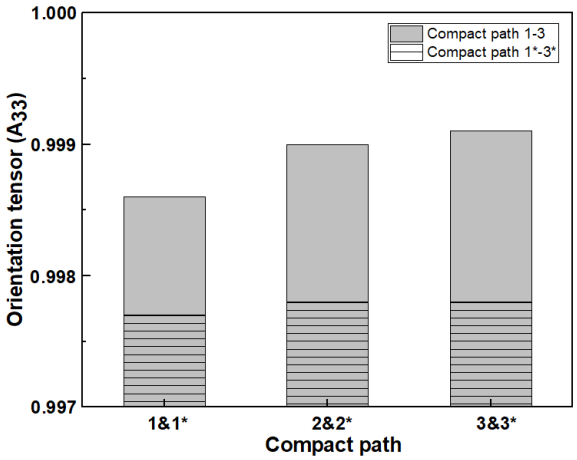

Figure 9.11 Orientation tensor A_{33} of compact paths 1 to 3 and 1* to 3*.

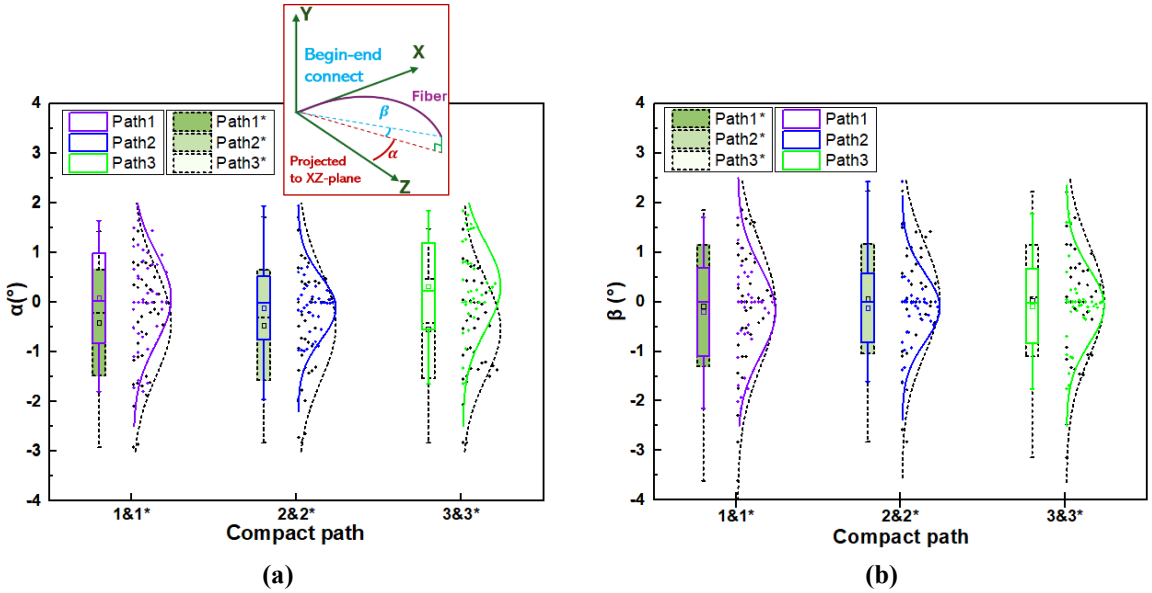

Figure 9.12 Boxplot of mis-orientation of fibers with compact paths 1 to 3 and 1 to 3*. (a) α (°), (b) β (°).

b) Contact numbers and contact angle.

The contact number between fibers, between fibers and plates, total contact number of compaction paths 1 to 3 and 1* to 3* is presented in Figure 9.13 and the contact angle between fibers in fiber's section θ and in fiber's length direction γ in Figure 9.14 and Table 9.4. After different compaction paths, the contact number keep almost same (Figure 9.13). The simulation of compaction of fibers with different paths leading to the same volume fraction and deformation implies that, although the compaction paths are different, the compaction process is quasi-static and the final deformation in the X and Y directions are the same (the morphology of the compaction channels is the same), and that the volume of the fiber bundles inside the box is essentially conserved during the compaction process. Although different compaction paths may initially lead to different internal alignments and stress distributions, the effect of this anisotropy diminishes as compaction proceeds, as the material structure tends to a stable configuration, so, the contact number are almost same for compact path 1, 2, 3 and also for compact path 1*, 2*, 3*.

The contact angles are more interesting to analyse because the straightening and bending of a fiber strongly depends on the loading direction. It has then to be noticed that the evolution and final value of γ is different for the different configurations. Path 3 induces a significant decrease in γ angle when 12 % is reached.

The distribution of θ is also an interesting indicator since it shows a much lower proportion of contacts from 20 to 45° in the path 3 than for the two others, this is mainly balance by a higher [0, 10] and [80, 90] (°) value.

This difference in the fibers contacts angles might explain why the relationship between the pressure is different (Figure 9.15) whereas the contact number is close.

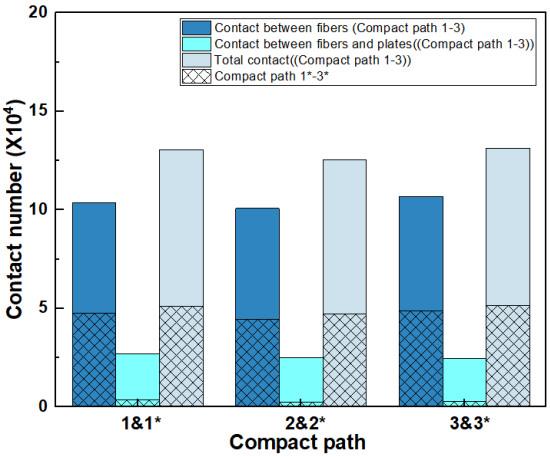

Figure 9.13 Contact number of compact paths 1 to 3 and 1* to 3*.

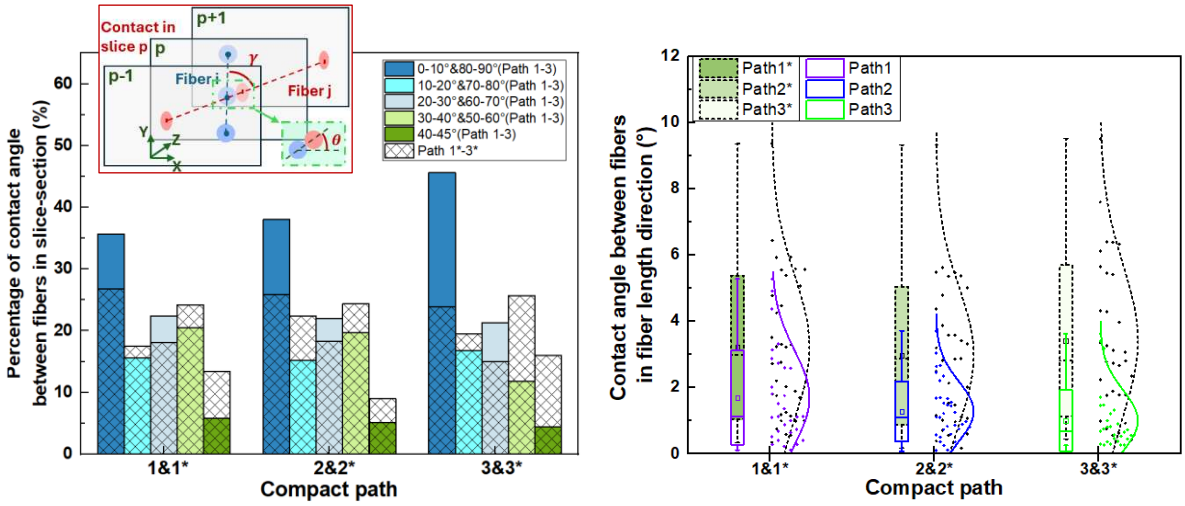

(a) (b)

Figure 9.14 Contact angle of compact paths 1 to 3 and 1* to 3*. (a) θ (°) in the fiber section, (b) γ (°) in the fiber length direction.

Table 9.4 Contact angle between fibers γ (°) in the fiber length direction.

	μ	σ	μ	σ	μ	σ
	1&1*		2&2*		3&3*	
$\varepsilon_{XX} = \varepsilon_{YY} = 12\%$	1.667	1.060	1.210	0.950	0.975	0. 83
$\varepsilon_{XX} = \varepsilon_{YY} = 6\%$	3.220	2.163	2.951	2.205	3.416	2.270

Figure 9.15 The schema of relationship between contact number and contact angle θ.

c) Crimp and curvature

The boxplot of crimp of geometry after compaction paths 1, 2 and 3 and 1*, 2* and 3* is presented in Figure 9.16, and the average and standard value of crimp in Table 9.5. In addition, Figure 9.17 shows the curvature radius of fibers in XZ and YZ plane. The crimp Boxplots indicates that the fibers with compaction path 3 is more crimped, but this difference is not significant. We obtain here again that the same final spaces between the fibers tends to bring the crimp toward 0, almost in the same way whatever the path, however, this does not imply that the fibers have the same trajectory.

This is confirmed by the study of the curvature Figure 9.17, indeed, if consistently converging toward curvature reduction, the evolution shows an opposite trend regarding the mostly accommodated angle between path 2 and 3. That mean the crimp reduction is obtained through a privileged realignment in two orthogonal direction. The final increase for R_{XZ} is higher for the Path 3 according to path 2 whether the R_{YZ} is lower. This opposite trend can then be related to the previous conclusion regarding the contact angles and the changes in the pressure relationship.

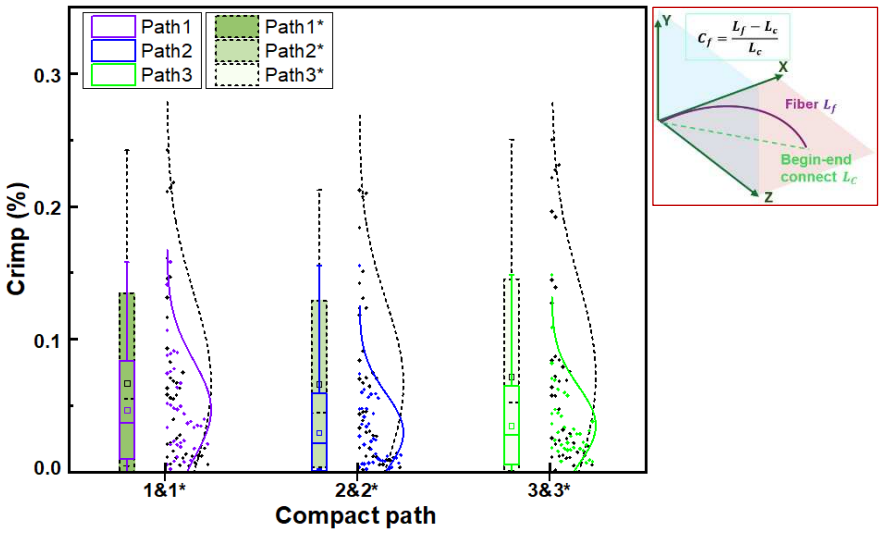

Figure 9.16 Crimp of compaction paths 1 to 3 and 1* to 3* (%).

Table 9.5 Crimp of compaction paths 1 to 3 and 1* to 3* (%).

	μ	σ	μ	σ	μ	σ
	1&1*		2&2*		3&3*	
$\varepsilon_{XX} = \varepsilon_{YY} = 12\%$	0.043	0.027	0.031	0.029	0.045	0.030
$\varepsilon_{XX} = \varepsilon_{YY} = 6\%$	0.067	0.068	0.066	0.062	0.070	0.072

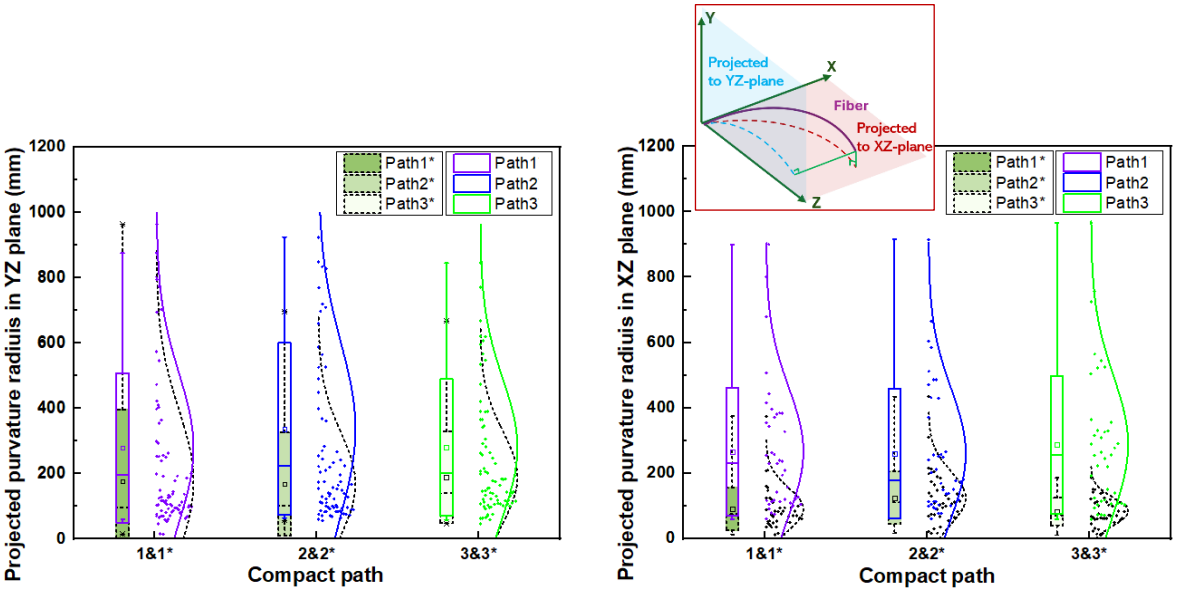

Figure 9.17 Curvature radii of compact p path 1-3 and 1*-3* (mm). (a) In YZ plane, (b) in XZ plane.

Table 9.6 Curvature radii of compact path 1-3 and 1*-3* in XZ and YZ plane (mm).

	$\overline{R_{XZ}}$		$\overline{R_{YZ}}$		$\overline{R_{XZ}}$		$\overline{R_{YZ}}$		$\overline{R_{XZ}}$		$\overline{R_{YZ}}$	
	μ	σ	μ	σ	μ	σ	μ	σ	μ	σ	μ	σ
	1&1*				2&2*				3&3*			
$\varepsilon_{XX} = \varepsilon_{YY} = 12\%$	260	200	278	222	260	198	336	260	287	210	279	209
$\varepsilon_{XX} = \varepsilon_{YY} = 6\%$	95	64	169	168	125	80	164	161	80	46	188	141

The influence of compaction path was considered here, the different compaction paths. The influence the compression response is significant whereas many indicators of the microstructure remain close. This seems to demonstrate that the contact angles between the fibers play a significant role in the compaction response even with an equivalent contact number. Here we have only few results and they need to be confirmed different microstructures and paths. The

compaction speed may also affect the fiber-fiber interactions as well as the final fiber arrangement. In the next section, the influence of compaction speed is considered.

9.2 Influence of compaction speed and V_f

9.2.1 Compaction speed

Figure 9.18 shows the compaction pressure in function of volume fraction with different compaction speeds: $V_0 = 10^3$ mm/min, , and then $V = 0.5V_0,\ 2V_0,\ 3V_0,\ 4V_0,\ 5V_0,\ 10V_0,\ 20V_0,\ 100V_0$, damping $\alpha = 10^5$ (this parameters was validated in Section 6). The 3D rending fiber bundle geometry after compaction with speed $V_0,\ 10V_0,\ 100V_0$ are presented in Figure 9.19. In the compaction simulation of fiber bundles, the higher the compaction speed, the higher the required compaction pressure. It is because the higher the compaction speed, the more significant the inertial effect of the fiber bundle during compaction (Haji et al., 2023; Haji Oussama, 2018). Rapidly moving fiber bundles require greater forces to overcome their momentum, especially when attempting to change their arrangements in a short period of time. At high compaction speeds, the microstructure inside the fiber bundle may not be able to answer instantly to external stresses modifications, i.e., the fibers may not be able to rearrange themselves effectively to reduce their volume and adapt the pressure. Friction and contact within the fibers may increase quickly, requiring greater external forces to change their alignment. This has to be put in relation with the relaxation phenomenon observed experimentally that would require to be studied in the next future. Because both are related to a viscous effect that seems to have a significant influence on the media response. A first approach is proposed in the next section, even if an intensive work is required to characterize it.

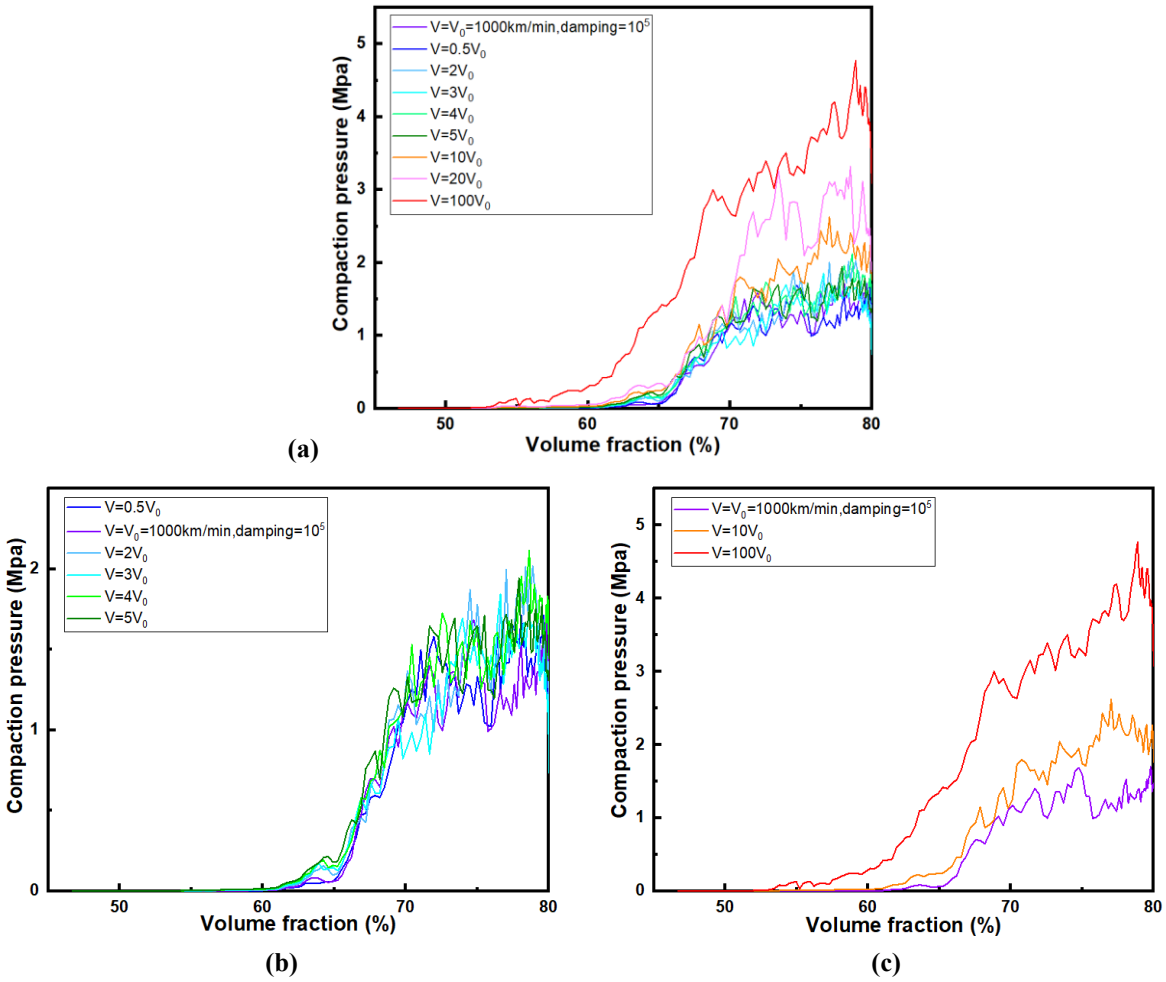

Figure 9.18 Relationship between compaction and volume fraction with different compaction speeds without relaxation step, the reference compaction speed V_0=1000 mm/min with damping coefficient $\alpha = 10^5$.

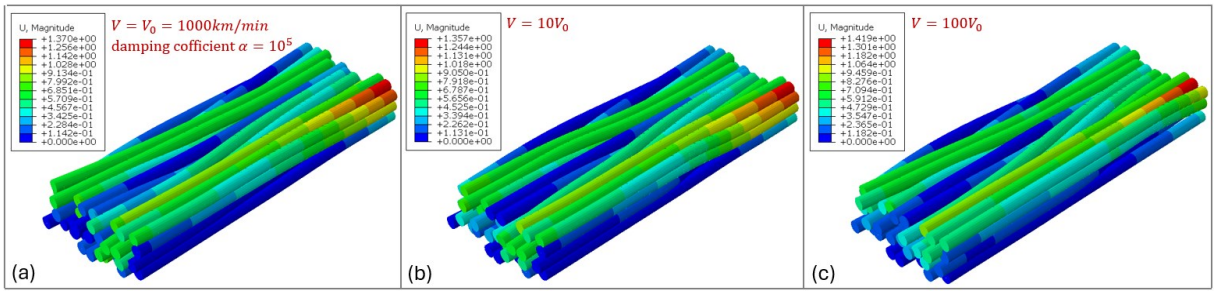

Figure 9.19 3D rending of geometry after compaction with different compaction speeds without relaxation step, the reference compaction speed V_0=1000 mm/min with damping coefficient $\alpha = 10^5$.

The relaxation phenomenon was observed in the experiment part of fiber bundle (section 6), so, the influence of relaxation of compaction is analyzed in this part. In the compaction simulation,

the “SMOOTH STEP” is used to define time-amplitude, ABAQUS®/Explicit automatically connects each data pair to a curve. Both the first-order and second-order derivatives of these curves are smooth and have a zero slope at each data point. Since both derivatives are smooth, it is possible to apply “SMOOTH STEP” displacement loads using only the initial and final data points, and the intermediate motions will be smooth. Thus, using a “SMOOTH” type of loading amplitude allows for quasi-static analysis without waves due to discontinuous loading rates(“ABAQUS Documentation (6.5-1),” n.d.). For example, Figure 9.20 shows the created “SMOOTH STEP” in ABAQUS/Explicit®. In the general compaction simulation, the “0-A” range was used in time-amplitude. In order to consider the relaxation step in the end of compaction simulation, the “A-B” step was considered as relaxation step.

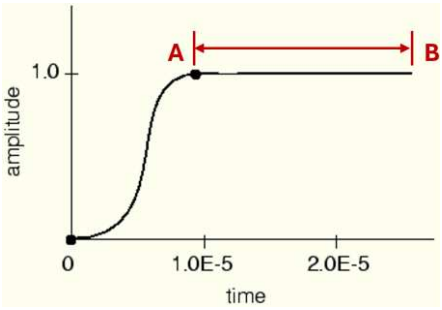

Figure 9.20 Scheme of displacement amplitude definition in ABAQUS®/Explicit (“ABAQUS Documentation (6.5-1),” n.d.).

The compaction pressure in function of step time (in ABAQUS®/Explicit) is presented in Figure 9.21, where the compaction without and with relaxation step was performed. The end of compaction tests without and with relaxation step are point A and B, respectively. The compaction curves without relaxation was consistent with ones with relaxation. Figure 9.22 presents the centerline of fiber bundle after compaction display, as the increase of compaction speed, the ΔAB increased, and the difference between fibers before and after relaxation step is more significant. This is because the relaxation in compaction pressure is bigger of $V = 100V_0$, the fibers arrangement in this period, so the fibers position changed before and after relaxation step.

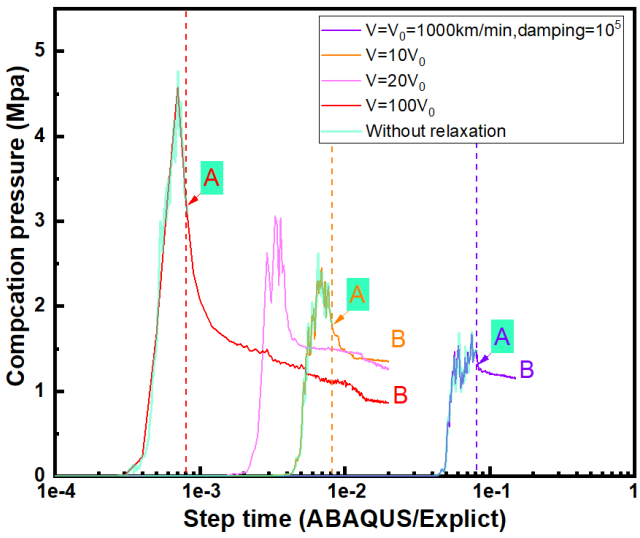

Figure 9.21 Compaction pressure with different compaction speeds with relaxation and no-relaxation step, the reference compaction speed V_0=1000 mm/min with damping coefficient $\alpha = 10^5$.

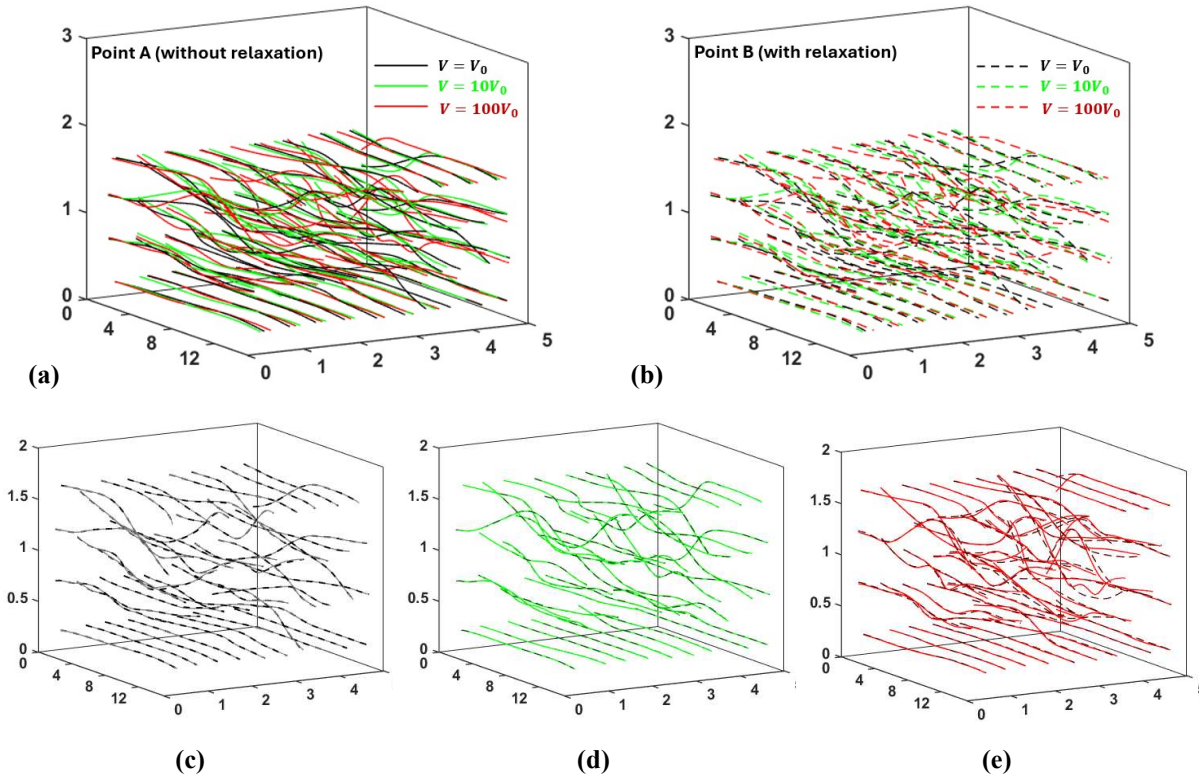

Figure 9.22 Centerline after compaction (a) without relaxation, compaction speed with V_0, $10V_0$, $100V_0$, (b) with relaxation, compaction speed with V_0, $10V_0$, $100V_0$, (c) with/without relaxation, compaction speed with V_0, (d) with/without relaxation, compaction speed with $10V_0$, (d) with/without relaxation, compaction speed with $100V_0$.

Figure 9.23 shows the compaction pressure in the function of step time of different end of the compaction V_f. In compaction tests of fiber bundles, the relaxation behavior of fiber bundles is related to the internal structure of the material, the compaction speed, in addition to the end density (volume fraction V_f). The relaxation effect is low at low final density of fiber bundle (V_f=70 %). At lower density, the internal space of the fiber bundle is larger, and the inter-fiber contact is weaker, so the fibers can be slightly adjusted and rearranged relatively easily during the initial compaction step, and thus the relaxation effect is not significant. As the V_f increases, the relaxation effect increases, the distance between fibers decreases, and contact increase. Thus, the internal stress relaxation is more pronounced when this V_f is maintained. However, it seems that at V_f=80 %, the fiber bundle becomes so dense that each fiber is almost in a locked state and the inter-fiber gaps are so small that the fibers can hardly move. At this stage, the fiber bundles might reach a self-locking state due to the high density, and the stress distribution is more uniform, so the relaxation effect is reduced. With further increase in volume fraction V_f=85 %, the relaxation step is difficult to dissociate form the instabilities due to the brutal changes in microstructure induced by stick-slip effects. These preliminary results require to be confirmed by other calculations and a deepened analysis in the microstructure.

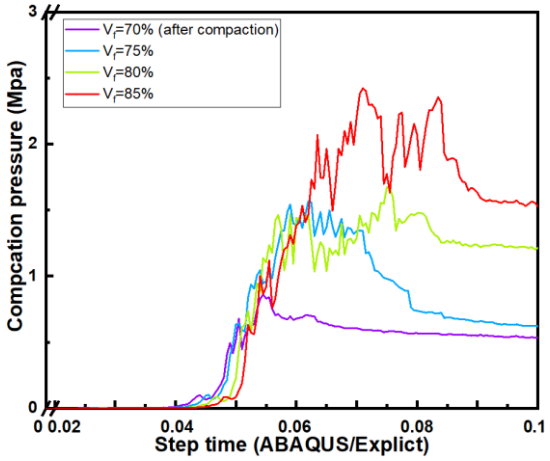

Figure 9.23 Influence of compaction pressure with different compaction states (V_f) with relaxation step.

9.3 Conclusion

In this section the effect of compaction parameters on the fiber bundle was discussed: compaction path, compaction speed, and final volume fraction V_f.

Concerning the compaction path: different compaction paths slightly affect the final morphology of the fibers, since the final compaction deformation is the same, the total contact number keep almost same. However, when fiber bundles achieve similar final V_f under different paths, the contact angle in the fiber' section θ and the contact angle in the fiber length direction with different compact path are different, implying that the fiber rearrangement trend to different with different compaction paths. This results in a different compression response which seems to indicate that the strain state cannot be directly put in relation with the stress state for fiber bundles. The accounting of the strain path in the mechanical behavior of fibrous media is a crucial issue and requires to be confirmed with further analysis.

As regards the compaction speed: as the compaction speed increases, the compaction pressure required for a fiber bundle to reach the same volume fraction increases. Rapid compaction may lead to different fiber deformation and rearrangement dynamics, while slower compaction may allow more time for the fibers to adapt to the pressure changes, leading to different internal structures and mechanical properties. The compaction speed has an important effect on the compaction behavior and relaxation effect of fiber bundles that has been noticed on the experimental tests. High speed compaction leads to different stress states and more pronounced relaxation.

V_f is a key parameter as regards compaction results and affects the density, mechanical properties and microstructure of the fiber bundle. Changes in V_f are directly related to fiber interactions, rearrangement dynamics, and final material properties. The final compaction density seems to affect also the relaxation step, which becomes more pronounced as V_f increases. However, after V_f reaches a certain level, the locking of the microstructure seems to reduce this effect.

Conclusion and perspective

The work presented in this manuscript aims to validate a virtual estimator of the mechanical behavior of roving-type fiber bundles to be able to carry out parametric and sensitivity studies of the different architectural parameters. To achieve this goal, the compaction/compression behavior was chosen because it is the most complex, which requires the most reorganization of the network. To carry out the study, a model containing 40 slightly entangled, almost parallel, polyester fibers with a diameter of 0.5 mm was chosen as a model sample. The sample was chosen to obtain a compromise between the possibility of the appearance of physical phenomena and the minimization of calculation costs. Finally, the compression test was chosen as the validation test.

To develop accurate models of fibrous assemblies, the strategy implemented is based on digital simulations of compaction/compression coupled with X-ray tomography. The objective is to obtain the true initial microstructure of the sample as well as its evolution during compaction/compression and finally, to obtain the behavior curves of the sample under compaction/compression. To do this, a post-processing strategy for tomography images of the fiber bundle was established, based on the extraction of the average lines of the fibers with the aim of modeling them, subsequently, by beam elements in Abaqus®/Explicit. The proposed approach allows automatic, effective, and accurate extraction of the average lines of the fibers of the fibrous assembly; this extraction/reconstruction was validated by superimposing the tomography images with the reconstructed profiles. In addition, the cassette/compaction channel containing the fibers during tomography was extracted and modeled via Catia V5® for geometry then modeled in Abaqus® by discrete rigid model.

In order to improve the simulation parameters, experimental single and cycled tension tests were carried out on the fibers to determine their Young's modulus; work was also carried out on the optimal size of the elements in order to reduce calculation times, but ensure accuracy at same time. Finally, the penetration control was carried out. Indeed, the spatial resolution of the tomograph and the precision of MATLAB’s automatic contour detection program can lead to slight shifts in the initial position of the fibers, which can lead to differences between the

positions of the fibers resulting from the simulation and those resulting from experimentation after testing. A penetration correction strategy was therefore implemented.

To be able to study the microstructure of fibers in the deformed state, indicators were defined, and the associated analysis tools were developed. The comparison indicators are the number of contacts within the fibrous assembly, the distribution of contact angles, the undulation of the fibers (radius of projected curvature in XZ and YZ plane, these planes are parallel to the fiber length (Z-axis)) and the orientation of the fibers (orientation tensor and mis-orientation around the Z axis of the direction of the fibers), as well as the compression pressure curves as a function of the fibers volume fraction.
Once the tools were created and the simulation parameters developed, three samples were used to validate the strategy by comparison between the numerical simulation and the experimental tests under tomograph combined compaction. The results show differences between experiments and simulations of a few percent for all the indicators. Although these results could still be improved, they make it possible to validate the simulation strategy and the microstructure analysis tools developed. The entire approach can then be used to work on the mechanical responses of new fibrous assemblies to different mechanical loading path, without requiring experimental tests.

It is then useful to create realistic virtual stochastic models of these assemblies. A strategy for creating virtual numerical random fiber bundle geometries with controlled structural parameters was thus developed. In this strategy, to avoid penetrations, the N fibers are generated in N layers and the generation of the final bundle is carried out in 3 steps: using a MATLAB program each straight fiber is created with a random position, a misorientation around the fiber axis is inserted; a point or several points of undulation are inserted on the fibers. Then, in order to make the assembly realistic, a gravity step is imposed in Abaqus®. This strategy of creation of a fiber bundle was validated by compaction/compression simulations with created 3 geometries, whose microstructural parameters correspond to those of sample 2 used for the experimental tests. Even if the macro behavior in compression shows some small differences between the generated

fiber bundle and the experiment, the results remain very consistent. The virtual generator created could therefore be used to carry out numerous virtual tests, in order to understand the influence of different structural and loading parameters.

The structural parameters studied are the undulation of the fibers, the slenderness, and the friction coefficient between fibers. The results obtained and the analysis of the microstructure indicators implemented made it possible to draw some initial conclusions, thus showing the potential of the developed strategy.

First, the initial alignment of the fibers is an important factor in the ability of the network to rearrange and deform; in fact, for perfectly parallel and aligned fibers, the few spaces between fibers do not allow them to move during the test; on the opposite, random aligned straight fibers allow more interactions during testing, for example, sliding and bending. These interactions generate longitudinal deformations and can produce local rearrangements. Finally, for undulated fibers, the undulation increases the ability of the fibers to interact with each other. The more undulated the fibers are, the more complex structures they are able to form during compaction, thereby increasing entanglement and therefore compressive stiffness.

Secondly, to test the effect of fiber slenderness, three models were compared with different fiber diameters (0.5 mm, 0.05 mm and 0.01 mm). As slenderness is an essential parameter of bending rigidity, fibers of smaller diameter are more able to deform under external loads and therefore more able to fill empty spaces, leading to more compacted assemblies under smaller pressures. Thus, the influence of the bending rigidity of the fibers on the compressive rigidity was shown.

Finally, in order to test the impact of the friction coefficient, 4 models were created, with friction coefficients of 0.2, 0.4, 0.6 and 0.8 and show that for low fibers volume fractions, at the beginning of the tests, the higher the friction coefficient, the higher the compression rigidity; for high fiber volume fractions, the effect of the friction coefficient on the compression stiffness disappears due to the locking of the microstructure. The friction coefficient is therefore an important parameter at the beginning of compression, but its effects decrease during the tests until they are no longer predominant.

All these analyzes also made it possible to show that the number of contacts in the microstructures, if it is a powerful parameter, does not allow to account for the evolution of

compression stiffness, even in the compaction step. Undulations, fiber and contact angles must also be taken into account.

Finally, the influence of the loading parameters was analyzed: the loading path as well as the loading speed and relaxation. To analyze the impact of these parameters, several models were created by varying the fibers volume fractions and the loading speeds. The results were able to illustrate the influence of these parameters on the microstructure and on the compression behavior. If the loading path has no significant influence on the number of contacts and the fibers crimp when the final strains are the same, they impact the rearrangement of the fibers, and in particular the contact angles which leads to a modification of the loading transfers. This results in a modification of the pressure/strain relationship. Thus, it seems that the same state of strain does not systematically lead to the same state of loads depending on the loading path, which is a key point for modeling at higher scales.

The effect of compaction speed is also interesting and was able to highlight that the more the speed increases, the more the pressure necessary to reach the same fiber volume fraction increases, highlighting the ability of the fibers to reorganize when the loading speeds are weak and, therefore, the importance of the relaxation phenomenon at low speed. The phenomenon of relaxation, observed during the tests, was also addressed. It is well reproduced by the model, and it seems that the volume fraction plays a role in the intensity of the relaxation. These last two points highlight viscous behavior, which would be interesting to study in more detail and which, once again, would need to be taken into account in modeling at higher scales.

All this highlights the important work carried out to put in place all the tools necessary to analyze the microstructure of fibrous media and the results presented, although preliminary, illustrate the potential of the strategy. However, there are still many lines to confirm and explore. The indicators have now been defined and the tools necessary for their extraction put in place. We should now be able to deeper go through the microstructure of fibrous assemblies using these tools. Likewise, significant work remains in carrying out simulations to take into account all the parameters, including:

- Loading paths
  - In this study, the simulated loadings are uniaxial or biaxial compression with different paths. However, the database created must be enriched with new microstructures, and new points of comparison to confirm the conclusions which are of major importance for the modeling of mechanical behavior.
  - Other paths could be interesting, such as unconfined compaction; during unconfined compaction, because of the lateral freedoms, the interactions between fibers and their deformations present greater freedom, allowing the fibers to move and reposition freely in the uncompacted direction.
  - Other types of loading are also to be tested to observe the response of the microstructure but also, more complex or multiaxial loadings in different orders with experimental validation under tomography. Biaxial compression tests under tomography would be particularly interesting to confirm the results.
- Hysteresis phenomena: it could be interesting to simulate loading/unloading cycled, in order to understand the responses to hysteresis phenomena, to be able to estimate the residual strain of the microstructure and its evolution.
- Shape of the fibrous network: another interesting option is to vary the shape of the fibrous network. For example, (Pham et al., 2020) carried out simulations of lenticular yarns compaction, which opens a new perspective to this study; indeed, in their study, the fibrous assembly has an idealized lenticular shape (depend on a/b ratios), as shown in Figure A. The fiber assembly is subjected to uniaxial or biaxial compaction, in order to observe the effect of different morphologies of fibrous assemblies and their change in microstructure during compaction. This approach helps to understand the dynamics of fibrous networks under compaction.

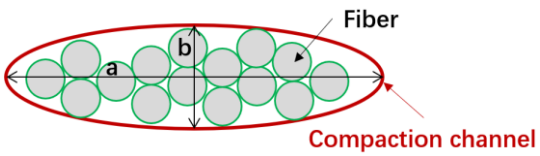

Figure A The lens-shaped compaction cannel.

- Influence of microstructural parameters: the simulation strategy developed here also made it possible to study the influence of microstructural parameters on the mechanical behavior. The generator created made it possible to take into account different parameters of the microstructure, such as the slenderness, curvature, deflection of the fibers in the different planes. Although the curvatures and slenderness of the fibers have been extensively studied here, there remains a lot of analysis to be carried out on the deflection, particularly from a quantitative point of view. It might be interesting, for example, to explore deeply how the degree of fiber deflection within the network affects the compaction behavior. Additionally, it is important to note that during the gravity contact stabilization process, the degree of fiber deflection may change and impact the accuracy of the results. Therefore, future work could improve the generator to reduce this error, and ensure that the degree of fiber deflection during the simulation perfectly matches the initial geometry.
- Simulate the transverse compaction behavior of untwisted or twisted yarns to predict the morphology of the cross-section and potential fiber damage.
- Number of fibers: in this study, a model sample of 40 fibers of 0.5mm diameter was taken into account. However, current technical fiber rovings are composed of hundreds to several thousand fibers of a few tens of microns diameter. In the future, it will be appropriate to produce fibrous assemblies that come closer and closer to reality, and to test their behavior under various loadings.
- Effect of sizing: taking into account sizing in simulations is also a fundamental line and a challenge in current research. The sizing process, during which the yarns are wet in a solution, makes it possible to improve their properties, such as the friction coefficient analyzed in this study. However, sizing also makes it possible to obtain other properties which are not studied here and represents a challenge due to their diversity: chemical composition, viscosity, quantity, etc. The definition of simulation parameters to take these properties into account will also require a significant number of experimental tests. To overcome this, several strategies can be implemented, such as the use of high-resolution imaging techniques to visualize the distribution of the

yarns sizing, and supply the microscopic parameters necessary for the development of more complex yarns models.

References

ABAQUS Documentation (6.5-1). (n.d.). In *ABAQUS documention (v6.5-1)*.

Abd El-Rahman, A. I., & Tucker, C. L. (2013). Mechanics of random discontinuous long-fiber thermoplastics. Part II: Direct simulation of uniaxial compression. *Journal of Rheology*, *57*, 1463–1489.

Abd El-Rahman, Ahmed I., & Tucker, C. L. (2013). Mechanics of random discontinuous long-fiber thermoplastics - Part I: Generation and characterization of initial geometry. *Journal of Applied Mechanics, Transactions ASME*, *80*.

Badel, P., Gauthier, S., Vidal-Sallé, E., & Boisse, P. (2009). Rate constitutive equations for computational analyses of textile composite reinforcement mechanical behaviour during forming. *Composites Part A: Applied Science and Manufacturing*, *40*, 997–1007.

Baudequin, M., Ryschenkow, G., & Roux, S. (1999). Non-linear elastic behavior of light fibrous materials. In *Eur. Phys. J. B* (Vol. 12).

Beil, N. B., & Roberts, W. W. (2002). Modeling and Computer Simulation of the Compressional Behavior of Fiber Assemblies. *Textile Research Journal*, *72*, 341–351.

Bier, A. M., Redel, M., & Schubert, D. W. (2023). Model to Predict Polymer Fibre Diameter during Melt Spinning. *Advances in Polymer Technology*, *2023*.

Boisse, P., Hamila, N., & Madeo, A. (2016). Modelling the development of defects during composite reinforcements and prepreg forming. *Philosophical Transactions of the Royal Society A: Mathematical, Physical and Engineering Sciences*, *374*. Royal Society of London.

Boisse, Philippe, Aimène, Y., Dogui, A., Dridi, S., Gatouillat, S., Hamila, N., … Vidal-Sallé, E. (2010). Hypoelastic, hyperelastic, discrete and semi-discrete approaches for textile composite reinforcement forming. *International Journal of Material Forming*, *3*, 1229–1240.

Cao, J., Akkerman, R., Boisse, P., Chen, J., Cheng, H. S., de Graaf, E. F., … Zhu, B. (2008). Characterization of mechanical behavior of woven fabrics: Experimental methods and benchmark results. *Composites Part A: Applied Science and Manufacturing*, *39*, 1037–1053.

Charmetant, A., Vidal-Sallé, E., & Boisse, P. (2011). Hyperelastic modelling for mesoscopic analyses of composite reinforcements. *Composites Science and Technology*, *71*, 1623–1631.

Chatti, F., Bouvet, C., Michon, G., & Poquillon, D. (2020). Numerical analysis of shear stiffness of an entangled cross-linked fibrous material. *International Journal of Solids and Structures*, 184.

Comas-Cardona, S., Le Grognec, P., Binetruy, C., & Krawczak, P. (2007). Unidirectional

compression of fibre reinforcements. Part 1: A non-linear elastic-plastic behaviour. *Composites Science and Technology*, *67*, 507–514.

Cornelissen, B. (2013). *The role of friction in tow mechanics* (University of Twente). University of Twente, Enschede, The Netherlands.

Crassous, J. (2023). Discrete-element-method model for frictional fibers. *Physical Review E*, *107*, 025003.

Czabaj, M. W., Riccio, M. L., & Whitacre, W. W. (2014). Numerical reconstruction of graphite/epoxy composite microstructure based on sub-micron resolution X-ray computed tomography. *Composites Science and Technology*, *105*, 174–182.

Daelemans, L., Tomme, B., Caglar, B., Michaud, V., Van Stappen, J., Cnudde, V., … Van Paepegem, W. (2021). Kinematic and mechanical response of dry woven fabrics in through-thickness compression: Virtual fiber modeling with mesh overlay technique and experimental validation. *Composites Science and Technology*, *207*.

Dalfi, H. K., Yousaf, Z., Selver, E., & Potluri, P. (2022). Influence of yarn hybridisation and fibre architecture on the compaction response of woven fabric preforms during composite manufacturing. *Journal of Industrial Textiles*, *51*, 5062S-5085S.

Durville, D. (2011). Microscopic approaches for understanding the mechanical behaviour of reinforcement in composites. In *Composite Reinforcements for Optimum Performance* (pp. 461–485). Elsevier.

Durville, Damien. (2005). Numerical simulation of entangled materials mechanical properties. *Journal of Materials Science*, *40*, 5941–5948.

Durville, Damien. (2008). *A finite element approach of the behaviour of woven materials at microscopic scale*.

Durville, Damien. (2010). Simulation of the mechanical behaviour of woven fabrics at the scale of fibers. *International Journal of Material Forming*, *3*, 1241–1251.

El-Ghezal Jeguirim, S., Fontaine, S., Wagner-Kocher, C., Moustaghfir, N., & Durville, D. (2012). Transverse compression behavior of polyamide 6.6 rovings: Experimental study. *Textile Research Journal*, *82*, 77–87.

Fiumarella, D., Boria, S., Belingardi, G., & Scattina, A. (2021). Experimental characterization and finite element modelling of a thermoplastic composite lamina subjected to large shear deformation. *Material Design & Processing Communications*, *3*.

Fourrier, G., Rassineux, A., Leroy, F. H., Hirsekorn, M., Fagiano, C., & Baranger, E. (2023). Automated conformal mesh generation chain for woven composites based on CT-scan images with low contrasts. *Composite Structures*, *308*.

Gassara, H. E. (2016). *Development of new measurement methods of transversal friction between fibers*.

Gassara, H. E., Barbier, G., Wagner Kocher, C., Sinoimeri, A., & Pumo, B. (2018).

Experimental evaluation of transverse friction between fibers. *Tribology International*, *119*, 112–122.

Guo, Y., Liu, Q., Li, Y., Li, Z., Jin, H., Wassgren, C., & Curtis, J. S. (2021). Discrete Element Method Model of Elastic Fiber Uniaxial Compression assemblies. *AIChE Journal*, *67*.

Haji, O., Song, X., Hivet, A., Rolland du Roscoat, S., Orgéas, L., Sinoimeri, A., … Blond, E. (2023). Modeling of Quasi-Parallel Fiber Networks at the Microscopic Scale. *Applied Composite Materials*, *30*, 653–675.

Haji Oussama. (2018). *A behaviour model of textile structures : Development, identification and implementation*.

Hivet, G., & Boisse, P. (2008). Consistent mesoscopic mechanical behaviour model for woven composite reinforcements in biaxial tension. *Composites Part B: Engineering*, *39*, 345–361.

Hwang, Y. T., Um, H. J., & Kim, H. S. (2023). Multi-scale progressive failure analysis of shear deformed woven fabric composites considering its pre-forming process. *Composites Part A: Applied Science and Manufacturing*, *174*.

Jeon, J. H., Yoon, C. K., Quan, Y. J., Choi, J. Y., Hong, S., Lee, W. Il, … Ahn, S. H. (2023). Effect of fiber entanglement in chopped glass fiber reinforced composite manufactured via long fiber spray-up molding. *Heliyon*, *9*.

Kidokoro, T., Arai, R., & Saeki, M. (2015). Investigation of dynamics simulation of granular particles using spherocylinder model. *Granular Matter*, *17*, 743–751.

Kim, Y. R., McCarthy, S. P., & Fanucci, J. P. (1991). Compressibility and relaxation of fiber reinforcements during composite processing. *Polymer Composites*, *12*, 13–19.

Latil, P., Orgéas, L., Geindreau, C., Dumont, P. J. J., & Rolland du Roscoat, S. (2011). Towards the 3D in situ characterisation of deformation micro-mechanisms within a compressed bundle of fibres. *Composites Science and Technology*, *71*, 480–488.

Li, L., Chen, L., & Li, J. C. (2011). Numerical generation technology for three-dimensional structure of high-performance fiber bundle. *Advanced Materials Research*, *332–334*, 1024–1027.

Li, Long, Zhao, Y., Yang, J., Zhang, J., & Duan, Y. (2015). An experimental investigation of compaction behavior of carbon non-crimp fabrics for liquid composite molding. *Journal of Materials Science*, *50*, 2960–2972.

Liang Yu. (2007). *X-ray fluorescence spectroscopy basics (X 射线荧光光谱分析基础)*. 科学出版社.

Long A C, & Clifford M J. (2007). *Composites forming technologies*. Elsevier.

Masse, J. P., Barbier, C., Salvo, L., Brechet, Y., Bouaziz, O., Bouvard, D., & Bréchet, Y. (2013). Description of the techniques and validation on virtual materials. *Journal of Materials Research*, *28*, 2852–2860.

Masse, J. P., & Poquillon, D. (2013). Mechanical behavior of entangled materials with or without cross-linked fibers. *Scripta Materialia*, *68*, 39–43.

Masse, J. P., Salvo, L., Rodney, D., Bréchet, Y., & Bouaziz, O. (2006). Influence of relative density on the architecture and mechanical behaviour of a steel metallic wool. *Scripta Materialia*, *54*, 1379–1383.

Meng, F. (2022, April 28). Computed tomography in process engineering. *Chemical Engineering Science*, Vol. 252. Elsevier Ltd.

Merchiers, J., Meurs, W., Deferme, W., Peeters, R., Buntinx, M., & Reddy, N. K. (2020). Influence of polymer concentration and nozzle material on centrifugal fiber spinning. *Polymers*, *12*.

Mezeix, L., Bouvet, C., Huez, J., & Poquillon, D. (2009). Mechanical behavior of entangled fibers and entangled cross-linked fibers during compression. *Journal of Materials Science*, *44*, 3652–3661.

Moustaghfir, N., El-Ghezal Jeguirim, S., Durville, D., Fontaine, S., & Wagner-Kocher, C. (2013). Transverse compression behavior of textile rovings: Finite element simulation and experimental study. *Journal of Materials Science*, *48*, 462–472.

Naouar, N., Vidal-Sallé, E., Schneider, J., Maire, E., & Boisse, P. (2014). Meso-scale FE analyses of textile composite reinforcement deformation based on X-ray computed tomography. *Composite Structures*, *116*, 165–176.

Park, J., & Kang, N. (2009). Applications of fiber models based on discrete element method to string vibration. *Journal of Mechanical Science and Technology*, *23*, 372–380.

Pham, Q. H., Ha-Minh, C., Chu, T. L., Kanit, T., & Imad, A. (2020). On microscopic and homogenized macroscopic analysis of one Kevlar® KM2 yarn under transverse compressive loading. *Mechanics Research Communications*, *104*.

Poquillon, D., Viguier, B., & Andrieu, E. (2005). Experimental data about mechanical behaviour during compression tests for various matted fibres. *Journal of Materials Science*, *40*, 5963–5970.

Prabhu, S., Naveen, D. K., Bangera, S., & Subrahmanya Bhat, B. (2020). Production of X-RAYS using X-RAY Tube. *Journal of Physics: Conference Series*, *1712*. IOP Publishing Ltd.

Rinaldi, R. G., Blacklock, M., Bale, H., Begley, M. R., & Cox, B. N. (2012). Generating virtual textile composite specimens using statistical data from micro-computed tomography: 3D tow representations. *Journal of the Mechanics and Physics of Solids*, *60*, 1561–1581.

Robitaille, F., & Gauvin, R. (1999). Compaction of textile reinforcements for composites manufacturing. III: Reorganization of the fiber network. *Polymer Composites*, *20*, 48–61.

Schmachtenberg, E., Schulte Zur Heide, J., & Töpker, J. (2005). Application of ultrasonics for the process control of Resin Transfer Moulding (RTM). *Polymer Testing*, *24*, 330–338.

Shanwan, A., Gassara, H. E., Barbier, G., & Sinoimeri, A. (2017). New experimental device for measuring the inter-fiber transversal friction. *IOP Conference Series: Materials Science and Engineering*, *254*. Institute of Physics Publishing.

Somashekar, A. A., Bickerton, S., & Bhattacharyya, D. (2011). Compression deformation of a biaxial stitched glass fibre reinforcement: Visualisation and image analysis using X-ray micro-CT. *Composites Part A: Applied Science and Manufacturing*, *42*, 140–150.

Somashekar, Arcot Arumugam. (2009). *Compression Deformation of Glass Fibre Reinforcements in Composites Manufacturing Processes*.

Stankovic, S. B. (2008). Compression hysteresis of fibrous systems. *Polymer Engineering and Science*, *48*, 676–682.

Stepan V Lomov. (2011). Deformability of textile performs in the manufacture of non-crimp fabric composites. In Stepan V Lomov (Ed.), *Non-Crimp Fabric Composites* (1st ed.).

Subramanian, G., & Picu, C. R. (2011). Mechanics of three-dimensional, nonbonded random fiber networks. *Physical Review E - Statistical, Nonlinear, and Soft Matter Physics*, *83*.

TEXTILES AND TEXTILE TECHNOLOGY. (n.d.).

THIERY, C. (2013). Tomographie à rayons X. *Techniques d'analyse*.

Toda, M., Grabowska, K., & Ciesielska-Wróbel, I. (2017). Application of micro-computed tomography (micro-CT) to study unevenness of the structure of yarns. *Textile Research Journal*, *87*, 351–368.

Toll, S. (1998). Packing mechanics of fiber reinforcements. *Polymer Engineering and Science*, *38*, 1337–1350.

Tourlonias, M., Bueno, M.-A., Fassi, G., Aktas, I., & Wielhorski, Y. (2019). Influence of friction angle between carbon single fibres and tows: Experimental analysis and analytical model. *Composites Part A: Applied Science and Manufacturing*, *124*, 105478.

van Wyk, C. M. (1946). 20—NOTE ON THE COMPRESSIBILITY OF WOOL. *Journal of the Textile Institute Transactions*, *37*, T285–T292.

Villarraga-Gómez, H., Herazo, E. L., & Smith, S. T. (2019, November 1). X-ray computed tomography: from medical imaging to dimensional metrology. *Precision Engineering*, Vol. 60, pp. 544–569. Elsevier Inc.

Wang, D., Naouar, N., Vidal-Salle, E., & Boisse, P. (2018). Longitudinal compression and Poisson ratio of fiber yarns in meso-scale finite element modeling of composite reinforcements. *Composites Part B: Engineering*, *141*, 9–19.

Wang, Y., Miao, Y., Swenson, D., Cheeseman, B. A., Yen, C. F., & LaMattina, B. (2010). Digital element approach for simulating impact and penetration of textiles. *International Journal of Impact Engineering*, *37*, 552–560.

Wang, Y., & Sun, X. (2001). Digital-element simulation of textile processes. *Composites*

Science and Technology, *61*, 311–319.

Wendling, A., Hivet, G., Vidal-Sallé, E., & Boisse, P. (2014). Consistent geometrical modelling of interlock fabrics. *Finite Elements in Analysis and Design*, *90*, 93–105.

Withers, P. J., Bouman, C., Carmignato, S., Cnudde, V., Grimaldi, D., Hagen, C. K., … Stock, S. R. (2021). X-ray computed tomography. *Nature Reviews Methods Primers*, *1*, 18.

Xiao, S., Wang, P., Soulat, D., & Gao, H. (2020). An exploration of the deformability behaviours dominated by braiding angle during the forming of the triaxial carbon fibre braids. *Composites Part A: Applied Science and Manufacturing*, *133*.

Xiao, S., Wang, P., Soulat, D., Legrand, X., & Gao, H. (2019). Towards the deformability of triaxial braided composite reinforcement during manufacturing. *Composites Part B: Engineering*, *169*, 209–220.

Xing, J. Z., Chen, L., & Li, J. C. (2010). Transverse elastic deformation behavior of aligned fiber bundles under bulk compressive pressure and longitudinal stress. *Advanced Materials Research*, *97–101*, 1689–1692.

Zhang, H., He, H., Gao, Y., Mady, A., Filipović, V., Dyck, M., … Liu, Y. (2023, February 1). Applications of Computed Tomography (CT) in environmental soil and plant sciences. *Soil and Tillage Research*, Vol. 226. Elsevier B.V.

Zheng, K., Cao, X., Jiang, Z., Chen, H., Qiu, B., Lu, W., … Wu, Z. (2024). Improved XCT image automatic segmentation for quantitative characterization of the meso-morphological features in the damaged braided composite fabric. *Composites Science and Technology*, *247*.

Zhou, G., Sun, X., & Wang, Y. (2004). Multi-chain digital element analysis in textile mechanics. *Composites Science and Technology*, *64*, 239–244.

Xinling SONG

Caractérisation expérimentale, modélisation et simulation à l'échelle microscopique du comportement mécanique des mèches de fibres

Résumé :

Le comportement mécanique d'un renfort fibreux est fondamental lors de sa mise en forme pour la fabrication des matériaux composites. Afin de prédire ce comportement, des essais mécaniques seuls ne sont pas suffisants. Il est donc nécessaire d'obtenir une véritable loi de comportement du renfort en fonction des paramètres de la structure fibreuse. L'objectif de cette thèse est d'étudier le comportement mécanique d'un assemblage de fibres quasi parallèles. Pour atteindre cet objectif, il est donc nécessaire de comprendre et quantifier l'influence des paramètres de l'architecture fibreuse sur son comportement mécanique. Une démarche mixte expérimentale/numérique est proposée. La stratégie numérique consiste à réaliser des simulations numériques par éléments finis, en dynamique explicite, en modélisant chaque fibre par une poutre B31, en contact les unes avec les autres. Au niveau expérimental, et en utilisant des assemblages de quelques dizaines de fibres modèles de 500 microns, des essais de compaction/compression sous tomographe sont réalisés. Ces essais permettent d'obtenir l'évolution de l'architecture fibreuse en fonction du chargement imposé et des conditions aux bords appliquées. Des indicateurs d'évolution de la microstructure sont alors définis afin d'analyser et post-traiter les résultats. Un algorithme de reconstruction permet de reconstruire un modèle numérique représentatif de l'assemblage testé, où chaque fibre est modélisée par une poutre B31. L'identification de la loi de comportement de la fibre permet alors de réaliser les simulations de la structure testée. La comparaison sur plusieurs types d'échantillons permet de valider la démarche numérique et ainsi de mettre au point un estimateur virtuel utilisable pour simuler le comportement d'assemblage non existant. Par la suite, une stratégie de création d'architectures fibreuses virtuelles est mise au point pour l'étude paramétrique. Celle-ci permet de créer rapidement des architectures de tout type avec des paramètres d'architectures maitrisés. Grâce à l'ensemble des étapes précédentes une étude paramétrique peut être menée et ainsi l'influence de certains paramètres peut être établie : paramètre de la microstructure initiale, diamètre des fibres, facteur de frottement fibre/fibre et trajet de chargement. Cette dernière étape permet de démontrer l'efficacité de la démarche propose et ouvre également de nombreuses perspectives.

Mots clés : Fibres, Composites, Mécanique, échelle microscopique, Modélisation

Experimental characterization, modelling and simulation at the microscale of the Mechanical behaviour of fibre bundles

Abstract:

The mechanical behaviour of a fibrous reinforcement is fundamental during its shaping for the manufacturing of composite materials. To predict this behaviour, mechanical tests alone are not sufficient. It is therefore necessary to obtain a true behaviour law of the reinforcement based on the parameters of the fibrous structure. The objective of this thesis is to study the mechanical behaviour of an assembly of quasi-parallel fibers. To achieve this objective, it is essential to understand and quantify the influence of the fibrous architecture's parameters on its mechanical behaviour. A mixed experimental/numerical approach is proposed. The numerical strategy involves conducting finite element simulations using explicit dynamics, where each fiber is modelled as a B31 beam, in contact with the others. Experimentally, using assemblies of a few dozen model fibers of 500 microns, compaction/compression tests are conducted under tomography. These tests allow for the observation of the evolution of the fibrous architecture depending on the imposed load and the applied boundary conditions. Microstructure evolution indicators are then defined to analyse and process the results. A reconstruction algorithm enables the creation of a representative numerical model of the tested assembly, where each fiber is modelled by a B31 beam. The identification of the fiber's behaviour law then allows for the simulation of the tested structure. Comparisons across several types of samples validate the numerical approach, thus enabling the development of a virtual estimator that can simulate the behaviour of non-existent assemblies. Subsequently, a strategy for creating virtual fibrous architectures is developed for parametric studies. This strategy allows for the rapid creation of various architectures with controlled parameters. With all the preceding steps, a parametric study can be conducted, establishing the influence of certain parameters: initial microstructure parameters, fiber diameter, fiber/fiber friction factor, and loading path. This final step demonstrates the effectiveness of the proposed approach and also opens up numerous future perspectives.

Keywords: Fibres, Composites, Mechanical behaviour, Microscale, Modelling

Laboratoire de Mécanique Gabriel Lamé (LaMé)

8 Rue Léonard de Vinci, 45100 Orléans